

TARGET DETECTION AND ENHANCEMENT IN HYPERSPPECTRAL DATA USING SUPER RESOLUTION MAPPING

A THESIS

**Submitted to the Delhi Technological University
for the award of the degree of**

**DOCTOR OF PHILOSOPHY
in
CIVIL ENGINEERING**

**by
AMRITA BHANDARI
(2K13/PHDCE/04)**



**DEPARTMENT OF CIVIL ENGINEERING
DELHI TECHNOLOGICAL UNIVERSITY
DELHI-110042 (INDIA)**

JULY, 2020

COPYRIGHT NOTICE

© DELHI TECHNOLOGICAL UNIVERSITY-2020

ALL RIGHTS RESERVED

DELHI TECHNOLOGICAL UNIVERSITY

(Formerly Delhi College of Engineering)

Shahbad Daultapur, Bawana Road, Delhi-110042, India



Declaration

I declare that the research work reported in the thesis entitled “**Target detection and enhancement in hyperspectral data using Super resolution mapping**” for the award of degree of *Doctor of Philosophy* in the *Department of Civil Engineering* has been carried out by me under the supervision of *Dr. K. C. Tiwari*, Professor in Multidisciplinary Centre for Geoinformatics, Delhi Technological University, Delhi, India.

The research work embodied in this thesis, except where otherwise indicated, is my original research. This thesis has not been submitted earlier in part or full or to any other University or Institute for the award of any degree or diploma. This thesis does not contain other person’s data, graphs, or other information, unless specifically acknowledged.

Amrita Bhandari
Research Scholar
(2K13/PHDCE/04)
Delhi Technological University

DELHI TECHNOLOGICAL UNIVERSITY
(Formerly Delhi College of Engineering)
Shahbad Daultpur, Bawana Road, Delhi-110042, India



Certificate

This is to certify that the thesis entitled "Target detection and enhancement in hyperspectral data using Super resolution mapping" submitted by Ms. AMRITA BHANDARI, (Reg. No.: 2K13/PHDCE/04) for the award of the degree of Doctor of Philosophy, to the Delhi Technological University, Delhi, is based on the original research work carried out by her. She has worked under my supervision and has fulfilled the requirements, which to my knowledge have reached the requisite standard for the submission of this thesis. It is further certified that the work embodied in this thesis is neither partially nor fully been submitted to any other university or institution for the award of any degree or diploma.

Dr. K.C. Tiwari
(Supervisor)
Professor, Civil Engineering
Delhi Technological University

Dr. Nirendra Dev
(DRC Chairman)
Civil Engineering
Delhi Technological University

Acknowledgements

“Great things are never done by one person; they are done by a team of people”

– Steve Jobs

Giving reference to the above said words, I sincerely appreciate the unceasing and perpetual support from some key – elements of my life.

First and foremost, I thank *the Almighty God*, for his strength, sustenance, and graces from the beginning of my academics up to this phase of being able to write the thesis for the doctoral degree. Through His choicest blessings, I could succeed in all the academic pursuits till date.

My humble appreciation and gratitude are reserved and due for my impeccable and ever – supportive supervisor *Dr. K.C. Tiwari* for his quintessential guidance and empathetic approach towards me over all these years of doing research. The cooperation, appreciations, critics and motivations received from him over this period helped in gracefully overcoming all the challenges and obstacles that came in the way.

I am indebted to the persistent support received from our Head of the Department, *Dr. Nirendra Dev*, and to all the members of *The Department of Civil Engineering* Delhi Technological University, Delhi who have always been available at the need of the hour. I would like to recognize the invaluable assistance obtained from my *Fellow Researchers of Multi-Disciplinary Centre of Geoinformatics*, Department of Civil Engineering, Delhi Technological University, Delhi, over all these years.

My words of thanks are due towards all my near and dear ones for their mental support and understanding approach that kept me motivated. My deepest gratitude goes to *my husband Mr. Pankaj Anand, my children Aadvika (6 years) and Aryavardhan (1 year)*

for showering me with their love and accommodating to the times that I could not be present with them. My humble regards are due towards my *mother Mrs. Anita Bhandari*, my *father Mr. D.K. Bhandari*, my *mother in law Mrs. Geeta Anand* and my *father-in-law Mr. Vijay Anand*, who have always guided and directed me to walk on the right path. I also appreciate all my relatives and friends for their wishes and encouragements.

Thank you so much everyone for standing beside me in this journey and keeping me work towards success!

Date:

(Amrita Bhandari)

Place: New Delhi

Abstract

Hyperspectral data, with its enhanced capabilities in terms of data capture in greater number of distinctive bands, has attracted the researchers over years to utilize and further analyze it for achieving the objectives of varied application areas. One such application area is target detection and target identification. The utilization of hyperspectral data in this field of application is still under active investigation. Several issues need to be addressed while performing detection of targets to achieve accurate results. It has been reported in literature that owing to the huge amount of data associated with the hyperspectral data, it needs to be reduced to a subset of useful bands corresponding the application under study. Dimensionality reduction has been one such method for the selection of the appropriate number of bands, however this needs to be carefully performed to ensure that there is no loss of target information. Also, due to the low spatial resolution of many sensors, there is another issue of mixed pixels, that needs to be addressed. Mixed pixels arise when more than one component jointly occupy a single pixel thereby complicating the detection of such mixed pixel targets. The problem aggravates due to the increased spectral variability which may arise due to a variety of reasons. Several techniques to handle the mixed pixels and the difficulties that arise in detection of such mixed pixel targets have been reported in literature. Spectral unmixing is one such method which aids the extraction of pure end members in the image and their corresponding abundance fractions in each pixel. However, this process needs careful handling as errors may occur in the generation of such end members and their abundance fractions. Besides, some literature is available to suggest that spectral index-based approach may also be considered for extraction of end members. The spectral unmixing methods provide the abundance fractions, but the exact spatial location of end members within the pixels remains unknown. In case of applications involving detection of targets such as tanks, aircrafts for

supporting the military applications, there is a requirement of proper identification of the target shape along with the detection of target location. Super resolution techniques have been proposed to optimize the abundance fractions to generate a subpixel map of the target but its implementation on hyperspectral data for recovery and identification of target is still limited. Moreover, the techniques are mostly based on random allocation and recursive optimizations that further complicate the process and add to the inaccuracy in detection and target identification.

Therefore, in view of these limitations, the objectives of this research which have been explored are as follows:

- a) To review various existing Dimension reduction algorithms with a view to achieve maximum possible Dimensionality reduction while ensuring minimal/no loss of the target data.
- b) To efficiently characterize the target and background spectral signatures for subpixel detection.
- c) To study various end member extraction techniques in available datasets using spectral unmixing and spectral indices-based approaches.
- d) Comparative assessment of random recursive technique with non-random non-recursive super resolution mapping technique, for subpixel target detection and enhancement.

In the first objective, a study of various combinations of dimensionality reduction (DR) techniques combined with full pixel and subpixel target detection (TD) algorithms has been performed to analyze the loss of target pixels in each case. Therefore, the tasks have been subdivided into

- a) Full pixel Target Detection with and without Dimensionality Reduction

- b) Full pixel Target Detection with and without Dimensionality Reduction, along with the study of impact of Background characterization and,
- c) Subpixel Target Detection with and without Dimensionality Reduction, along with the study of impact of Background characterization

For achieving the tasks mentioned above, two different sets of **hyperspectral datasets** have been explored. From the experiments it has been observed that in the case of full pixel targets, both dimensionality reduction and target detection result in the loss of target information, however, there is a greater loss of target information in the case when dimensionality reduction precedes target detection in comparison to a case where target detection is applied without dimensionality reduction. Background characterization appears to aid in improvement of full pixel target detection, and K-means is seen to provide better results of detection. In the case of subpixel target detection, however, there appears to be loss of subpixel target information in the case where detection alone is performed in comparison to a case where dimensionality reduction precedes target detection.

In the second objective, the focus is on target and background subspaces, and how these subspaces aid or inhibit the process of detection of full pixel and mixed pixel targets has been discussed. The tasks outlined in this objective are:

- a) Detection of low probability full pixel / subpixel targets with known spectral signatures,
- b) Detection of targets using background and target subspaces,
- c) Analysis of the impact of various combinations of background subspaces on full pixel and subpixel target detection, and,
- d) Analysis of the impact of illumination conditions on the targets.

Various conclusions have been drawn from the results obtained. In case of detection using target and background subspaces, it may be concluded that for any given algorithm, if

the algorithm is performing well for detection of target pixels, the different background subspaces appear to have only marginal impact. Also, in case of analysis of target detection algorithms, Matched Filter is observed to perform better than other algorithms considered. It has been observed that illumination affects the detection of targets immensely, where target pixels of targets in full illumination placed over Gravel roads and Grass are detected well in comparison to those under trees. Also, the targets in partial shade are detected whereas the targets in full shade are not detected by the above discussed algorithms for any combination of background subspace. After an analysis of the spectral profiles, it has been concluded that the surrounding vegetation (trees) has a greater impact on the spectral behaviour of pixel containing blue felt target. The gravel roads have minimum impact on spectral variation of this target out of the three background types. This appears to indicate that spectral contrast / similarity between the target and the background has a significant role in its detection.

In the third objective, the end member extraction in mixed pixels using Spectral Unmixing and Spectral Indices based approaches has been performed. Accordingly, there are three major tasks that have been explored / studied in this chapter.

- a) End member extraction and abundance estimation using spectral unmixing,
- b) Evaluating spectral indices for end member identification, and

In case of spectral unmixing, it has been observed that ICA-EEA and Nfindr perform best while recovering the image end members including the target spectra, followed by ATGP, while PPI performed poorly in this case. Also Spectral indices provide a suitable way to extract / generate end members.

The fourth objective further extends the study of extraction of full pixel and subpixel targets in hyperspectral data by optimizing the spatial distribution of subpixels inside any given pixel based on the available abundance fractions. The super resolution has been studied as a means to suggest the most optimized spatial distribution/ arrangement of these subpixels

belonging to different end members/ components inside the mixed pixel. Random recursive pixel swapping method and the non – random non - recursive inverse Euclidean distance method have been studied on synthetic data sets and analyzed in terms of computation time and accuracy of detections. It has been observed that inverse Euclidean distance-based method (IED) (for binary class problems) certainly performs better than the PS (Pixel swap) in terms of accuracy for both the synthetic and hyperspectral data sets.

In this research, certain major issues, problems and gaps in target detection and enhancement such as size of targets, spectral variability, problem of mixed pixels, advantage of non-random non-recursive super resolution algorithms *etc.* have been explored. Some of the major findings / contributions are briefly mentioned here. Both dimensionality reduction (DR) and target detection (TD) lead to a loss of target information, however there is a greater loss of information when DR precedes TD. However, in the case of subpixel targets, there appears to be a loss of subpixel target information when TD alone is performed. Similarly, it has been found that non-random non-recursive algorithms definitely perform better than random recursive algorithms both in synthetic as well as hyperspectral data. While several minor / major issues in target detection have been explored in this research, there still remain many more issues in target detection and enhancement that need to be explored in future particularly using hyperspectral data.

Table of Contents

Declaration	i
Certificate	ii
Acknowledgements	iii
Abstract	v-ix
Table of Contents	x-xv
List of Publications	xvi
List of Figures	xvii-xxi
List of Tables	xxii-xxiv
List of Abbreviations	xxv-xxix

CHAPTER 1 TARGET DETECTION AND ENHANCEMENT IN HYPERSPECTRAL DATA USING SUPER RESOLUTION MAPPING

1 – 24

1.1	Motivation	1
1.2	Introduction to the Problem	1
1.2.1	Target Detection (TD) in Hyperspectral Data	2
1.2.2	Super Resolution Mapping	7
1.2.2.1	Definition	7
1.2.2.2	Concept of Super Resolution	8
1.2.2.3	Review of Existing Super Resolution	10
	Approaches	
1.3	Research Gaps	14
1.3.1	Loss of Target Information During Dimensionality Reduction	14
1.3.2	Assessment of Background Characterization in Subpixel Target Detection	16
1.3.3	Errors in Unmixing, Comparative Assessment of Unmixing Algorithms and Alternative approaches in Abundance Fraction Estimation.	17
1.3.4	Random Recursive Vs Non-Random Non-Recursive Super Resolution Approaches	19

1.4	Research Objectives	22
1.5	Organization of Thesis	22

CHAPTER 2 DIMENSIONALITY REDUCTION WHILE ENSURING MINIMAL OR NO-LOSS OF TARGET DATA 25-56

2.1	Introduction to the Problem	25
2.1.1	Selection of TD and DR algorithms	26
2.2	Experimental Data Set	30
2.2.1	Data Set-1: SHARE-2010	30
2.2.1.1	Acquisition and Characteristics of Data Set-1	31
2.2.2	Data Set-2: SHARE-2012	31
2.2.2.1	Acquisition and Characteristics of Data Set-2	32
2.2.3	Ground Data Collection	34
2.3	Methodology and Implementation	36
2.3.1	Full pixel Target Detection with and without Dimensionality Reduction	37
2.3.2	Full pixel Target Detection with and without Dimensionality Reduction and Background characterization	39
2.3.3	Subpixel Target Detection with and without Dimensionality Reduction and Background characterization	40
2.4	Results and Discussions	40
2.4.1	Full pixel Target Detection without Dimensionality Reduction in Data Set-1	40
2.4.2	Dimensionality Reduction linked Full pixel Target Detection In Data Set-1	42
2.4.3	Full pixel Target Detection without Dimensionality Reduction in Data Set-2 without considering Background characterization	43
2.4.4	Dimensionality Reduction linked Full pixel Target Detection in Data Set-2 considering Background characterization	44

2.4.5	Subpixel Target Detection in Data Set-2 considering Background characterization	49
2.4.5.1	Dimensionality Reduction linked Subpixel Target Detection in Data Set-2 considering Background characterization	49
2.4.5.2	Subpixel Target Detection without Dimensionality Reduction in Data Set-2 considering Background characterization	52
2.5	Conclusions	56

CHAPTER 3 FULL PIXEL AND SUBPIXEL TARGET DETECTION USING TARGET AND BACKGROUND SUBSPACES 58-87

3.1	Introduction to the Problem	58
3.2	Experimental Data Set	59
3.2.1	Data Set-2 (Subset S2)	59
3.2.2	Data Set-3: SHARE-2012 (Subset S3)	60
3.2.2.1	Targets in Data Set-3	61
3.3	Target and Background Subspaces	63
3.3.1	Theoretical explanation	64
3.4	Methodology and Implementation	65
3.5	Results and Discussions	67
3.5.1	Assessment of subpixel target detection on Subset S2	68
3.5.2	Impact of different background types on the detection of target (Data Set – 3)	68
3.5.3	Target Detection in different Background subspaces	70
3.5.3.1	Target Detection using Background subspaces – Mixed(Trees, Grass, Roads(Gravel) and Red_Felt)	70
3.5.3.2	Target Detection using Background subspace – Trees	72
3.5.3.3	Target Detection using Background subspace – Grass	74
3.5.3.4	Target Detection using Background subspace –	

Gravel Roads	76
3.5.3.5 Analysis of the impact of different background subspaces on the detection of target	78
3.5.4 Impact of background subspaces and illumination conditions on detection	81
3.6 Conclusions	85
CHAPTER 4 END MEMBER EXTRACTION IN MIXED PIXELS USING SPECTRAL UNMIXING AND SPECTRAL INDICES APPROACHES	88-139
4.1 Introduction to the Problem	88
4.2 Spectral Unmixing and Spectral Indices based approach for end member	90
4.2.1 Review of spectral unmixing based approaches	90
4.2.1.1 Spectral Unmixing for end member extraction and Abundance Estimation	90
4.2.1.2 Limitations of Spectral unmixing	94
4.2.2 Concept of Spectral Indices for end member identification	96
4.2.2.1 Brief review of existing spectral indices	97
4.2.2.2 Development of spectral indices for hyperspectral data	101
4.3 Experimental Data Set	104
4.3.1 End member extraction and abundance estimation using spectral unmixing	105
4.3.2 Evaluating spectral indices for end member extraction.	107
4.3.2.1 Data Acquisition and characteristics	108
4.3.2.2 Ground truth Data	110
4.3.2.3 Spatial subsets	111
4.4 Methodology	113
4.4.1 End member extraction and abundance estimation using spectral unmixing	113
4.4.1.1 Identification of pure end members for the image	113

4.4.1.2	Generation of abundance maps using FCLS	113
4.4.1.3	Computation of Fractional abundances	114
4.4.1.4	Accuracy assessment	114
4.4.2	Evaluating Spectral Indices for end member identification	115
4.5	Results and Discussions	115
4.5.1	End member Extraction and Abundance Estimation using Spectral Unmixing	115
4.5.1.1	Identification of pure end members for the image	115
4.5.1.2	Generation of abundance maps using FCLS	117
4.5.1.3	Computation of Fractional abundances	121
4.5.1.4	Accuracy assessment	124
4.5.2	Evaluating Spectral Indices for end member identification	127
4.5.2.1	Spectral Library creation	127
4.5.2.2	Selection of appropriate wavelength regions	132
4.5.2.3	Implementation of Spectral Indices	132
4.6	Conclusions	139
CHAPTER 5 A NON - RANDOM, NON – RECURSIVE SUPER RESOLUTION MAPPING TECHNIQUE		140-179
5.1	Introduction	140
5.2	Limitations of Random, Recursive Super Resolution Algorithms	143
5.3	Experimental Data Set	145
5.3.1	Synthetic Data	145
5.3.2	Hyperspectral Data	146
5.3.3	Multi - sensor, Multi – resolution, Temporal Urban dataset	148
5.4	Methodology and Implementation	149
5.4.1	Common Aspects of both Random Recursive (Pixel Swap) and Non-random Non- Recursive (Inverse Euclidean Distance) Super resolution Algorithms	149

5.4.2	Random Recursive (Pixel Swap) Super resolution Algorithm	151
5.4.3	Non - Random and Non - Recursive (Inverse Euclidean Distance) Super resolution Algorithm	153
5.4.4	Implementation	158
5.4.4.1	Implementations on Synthetic Data	158
5.4.4.2	Implementations on Hyperspectral Data	159
5.4.4.3	Implementations on Multi - sensor, Multi – resolution, Temporal Urban Data	159
5.5	Results and Discussions	159
5.5.1	Super Resolution using Synthetic Data	160
5.5.2	Super Resolution Using Hyperspectral (<i>AVIRIS</i>) Data	168
5.5.3	Preliminary results on Multi-Sensor, Multi-Resolution, Temporal Urban dataset	173
5.6	Conclusions	178
CHAPTER 6 SUMMARY, CONCLUSIONS, CONTRIBUTIONS AND FUTURE WORK		181-180
6.1	General	181
6.2	Objectives and Methodology	181
6.3	Conclusions	183
6.4	Major Contributions	184
6.5	Limitations	187
6.6	Future Work	188
References		190 - 207
Brief Biodata of the Author		208

List of Publications

A. International Journals

- I.** Bhandari, A.; Tiwari, K.C. (2019), “Loss of target information in full pixel and subpixel target detection in hyperspectral data with and without dimensionality reduction”, *Evolving Systems*. Springer, 1-16. DOI: <https://doi.org/10.1007/s12530-019-09265-w>. (**Status- Paper Published**).
- II.** Dr. K. C. Tiwari, Amrita Bhandari (2020). “A Euclidean Distance based Super Resolution method for Sub Pixel target detection in Hyperspectral Images”, **GIS Business**, <https://journals.Eduinde.org/index.php/gis/article/view/18901>. 15(2), 104-124. (**Status- Paper Published**).
- III.** Amrita Bhandari & K. C. Tiwari, “Identification for Urban Land Cover Using Hyperspectral Data by Spectral Index Analysis”, (**Status- In Progress**).

B. International Conferences

- I.** Amrita, K C Tiwari (2016) “A comparative assessment of various super-resolution techniques in target detection and enhancement using hyperspectral data”, *Proc. Of SPIE Vol. 9880*, Multispectral, Hyperspectral, and Ultraspectral Remote Sensing Technology, Techniques and Applications VI, 98801V. (**Status - Paper Published**).
- II.** Amrita Bhandari, Dr. K.C. Tiwari (2015), “A Review of Spectral Unmixing Techniques in Target Detection”, *International Journal of Engineering Technology, Management and Applied Sciences*, September 2015, Volume 3, Special Issue, ISSN 2349-4476 (**Status - Paper Published**).

List of Figures

Figure No.	Title	Page No.
1.1	Target in Hyperspectral Data	3
1.2	Target spectra used in spectral modelling and problems of spectral modelling	4
1.3	Depiction of targets in real life scenario.	5
1.4	Cases in which a target may occupy a pixel in hyperspectral images	6
1.5	Super resolution mapping	10
	(a) Natural ground cover layout with vegetation (green), soil (brown) and Urban area (Grey) classes	
	(b) Capture of ground layout in a 2x2 image	
	(c) super resolution at scale factor of 3 and	
	(d) super resolution mapping at scale factor of 5.	
1.6	Organization of the Thesis in the form of a flowchart	24
2.1	(a). RGB image showing Cooke city and surrounding terrain,	31
	(b). A zoomed-in part of Cooke city, showing locations of V1, V2 and V3.,	
	(c). Spectral signatures of vehicles V1, V2 and V3 present in data,	
	(d). Spatial subset S1 of 190x84 pixels selected from available image of Cooke city	
2.2	(a). Mosaic of SpecTIR images in the visible spectrum for the morning pass over the main ground truth site,	32
	(b). A zoomed in picture of the unmixing target Y1.	
	(c). RGB image of Targets Y1 and Y2 selected for unmixing target detection experiment in a Spatial subset S2 of 150x150 pixels placed on asphalt court.	
2.3	Google earth image of the AVON city showing the line of sight.	33
2.4	Images from the Ground truth collection done during the SHARE 2012 campaign	34
2.5	Spectral signatures of targets Yellow felt and Yellow cotton	34

2.6	Flowchart explaining the steps followed to achieve the objectives of this chapter	38
2.7	Endmember spectra obtained from (a). SMACC, (b). K-Means	46
2.8	A result of performing LMM on a 150x150 spatial subset S2	50
3.1	Mixed pixel target Y1 and full pixel target Y2 in subset S2	60
3.2	True color representation of subset S3 of size 140x244 in visible spectrum	60
3.3	Ground spectra for target materials and the background types	61
3.4	Annotated aerial image of Avon site with target locations identified	62
3.5	Defining the target and background subspaces	63
3.6	Flowchart representing the steps followed to perform full pixel and sub pixel target detection using target and background subspaces	67
3.7	Spectral variations observed in the case of target Blue Felt when it has been placed over different background types	69
3.8	Results of detection considering mixed background subspace for algorithms a) MF b) OSP c) ACE and d) TCIMF	71
3.9	Results of detection considering background subspace - Trees for algorithms a) MF b) OSP c) ACE and d) TCIMF	73
3.10	Results of detection considering background subspace – Grass for algorithms a) MF b) OSP c) ACE and d) TCIMF	75
3.11	Results of detection considering background subspace – (Gravel) Roads for algorithms a) MF b) OSP c) ACE and d) TCIMF	77
3.12	Graphic representation of the results of detection considering four different combinations of background subspaces.	80
4.1	Flowchart representing the order of implementation to create spectral library	102
4.2	A Flowchart for step by step explanation of implementing spectral indices for end member extraction	104
4.3	A true colour representation of spatial subset 4 (100x112) selected from Data set – 2, target YF is marked with red circle.	106
4.4	A zoomed in RGB image depicting the target YF placed on the asphalt court.	106
4.5	Flight paths during AVIRIS-NG data collection campaign	108

4.6	RGB image showing Ahmedabad city and the site ID's allotted to 15 landmarks.	109
4.7	Zoomed image showing the Site id 1 – Ten Acre Mall	110
4.8	Zoomed image showing the Site id 2 – Kankaria Railway Yard	110
4.9	Field pictures taken during the ground data collection.	111
4.10	(a) Subset SS1 (b) Subset SS2	112
4.11	Flowchart to show the steps of implementation for spectral unmixing	114
4.12	(a). The graph representing the spectra of target obtained from the image in red and the spectra recorded using ground truth values in blue. (b). True color image representing the components 2,5,9 in the reduced image (20 bands) after performing PCT (c). The gray scale image representing the component number 10 in the reduced set.	116
4.13	End members recovered using (a) ATGP, (b) ICA-EEA (c) NFindr and (d) PPI	117
4.14	Abundance maps generated using ATGP	118
4.15	Abundance maps generated using N-Findr	119
4.16	Abundance maps generated using ICA-EEA	120
4.17	Combined abundance image showing error is shown for (a) ATGP, (b) ICA-EEA, (c) NFindr.	121
4.19	ROC curves obtained for (a) ATGP, (b) ICA-EEA, (c) NFindr.	125
4.20	Histograms showing errors obtained for (a) ATGP, (b) ICA-EEA, (c) NFindr.	126
4.21	Spectral library for Impervious surfaces – Road (a). Parking lot-Road (Bitumen), (b). Bitumen Road (c). Concrete Road	127
4.22	Spectral library for Impervious surfaces – Roof (a). Asbestos sheet, (b) Red mangalore tile roof, (c) bitumen membrane roof, (d) reinforced cement, (e) wood tile roof, (f) bitumen water proofing, (g) Corrugated GI sheet, (h) corrugated GI sheet in shadow, (i)AC duct Iron, (j)convention hall metal sheet and (k) convention hall metal sheet shadow, (l) PVC fibre, (m) Polythene blue, (n) polythene black, (o) green cloth shed, (p) redcarpet cloth, (q) plastic+cloth.	128-129

4.23	Spectral library for Pervious surfaces – Soil (a). Bare soil, (b). Ground, (c) Sand, (d) unpaved soil, (e) excavation soil	130
4.24	Spectral library for Pervious surfaces – Vegetation (a). Bushes, (b). Lawn grass	130
4.25	Impervious surface - Roof and roads (targets) detection using new built up index (NBI)	132
4.26	Impervious surface - Roof and roads (targets) detection using Normalised different built up index (NDBI)	133
4.27	Impervious surface - Roof and roads (targets) detection using Normalised built up area index (NBAI).	133
4.28	Impervious surface - Roof and roads (targets) detection using - The band ratio for built up area (BRBA)	134
4.29	Impervious surface detection using MBI	135
4.30	Google Earth images of target sites (a) Ten Acre Mall, (b) Kankaria Railway Yard	135
4.31	Impervious surface extraction and corresponding subtraction images for site Kankaria Railway Yard using (b,g) NBI (c,h) NBAI (d,i) BRBA (e,j) MBI (f,k) NDBI	137
4.32	Impervious surface extraction and corresponding subtraction images for site Ten Acre Mall using (b,g) NBI (c,h) NBAI (d,i) BRBA (e,j) MBI (f,k) NDBI	137
5.1	30x30 pixels approximating the shape of (a) a vehicle (Synthetic- I) (b) a temple (Synthetic- II) (c) a circle (Synthetic- III) (d) an Aircraft (Synthetic- IV). Edges of these shapes have fractions from 0.25 to 0.9.	146
5.2	(a). Subset of 200x200 pixels selected from AVIRIS Dataset containing five targets: T1, T2, T3, T4, T5 (b). Spatially segmented image of 40x40 pixel size, with three targets: T3, T4 and T5 (c). Spatially segmented image of 40x40 pixel size, with two targets: T1, and T2	147

5.3	(a). Original Images of Udaipur region acquired from different sensors	148
	(b). Images obtained as results of spectral unmixing using LMM	
5.4	(a) An $M \times N$ Image array for super resolution,	153
	(b) 8- pixel neighbourhood.	
	(c) Consideration of pixel for super resolution mapping	
5.5	(a) 2x2 pixel neighbourhood.	154
	(b) 4x4 pixel neighbourhood.	
	(c) 8x8 pixel neighbourhood	
5.6	Abundance fractions of endmember in PX1 to PX9 in a 3x3 pixel array is af1 to af9	155
5.7	Super resolution in case of Synthetic-I data containing targets approximating the shape a vehicle	164
5.8	Super resolution in case of synthetic-II data containing targets approximating the shape a temple	165
5.9	Super resolution in case of synthetic-III data containing targets approximating the shape a circle	166
5.10	Super resolution in case of synthetic-IV data containing targets approximating the shape of an aircraft	167
5.11	Super resolution of AVIRIS data using Atkinson's pixel swapping method	170
5.12	Super resolution of AVIRIS data using inverse Euclidean distance- based method	171
5.13	RGB implementation of inverse Euclidean distance based super- resolved AVIRIS data	172
5.14	Super Resolution in Landsat – 8	174
5.15	Super Resolution in SENTINEL -2B	175
5.16	Super Resolution in AVIRIS – NG	176
5.17	Comparison of Super Resolution in Different Data Sets of Different Resolutions	177

List of Tables

Table No.	Title	Page No.
1.1	Target Categorization	3
1.2	Target detection process	7
1.3	A review of some of the existing super resolution mapping techniques	13,14
2.1	General acquisition parameters for Data Set-1	30
2.2	General acquisition parameters for Data Set-2	32
2.3	A summary of Data sets, targets and target pixels selected for the implementation.	35
2.4	Full pixel TD results for 126 bands and window of size 20x30 pixels in Subset S1 of Data set-1	41
2.5	DR linked TD results and their assessment using a window of size 20x30	42
2.6	Full pixel TD results for 360 bands, targets, and a window of size 20x30 pixels in Data set-2, without DR and without background characterization.	44
2.7	DR linked TD results for targets and their assessment using a window of size 20x30 – Data set-2 and without background characterization	45
2.8	TD results and their assessment using a window of size 20x30 pixels – Data set-2 with background characterization using SMACC and K-Means.	46
2.9	DR linked TD results for target - yellow felt and their assessment using a window of size 20x30 pixels – Data set-2 and background characterization using SMACC	47
2.10	DR linked TD results for target - yellow felt and their assessment using a window of size 20x30 pixels – Data set-2 and background characterization using K-MEANS.	48
2.11	(a). Fractional composition obtained after LMM of yellow felt in Y1 (b). Fractional composition obtained after LMM of yellow cotton in Y1	50

2.12	Fractional compositions of both yellow felt and yellow cotton in the 8x8 pixels in subset S2	51
2.13	Values corresponding to target detected / not detected in the 8x8 pixels panel.	52
2.14	(a): Fractional composition obtained after LMM of yellow felt in Y1 (b): Fractional composition obtained after LMM of yellow cotton in Y1	53
2.15	Fractional compositions of both yellow felt and yellow cotton in the 8x8 pixels in subset S2	53
2.16	Values corresponding to target detected / not detected in the 8x8 pixels panel.	54
2.17	A summary of results obtained for target detection using various combinations of DR and TD algorithms for full pixel and subpixel targets	56
3.1	Table representing targets under considerations and target ID's allotted to blue felt targets for present work and the super category to which targets belong.	62
3.2	Target detection results for Blue Felt using different TD algorithms for Mixed background subspace (image size of 140x244).	71
3.3	Target detection results using different TD algorithms for Trees as background subspace (image size of 140x244)	73
3.4	Target detection results using different TD algorithms for Grass as background subspace (image size of 140x244).	75
3.5	Target detection results using different TD algorithms for Roads (Gravel) background subspace (image size of 140x244).	77
3.6	Target detection results for target Blue Felt after performing characterization using target and background subspaces	79
3.7	Results of detection wrt the illumination conditions for target placements with mixed, trees, grass and gravel roads as background subspace.	82
4.1	A summary of spectral unmixing algorithms for hyperspectral images	92,93
4.2	(a) Level-wise categorization of major impervious surfaces.	97
	(b) Level-wise categorization of major pervious surfaces	97

4.3	Spectral indices for identification of pervious surfaces	98,99
4.4	Spectral indices for impervious surfaces	100
4.5	General acquisition parameters for Data set – 4	108
4.6	Site ID's allocated to a few areas in Hyperspectral data collected by AVIRIS -NG sensor over Ahmedabad city	109
4.7	Levels of division of surface types	112
4.8	Abundance fraction of yellow felt in mixed pixel target YF (8x8) – ATGP	122
4.9	Abundance fraction of yellow felt in mixed pixel target YF (8x8) – ICA-EEA	122
4.10	Abundance fraction of yellow felt in mixed pixel target YF (8x8) – Nfindr	122
4.11	Values corresponding to target detected/non detected in YF (8x8) – ATGP	123
4.12	Values corresponding to target detected/non detected in YF (8x8) – ICA-EEA	123
4.13	Values corresponding to target detected/non detected in YF (8x8) – Nfindr	123
4.14	Accuracy of unmixing results obtained using three selected algorithms.	124
4.15	Selection of appropriate spectral bands	131
4.16	Assessment of pixels detected using Spectral Indices	138
5.1	Data specifications of hyperspectral data of Urban region	149
5.2	Computation of the number of subpixels attracted to the neighbourhood pixels	157
5.3	Classification accuracy for shape approximating vehicle (Synthetic-I)	163
5.4	Classification accuracy for shape approximating temple (Synthetic-II)	163
5.5	Classification accuracy for shape approximating circle (Synthetic-III)	163
5.6	Classification accuracy for shape approximating aircraft (Synthetic-IV)	163
5.7	Computation time using IED on Multi-sensor, Multi- resolution Temporal Urban data	178

List of Abbreviations

ACE	Adaptive Coherence Estimator
ACORN	Atmospheric correction now
ANN	Artificial Neural Network
ATREM	Atmospheric removal program
ATCOR	Atmospheric correction
ATGP	Automatic target detection procedure
AVIRIS-NG	Airborne Visible/Infrared Imaging Spectrometer, New Generation
BAEI	Built-Up Extraction Index
CCA	Connected Component Analysis
CEM	Constrained Energy Minimization
CP	Central Pixel
CPU	Central Processing Unit
DR	Dimensionality Reduction
EL	Empirical Line
EM	Electro Magnetic
ENVI	Environment for Visualizing Images
FCLS	Fully constrained least squares algorithm
FF	Flat Field
FLAASH	Fast Line-of-sight atmospheric analysis of spectral Hypercube

FOV	Field-Of-View
FN	False Negatives
FP	False Positives
GCP	Ground Control points
GRVI	Green Ratio Vegetation Index
GSD	Ground Sampling Data
HATCH	High accuracy atmospheric correction of hyperspectral data
HNN	Hopfield Neural Network
HS	Hyperspectral
HYSI	Hyperspectral Imaging
IAR	Internal Average Reflectance
ICA	Independent Component Analysis
ICA-EEA	Independent Component Analysis – end member extraction
IFOV	Instantaneous Field-Of -View
IED	Inverse Euclidean Distance
IR	Infra-Red
ISRO	Indian Space Research Organization
LDA	Linear Discriminant Analysis
LIDAR	Light Detection and Ranging
LMM	Linear Mixture Model
LWIR	Long Wave Infrared

MATLAB	Matrix Laboratory
MBI	Morphological Building Index
MIR	Middle Infrared
MF	Matched Filter
MNDWI	Modified Normalized Difference Water Index
MNF	Minimum Noise Fraction
MRF	Markov Random Field
MTMF	Mixture tuned Matched filter
NASA	National Aeronautics and Space Administration
NBAI	Normalized Built-Up Area Index
NDBI	Normalized Difference Built-Up Index
NDCI	Normalized Difference Clay Index
NDISI	Normalized Difference Impervious Surface Index
NDMI	Normalized Difference Moisture Index
NDSI	Normalized Difference Snow Index
NDVI	Normalized Difference Vegetation Index
NDWI	Normalized Difference Water Index
NED	Normalised Euclidean Distance
NIR	Near-Infrared
OIF	Optimum Index Factor
OSAVI	Optimized Soil Adjusted Vegetation Index

OSP	Orthogonal subspace projection
PAN	Panchromatic
PCA	Principal Component Analysis
PCT	Principal Component Transformation
PPI	Pixel purity index
PSO	Particle Swarm Optimisation
QUAC	Quick Atmospheric Correction
RDVI	Renormalized Difference Vegetation Index
RIT	Rochester Institute of Technology
RS	Remote Sensing
SAM	Spectral Angle Mapper
SAVI	Soil Adjusted Vegetation Index
SID	Spectral Information Divergence
SI	Spectral Indices
SMACC	Sequential Maximum Angle Convex Cone
SRCI	Simple Ratio Clay Index
SVM	Support Vector Machine
SWIR	Short Wave Infrared
TD	Target Detection
TP	True positives
TN	True Negatives

VIS	Visible
VHR	Very High Resolution
VNIR	Visible and Near Infrared

Chapter 1:

Target Detection and Enhancement in Hyperspectral Data using Super Resolution Mapping

1.1 Motivation

India, since its independence in 1947, has experienced regular invasions from across its northern borders. It has fought several bitter wars with its two major northern adversaries who always seem to be colluding to nibble away Indian territories or dominate various roads connecting the state of Jammu and Kashmir with the rest of India. Earlier India did not have an advanced space technology, but now it is amongst top few countries of the worlds having advanced space technologies. Yet there are several constraints of image processing and interpretation such as low spatial resolution that necessitate development of advanced satellite image processing and information extraction techniques. In the absence these advanced techniques, the country, despite having huge of amounts of satellite data, is still unable to regularly monitor the intrusions from across the borders.

The Kargil intrusion of 1999 and the recent Chinese intrusions of 2020 across LAC are some of the examples. One such technique that needs to be evolved is *Super Resolution* which may address the issue of low spatial resolution and facilitate the comparison of multi-sensor multi-resolution data. This is also one of the key requirements of the Indian Defence Forces and it therefore continues to be an Indian Defence Innovation Challenge even in 2020 (<https://idex.gov.in/>).

1.2 Introduction to the Problem

This section discusses the contours of the problem presented in this thesis. This is done in two subsections, first a discussion on relevant aspects of target detection in

hyperspectral data is presented, and then the concept and problems in super resolution is discussed.

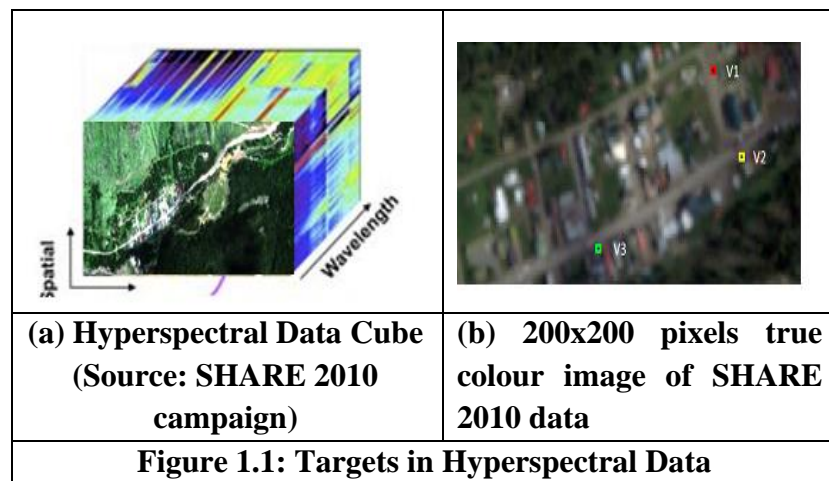
1.2.1 Target Detection (TD) in Hyperspectral Data

Remote Sensing technologies have revolutionized the field of security and surveillance by significantly improving the processes involved in detection, monitoring, processing, extracting, analyzing, and visualizing the information related to any feature or object lying on the surface of Earth without direct physical contact with it (Stojce 2019, Camps-Valls *et al.* 2011, Richards 1999). This definition mostly applies to the earth observation from an airborne or a space-borne platform. These platforms are equipped with highly advanced sensors to acquire images that assist the users to remotely “sense” the features on the surface of the Earth, thereby resulting in an exponential rise in the applications seeking to explore Mother Earth from the space (Mark 2017, Launius. Roger D, 2005, Launius. Roger D, 1994). There have been continuous developments in the various fields associated with remote sensing such as sensor technologies, image processing *etc.*

Fuelled by the requirements of higher accuracy in remote sensing applications, the data acquisition process has undergone significant qualitative and quantitative upgradation. The spatial resolution of the sensors has evolved over time, and so has the spectral resolution from single band coarse resolution panchromatic data to multiple bands multispectral data and now to hyperspectral data consisting of hundreds of bands (Rustamov *et al.* 2018, Dalla *et al.* 2011, Cracknell 1998). Hyperspectral sensors, currently available, have the capability to capture the data of earth surface in hundreds of contiguous, narrow spectral bands (Ghamisi *et al.* 2017). This has allowed in-depth examination of the earth’s features which was otherwise not possible with Coarse resolution data (Chen *et al.* 2020, Stuart *et al.* 2019). Enhanced spectral capability has greatly improved accuracies in

several applications particularly those related to target detection and identification (Freitas *et al.* 2018, Davood *et al.* 2012).

A target refers to an object / feature on earth surface with known spectral signature that is of interest to the users as shown in Figure 1.1 (Maria *et al.* 2016, Manolakis *et al.* 2000). Thus, Target detection (TD) refers to the process of searching the pixels of interest in a hyperspectral data cube using its known spectral signatures (Maria *et al.* 2016, Eismann 2012, Bitar *et al.* 2020, Shaw *et al.* 2003).



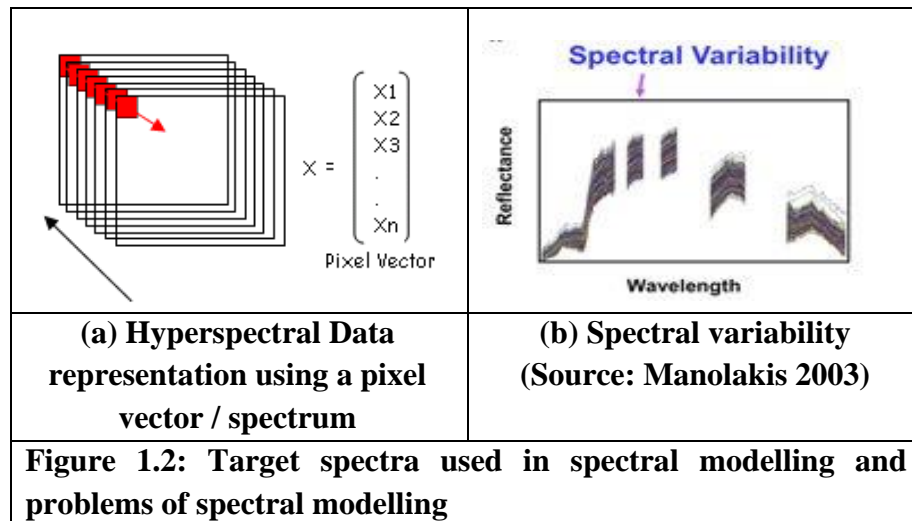
Target detection using hyperspectral data is affected by its location, condition, shape, size *etc.* and is accordingly classified as shown in Table 1.1 (Gautam *et al.* 2020, Arora and Tiwari, 2013).

Table 1.1 – Target Categorization

Target categorization constraint	Target Classification
Target Location	Surface, Subsurface or Air
Target Condition	Full illumination / Hidden / Camouflaged / buried
Target Shape	Point/ Linear / Area
Target Size	Group of pixels, full pixel, or mixed pixel

Most target detection algorithms are based on spectral modelling and are classified as spectral matching algorithms or anomaly detection algorithms. All such algorithms which are spectrally modelled make use of library spectra making *a-priori* availability of target spectra/ information necessary (Song *et al.* 2020). Besides, all spectrally modelled algorithms suffer from the fact that most of the artificial targets exhibit high spectral variability (Zhang and Gaigai, 2020).

Figure 1.2 shows hyperspectral data representation using a pixel vector / spectrum and the spectral variability. In case, library spectra are not available, then the target detection requires extraction of endmember spectra from the scene itself.



Now, based on the foregoing background on target detection, the detection problem can be cast as a hypothesis testing problem (Manolakis *et al.* 2016), where the two hypotheses are,

Null Hypothesis

$$H_0 : r = s_b a_b + w$$

(Target absent)

1.1

And,

Alternative Hypothesis

$$H_1 : r = s_t a_t + s_b a_b + w$$

(Target present)

1.2

, where s_t and s_b are the spectral signature of target and background and a_t and a_b are the corresponding abundance fractions.

The above hypothesis testing problem is often solved using a goodness of fit measure applied between known target spectra (available from the spectral libraries or a known spectrum drawn from the image itself) and the unknown target spectra in the image scene. This may be sufficient to indicate detection.

Target Detection differs from Classification in the fact that while classification assigns a pixel to multiple classes, target detection is hypothesis testing problem with the hypothesis being – either target is present, or target is not present (Manolakis *et al.* 2016).

In most target detection applications, targets are generally small as shown in Figure 1.3 thus occupying less than 1% of total pixels in the captured image (Davood *et al.* 2012).

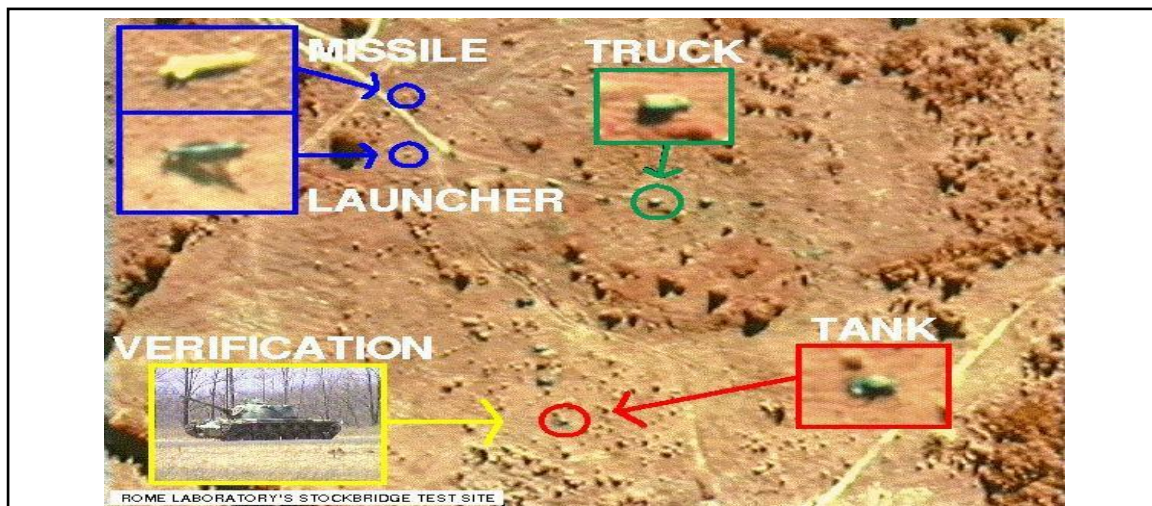


Figure 1.3: Depiction of targets in real life scenario (www.globalsecurity.org)

Because of small size, many targets of military interest in hyperspectral images, at the spatial scale of measurements, often occupy only a few pixels fully (Khan *et al.* 2018, Chang 2013, Chang, 2003). Detection and recognition of these small targets, therefore,

continue to pose problems in coarser spatial resolution data and thus require them to be resolved both spatially and spectrally (Manolakis *et al.* 2003, Zhang *et al.* 2013, Xian-Hua, 2019) as shown in Figure 1.4. For example, a small target may reside fully in one pixel and simultaneously also occupy several other pixels in the neighbourhood only partially (Manolakis *et al.* 2001). Alternatively, it may lie entirely within one single pixel.

The first case may give few fully resolved pixels and several mixed pixels, while the second case gives an unresolved pixel. The problem in each of these cases is referred to as subpixel target detection. Therefore, many parameters linked with target of interest such as its location, condition, shape, size *etc.* influence the target detection process, thereby increasing the complexity (Arora and Tiwari, 2013).

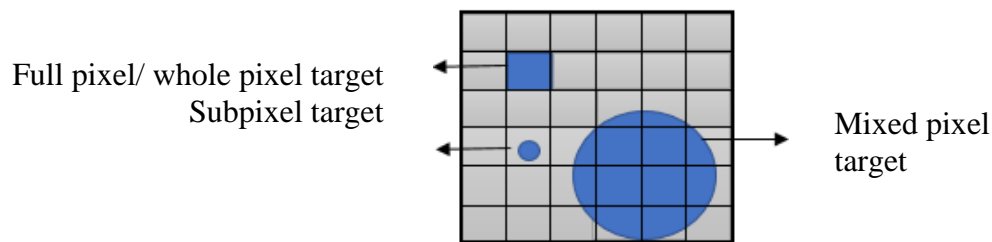


Figure 1.4: Cases in which a target may occupy a pixel in hyperspectral images

Target detection, thus, faces several challenges such as small size of the target, spectral variability, mixed pixels *etc.* The conventional target detection algorithms utilize the spectral signature of the target. The spectral signature is of any target, however, exhibits a lot of variation known as spectral variability due to varying illumination, location, and condition (surface, subsurface, underwater *etc.*) of the target, difference in compositions of different instances of the target, atmospheric and background noise, spectrometer error, self - shadowing other sensor limitations *etc.* (Shaw *et al.* 2003). Spectral variability is a major challenge in performing the target detection (Wendel and Underwood, 2017, Manolakis, 2016).

Besides, most of the commonly available Target Detection algorithms detect only full pixel targets while the entire TD process involves five steps as explained in Table 1.2 (Chang, 2003). Detection merely implies differentiation between full pixel signatures of a target and the background. The applicability of target detection in hyperspectral images gets restricted depending upon whether all or some of these steps of the target detection process can be completed. Target detection encompassing the entire process, as given below, may therefore necessitate detection of not only full pixels of a target but also the recovery of all the subpixel components of targets residing in several surrounding pixels.

Terms	Explanation
Detection	To separate a target signature from background signatures
Classification	Grouping of signatures exhibiting similar spectral signatures into a single class.
Discrimination	Distinguish two classified targets from one another. Classification does not lead to automatic discrimination and vice versa.
Identification /Recognition	Target identifier requires a priori knowledge of database such as a spectral library and implies matching of target spectra with reference spectra
Quantification	Counting the detected targets of a given type.

1.2.2 Super resolution Mapping

This section discusses the definition and concept of super resolution as presented in this thesis.

1.2.2.1 Definition

Super resolution (SR) is defined as the process that aims at increasing image resolution through various image processing techniques (Qingxiang, 2018). The SR process synthesizes sub-pixel information in imagery to increase the resolution of the image. Typical synthesis techniques include: (i) interpolation of nearby pixels within the image

(ii) interpolation of nearby frames within a video and, (iii) frequency filtering to reduce noise from nearby imageries *etc* (Yang *et al.* 2015).

None of the methods mentioned in previous paragraph, however, make use of the abundance fractions of the target inside a pixel and therefore may not be an effective solution to the problem of mixed pixels and subpixel target detection. Super resolution mapping is therefore defined as a target enhancement technique that enhances the spatial resolution of image and produces the classification results at a sub-pixel scale. Here, SR is used to estimate the location of target / target component within a pixel, with the proportion of classes determined from a soft classification technique (Zhou *et al.* 2011).

Super resolution mapping is thus a result of an optimization of subpixel class proportions within or between the pixels according to their relative abundance fractions to derive a subpixel map at a spatial resolution finer than that of the coarse resolution (Muad and Foody, 2012, Xu *et al.* 2014).

1.2.2.2 Concept of Super resolution

To understand the concept, consider any satellite image data with 8 bands. In this image every pixel has 8 different intensity values corresponding to the 8 bands for each pixel. Now say, the spatial resolution is 30 meters. Let us consider an example of an object (target) lying with two natural ground cover classes as they usually exist in nature. One such layout is shown in Figure 1.5 (a). It contains one object (target) and two different land cover types. The target is shown in brown color, vegetation in green and urban area in grey. Next, when this layout is captured in a pixel-based image of say 30-meter resolution, it gets represented as shown in Figure 1.5 (b). It may be seen in 1.5 (b), that the exact ground layout, shape, size, and area of the object (target) as well as the ground cover classes have been lost in the pixel-based representation. This often leads to incorrect assessment of target

and ground cover classes. This has severe implications in target detection applications. It is therefore important to recover the correct proportions of target / each class in each pixel.

As defined earlier, super resolution is the process that synthesizes sub-pixel information in imagery to increase the resolution of the image. This is done in two steps, first, abundance fractions of the object (target) and the two ground cover types are determined using spectral unmixing. The abundance fraction gives the percent area occupied by the target and other ground cover classes in the coarse pixel. Spectral unmixing, however, does not give the spatial distribution of the abundance fractions within the pixel.

To arrive at the optimal spatial distribution of the abundance fractions within the pixel, a suitable scale factor for super resolution that gives the ratio of pixel resolution enhancement needs to be fixed. For the present example, let us consider scale factors of 3 and 5. This in essence means that each pixel will be subdivided into 3x3, 5x5 subpixels. Next these subpixels will be assigned to the object (target) and ground cover class in the ratio of their abundance fractions. To determine their spatial distribution, certain mapping algorithms as discussed in the next sub section are made use of. Finally, we arrive at an enhanced image as shown in Figure 1.5 (c) and 1.5 (d). It may be observed that 1.5 (d) which is at a scale factor of 5 presents a much better enhancement than 1.5 (c) and is also much nearer to the image at 1.5 (a). It may appear that if scale factors are linearly increased, it may result in greater enhancements, but it is not so because of the computational complexities involved in the optimization process. This is explained in the research gaps subsequently.

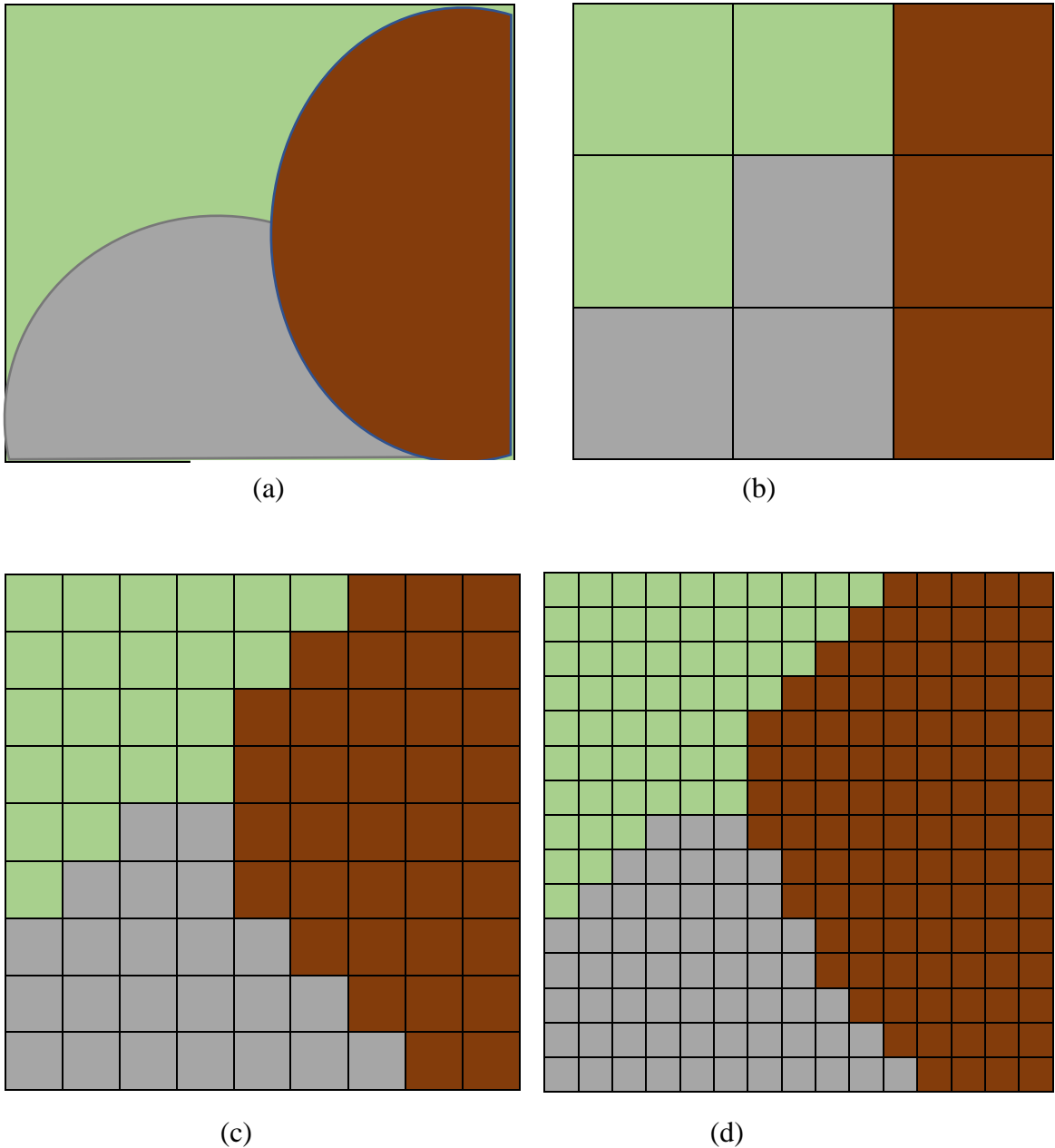


Figure 1.5: Super resolution mapping (a) Natural ground cover layout with vegetation (green), soil (brown) and Urban area (Grey) classes (b) Capture of ground layout in a 2x2 image (c) super resolution at scale factor of 3 and (d) super resolution mapping at scale factor of 5.

1.2.2.3 Review of Existing Super resolution Approaches

The problem of determining spatial distribution of subpixels (based on abundance fractions estimated using spectral unmixing) has involved researchers since a long time because this would effectively solve the problem of mixed pixels and the subpixel target detection. Several algorithms have been reported in the literature to deal with this problem.

W. Schneider had attempted subpixel mapping of linear features based on a 3 pixel by 3 pixel kernel or moving window (Schneider 1993), which was later fine-tuned by W. Schneider and J. Steinwendner to include neural network prediction of vector boundaries, but is restricted to remotely sensed images and the detection of linear features (Steinwendner *et al.* 1998 and Schneider 1993).

Atkinson proposed a method called **Pixel Swap Algorithm** (2001 and 2005) to achieve subpixel mapping. It was proposed to divide each pixel into smaller pixels called subpixels. The task is then to assign each subpixel to an appropriate class according to the fractions in the subpixel classification. The objective of this algorithm is to change the spatial arrangement of subpixels in such a way that the spatial correlation between neighboring subpixels is maximized. The results obtained from soft classification (to identify the land cover class within each pixel) are utilized for transformation into subpixel classes. The method of initialization is a measure to compute the accuracy and efficiency of mapping at subpixel level. A random initialization is considered and further the algorithm intends to find the spatial arrangement of subpixels and works in a recursive manner to find their correct allocation by finding the maximum correlation among the neighboring subpixels. This algorithm works for a binary land cover class problem and not for multi class problem. Land cover class proportions for each pixel obtained from a soft classification (or unmixing) are input to the Pixel Swap algorithm. Based on the scale factor, the number of subpixels is calculated corresponding to the pixel in the coarse spatial resolution image. The number of subpixels for any given target/class in each pixel remains fixed throughout the Pixel Swap procedure. During this Pixel swapping process, each subpixel is allocated to a single land cover class such that the original class fractions in the coarse resolution image are maintained (Atkinson, 2005).

Tatem *et al.* introduced a technique called **Hopfield Neural Network (HNN)** subpixel mapping as well as for recreation of spatial pattern. The widespread feedforward back-propagated ANN that is used for sub-pixel classification were applied by Mertens *et al.* and even combined with wavelet theory (Tatem *et al.* 2001, 2002, Mertens *et al.* 2003, 2006). HNN is a fully connected recurrent network, which works by mapping the spatial distribution of the class components within each pixel. This is formulated as a constraint satisfaction problem, and an optimal solution to this problem is determined by the minimum of an energy function coded into a Hopfield neural network. The network architecture is arranged to represent a finer spatial resolution image, and constraints within the energy function determined the spatial layout of binary neuron activations within this arrangement. This algorithm finds the minimum of the energy function, which corresponds to a bipolar map of class components within each pixel.

Kennedy and Eberhart,1995 proposed **Particle Swarm Optimization (PSO)** and Wang *et al.* 2012 proposed PSO based Super Resolution Mapping, inspired by the social behavior of bird flocking or fish schooling for food. It is an evolutionary computation technique based on swarm intelligence. PSO performs the global searching strategy based on community and avoids complex genetic operators with a simple speed offset model that requires fewer parameters. It traces the current searching situation and tunes the strategy when necessary for strong memory, which makes PSO easy to realize.

The Markov Random Field (MRF) is a technique that can be used to model contextual information (Geman and Geman, 1984). Kasetkasem *et al.*, 2005 used the MRF to generate super resolution for land cover mapping in remote sensing imagery. Every map is assumed to have Markov property. This approach assumes spatial dependence within and between pixels, in which two adjacent pixels are more likely to belong to the same land

cover class. Homogeneous regions of the land cover are more likely to be mapped by this model than isolated pixels. As a result, the isolated pixels tended to be ignored. Unlike many other super resolution mapping techniques, the MRF based super resolution is not dependent on a soft classification technique. Therefore, the MRF based method is not affected by inaccuracy of the soft classification.

Inverse Euclidean Distance (IED) based method was proposed by Tiwari *et al.* 2011 which was based on binary class problems to perform super resolution on synthetic as well as hyperspectral datasets. A summary of the algorithms mentioned above is also presented in Table 1.3.

Table 1.3: A review of some of the existing super resolution mapping techniques.

Algorithms	Properties	Advantages	Limitations
PS (Pixel Swap) (Atkinson. 2001 and 2005)	PS maintains the class composition information conveyed by the soft classification	If the soft classification is accurate, PS may be more suitable than the HNN for super resolution mapping.	Highly sensitive to the accuracy of that classification. Fails to consider the correlation between subpixels adequately. Iterative and consumes more time
HNN(Hopfeild Neural network) (Tatem <i>et al.</i> 2001, 2002, Mertens <i>et al.</i> 2003, 2006)	The neural network depends on the training and needs training for different types of classification. The network uses a energy function with several constraints converging to a minimum. After the implementation for features larger than a pixel, they expanded the method so it was also applicable for subpixel features.	Based on the energy minimization principle.	The mixture model as well as fuzzy c-means implementation needs pure pixels in an image, which are not always present. Produces rounded corners and, therefore, may poorly represent land cover patches with complex shape Predicted location of land covers within the area of a pixel may be imperfect, especially if there are small land cover patches

PSO (Particle swarm optimisation) Kennedy and Eberhart, 1995 Wang <i>et al.</i> 2012	It is an evolutionary computation technique based on swarm intelligence. Global search strategy is based on community and avoids complex genetic operators with a simple speed-offset model	It requires fewer parameters. It traces the current searching situation and tunes the strategy when necessary for strong memory, which makes PSO easy to realize.	PSO is not a unique optimization algorithm to search the optimal solution. It is an iterative algorithm where the swarm Swarm goes through evolution a number of times adding to the computation time and complexity.
MRF (Markov Random Fields) (Geman and Geman, 1984, Kasetkasem <i>et al.</i> , 2005)	Markov Random Fields (MRF) is based on the Bayesian probability theory, and includes this knowledge in the two key elements: the prior and conditional probability density functions.	It considers the likelihood of similar end members lying in neighbourhood pixels. The basic assumption is that, in a hyperspectral image, it is very likely that two neighboring pixels will have the class same label.	When different amount of classes are implemented, it is noticed the algorithm needs more iterations because the algorithm chooses a class randomly and measures the energy of that chosen class.
IED (Tiwari <i>et al.</i> 2011)	Inverse euclidean distance works on binary class problems	It considers the attraction from clique pixels surrounding the pixel under observation.	It is a non recursive algorithm that is based on non random allocations of subpixels.

1.3 Research Gaps

This section presents a discussion on the research gaps identified.

1.3.1 Loss of Target Information During Dimensionality Reduction

The spatial resolution of the sensors have evolved over time, however, the targets of interest particularly in military target detection are usually exceedingly small as compared to the spatial resolution of most of the sensor (Freitas *et al.* 2018, Davood *et al.* 2012). In some cases, there may be a sensor of appropriate resolution but it may either be prohibitively costly or may not be available for the period or area required (Eckardt and Reulke, 2018). Similarly, many targets of military interest may be of such composition that

many sensors may fail to resolve it even spectrally. Thus, the requirement of data with high spatial and/or spectral resolution continues to be a challenge (Garzonio *et al.* 2017).

In terms of spatial resolution, the sensors can be a coarse resolution sensor (approximately over 1km), medium resolution (approximately over 100 m) or fine resolution sensor (approximately between 5m-100m) that captures the data in different spatial ranges (Govender *et al.* 2017, Landgrebe D 1999, Honkavaara *et al.* 2013, Wilcox *et al.* 2018). On the other hand, spectral resolution describes the ability of a sensor to define fine wavelength intervals. The finer the spectral resolution, the narrower the wavelength range for a particular channel or band (Garzonio *et al.* 2017). Current imaging sensors provide panchromatic data (which is single band data), multispectral data which is up to 10 bands and hyperspectral data which is 100s of narrow contiguous bands (Bioucas-Dias *et al.* 2013). It is obvious that finer spatial and spectral resolutions are beneficial in addressing issues arising in hyperspectral remote sensing.

The number of spectral channels used by the sensor to acquire data defines the dimension of hyperspectral data which is generally high (Bioucas-Dias *et al.* 2013). Analysis of hyperspectral data in any remote sensing application follows a definite process which involves dimensionality reduction in view of large amount of spectral content.

Thus, the large content implies greater storage and processing resources, and highly correlated bands with lot of redundant information (Prasad *et al.* 2001). Therefore, in applications involving hyperspectral data when the number of bands reaches a certain limit, the overall accuracy of detection often decreases resulting in Hughes phenomenon (Chang, 2007). The process of reducing the number of bands to identify the most suitable ones for achieving the objectives of the application, is termed known as Dimensionality reduction. In view of the computational complexity arising out of the high dimension / narrow spectral bands / redundant information, Dimensionality reduction in hyperspectral data therefore

becomes an essential step because it improves the signal to noise ratio (Şimşek *et al.* 2020, Muhammad Haq 2011, Koonsanit *et al.* 2012).

Data pre-processing such as atmospheric and geometric corrections, removal of bad bands/redundant information (through band selection or dimensionality reduction) and is an essential requirement in all remote sensing applications including target detection. The pre-processed data is then analyzed for detection of targets of interest (Willett *et al.* 2014). Dimensionality reduction (DR) evaluates the optimality criteria for all possible combinations of a subset of bands out of total number of bands and selects a combination that minimizes or maximizes the criteria (Koonsanit *et al.* 2012, Song *et al.* 2007, Rhonda *et al.* 2008). Optimum and suboptimum search methods are available to achieve this, but these may either be computationally demanding or infeasible to implement (Webb and Copsey, 2011). However, the challenge is here to ensure that there should not be any loss of target information in various stages of data pre-processing because the spatial and spectral presence of the military target of interest in the image itself be very limited. While performing dimensionality reduction, certain information in the case of subpixel and mixed pixel targets might be lost leading to a failure of the entire target detection process (Muhammad *et al.* 2011, Webb and Copsey 2011, Lillesand *et al.* 2008).

Therefore, in target detection applications, it assumes significance to study various combinations of dimensionality reduction (DR) techniques combined with full pixel and subpixel target detection (TD) algorithms (Binol *et al.* 2016).

1.3.2 Assessment of Background Characterization in Subpixel Target Detection

The challenge in subpixel target detection further lies in separating the target's spectral signature from the competing background signatures. It is well known that for detection of mixed pixel targets, both spatial and spectral properties of the data may be exploited and utilized (Chang *et al.* 2004, Clark 2016, Cohen *et al.* 2016). Since the

retrieved spectra, in case of mixed pixel targets, is a combination of both the target as well as rest of the end members present in the pixel (Bitar *et al.* 2018, Lu *et al.* 2013, Govender *et al.* 2011, Boardman *et al.* 1995), it is of significance to consider the spectra of non-target end members as background (Chang *et al.* 2020).

Also, in the case of mixed pixel targets, the interference is more from the non – target end members present within the pixel also known as background components, which may further affect accurate detection of subpixel targets (Zhao *et al.* 2016, Eismann 2012, Manolakis, 2000, Cohen *et al.* 2012). Therefore, the study of impact of background characterization on the recovery of target pixels is also equally significant (Jiao *et al.* 2018).

It is studied from literature that there exist large number of parameters which can adversely affect the accuracy of detection algorithms (Gross *et al.* 2015). Therefore, for the evaluation of effectiveness of detection algorithms, it seems suitable to perform a detailed assessment on the impact of the various parameters affecting the detection. One such parameter for efficient subpixel target detection is the study of impact of target conditions (full illuminations or shade). The detection of target in such cases is performed by analyzing the spectral profiles. The target location (placement of target over different background types) is also known to influence the process of detection and thus may be considered to study the variation in target detection (Gross *et al.* 2015). Overall, an empirical analysis of impact of four parameters: illumination condition, background analysis, color of target and selection of algorithm for target detection needs to be evaluated to improve the results and accuracy of detection.

1.3.3 Errors in Unmixing, Comparative Assessment of Unmixing Algorithms and Alternative approaches in Abundance Fraction Estimation.

The process of decomposing the observed spectrum of a mixed pixel into a collection of constituent end members and their corresponding abundance fractions is

known as spectral unmixing (Marinoni *et al.*, 2017). There are several models reported in literature to perform this, however, due to the simplicity, Linear mixture model is most widely used amongst various mixture models available thus far (Marinoni *et al.*, 2017, Liu *et al.* 2016, Rai *et al.* 2014, Keshava, 2003, Keshava 2002). Besides, multilayer neural networks and neuro fuzzy methods too are also used to recover the mixed components (Kerekes *et al.* 2013, Chen *et al.* 2016, Guifoyle *et al.* 2001). Unmixing techniques utilize the target information that may be available *a-priori* in the spectral libraries or may be taken from the scene itself. In the scene, an endmember is identified as a pure pixel with a unique spectral response different from other present components present in the image (Karbhari *et al.* 2019). A linear mixture model (LMM) is widely used unmixing algorithm that models the spectra of a pixel as a linear combination of individual end member spectra and its abundance fraction. The general equation for LMM is explained in equation 1.3:

$$x = \sum_{k=1}^M a_k s_k + w \quad 1.3$$

Where, x , spectrum of the mixed pixel,

s_k , spectra of the end members,

a_k , is their abundances;

M , number of the end members;

W , L dimensional error vector accounting for lack of fit and noise effects

The abundance fractions obtained using various mixture models, however, indicate only the relative abundances of the end members and do not give the spatial distribution of these inside the given pixels (Shao *et al.* 2018).

There are a few other issues too in spectral unmixing which complicate subpixel and mixed pixel target detection. For subpixel target detection, first, the abundance fractions of the end members present within the pixel needs to be determined (Gao *et al.*

2015, Du and Zhang 2014, Jiao *et al.* 2018, Heylen et a. 2016, Guo et al 2009, Li *et al.* 2011, Keshava 2002). Pure pixels can be used to determine the end members, the total number of components and the covered percentage of each component in a mixed pixel (Shao *et al.* 2018). These pure pixels represent the endmembers that may be present within a mixed pixel. Thus, if for every end member type a pure pixel can be found, abundance fractions within mixed pixels can be calculated. Alternatively, abundance fractions may be estimated provided the endmember spectra are known from existing spectral libraries (Rosin, 2001, Vikhamar *et al.* 2002). The extraction of end members may also be explored using alternative approaches owing to the limitations of the unmixing approaches such as spectral unmixing based approaches are completely dependent on the spectra and do not consider any wavelength based absorption variation (Zhang *et al.* 2006).

To overcome such limitations, an alternative technique *i.e.*, Spectral Indices has been explored for end member identification. In most of the available hyperspectral data of the urban region, the identification and mapping of the extent of impervious surfaces is an important task (Shih *et al.* 2020) and therefore spectral indices can be considered in extraction of abundance fractions of impervious surfaces.

Several spectral indices have been proposed and implemented such as Normalized Difference Built up Index (NDBI), Built up area extraction index (BAEI) (Zha *et al.* 2003), Normalized Built-up Area Index (NBAI) (Bouzekri *et al.* 2015, Xu, 2010, Wolf, 2010) *etc.* However, the identification of (target) impervious surfaces using hyperspectral data is limited due to high dimensionality and greater processing time. Hence, the optimal wavelength regions that contain specific and significant information related to the target under consideration need to be identified prior to the implementation of spectral indices.

1.3.4 Random Recursive Vs Non-Random Non-Recursive Super Resolution Approaches

From Figure 1.5 (c) and 1.5 (d) discussed earlier, it may appear that if the scale factor is increased linearly it will result in continuous resolution enhancement. However, most of these super resolution algorithms work on random allocation of location to the subpixels of different end members within the pixel. Being based on recursive optimisation, the implementation of algorithm commences with random allocation of subpixels and the number of subpixels allocated to each class depends upon its fractions. Random allocation of subpixels are time consuming, computationally complex and follow a process that decreases the accuracy of the subpixel mapping results (Wang *et al.* 2006, Wang 2013). In addition, the subpixels are randomly distributed, and a series of iterations are required to cluster those subpixels based on a distance weighed attractiveness function. Since all the subpixels of a given target/class based on its abundance fraction are likely to be clustered together, this iterative procedure only leads to additional computational constraint (Atkinson, 2001 and 2005).

In the case of linear targets, the algorithm works well only when the targets are at least one pixel wide and fails for targets which are about one half of the width of the pixel. Besides, certain subpixels once allocated to the incorrect class, continue to cluster the misclassified pixels (Atkinson, 2001 and 2005).

Further, these techniques generally use a non-linear parameter in the calculation of distance dependent weight, which may not be determined deterministically for different scale factors and may vary for different applications. This adds uncertainty to the procedure. As a result, the convergence of the algorithm usually becomes difficult to achieve (Atkinson, 2001 and 2005).

Thus, there is a need to overcome the limitations in case of random-recursive algorithms, as reported in the literature (Zhong *et al.* 2015, Xian 2019, Wang *et al.* 2012, Wang *et al.* 2017). Both these types of algorithms *i.e.*, random-recursive, and non-random

non-recursive super resolution algorithms may have their own advantages and disadvantages. For example, in the case of a random recursive algorithm, a linear increase in scale factors could result in large number of subpixels getting randomly initialized that may never converge correctly. Similarly, in the case of non-random non-recursive algorithms, these may fail to correctly map the non-linearity present in the scene. Therefore, both these algorithms need to be examined at different scale factors for their usefulness.

Based on the foregoing review, the research gaps which have been considered for the present study are summarised as follows,

- (a) The size of the target of interest for applications such as military target detection is generally small and requires both spectral as well as spatial detection. Also, hyperspectral data has large spectral content and thus requires Dimensionality reduction (DR) which leads to loss of target information both at full pixel and subpixel level. Loss of target information in the process of dimensionality reduction therefore needs to be explored.
- (b) Subpixel target detection is impacted by several factors such as background signatures. Errors may also occur in generation of initial abundance maps. There is thus a requirement of studying background characterization
- (c) Spectral unmixing and determination of abundance fractions is an essential prerequisite for carrying out super resolution mapping. Any inaccuracy in determination of abundance fractions would impact recovery of the subpixel component of the target. It is therefore important to identify suitable algorithms and techniques that provide better estimations of abundance fractions.
- (d) Most of the super resolution algorithms proposed in literature work on random allocation of subpixels and follow an iterative procedure that leads to higher computational time and algorithm complexity. Besides, it is also possible some of

these algorithms for certain data may never converge. Therefore, there is a requirement to assess the performance of random-recursive super resolution algorithms with non-random, non-recursive super resolution.

1.4 Research Objectives

The main aim of this research is to analyze existing and to develop a new approach for target detection and enhancement in hyperspectral data using super resolution mapping. This is achieved by exploring spatial and spectral properties of data. The objectives of this research are enumerated below:

- a) To review various existing Dimension reduction algorithms with a view to achieve maximum possible Dimensionality reduction while ensuring minimal/no loss of the target data.
- b) To efficiently characterize the target and background spectral signatures for subpixel detection.
- c) To study various end member extraction techniques in available datasets using spectral unmixing and spectral indices-based approaches.
- d) Comparative assessment of random recursive technique with non-random non-recursive super resolution mapping technique, for subpixel target detection and enhancement.

1.5 Organisation of Thesis

The work in this thesis is organized into Eight Chapters including the present Introduction section. **Chapter 1** is dedicated to the basic concepts of remote sensing, the data acquisition, its pre – processing and analysis using the data description. It also gives an insight into the various issues that need to be dealt while performing target detection as well as the utilization of remote sensing data for target detection. The problem of mixed pixels, its impact on target detection and possibilities to address the issues using spectral

unmixing is also covered. An introduction to super resolution mapping is also given. This chapter also covers the research gaps found in the literature and the objectives of this work.

The problem statements, experimental datasets, methodology and a step-by-step explanation of tasks, discussion of results and brief conclusions corresponding to each objective is explained under the **Chapters 2 to 6**.

Chapter 2 investigates the various existing Dimensionality reduction algorithms with a view to achieve maximum possible Dimensionality reduction while ensuring minimal or no loss of the target data.

Chapter 3 discusses the efficient characterization of target and background spectral signatures for full pixel and subpixel target detection.

Chapter 4 highlights a study of various proposed end member extraction techniques for mixed pixels. Another approach for end member extraction using spectral index has been discussed. A comparative analysis is further done to study and assess the extracted end members, generated abundance maps and to compute the errors.

Chapter 5 elaborates the non-random non-recursive approach for identification of targets via super resolution and highlights a comparative study that is performed on datasets to analyze the accuracy of two different super resolution approaches selected from literature, in terms of the algorithm efficiency and computation time.

Chapter-6 provides the conclusions. Major contributions of this research, limitations and the future scope of research are also covered under this chapter. Flowchart giving the organization is shown in Figure 1.6.

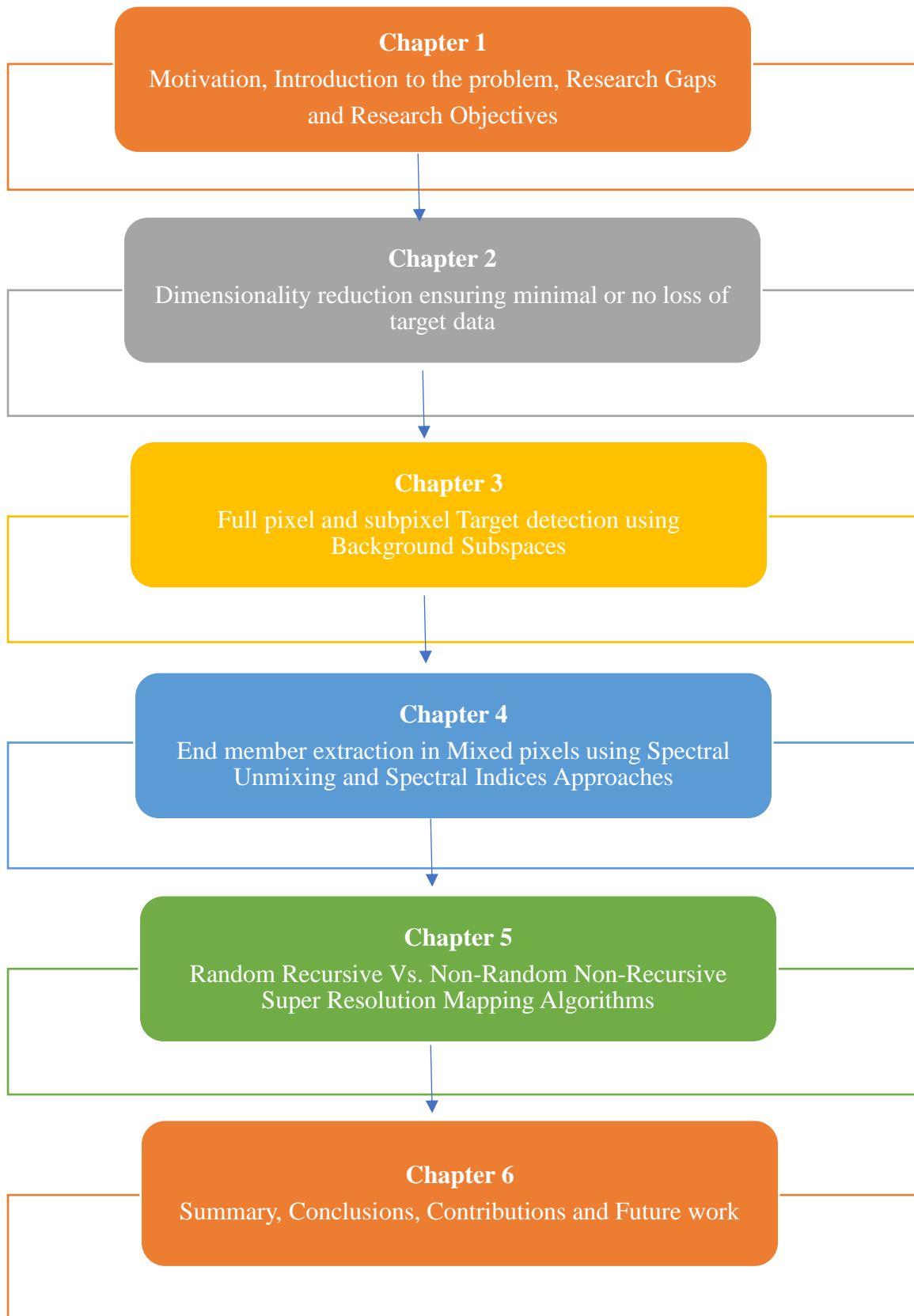


Figure 1.6: Organization of the Thesis in the form of a flowchart

Chapter 2

Dimensionality Reduction while ensuring minimal or no-loss of Target Data

2.1 Introduction to the Problem

The objective of target detection algorithms is to analyze the remote sensing data and detect the targets of interest automatically or with very less human intervention (Bitar *et al.* 2020, Gautam *et al.* 2020, Wang *et al.* 2017, Zhao *et al.* 2016, Maria *et al.* 2016, Zhang *et al.* 2014, Nasrabadi 2014, Eismann 2012, Wang *et al.* 2013). Target detection using hyperspectral data has several issues that need to be addressed (Freitas *et al.* 2018, Gao *et al.* 2015). First issue being that based upon the spatial resolution, the targets may be defined as full pixel (target occupies one full pixel) or subpixel target (target occupies the pixel partially or is completely embedded). Most target detection algorithms can at best detect full pixel targets, leaving out several partially occupied / mixed pixels (Snyder *et al.* 2008, Wang and Xue 2018, Zhang *et al.* 2015, Zhang 2020, Zhao 2016, Jiao *et al.* 2018, Kelly 1986, Chen *et al.* 2011, Cisz *et al.* 2005). This reduces the number of detected pixels of the target (all pixels not being full pixels) and it is a challenge to recover all the pixels (both full and partially occupied) (Cohen *et al.* 2012, Keshava 2003, Bakken *et al.* 2019).

Besides this, the large number of bands in hyperspectral data result in an increase in the volume of data and hence add to the problems of data transmission, storage, and analysis (Simsek *et al.* 2020). Due to greater number of bands, all of which may not be required by the underlying application, dimensionality reduction is performed to reduce the data volume and to find the most suitable bands for obtaining the required results (Binol *et al.* 2016, Manolakis 2016, Agarwal *et al.* 2007, Shippert 2004). However, while performing dimensionality reduction, certain information in the case of subpixel and mixed pixel

targets might be lost leading to a failure of the entire target detection process (Muhammad *et al.* 2011, Webb and Copsey 2011, Lillesand *et al.* 2008).

Therefore, in target detection applications, it assumes significance to study various combinations of dimensionality reduction (DR) techniques combined with full pixel and subpixel target detection (TD) algorithms (Binol *et al.* 2016, Rotman *et al.* 2010). In addition, the study of impact of background characterization on the recovery of target pixels is also equally significant (Jiao *et al.* 2018). These issues have been explored in this study and to do so, the following tasks were implemented.

Task 1: Full pixel Target Detection with and without Dimensionality Reduction

Task 2: Full pixel Target Detection with and without Dimensionality Reduction, along with the study of impact of Background characterization

Task 3: Subpixel Target Detection with and without Dimensionality Reduction, along with the study of impact of Background characterization

2.1.1 Selection of TD and DR Algorithms

The literature reports many algorithms for TD and DR out of which a few have been selected for the present work as explained below.

TD Algorithms

TD in this work is done using algorithms, Spectral Angle Mapper (SAM) (Hao *et al.* 2020, Imani, 2019), Adaptive Coherence Estimator (ACE) (Gautam *et al.* 2020, Zeumann *et al.* 2017, Manolakis *et al.* 2003), Matched filter(MF) (Geng *et al.* 2017, Gao *et al.* 2015, Manolakis *et al.* 2000), Constrained Energy Maximization (CEM) (Zhao *et al.* 2019, Chang *et al.* 2000), Mixture Tuned Matched Filter (MTMF) (Shang *et al.* 2020, Boardman 1998), Normalised Euclidean Distance (NED) (Zhang *et al.* 2018), Target constrained interference minimised matched filter (TCIMF) (Shang *et al.* 2020, Ren *et al.*

2000, Du 2004), Spectral information divergence (SID) (Zhang *et al.* 2015) and Orthogonal subspace projection (OSP) (Dadon *et al.* 2016, Chang 2005) selected from the literature.

SAM is background independent algorithm where only *a-priori* information related to target spectra needs to be known. Literature review suggests that despite the wide use of SAM, it is not much efficient in modelling of target spectrum under different illumination conditions (Hao *et al.* 2020, Imani, 2019). Algorithm that focuses on modelling the background is ACE, which follows a generalized likelihood ratio approach (Gautam *et al.* 2020, Zeumann *et al.* 2017, Manolakis *et al.* 2003). After replacing normalization value in ACE by variance MF is obtained (Geng *et al.* 2017, Manolakis *et al.* 2000). It was shown by Manolakis *et al.* in 2001, that for a limited dataset, although each of the algorithms exhibited some degree of success in TD, ACE performs best.

CEM (Ferrand *et al.* 2004) minimizes the response of unknown background signatures while maintaining that of target at a desired constant level and is useful when interest is only in one target and there is *a-priori* availability of its spectral signature. However, it does not perform well in the presence of low probability background signatures and is sensitive to noise (Zhao *et al.* 2019, Chang *et al.* 2000, Scott 2002). MTMF (Shang *et al.* 2020, Boardman 1998) operates on MNF transformed data and uses MF along with an added output infeasibility (INF) score. Targets have large MF values and small infeasibility scores (SMF). ENVI software displays a plot of SMF vs. INF where end user manually selects appropriate target pixels based on the criteria previously described. OSP works on *a priori* availability of data. In this technique, spectral signature of target of interest is taken as desired signature and background spectral signatures are considered as undesired signatures (Muhammad 2011). OSP seeks to reduce data dimensionality, suppresses undesired background signatures, and maximizes SNR of target spectrum. OSP is suitable for detection of manmade objects (Dadon *et al.* 2016, Chang 2005). NED

normalizes the vectors first by dividing each vector by its mean and then computing the Euclidean distance between two vectors (Zhang *et al.* 2018). SSM (Chen *et al.* 1987) is also based on computation of Euclidean distance between spectra of a pixel and reference spectrum to measure the similarity amongst them.

DR Algorithms

Principal component analysis (PCA):

PCA states that neighbouring bands of all hyperspectral images are highly correlated and give almost same information about a target. It aims to identify and collect PC's (principal components), and to find their significance by using eigenvalues (Willet *et al.* 2014, Farrell *et al.* 2005).

High dimensional data is converted to PC's using Eigen vectors which are orthogonal to each other. PC's are ordered in order of decreasing variance (Harsanyi 1994, Du and Chang, 2004). Only the first few components which are in direction of maximum variation contain required information and are selected (Koonsanit *et al.* 2012).

The number of PC's containing relevant information are very less as compared to the total number of bands (Priyadarshini *et al.* 2019). Bands retained are identified by accumulated sum of variance and eigenvalues. In the case of hyperspectral data, there is always a high computational cost and memory requirement (Zabalza *et al.* 2014). There is a likelihood of loss of small targets using PCA (Ramakrishna *et al.* 2005, Chang 2003 and Chang *et al.* 2004).

Independent component analysis (ICA):

ICA assumes that spectra of components in any pixel is not related and presence of one substance in a mixed pixel should not interfere with scattering of another, regardless of

quantity in which they appear. It finds statistically independent components and a-priori information about targets is not needed.

ICA transforms the set of randomly mixed signals into corresponding mutually independent components. The selection of an Independent Component (IC) is based on its score produced by 2 measures: skewness and kurtosis (Wang *et al.* 2006).

ICA has been reported to be effective in case of small targets (Wang *et al.* 2006, Tiwari *et al.* 2011), however not much work has been reported regarding loss of target information using ICA.

Minimum Noise Fraction (MNF):

MNF works on the principle of computing the eigen vectors and maximizing signal-to-noise ratio. Once the Eigenvectors are computed, individual covariance matrices are created. Noise levels are obtained from PCA of the covariance matrices.

Decomposition of a signal into components is done on basis of ratio of noise to signal power (Kruse *et al.* 2003). Larger values of eigenvectors identify signal components which exhibit highest noise fractions, while smaller eigenvalues identify the opposite. A set of obtained random variables can be truncated to retain only those bands that have useful SNR (Sharma *et al.* 2020). The selection of number of truncated bands must ensure an optimal number of bands so as not to contain either too much noise or too little target information (Gholizadeh *et al.* 2011).

The above discussion on three different types of DR algorithms is a broad categorisation and each of these algorithms would depend upon multiple factors such as nature of the study site, data quality, inference or adjacency effect, nature of the objects within the image, radiometric accuracy and resolutions *etc.* Therefore, each of these algorithms have their

own advantages and disadvantages in DR, however, in this study these algorithms are being examined only from the point of view of loss of target information while performing DR.

2.2 Experimental Data Set

It has been observed from the literature review as explained in section 1.3 and 1.4 that hyperspectral data can be analyzed and utilized for detection of full pixel and subpixel targets. Therefore, for achieving the tasks mentioned in above section, two sets of **hyperspectral datasets** have been explored to perform the experiments.

2.2.1 Data Set-1: SHARE-2010

In July 2006, Rochester Institute of Technology, USA, conducted a data collection campaign in Cooke City. The region includes a variety of natural and man-made objects as shown in Figure 2.1 (a).

2.2.1.1 Acquisition and Characteristics of Data Set-1

Table 2.1: General acquisition parameters for Data Set-1

Sensor	Data Type	Data size	Spectral Resolution	Spectral region	Spatial Resolution
HyMap Sensor	Hyperspectral	280x800 pixels	126 contiguous bands, at 0.45 - 2.5 nm interval	390-2450 nm	3 meters

The sensor captured some vehicles and fabric panels of various sizes placed in and around RIT campus. For this study, three vehicles: V1 (Green Chevy Blazer), V2 (White Toyota T100) and V3 (Red Subaru GL); which occupy a few pixels (but are visually difficult to detect) and placed in different locations are chosen as targets (Figure 2.1 (b)).

Each vehicle has 8 full pixels around 1 mixed pixel in data, making a total of 9 target pixels of every vehicle. Spectral signatures of vehicles are shown in Figure 2.1 (c).

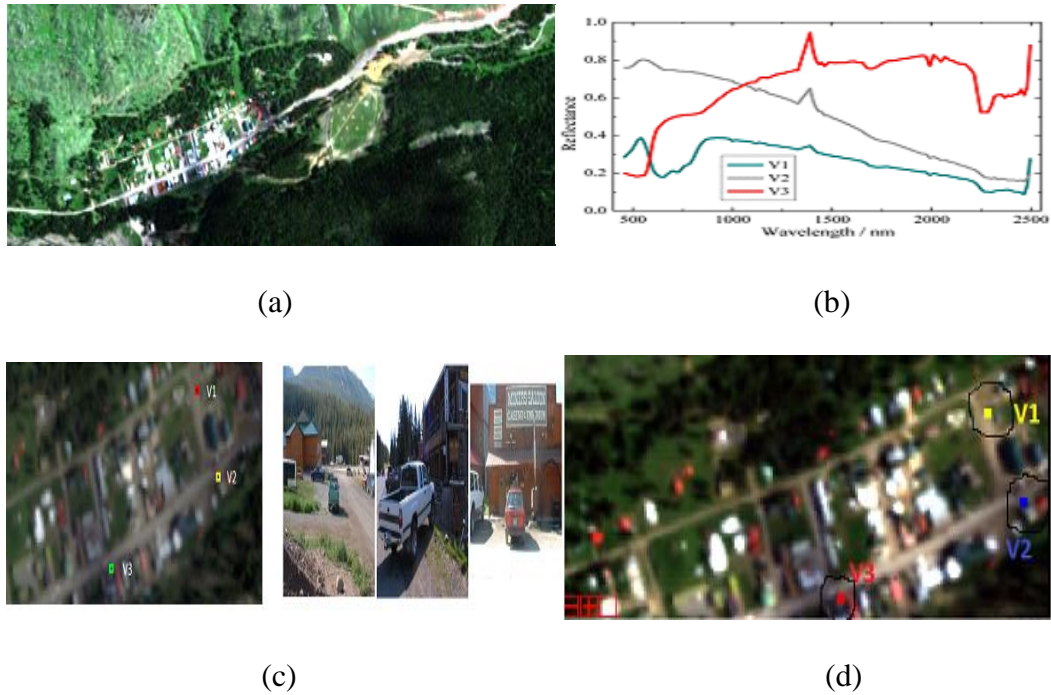


Figure 2.1: (a). RGB image showing Cooke city and surrounding terrain, (b). A zoomed in part of Cooke city, showing locations of V1, V2 and V3., (c). Spectral signatures of vehicles V1, V2 and V3 present in data, (d). Spatial subset S1 of 190x84 pixels selected from available image of Cooke city

A spatial subset (S1) of 190x84 pixels from an entire image of 280x800 pixels is chosen for implementation (to reduce complexity and computational time) as shown in Figure 2.1 (d).

2.2.2 Data Set-2: SHARE-2012

A multi-modal (hyperspectral, multispectral, and LIDAR) imaging data collection campaign was conducted in Avon, NY on September 20, 2012 by RIT in conjunction with SpectTIR, LLC, the Air Force Research Lab, the Naval Research Lab, United Technologies Aerospace Systems and MITRE. The region includes a variety of natural and man-made objects.

From the entire data, Data set for Avon city (Figure 2.2 (a), Figure 2.3 with acquisition parameters as shown in Table 2.2 has been selected to conduct experiments for evaluation of subpixel detection and unmixing algorithms. Data contains an image and related GLT files.

Table 2.2: General acquisition parameters for Data Set-2

Sensor	Data Type	Data size	Spectral Resolution	Spectral region	Spatial Resolution
Prospectir-VS	Hyperspectral	280x800 pixels	360 bands, 5 nm interval	~400 nm to ~2450 nm	1 m, 0.5 m

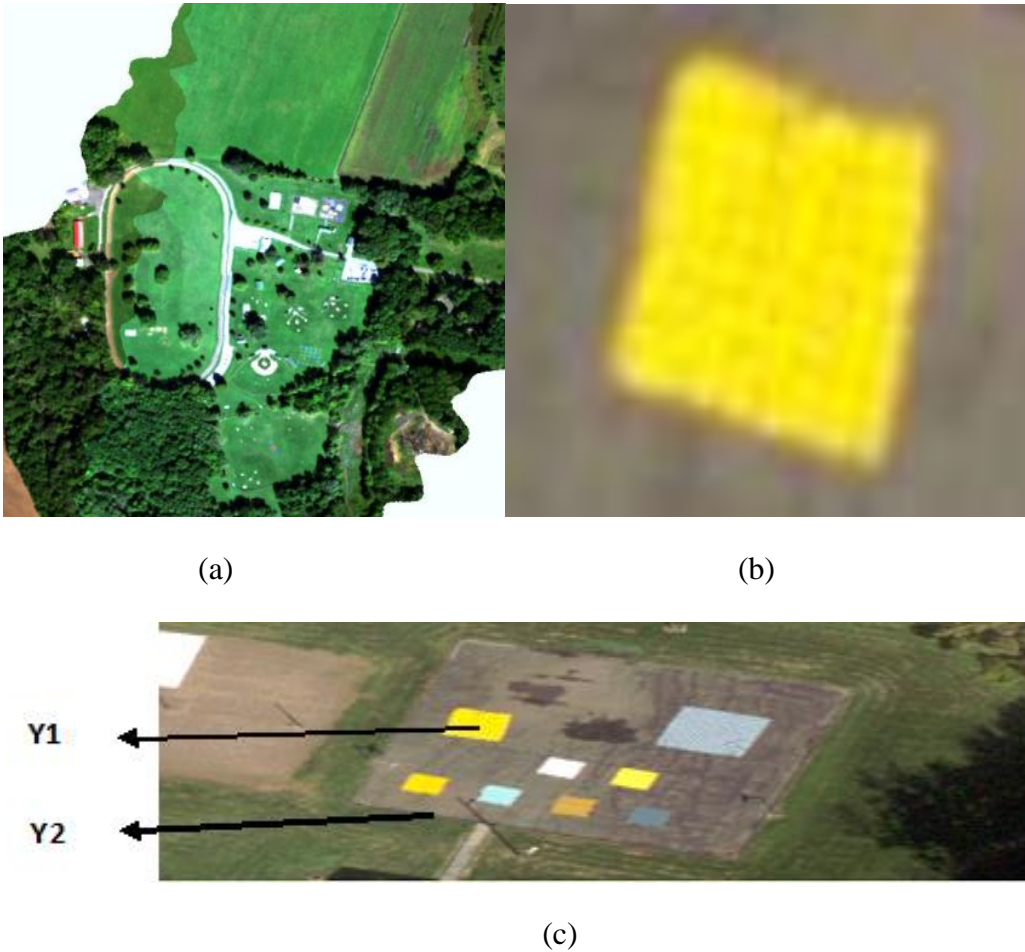


Figure 2.2: (a). Mosaic of SpecTIR images in the visible spectrum for the morning pass over the main ground truth site, (b). A zoomed in picture of the unmixing target Y1. (c). RGB image of Targets Y1 and Y2 selected for unmixing target detection experiment in a Spatial subset S2 of 150x150 pixels placed on asphalt court.

2.2.2.1 Acquisition and Characteristics of Data Set-2



Figure 2.3: Google earth image of the AVON city showing the line of sight.

For target detection experiment, the deployment contains many fabric and wooden panels placed at different locations around the city. One such panel is a blue target (24 rows x 24 columns) visible in upper right area of asphalt court while yellow target (16 rows x 16 columns) is placed in upper left as shown in Figure 2.3 (c). For unmixing and target detection experiment, these two sets of unique checkerboard type targets were designed so that a precise knowledge of the end members and their area fractions are known a-priori to perform further assessments and analysis.

The yellow target is a mixed pixel target containing yellow felt and yellow cotton arranged in a 2x2 repeating pattern in the ratio of 75% and 25% of area fraction per pixel (comprising of 3 yellow felt squares and 1 yellow cotton square) respectively. Spectral signatures of yellow felt and yellow cotton are shown in Figure 2.5. Also, for enabling the in-scene detection of targets, six whole panels of fabrics (10 rows x 10 columns each) were placed below mixed pixel targets. Two small panels placed just below and to the left of the blue target are pink felt (on the left) and yellow cotton (on the right).

For this work, a spatial subset (S2) of 150x150 pixels from entire data set is chosen for implementation and targets chosen are a mixed pixel target Y1 (8x8 pixels) and a full pixel target Y2 (5x5 pixels).

2.2.3 Ground Data Collection

Extensive ground collection was done for this data set during the morning pass and the evening pass. Two such images taken during the collection campaign are shown as examples in Figure 2.4.



Figure 2.4: Images from the Ground truth collection done during the SHARE 2012 campaign

The obtained ground truth along with the data was further resampled according to the image wavelengths. The resampled data was then utilised to make comparative assessments. A summary of targets under consideration for both the data sets selected for the present work is shown in Table 2.3.

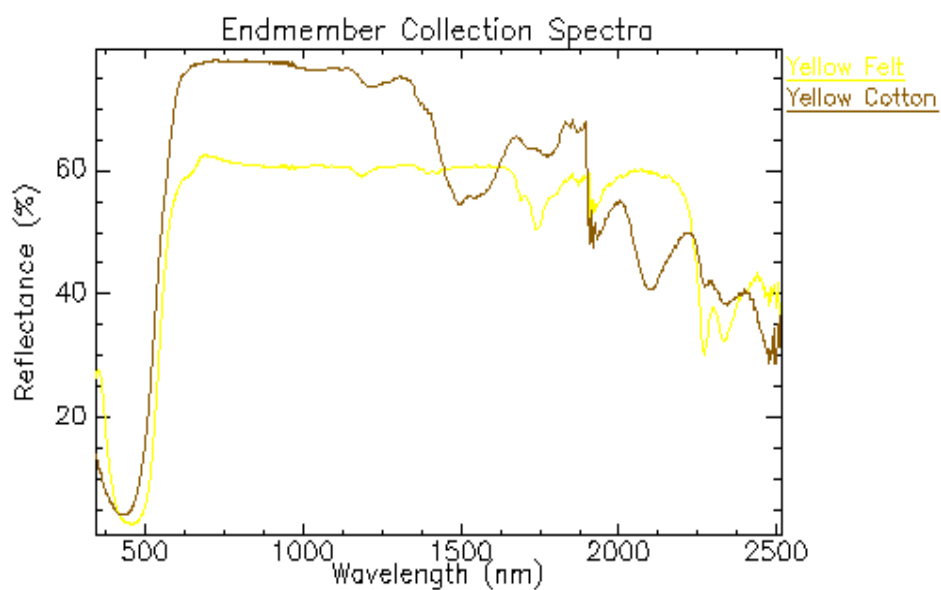


Figure 2.5: Spectral signatures of targets Yellow felt and Yellow cotton.

Table 2.3: A summary of Data sets, targets and target pixels selected for the implementation.

Data set	Original Data size	Subset size	Targets		Target pixel count
DATA SET-1	280X800	S1, 190X84	V1		9
			V2		9
			V3		9
DATA SET-2 Y1 is a mixed pixel target (in ratio 75% and 25%)	280X800	S2, 150X150	Y1		64
			Y2		25

2.3 Methodology and Implementation

The **methodology** explains the implementation procedure for the three tasks, Full pixel Target Detection with and without Dimensionality Reduction, Full pixel Target Detection with and without Dimensionality Reduction along with the study of impact of Background characterization and Subpixel Target Detection with and without Dimensionality Reduction and along with the study of impact of Background characterization.

A common procedure for all three tasks includes the extraction of subsets S1 and S2 from the atmospherically correct and geo-referenced datasets. The implementation of **Target Detection (TD)** is done using algorithms SAM, ACE, MF, CEM, MTMF, NED, TCIMF, SID and OSP selected from the literature.

Dimensionality reduction (DR) is performed using PCA, ICA and MNF. The following order is then followed to achieve the tasks outlined for this objective. **Spectral unmixing** techniques for resolving subpixel targets used in this research are LMM (Linear spectral unmixing) (Manolakis *et al.* 2001), and **Background characterization** using K-Means (Keshava *et al.* 2000), SMACC (Sequential Maximum Angle Convex Cone) (Chen 1987). The entire methodology includes following steps and are also shown in the form of a flowchart in Figure 2.6:

- Step 1: Obtain atmospherically correct and geo – referenced Data sets 1 and 2.
- Step 2: Create spatial subsets S, S2 from Data set-1 and Data set-2, respectively.
- Step 3: Perform Full pixel TD on Data set-1, with and without DR.
- Step 4: Perform Full pixel TD without DR without Background characterization, DR linked full pixel TD without Background characterization and implement Background characterization using SMACC and K – means.

Step 5: Perform a comparative assessment of TD algorithms using confusion matrix and obtain the best performing TD algorithm.

Step 6: Perform a comparative assessment of DR linked full pixel TD algorithms using confusion matrix and thus obtain best performing DR linked TD algorithm.

Step 7: Perform DR linked subpixel TD using spectral unmixing by LMM and evaluate the target pixels detected vs. target pixels lost.

2.3.1 Full pixel Target Detection with and without Dimensionality Reduction

TD has been implemented using selected TD algorithms on subset S1 for each target (V1, V2, and V3) without performing DR. An assessment of all the results obtained for every combination of algorithm and target is done to select an optimum value of threshold. Different thresholds have been explored to maximize the detections and minimize false positives. Outcomes for all the sets of experiments for a window of 20x30 pixels and results of computations of the values for true positives (TP), false positives (FP), true negatives (TN), and false negatives (FN) are noted. Post analysis, the best performing TD algorithm is selected for further processing.

To study the impact of DR linked full pixel TD, DR algorithms ICA, PCA and MNF are implemented. ICA based dimensionality reduced dataset contains more information in the initial bands and the noise or information with little spatial structure appear last (Hyvarinen *et al.* 2000, Song *et al.* 2007). Noise is removed using a forward transform and bands containing coherent images are determined. Threshold selected for this is 0.0001 with iterations of 100. Thereafter, sets of different good ICA bands *i.e.*, 10 bands, 15 bands, 20 bands, 25 bands, 30 bands have been analyzed and 20 bands containing maximum information and minimum noise are selected.

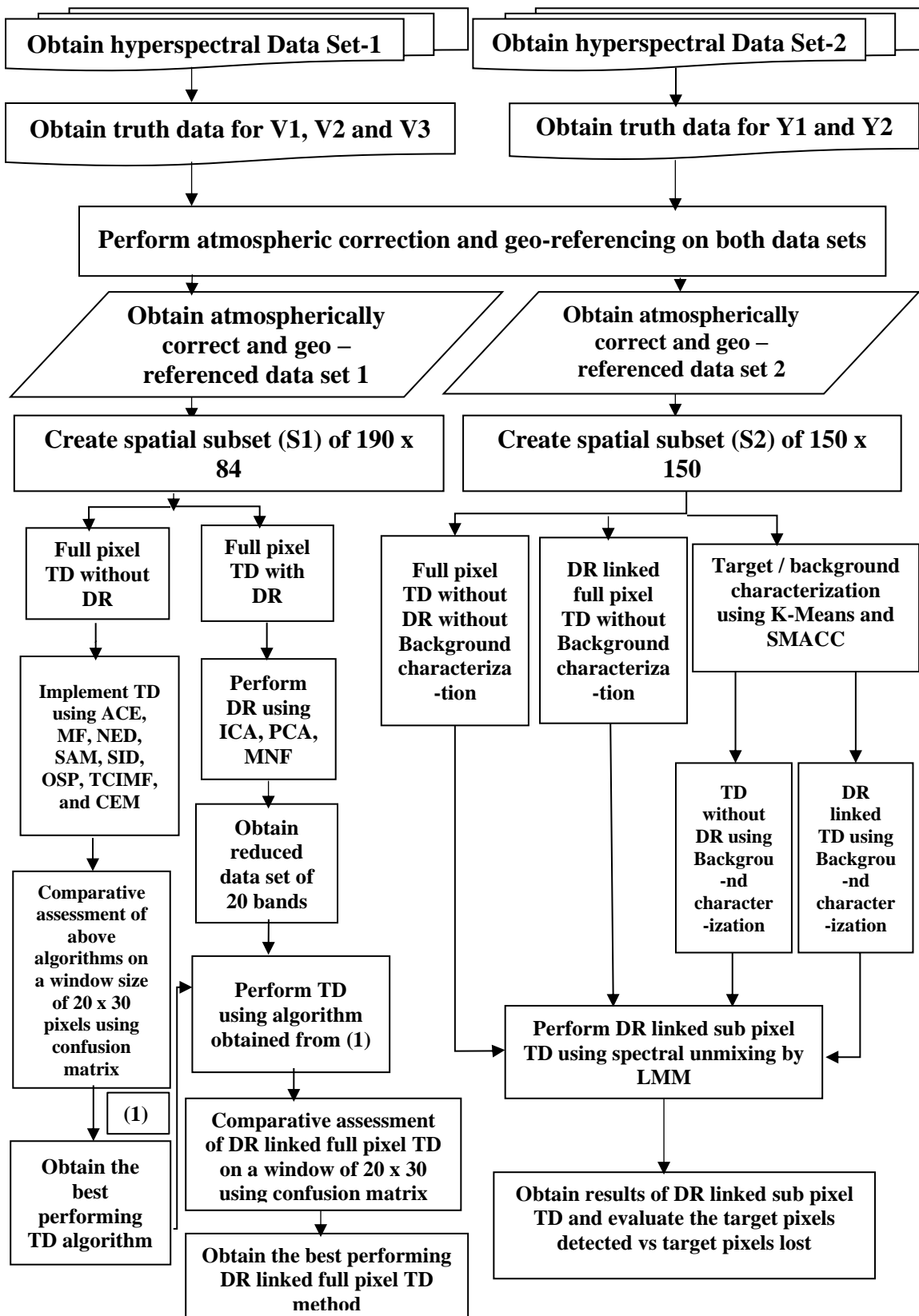


Figure 2.6: Flowchart explaining the steps followed to achieve the objectives of this chapter.

Next PCA is applied. Since maximum information is contained in first few PCA bands while the last bands appear noisy (Agarwal *et al.* 2007, Chang *et al.* 2004, Harsanyi *et al.* 1994, Koonsanit *et al.* 2012, Zabalza *et al.* 2014), again sets of different good PCA bands *i.e.*, first 10 bands, 15 bands, 20 bands, 25 bands, 30 bands have been analyzed for PCA and 20 bands containing maximum information and minimum noise are selected. MNF is then implemented which computes mean of each band, finds covariance statistics for noise and eigenvalues (Green *et al.* 1988, Rhonda *et al.* 2008). Output obtained contains eigenvalues plot. Bands with large eigenvalues (>1) contain data and the bands with eigenvalues near 1 contain noise. Thus 20 best bands out of 126 bands have been selected.

Further DR linked full pixel TD is performed on reduced spectral subset of 20 bands (window size of 20x30 pixels) selected respectively after ICA, PCA and MNF reduction. Accuracy assessment has been done using confusion matrix (Davood *et al.* 2012, Binol *et al.* 2016) and corresponding accuracy percentage is calculated

2.3.2 Full pixel Target Detection with and without Dimensionality Reduction and Background characterization

In subset S2, first full pixel TD without background characterization is performed. Results are analyzed to find out the best performing TD algorithm. Further analysis is done for DR linked full pixel TD without background characterization using MNF, ICA, PCA as DR algorithms.

Following this, the background characterization algorithms, K-Means and SMACC, have been implemented and further TD is done. After performing background characterization, the spectra of non - target components are attributed to the target detection algorithms which subsequently is analyzed for studying if there is an increase or decrease in detection of target pixels.

Thereafter, DR linked TD with background characterization is implemented to find out the best DR linked TD algorithm that gives minimal / no loss of target data.

2.3.3 Subpixel Target Detection with and without Dimensionality Reduction and Background characterization

One part of target under consideration (Y1) in subset S2 is a mixture of yellow felt and yellow cotton. Thus, for subpixel TD and to find their respective compositions in Y1, spectral unmixing is done using LMM. Once their respective abundance fractions are retrieved, a new table is reconstructed for Y1 in the format of actual placement at the time of data collect as discussed in section 2.2.2. Thereafter, based on chosen threshold values, subpixel TD results are evaluated.

Spectral unmixing using LMM is performed afterwards without DR and without background characterization on S2. Again, after computation of abundance fractions, values for detection for yellow felt and yellow cotton are obtained. Results of subpixel TD with DR is then compared to results obtained without DR.

All implementations have been done using **MATLAB R2015a** and **ENVI 5.2**.

2.4 Results and Discussions

Based on the above methodology, the **discussion of results** at each step of the implementation stage is presented in the following subsections:

2.4.1 Full pixel Target Detection without Dimensionality Reduction in Data Set-1

The implementations have been done using the target detection algorithms mentioned in section 2.3. The results of computations of the values for TP (true positives), FP (false positives), TN (true negatives), and FN (false negatives) for a window of 20x30 pixels, with respect to the target pixels have been tabulated in Table 2.4.

Table 2.4: Full pixel TD results for 126 bands and window of size 20x30 pixels in Subset S1 of Data set-1

Sr. No	TD algorithm	Target ID's	TP (targets)	FN (loss)	FP (alarms)	TN	Accuracy
1.	ACE	V1	9	0	1	590	99.83%
		V2	9	0	2	589	99.66%
		V3	9	0	2	589	99.66%
2.	MF	V1	9	0	2	589	99.66%
		V2	8	1	3	588	99.33%
		V3	8	1	2	589	99.50%
3.	NED	V1	7	2	21	570	96.16%
		V2	6	3	45	546	92.00%
		V3	6	3	131	460	77.60%
4.	SAM	V1	6	3	30	561	94.50%
		V2	7	2	49	542	91.50%
		V3	6	3	89	502	84.60%
5.	SID	V1	7	2	35	556	93.80%
		V2	6	3	46	545	93.50%
		V3	4	5	47	544	91.30%
6.	OSP	V1	4	5	29	562	94.30%
		V2	4	5	16	575	96.50%
		V3	4	5	38	553	92.83%
7.	TCIMF	V1	4	5	84	507	85.16%
		V2	4	5	143	448	75.33%
		V3	3	6	75	516	86.50%
8.	CEM	V1	4	5	321	270	45.66%
		V2	3	6	291	300	50.50%
		V3	6	3	423	168	29.00%

Following is **observed** from Table 2.4:

ACE detects all 9 target pixels of V1, V2, V3 with very less FP. However, MF detects 9 pixels for V1 and 8 pixels for V2 and V3 (both) with a slight increase in FP. NED and SAM further reduce the detected target pixels to 6 and 7 out of 9 but FPs are much higher. CEM gives the highest FPs.

Following may be thus **deduced** from these observations:

Since ACE detects all target pixels with very low FP and outperforms all other algorithms, it has been considered further to check results for DR linked TD. Second-best TD algorithm that detects higher number of target pixels, but less FP is MF and can therefore be retained for the next step of implementations.

2.4.2 Dimensionality Reduction linked Full pixel Target Detection In Data Set-1

To perform full pixel TD with DR on Dataset 1; ICA, PCA and MNF are implemented on subset S1 and further DR linked TD is carried on dimensionally reduced spectral subset of 20 bands.

Accuracy assessment has been done using confusion matrix. Results obtained for a window of 20x30 pixels are shown in Table 2.5.

Table 2.5: DR linked TD results and their assessment using a window of size 20x30.

Sr. No	DR algorithm	TD algorithm	Target ID's	Number of bands selected out of 126	TP (targets)	FP (alarms)	FN (loss)	TN	Accuracy
1	ICA	ACE	V1	20	7	4	2	587	97.83%
			V2		7	7	2	584	98.33%
			V3		8	1	1	590	98.33%
		MF	V1	20	3	13	6	578	96.83%
			V2		4	21	5	570	95.00%
			V3		7	20	2	571	95.33%
2	PCA	ACE	V1	20	7	5	2	586	97.00%
			V2		8	9	1	582	97.00%
			V3		7	22	2	569	94.83%
		MF	V1	20	4	19	5	572	95.50%
			V2		8	18	1	573	95.67%
			V3		4	27	5	564	94.17%
3	MNF	ACE	V1	20	7	11	2	579	96.50%
			V2		8	12	1	579	96.83%
			V3		8	16	1	575	95.83%
		MF	V1	20	1	23	8	568	94.67%
			V2		8	19	1	572	95.50%
			V3		3	34	6	557	93.00%

Following is **observed** from Table 2.5:

ICA with ACE detects 7,7,8 target pixels for V1, V2, V3 respectively and gives comparatively much lower false alarms with highest accuracy of detection $\approx 98.33\%$. PCA with ACE detects 7,8,7 pixels for V1, V2, V3 respectively but with higher false alarms decreasing the accuracy to 97% (V1, V2) and 94.83% (V3). MNF with ACE detect 7,8,8

target pixels for V1, V2, V3 respectively, however, false alarms have increased thus decreasing accuracy to 96.50% (V1), 96.83% (V2) and 95.83% (V3).

On the other hand, these DR algorithms when linked with MF, exhibit a very sharp decrease in detection of target pixels. Accuracy of $\approx 95\%$ is achieved for PCA with MF, around 94% in case of MNF with MF, however, ICA with MF still performs better (than MNF or PCA) with accuracy $\approx 96\%$.

Following may be thus **deduced** from the observations:

It appears that ICA performs better for DR assuring minimal loss of target data and higher accuracy after applying ACE for TD. A comparison of Table 2.4 (TD without DR) with Table 2.5 (TD with DR), also leads us to deduce that there is reduction in detected target pixels in case of TD with DR.

In the case of TD using ACE without DR, number of target pixels detected successfully are more but when same TD algorithm is applied after ICA, there is a loss of target pixels. Results therefore give us a platform for usage of ICA linked ACE as a better DR linked TD algorithm ensuring minimal loss of target data.

2.4.3 Full pixel Target Detection without Dimensionality Reduction in Data Set- 2 without considering Background characterization

Target Detection is achieved on subset S2 of Dataset 2, in which, first part of selected target is subpixel target (a mixture of yellow felt and yellow cotton) and total number of pixels of is 64 pixels.

Second part of the target which is a full pixel target (a yellow felt), occupies 25 pixels in the image. Therefore, total target pixels under considerations are 89 pixels. First, TD is performed on atmospherically corrected and georeferenced data using MF, TCIMF, SAM, ACE, SID, CEM, NED and OSP. Results are shown in Table 2.6.

Table 2.6: Full pixel TD results for 360 bands, targets, and a window of size 20x30 pixels in Data set - 2, without DR and without background characterization.

Sr. No	TD algorithm	TP (targets)	FN (loss)	FP (alarms)	TN	Accuracy
1.	MF	71	18	3	508	96.50%
2.	TCIMF	67	22	4	507	95.66%
3.	SAM	60	29	1	510	95.00%
4.	ACE	55	34	3	508	93.83%
5.	SID	42	47	2	509	91.83%
6.	CEM	60	29	76	435	82.50%
7.	NED	44	45	13	498	90.33%
8.	OSP	44	45	121	390	72.33%

Following is **observed** from Table 2.6:

MF detects 71 out of total 89 pixels with very less false alarms (3 pixels) and a loss of 18 target pixels. TCIMF gives loss of 22 pixels with false alarms of 4. With SAM, the detection further reduces to 60 target pixels with false alarm of 1. However, with ACE and SID, the detection reduces to 55 and 42 pixels respectively, thereby incurring an increased loss of target pixels.

Thus, it is **deduced** based on these observations that, MF, TCIMF and SAM detect more target pixels and therefore suitable for the study of DR linked TD.

2.4.4 Dimensionality Reduction linked Full pixel Target Detection In Data Set-2 considering Background characterization

Target Detection is carried out in two steps, using background characterization (SMACC and K-Means) and without using background characterization.

Results for DR linked TD without background characterization are shown in Table 2.7.

Table 2.7: DR linked TD results for targets and their assessment using a window of size 20x30 – Data set-2 and without background characterization.

Sr. No	DR algorithm	TD algorithm	Number of bands selected out of 360	TP (targets)	FP (alarms)	FN (loss)	TN	Accuracy
1	MNF	MF	20	67	8	22	503	95.00%
		TCIMF	20	69	11	20	500	94.83%
		SAM	20	73	21	16	490	93.83%
2	ICA	MF	20	66	13	23	498	94.00%
		TCIMF	20	59	11	30	500	93.17%
		SAM	20	69	17	20	494	93.83%
3	PCA	MF	20	66	7	23	504	95.00%
		TCIMF	20	40	11	49	500	90.00%
		SAM	20	35	10	54	501	89.33%

Following is **observed** from the results of Table 2.7:

MNF with MF detects 67 target pixels and 8 false alarms attaining an accuracy of 95%, which is reduced to 94.83% in MNF with TCIMF but here the false alarms increase to 11. With SAM, number of target pixels retained observe an increase with 73 pixels, however, false alarms increase further to 21 pixels reducing the accuracy to 93.83%.

ICA with MF delivers highest accuracy of 94% with successful detection of 66 target pixels. ICA with TCIMF attains accuracy of 93.17% while ICA with SAM detects 69 target pixels: higher than MF and TCIMF, but with 17 false alarms.

PCA with MF gives 95% accuracy, TCIMF delivers accuracy of 90% and SAM performs poorly in this case with 89.33% accuracy.

Thus, it is **deduced** from the observations that,

MNF with MF provides better results of detection ensuring minimal loss of the target data. Therefore, a combination MNF as DR and MF as TD algorithm may be considered further.

TD is next carried on by defining and submitting the background spectra (retrieved using background characterization algorithms SMACC and K-Means) to the target detection

algorithm. Background spectra for six end members are retrieved in both the cases and have been considered for a window size of 20x30 pixels. Spectra that have been obtained for background end members for both SMACC and K-Means are shown in Figure 2.7 (a) and 2.7 (b) respectively.

Background characterization is done followed by TD using MF, TCIMF and SAM without DR. Results obtained for this study are shown in Table 2.8.

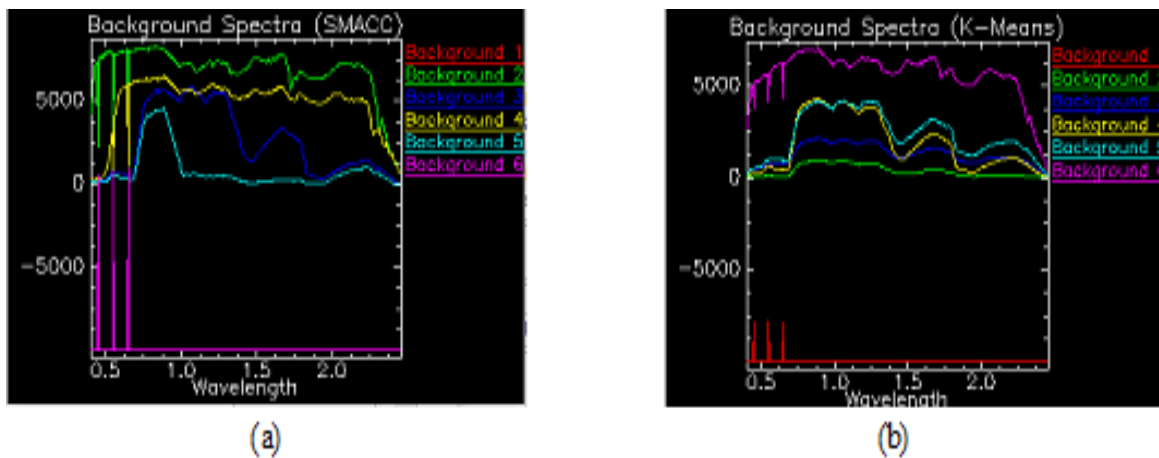


Figure 2.7: Endmember spectra obtained from (a). SMACC, (b). K-Means

Table 2.8: TD results and their assessment using a window of size 20x30 pixels – Data set-2 with background characterization using SMACC and K-Means.

Sr No	TD algorithm	Background characterization using SMACC and K-Means	Number of bands selected out of 360	TP (targets)	FP (alarms)	FN (loss)	TN	Accuracy
1	MF	SMACC	20	66	13	23	498	94.00%
		K-Means		68	11	21	500	94.67%
2	TCIMF	SMACC	20	40	15	49	496	89.33%
		K-Means		52	14	37	497	91.50%
3	SAM	SMACC	20	66	16	23	495	93.50%
		K-Means		68	16	21	495	94.17%

Following has been **observed** from Table 2.8:

MF using SMACC gives lower accuracy (94%) as compared to K-means which gives an accuracy of 94.67%. TCIMF retains fewer target pixels with both SMACC and K-Means *i.e.* 40 pixels and 52 pixels, *i.e.* with a loss of 49 pixels and 37 pixels respectively. SAM performs better with detection of 66 and 68 target pixels for SMACC and K-Means respectively with false alarms of 16 pixels in each case. The false alarms are higher than that for MF, thereby reducing the accuracy to 93.5%(SMACC) and 94.17%(K-Means).

It may therefore be **deduced** from the observations that K-means here retains more target pixels in all cases as compared to SMACC.

DR linked TD is then implemented using ICA, MNF, and PCA as DR algorithms and MF, TCIMF, and SAM as TD algorithms. Detection process was aided using the background characterization and results using both SMACC and K-Means and further, TD results have been shown in Tables 2.9 and 2.10 respectively

Table 2.9: DR linked TD results for target - yellow felt and their assessment using a window of size 20x30 pixels – Data set-2 and background characterization using SMACC

Sr. No	DR algorithm	TD algorithm	Number of bands selected out of 360	TP (targets)	FP (alarms)	FN (loss)	TN	Accuracy
1	MNF	MF	20	67	8	22	503	95.00%
		TCIMF	20	53	4	36	507	93.33%
		SAM	20	68	10	21	501	94.83%
2	ICA	MF	20	68	11	21	500	94.67%
		TCIMF	20	47	7	42	504	91.83%
		SAM	20	68	13	21	498	94.33%
3	PCA	MF	20	67	6	22	507	95.13%
		TCIMF	20	18	6	71	505	87.17%
		SAM	20	34	0	55	511	90.83%

Following is **observed** from the above Table 2.9:

While implementing background characterization using SMACC, with DR as MNF and with TD as MF, 67 target pixels are retained (in comparison to TD without DR which is 71 pixels) at an accuracy of 95%. With TCIMF, accuracy is 93.33% while SAM on the other hand gives accuracy of 94.83%. Thus, SAM performs better with DR as compared to SAM without DR.

With ICA and MF, accuracy reduces to 94.67%, which reduces further to 91.83% in case of TCIMF. With SAM, however, target pixels retained are 68 but alarms increase to 13 which reduces accuracy to 94.33%. With PCA, accuracy with SAM is reduced to 90.83 % but with MF it is 95.13%. TCIMF performs poorly in this case. Thus, SAM with DR as MNF, detects more target pixels thereby incurring minimal loss of target data, followed by MF.

It may be **deduced** from the observations listed above that MF, in all the cases (*i.e.* with DR as MNF, ICA, and PCA) gives nearly consistent results of detection and may also be considered for further TD.

DR linked TD is then performed using background characterization as K-Means. The results have been compiled in Table 2.10.

Table 2.10: DR linked TD results for target - yellow felt and their assessment using a window of size 20x30 pixels – Data set-2 and background characterization using K-MEANS.

Sr. No	DR algorithm	TD algorithm	Number of bands out of 360	TP (targets)	FP (alarms)	FN (loss)	TN	Accuracy
1	ICA	MF	20	67	0	22	511	96.33%
		TCIMF	20	59	3	30	508	94.50%
		SAM	20	68	13	21	498	94.33%
2	MNF	MF	20	70	15	19	496	94.33%
		TCIMF	20	55	0	34	511	94.33%
		SAM	20	68	10	21	501	94.83%
3	PCA	MF	20	68	11	21	500	94.67%
		TCIMF	20	60	0	29	511	95.17%
		SAM	20	34	0	55	511	90.83%

Following is **observed** from Table 2.10:

MF with ICA gives accuracy of 96.33%, MF with MNF detects 70 target pixels which is the highest but false alarms are 15 which is reduced in case of SAM to 10 thus increasing accuracy to 94.83%. MF with PCA retains 68 target pixels out of 89 which is highest when PCA is used as a DR algorithm. With SAM and ICA, the loss is 21 pixels, but false alarms are 13. TCIMF with ICA performs worst with accuracy of 94.5%. SAM, however, performs the worst with PCA and K-Means with a loss of 55 pixels. TCIMF comparatively works better with DR as PCA detecting 60 target pixels.

So, it may be seen that MF, in all the cases (MNF, ICA, and PCA) gives nearly consistent results with K-Means. ICA linked MF gives highest accuracy of the three, but maximum target pixels are retained with MNF+MF (70 pixels out of 89).

It may be **deduced** from the observations that:

Overall, the results of detection are improved with K-Means in comparison to SMACC. A combination of MF as TD algorithms with all the three DR algorithms (ICA, MNF and PCA) proves worthy and gives the better results of detection

2.4.5 Subpixel Target Detection in Data Set-2 considering Background characterization

In this section, the effect of providing background spectra to the TD algorithms on the detection of subpixel target has been explained. The implementations have been carried out on spatial subset S2 taken from Data Set-2.

2.4.5.1 Dimensionality Reduction linked Subpixel Target Detection In Data Set-2 considering Background characterization

TD algorithms discussed above detect only yellow felt and assign whole pixel to it. DR chosen for this process is ICA and TD chosen is MF, based on results obtained for DR linked TD background characterization using K-Means in Table 2.10. Target under

consideration is Y1 as shown in Figure 2.2 (c). A result of performing LMM on a 150x150 spatial subset S2 is shown in Figure 2.8.

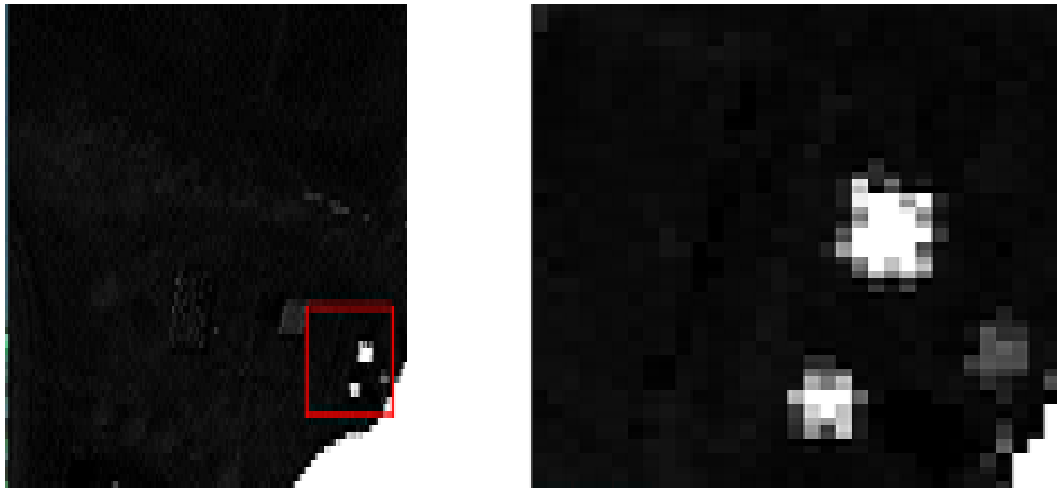


Figure 2.8: A result of performing LMM on a 150x150 spatial subset S2

After spectral unmixing, two tables Table 2.11 (a) and (b), have been generated containing abundance fractions of Yellow felt and Yellow cotton respectively in Y1 (8x8 pixels).

Table 2.11 (a). Fractional composition obtained after LMM of yellow felt in Y1

0.71	0.85	0.63	0.83	0.86	0.86	1.04	0.76
0.33	0.76	0.66	0.66	0.77	0.76	0.93	0.76
0.76	0.71	0.28	0.71	0.72	0.88	0.89	0.75
0.71	0.72	0.51	0.5	0.7	0.89	0.9	0.59
0.71	0.76	0.54	0.81	0.81	0.71	0.92	0.78
0.76	0.45	0.45	0.88	0.87	0.91	0.86	0.43
0.71	0.28	0.89	0.86	0.9	0.9	0.91	0.55
0.71	0.71	0.62	0.74	0.71	0.71	0.76	0.76

Table 2.11 (b). Fractional composition obtained after LMM of yellow cotton in Y1

0.34	0.22	0.22	0.23	0.21	0.21	0	0.24
0.79	0.33	0.23	0.23	0.23	0.24	0.07	0.24
0.35	0.21	0.71	0.23	0.23	0.21	0.21	0.25
0.25	0.21	0.23	0.23	0.25	0.21	0.08	0.25
0.26	0.22	0.22	0.23	0.55	0.18	0	0.22
0.2	0.21	0.24	0.21	0.2	0.25	0.21	0.38
0.15	0.15	0.23	0.31	0.3	0.15	0.15	0.23
0.22	0.22	0.25	0.25	0.25	0.21	0.22	0.24

Based on results, we have tried to reconstruct a table for Y1 (8x8 pixels) in the format of the actual placement of yellow felt (75%) and yellow cotton (25%) blocks at the time of data collect. Table 2.12 shows the fractional compositions of both yellow felt and yellow cotton in the 8x8 pixels in subset S2. Yellow colored portion represents fractional composition of Yellow felt and pale colored portion represents composition of Yellow cotton in Y1.

Table 2.12: Fractional compositions of both yellow felt and yellow cotton in the 8x8 pixels in subset S2

	.34		.22		.22		.23		.21		.21		0		.24
.71		.85		.63		.83		.86		.86		1.04		.76	
	.79		.33		.23		.23		.23		.24		.07		.24
.33		.76		.66		.66		.77		.76		.93		.76	
	.35		.21		.71		.23		.23		.21		.21		.25
.76		.71		.28		.71		.72		.88		.89		.75	
	.25		.21		.23		.23		.25		.21		.08		.25
.71		.72		.51		.50		.70		.89		.90		.59	
	.26		.22		.22		.23		.55		.18		0		.22
.71		.76		.54		.81		.81		.71		.92		.78	
	.20		.21		.24		.21		.20		.25		.21		.38
.76		.45		.45		.88		.87		.91		.86		.43	
	.15		.15		.23		.31		.30		.15		.15		.23
.71		.28		.89		.86		.90		.90		.91		.55	
	.22		.22		.25		.25		.25		.21		.22		.24
.71		.71		.62		.74		.71		.71		.76		.76	

Now, a random value of 1 is assigned to indicate the target detection if fractional abundance value is greater than 40% for Yellow felt and greater than 10% for yellow cotton in every pixel; otherwise, it is assigned a value of 0. This aids in understanding the presence or absence of the target in the pixel. These assigned values are shown in Table 2.13. The results, however, may vary for different values of threshold while implementing the detection algorithms.

Table 2.13: Values corresponding to target detected / not detected in the 8x8 pixels panel.

1	1	1	1	1	1	1	0	1
1	1	1	1	1	1	1	1	1
0	1	1	1	1	1	1	1	1
1	1	0	1	1	1	1	1	1
1	1	1	1	1	1	1	0	1
1	1	1	1	1	1	1	0	1
1	1	1	1	1	1	1	1	1
1	0	1	1	1	1	1	1	1
1	1	1	1	1	1	1	1	1

Based on these values, it is **observed** that the subpixel TD results are:

Yellow felt:

Target pixels detected = 61 / 64,

Target pixels not detected = 03 / 64

Yellow cotton:

Target pixels detected = 60 / 64,

Target pixels not detected = 04 / 64

2.4.5.2 Sub-pixel Target Detection without Dimensionality Reduction in Data Set-2 considering Background characterization

Next, Spectral unmixing using LMM is performed without DR and without background characterization on same subset. Results obtained for Yellow felt and Yellow cotton have been shown in Table 2.14 (a) and (b) respectively.

Table 2.14 (a): Fractional composition obtained after LMM of yellow felt in Y1

0.01	0	0.02	0.01	0.18	0.05	0.05	0.03
0.01	0.05	0.1	0.5	0.18	0.36	0.03	0.08
0.01	0.01	0.1	0.64	0.86	0.78	0.43	0.81
0	0.04	0.03	0.36	1	0.96	1	0.49
0	0.01	0.25	1	0.98	1	0.89	0.91
0.02	0.05	0.42	0.94	0.87	1	0.87	0.25
0.02	0.05	0.05	0.26	0.65	0.55	0.87	0.5
0.02	0.02	0.01	0.01	0.08	0.07	0.15	0.01

Table 2.14 (b): Fractional composition obtained after LMM of yellow cotton in Y1
Fractional composition obtained after LMM of yellow cotton in Y1

0.02	0	0.03	0.03	0.14	0.01	0.02	0.04
0	0	0	0.03	0.11	0.06	0.14	0.05
0.02	0.02	0.16	0.01	0.08	0.21	0.07	0.19
0	0.05	0.16	0.07	0.07	0.12	0.11	0.28
0.01	0.02	0.01	0.01	0.08	0.06	0.1	0.1
0.01	0.01	0.22	0.03	0.16	0.04	0	0.1
0.02	0.01	0.05	0.22	0.22	0	0.04	0
0	0.01	0.03	0.04	0.03	0.02	0	0.04

Based on the results, again a table for Y1 (8x8 pixels) has been reconstructed in format of the actual placement of yellow felt (75%) and yellow cotton (25%) blocks at the time of data collect. Table 2.15 shows fractional compositions of both yellow felt and yellow cotton in 8x8 pixels in subset S2.

Table 2.15: Fractional compositions of both yellow felt and yellow cotton in the 8x8 pixels in subset S2

0.01	0.02	0	0.03	0.03	0.14	0.01	0.02	0.04
0	0	0	0.03	0.11	0.06	0.14	0.05	0.05
0.01	0.05	0.1	0.5	0.18	0.36	0.03	0.08	0.08
0.02	0.02	0.16	0.01	0.08	0.21	0.07	0.19	0.19
0	0.05	0.16	0.07	0.07	0.12	0.11	0.28	0.28
0	0.04	0.03	0.36	1	0.96	1	0.49	0.49
0	0.01	0.25	1	0.98	1	0.89	0.91	0.91
0.02	0.05	0.42	0.94	0.87	1	0.87	0.25	0.25
0.02	0.05	0.05	0.26	0.65	0.55	0.87	0.5	0.5
0	0.01	0.03	0.04	0.03	0.02	0	0.04	0.04
0.02	0.02	0.01	0.01	0.08	0.07	0.15	0.01	0.01

Again, by randomly assigning value of target detected to 1 for values of fractional abundances greater than 40% for Yellow felt and to 0 for values greater than 10% for yellow cotton in every pixel, certain values for detection are obtained as shown in Table 2.16.

Based on the obtained values, it is observed that subpixel TD results are:

Yellow felt:

Target pixels detected = 24 / 64,

Target pixels not detected = 40 / 64

Yellow cotton:

Target pixels detected = 17 / 64,

Target pixels not detected = 47 / 64

Table 2.16: Values corresponding to target detected / not detected in the 8x8 pixels panel.

0	0	0	0	0	1	0	0	0	0
0	0	0	1	0	0	0	0	1	0
0	0	0	1	0	1	1	1	0	1
0	0	0	0	0	1	1	1	1	1
0	0	0	1	0	1	1	1	1	1
0	0	1	1	1	1	1	1	0	1
0	0	0	0	1	1	1	1	0	0
0	0	0	0	0	0	0	0	0	0

Following are the **observations** in the case of subpixel TD of **Yellow felt** (75%) in target Y1:

Subpixel TD without DR, without background characterization:

Only 24 out of 64 pixels are detected.

Subpixel TD with DR, with background characterization:

With ICA, linked TD (MF), using background characterization(K-Means), detection improves to 61 pixels out of total 64 target pixels.

Similarly, **observations** for subpixel TD of **Yellow cotton** (25%) in target Y1 are:

Subpixel TD without DR, without background characterization:

Only 17 out of 64 pixels are detected.

Subpixel TD with DR, with background characterization:

With ICA, linked TD(MF), using background characterization (K-Means), detection improves to 60 pixels out of total 64 target pixels.

Thus, it may be **deduced** from the observations that:

Subpixel target detection with dimensionality reduction provides better results in comparison to results obtained without dimensionality reduction. Also, background characterization immensely aids the detection of subpixel targets resulting in minimal loss of target data.

A summary of all the obtained results for various combinations of DR and TD algorithms (already explained in detail under sections 2.4.1 to 2.4.5), have been compiled for an easy reference in Table 2.17 below.

Table 2.17: A summary of results obtained for target detection using various combinations of DR and TD algorithms for full pixel and subpixel targets

DATA SET-1	Without DR	With DR
Full pixel TD	<ul style="list-style-type: none"> • ACE detects all target Pixels, gives lowest FP • MF detects well with loss of only 1 target pixel 	<ul style="list-style-type: none"> • Detection of target pixels is reduced • However, with ICA linked ACE, the detection is more as compared to other combinations, thus incurring minimal loss of target pixels
DATA SET-2	Without DR	With DR
Full Pixel TD without Background characterization	<ul style="list-style-type: none"> • MF outperforms followed by TCIMF. • SAM also performs reasonably better than all other algorithms implemented 	<ul style="list-style-type: none"> • MNF outperforms as DR and MF outperforms as TD
Full Pixel TD with Background Characterization	<ul style="list-style-type: none"> • MF using K-Means as B/G characterization outperforms with highest accuracy 	<ul style="list-style-type: none"> • ICA linked MF gives maximum accuracy with K-Means. • Overall K-Means outperforms SMACC
DATA SET-2	Without DR, Without B/G	With DR (ICA), With B/G (K-Means)
Subpixel TD with MF	<ul style="list-style-type: none"> • Detection is very low. • For Yellow Felt, there is a loss of 40 target pixels out of 64 • Whereas for Yellow Cotton, there is a loss of 47 target pixels out of 64 	<ul style="list-style-type: none"> • Detection improved. • For Yellow Felt, there is successful detection of 61 target pixels out of 64, • For Yellow Cotton, there is a successful detection of 60 target pixels out of 64.

2.5 Conclusions

In this chapter, various combinations of dimensionality reduction algorithms (ICA, PCA and MNF) and target detection algorithms (SAM, ACE, MF, CEM, MTMF, NED, TCIMF, SID and OSP) have been studied with a view to achieve maximum possible dimensionality reduction while ensuring minimal or no loss of the target data. This work appears to aid the objectives and tasks related to the detection of targets of interest in hyperspectral data which is known to contain large number of narrow contiguous bands.

Therefore, reducing the number of bands to a useful subset increases the probability of detection by reducing the unwanted information contained in the noisy bands. In addition, it reduces the computation time and provides an ease to analyze the hyperspectral data for detection of targets of interest particularly those targets which are exceedingly small in comparison to the image size.

From the summary given in Table 2.17 and the deductions of the results of detection, it may be concluded that the target detection process needs to be carefully executed as it leads to loss of certain information. The emphasis needs to be put on retaining the maximum information related to the target of interest. It can be further concluded that in the case of full pixel targets, both dimensionality reduction and target detection result in the loss of target information, however, there is a greater loss of target information in the case when dimensionality reduction precedes target detection in comparison to a case where target detection is applied without dimensionality reduction.

Background characterization appears to aid in improvement of full pixel target detection, and K-means is seen to provide better results of detection. In the case of subpixel target detection, however, there appears to be loss of subpixel target information in the case where detection alone is performed in comparison to a case where dimensionality reduction precedes target detection.

The above-mentioned results have been obtained using limited dataset made available as part of SHARE - 2010, 2012 campaigns and may need to be verified with other available high-resolution datasets.

Chapter 3

Full Pixel and Subpixel Target Detection using Target and Background Subspaces

3.1 Introduction to the Problem

In chapter 2, we have discussed in detail the impact of dimensionality reduction on loss / recovery of target pixels while performing target detection in case of full pixel as well as subpixel targets. It was also explained how subpixel target detection responded when targets were selected to be mixed pixel targets (placed on asphalt court) and how these were detected using various combinations of dimensionality reduction and target detection algorithms. In addition, the characterization of backgrounds using a few algorithms have been discussed in detail there.

In the present chapter, the focus is on target and background subspaces, and how these subspaces aid or inhibit the process of detection of full pixel and mixed pixel targets has been discussed. It is well known that for detection of mixed pixel targets, both spatial and spectral properties of the data may be exploited and utilized (Chang *et al.* 2004, Clark 2016, Cohen *et al.* 2016). Since the retrieved spectra, in case of mixed pixel targets, is a combination of both the target as well as rest of the end members present in the pixel (Bitar *et al.* 2018, Lu *et al.* 2013, Govender *et al.* 2011, Boardman *et al.* 1995), it is of significance to consider the spectra of non-target end members as background (Chang *et al.* 2020).

For separation of the target spectra from the non-target end members, spectral unmixing (linear or non- linear) is performed (Helen *et al.* 2016, Helen *et al.* 2014, Chang *et al.* 2017). While considering the detection of full pixel targets, we need to address two major issues that can affect the accurate detection – noise (from the instrument or external) and the atmospheric interference. However, in the case of mixed pixel targets, the

interference is more from the non – target end members present within the pixel also known as background components, which may further affect accurate detection of subpixel targets (Zhao *et al.* 2016, Eismann 2012, Manolakis, 2000, Cohen *et al.*2012).

The **tasks** outlined in this chapter are, to detect low probability full pixel / subpixel targets with known spectral signatures, to detect targets using background and target subspaces, to analyze the impact of various combinations of background subspaces on full pixel and subpixel target detection and to analyze the impact of illumination conditions on the targets.

For the present work, the target detection algorithms that have been selected are, Matched Filter (MF), Orthogonal subspace projection (OSP), Adaptive coherence estimator (ACE) and Target constrained interference minimized filter (TCIMF). These have been shortlisted from the algorithms studied from literature as well as a list of algorithms implemented in Chapter 2. The performance of these four algorithms is seen to be better than a group of algorithms discussed there.

3.2 Experimental Data Set

Two set of **data sets** have been used to perform the experiments and tasks explained under section 3.1 above.

3.2.1 Data set – 2 (Subset S2)

One such data set is a spatial subset S2 that has been taken from Data set-2 (SHARE 2012) as shown in Figure 2.2 (c) and already explained in section 2.2.2. Here the targets under consideration are a mixed pixel target Y1 and a full pixel target Y2 as shown in Figure 3.1.



Figure 3.1: Mixed pixel target Y1 and full pixel target Y2 in subset S2

3.2.2 Data Set-3: SHARE-2012 (Subset S3)

Another data set that has been used for this work is also a spatial subset of size 140×244 , that has been extracted from SHARE-2012 data set (Data set-2) which was collected in September 2012 over Avon city by RIT, Air force research lab and a few other research laboratories. This subset, however, contains different targets placed at different locations around the campus and is labelled as Data set-3 (Subset S3) for future references (Figure. 3.2).



Figure 3.2: True color representation of subset S3 of size 140×244 in visible spectrum

In this subset, Red and Blue Felt fabric targets of 3x3 and 2x2 meters can be seen placed around the Avon site. The set of targets used are same, however, the background and illumination conditions in each case is different. Specifically, the target pairs are placed in open (full illumination) on dirt / gravel road, grass and in partial / full shade of the trees. In total, nine unique placements of these red and blue targets were obtained during the data collection campaign.

3.2.2.1 Targets in Data Set-3

The target under study for the present work is Blue Felt. Ground reflectance spectra of the target material and the various background types have been obtained, resampled to the image wavelengths and are represented in Figure 3.3 below.

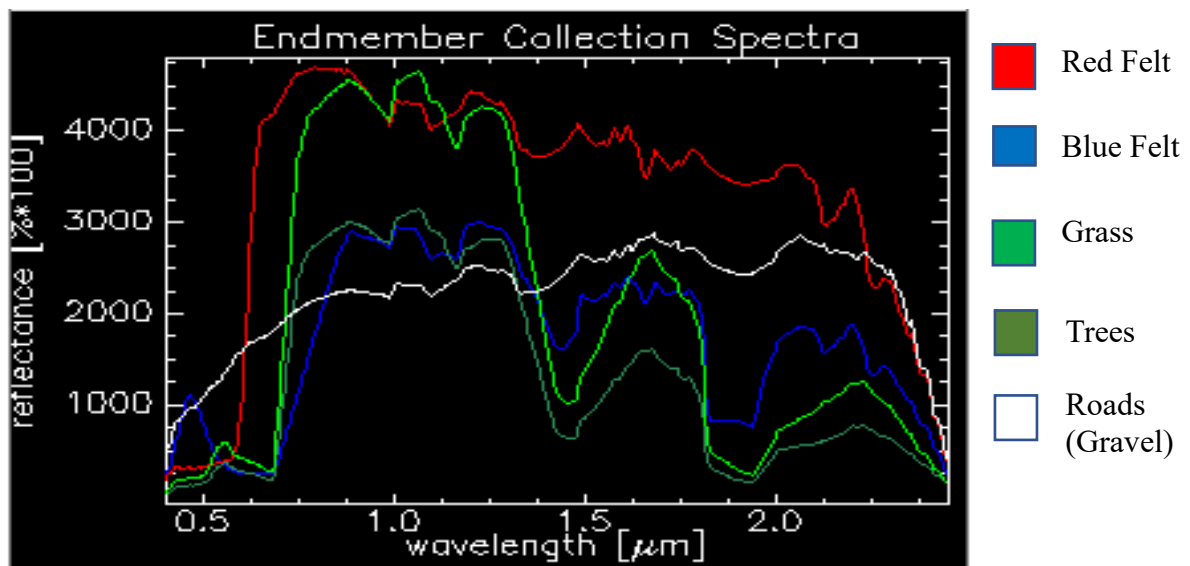


Figure 3.3: Ground spectra for target materials and the background types

For the present work, a total of nine blue felt targets have been selected from twelve blue felt targets placed around the campus, as shown in Figure 3.4. These are further labeled as T1, T2, T3, T4, T5, T6, T7, T8, T9. The category to which these targets belong, as well the total number of target pixels corresponding to each, is also explained in Table 3.1. Therefore, total number of pixels belonging to all these nine targets under study are 56.

Table 3.1: Table representing targets under considerations and target ID's allotted to blue felt targets for present work and the super category to which targets belong.

Target ID (Blue Felt)	Category	Pixels
T1 (2x2) and T2 (3x3)	Gravel (Road)	T1=4, T2=9
T3 (2x2) and T4 (3x3)	Open Field (Grass)	T3=4, T4=9
T5 (2x2)	Path (shade)	T5=4
T6 (2x2)	Single Tree (Partially shaded)	T6=4
T7 (3x3)	Treeline Pair (Partially shaded)	T7=9
T8 (3x3) and T9 (2x2)	Treeline Quad (under trees)	T8=9, T9=4
Total		56

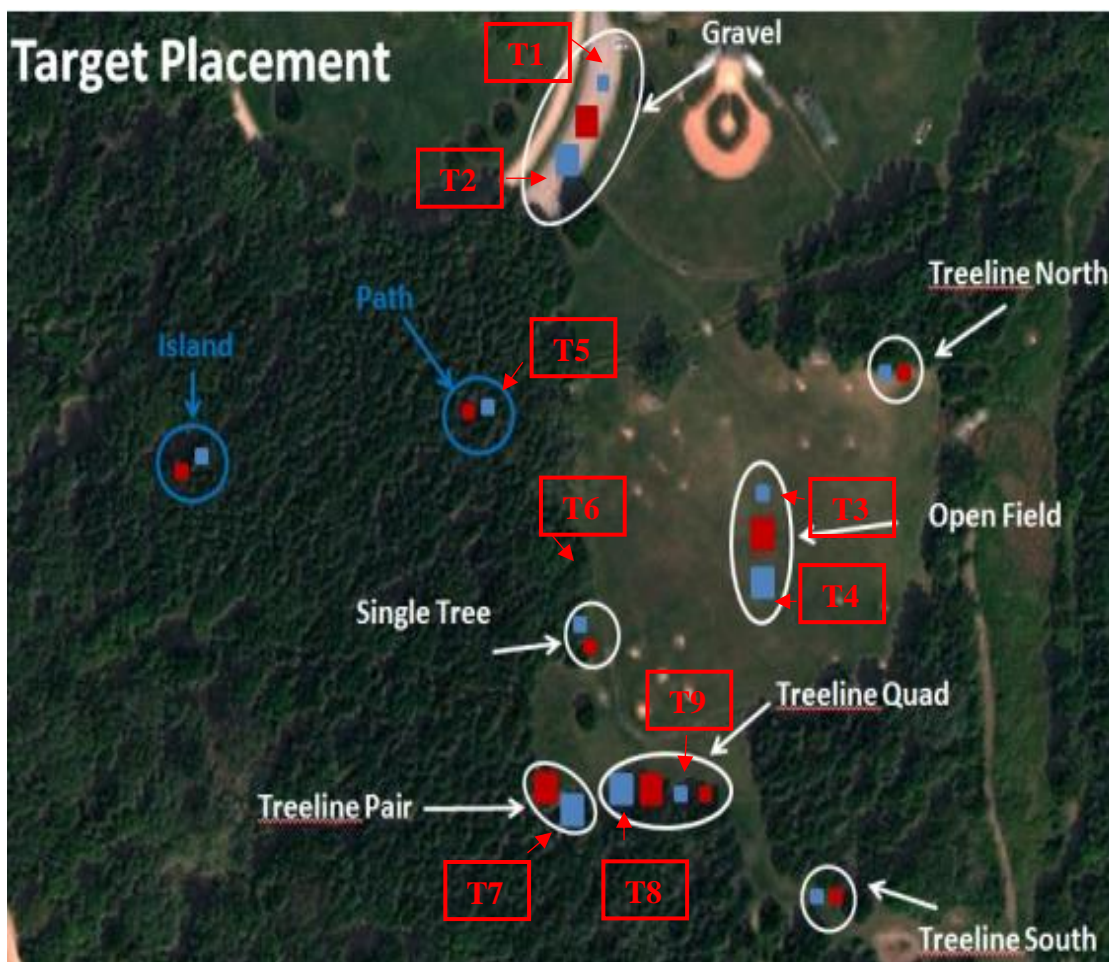


Figure 3.4: Annotated aerial image of Avon site with target locations identified.

3.3 Target and Background Subspaces

The target detection process in the case of mixed pixel targets, generates the need to study and understand whether the pixel under observation contains a single spectral signature or is a combination (linear or non-linear) of different end members present within the pixel. Thus, the spectra of the pixel has been divided into the target spectra and the background spectra (Liu *et al.* 2017, Zhang *et al.* 2015, Xiaochen *et al.* 2020, Nasrabadi, 2014, Chang *et al.* 2020, Du and Zhang 2004, Song *et al.* 2020, Wang and Xue 2017, Wang and Xue 2018, Bajorski *et al.* 2004).

The target spectra if present in the pixel form a part of the target subspace and spectra of the rest of the end members present within the pixel form a part of the background subspace (Figure 3.5).

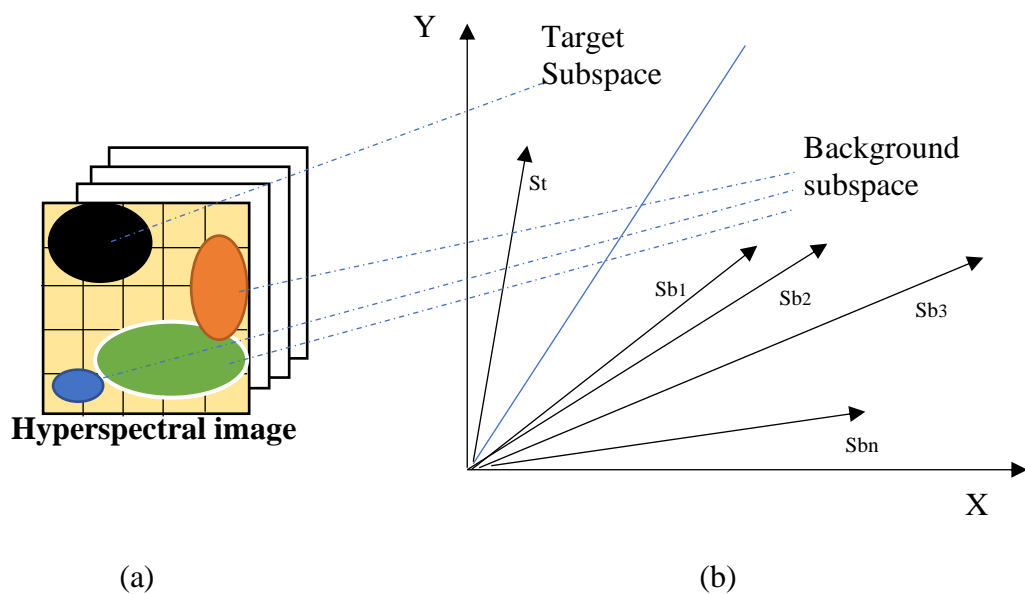


Figure 3.5: Defining the target and background subspaces.

As explained in Figure 3.5 (a), the target is represented in black colour and the rest of the end members form a part of the background subspace. The other major end members

considered are trees as represented in green, pale yellow represents the grass, blue represents the water (pond) and orange represents the soil. Here, the target vector forms the part of the target subspace and end members grass, trees, soil and water are added as part of background subspace according to the equations 3.1 and 3.2 explained in section 3.3.1.

This division of subspaces has been implemented to study,

- (i) If the target – background separation increases the detection of target pixels;
- (ii) Whether it leads to a loss of target pixels or the detection remains the same.
- (iii) In addition, a background threshold is used to calculate the fraction of non – target spectra in pixel. The range for threshold values is usually from 0.5 to 1.0. For example, a value of 1.0 indicates that the entire image pixels will be computed to calculate the statistics for the background while a value of 0.5 indicates that 50% of the pixels of the image will be under consideration.

3.3.1 Theoretical explanation

Subpixel and full pixel Target and Background subspace specification is done as follows (Manolakis *et al.* 2005, Chang *et al.* 2000):

$$x = \sum_{p=1}^R a_p s_p + w = \sum_{p=1 \text{ to } q} a_p s_p + \sum_{p=q+1}^R a_p s_p s_b + w \quad (3.1)$$

$$x = Sa + w = S_t a_t + S_b a_b + w \quad (3.2)$$

where,

x represents the spectrum obtained for the mixed pixel under observation,

s_p represents the spectra of the end members,

a_p are their abundances,

R is the total number of end members,

w represents the noise / interference.

The spectra obtained for a pixel has been subdivided into:

1. $\sum_{p=1toq} a_p S_p$, which represents the target subspace,
2. $\sum_{p=q+1}^R a_p S_p S_b$, which represents the background subspace and,
3. W , noise.

Now, there can appear three cases while evaluating a pixel, that may be considered for target detection:

- i. Target present and Background absent – Full pixel target
- ii. Target present and Background present – Subpixel / mixed pixel
- iii. Target absent and Background present – Subpixels are removed from further analysis and narrows down the set of pixels for consideration for target detection.

3.4 Methodology and Implementation

The **methodology** used in this objective has similar initial implementation steps as discussed in Chapter 2 under section 2.3. Once the initial mandatory steps of performing corrections on the data, creating spatial subset, resampling the ground truth information *etc.* have been performed, end member extraction is then carried out on the data using in-scene spectra. Linear mixture model (LMM) has been implemented for end member identification and their abundance estimation within the pixel.

The detection of targets is done by defining target and background subspaces. Utilizing these variables (spectral information and pixel type), target and background subspaces are obtained, and the detection of targets is further done using dimensionality reduction algorithm (DR) as MNF and target detection algorithms (TD) as MF, OSP, ACE and TCIMF. These algorithms have been selected, considering their performances in detection of targets, in terms of accuracy, minimal loss of target information and computation complexity, as studied in chapter 2.

The target subspace contains the target spectra of Blue felt, also represented as T (Blue_Felt). The background subspace contains mixed background end member spectra of Grass, Trees, Gravel Road and a combination of these, also represented as Mixed (Grass+ Trees+ Roads (Gravel)), Grass, Roads, Red Felt). Here the Red Felt spectra has only been considered as a part of mixed background subspace as its spectra is a part of the background spectra and may aid the efficient detection of target, however, while considering the different subsets of background subspace it has not been considered, as the target blue felt has not been kept over this red felt in the data. The target has been kept over roads, grass and under trees and therefore, these have been considered individually for detection of targets.

The study of impact of target conditions (full illuminations or shade) on the detection of target is performed by analyzing the spectral profiles. The target location (placement of target over different background types) is also considered to study the variation in target detection.

After performing detection, a comparative assessment / analysis of the impact of background subspaces, impact of illumination conditions, impact of target detection algorithm implemented, and impact of background types on target detection is done. The subpixel and full pixel target detection and its analysis on Data Set-2, subset S2 have been explained in detail in Chapter 2 under sections 2.4.3 to 2.4.5. The flowchart representing the steps followed is shown in Figure 3.6.

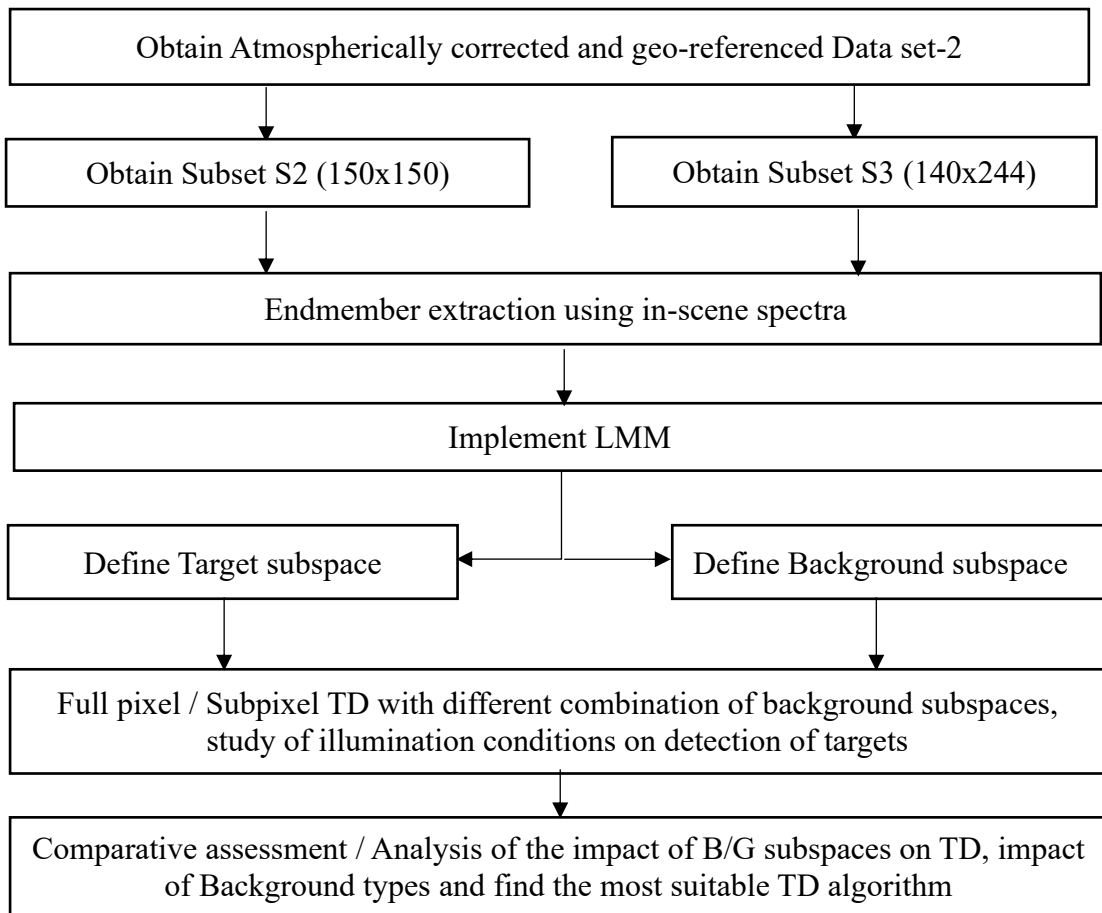


Figure 3.6: Flowchart representing the steps followed to perform full pixel and subpixel target detection using target and background subspaces.

3.5 Results and Discussions

In this section, first, the results of assessment of subpixel target detection using Subset S2 of Data set 2 is discussed. After this, the study and analysis of target spectra placed over different background types in subset S3 has been discussed. Thereafter, target detection using different background subspaces and a combination of subsets of mixed background subspaces is performed on subset S2. Following this, an analysis of the obtained results has been done. Lastly, the different cases of illuminations for different combinations of background subspaces have been discussed. All this is explained step by step under each subsection below.

3.5.1 Assessment of subpixel target detection on Subset S2

It has been observed from the results obtained in Section 2.4.3 - 2.4.5 (Chapter 2), that when subpixel detection is performed using MF (Matched filter). This result is briefly being discussed here again because in chapter 2 the focus was on loss of target pixels using dimensionality reduction and background characterization. The same is also relevant here in full pixel and subpixel target detection:

Without dimensionality reduction, without using Background characterization:

- i. Detection of targets is very low,
- ii. For Yellow Felt, there is a loss of 40 target pixels out of total 64 target pixels,
- iii. Whereas, for Yellow Cotton, there is a loss of 47 target pixels out of 64.

With dimensionality reduction (ICA), using Background characterization (K-means):

- i. Detection of targets is observed to show an improvement.
- ii. For Yellow Felt, there is a loss of only 3 target pixels out of total 64 target pixels,
- iii. Whereas, for Yellow Cotton, there is a loss of only 4 target pixels out of 64.

Thus it may be **deduced** that:

In case of subpixel target detection there appears to be loss of subpixel target information in the case where detection alone is performed in comparison to a case where dimensionality reduction precedes target detection.

The background characterization aids in increasing the accuracy of detection of subpixel targets.

3.5.2 Impact of different Background types on the detection of target (Data set -3)

The spectra of the target Blue Felt has been analysed to observe the variation in spectral behaviour when it has been placed over different background types. Following background types have been considered:

- i. Roads (Gravel)
- ii. Grass (Vegetation)
- iii. Trees-1 (Partial shade) – in terms of covering the target
- iv. Trees-2 (Complete shade)

This has been done to study the impact of varied background types on the detection of targets. Figure 3.7 represents this variation in spectral profile of target Blue Felt.

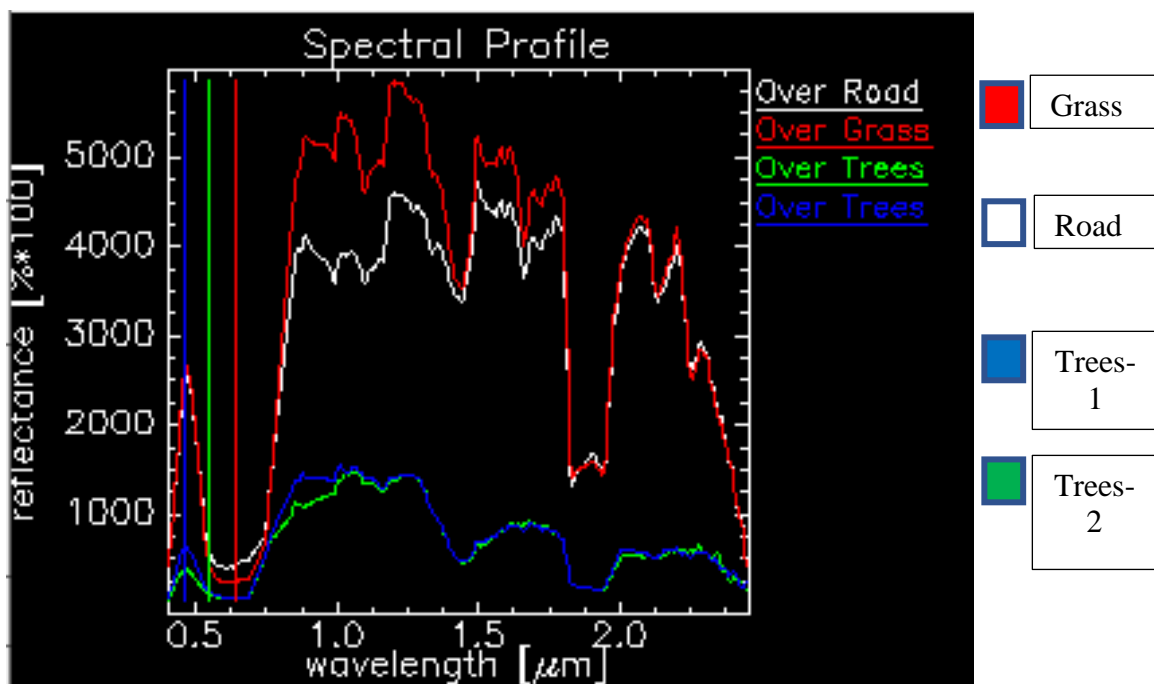


Figure 3.7: Spectral variations observed in the case of target Blue Felt when it has been placed over different background types.

Maximum spectral variation has been observed in the case where target has been placed under trees / shade of trees. Also, there is a greater amount of variation (dips) in the spectral reflectance values (curves represented in blue and green color in Figure 3.4) as compared to the spectra obtained when it is placed over Road and Grass. Maximum variations are observed in the case when target has been placed under trees (both partial and complete shade) at:

- a. 0.40-0.50 (wavelengths in micrometre) - Visible region of the EM spectrum
- b. 0.70-0.90 (wavelengths in micrometre) - VNIR region of the EM spectrum
- c. 1.90-1.99 (wavelengths in micrometre) - Early SWIR region of the EM spectrum

Similar observations can be made with respect to the roads and grass spectra. Further, all the above variations are observed primarily in the visible/IR region. Therefore, it appears that illumination plays a dominant role than the background type.

3.5.3 Target detection in different Background Subspaces

In this section, the target detection has been performed using MF, ACE, OSP and TCIMF considering different combinations of background subspaces and their subsets to study the loss of target pixels. Results are explained in each of the following sub sections.

3.5.3.1 Target detection using Background Subspace - Mixed(Trees, Grass, Roads (Gravel) and Red_Felt)

In this case, the target detection has been performed considering the background subspace as a combination of background types (*i.e.* Trees, Grass, Gravel roads, Red Felt). Here the spectra for Red Felt is also included in the mixed background subspace to assess the results of detection algorithms.

The results of detection are shown in Figure 3.8 and the numeric values of detections have been tabulated in Table 3.2.

The computations for the values of true positives, false positives, true negatives and false negatives has been done to represent the detection results and is represented as TP, FP, TN and FN respectively.

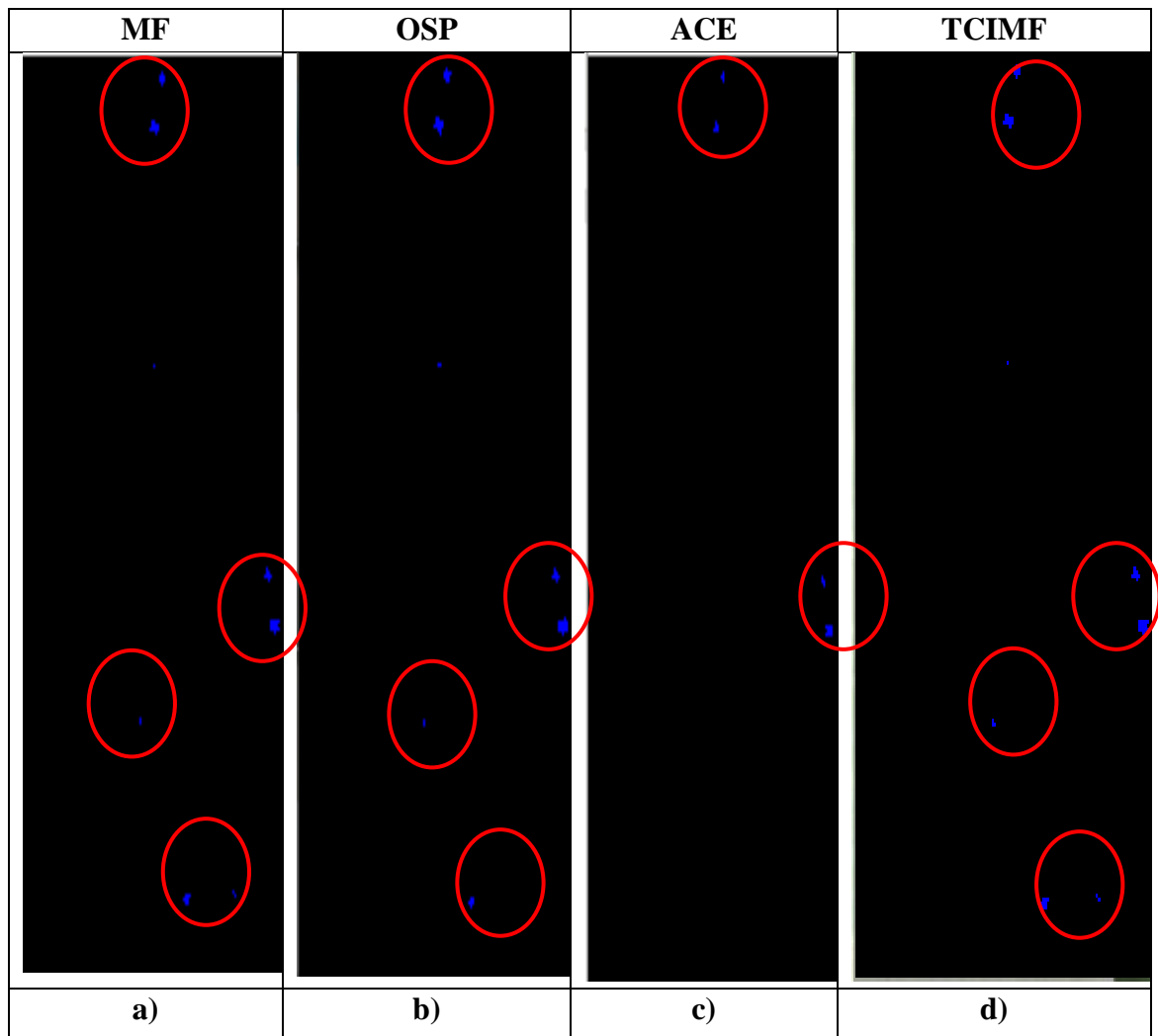


Figure 3.8 Results of detection considering mixed background subspace for algorithms a) MF b) OSP c) ACE and d) TCIMF

Table 3.2: Target detection results for Blue Felt using different TD algorithms for Mixed background subspace (image size of 140x244).

Target subspace – Blue Felt Total target pixels – 56		Background subspace – Mixed (Trees, Grass, Roads (Gravel), Red Felt)			
TD algorithm	Pixels detected in the entire image	TP	FP	FN	TN
MF	59	38	21	18	34083
ACE	25	21	4	35	34100
OSP	59	33	26	23	34078
TCIMF	59	37	22	19	34082

Following is **observed** from the results shown in Table 3.2:

With mixed background subspace, a total of 59 pixels have been detected from the entire input data using MF out of which the target pixels (true positives) detected are 38 and false positives are 21. Also in this case, TCIMF detects a total of 59 pixels out of which target pixels detected are 37 and false positives are 22. This performance in mixed subspace is better than OSP, which detects 33 target pixels and gives 26 false positives.

ACE performs poorly in this case with detection of only 21 target pixels out of 25 total pixels detected in the entire image. False positives are less in this case but this is probably due to the case that detection on the whole is very poor as compared to other algorithms.

From the observations mentioned above, following may be inferred:

TCIMF, and MF appear to be a better performing algorithms in comparison to OSP and ACE in this case. Both these algorithms detect a total of 59 pixels, three pixels higher than the actual number of target pixels, and each having true positives of 38 and 37 pixels respectively. Thus, these algorithms appear to give approximately 66%-67% true positives in the case of mixed background subspace.

3.5.3.2 Target detection using Background Subspace – Trees

To study impact of individual background types on detection results, the implementations have been done separately for the subsets of the background subspace. The results of detection when Trees form a part of background subspace are discussed in this subsection.

Detections obtained using target detection algorithms are shown in Figure 3.9. The numeric values obtained in terms of TP (true positives), TN (true negatives), FP (false positives) and FN (False negatives) are tabulated in Table 3.4.

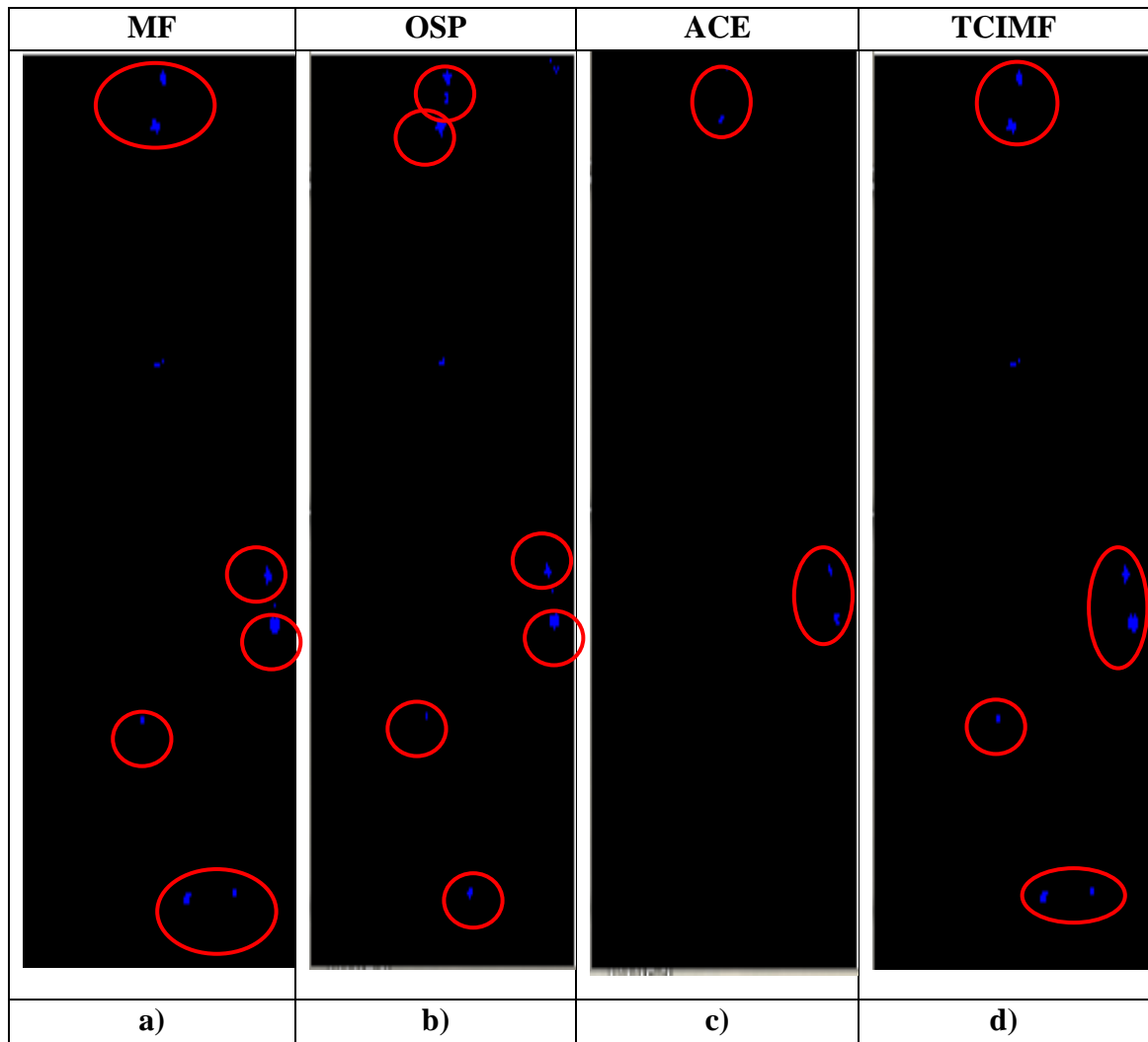


Figure 3.9 Results of detection considering background subspace - Trees for algorithms a) MF b) OSP c) ACE and d) TCIMF

Table 3.3: Target detection results using different TD algorithms for Trees as background subspace (image size of 140x244)

Target subspace – Blue Felt Total target pixels – 56		Background subspace – Trees			
TD algorithm	Pixels detected in the entire image	TP	FP	FN	TN
MF	74	38	36	18	34068
ACE	16	11	5	45	34059
OSP	74	32	42	24	34080
TCIMF	71	40	31	16	34088

The following is **observed** from the results:

When the background subspace only contains the spectra of trees, MF is detects 38 target pixels (true positives) out of the total detections of 74 pixels in the image, however, the false positives increase to 36 pixels as compared to the results of detection when background subspace is considered to be mixed background as shown in Table 3.2.

Also, in this subset of the background subspace, TCIMF detects 40 target pixels out of total detections of 74 pixels and false positives are 31.

However, OSP detects 32 target pixels when trees are considered as background subspace, but the false positives increase to 41. In addition, ACE detects poorly in this case as well with detection of only 11 target pixels with a rise in false positives to 45.

From the observations mentioned above, following may be **inferred**:

Here, TCIMF, and MF once again appear perform better than OSP and ACE. Both these algorithms detect a total of 71 and 74 pixels respectively, fifteen and eighteen pixels higher than the actual number of target pixels, and each having true positives of 40 and 38 pixels respectively. Here, the false positives for MF and TCIMF respectively are also 36 and 31. Thus in this case, these algorithms appear to give approximately 67-71% true positives.

Here it appears that the trees subspace gives a marginal improvement over mixed subspace.

3.5.3.3 Target detection using Background Subspace – Grass

The results obtained with the grass spectra as a subset of background subspace are shown in Figure 3.10. The numeric values corresponding to the pixels detected and pixels lost are tabulated in Table 3.4.

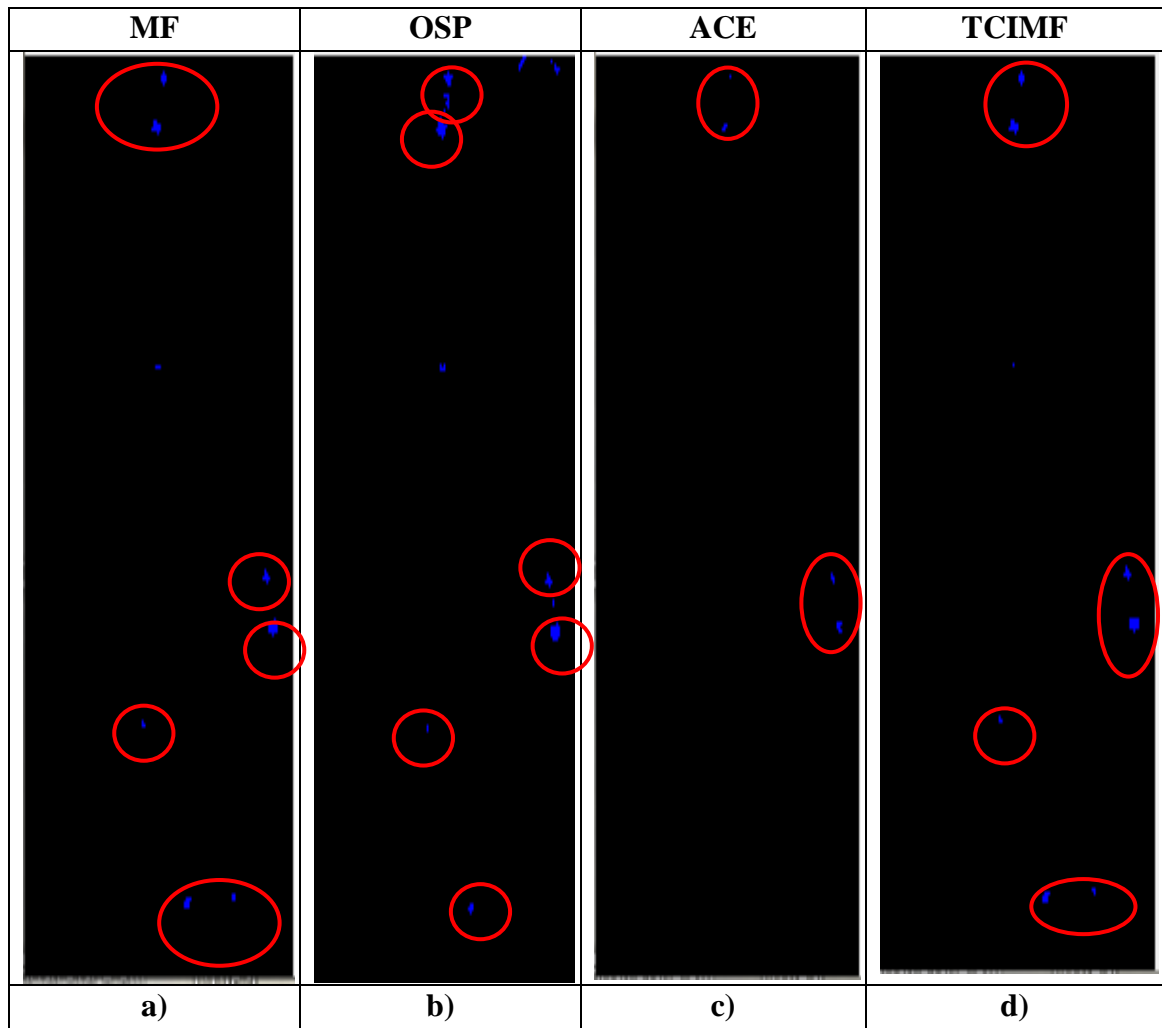


Figure 3.10 Results of detection considering background subspace – Grass for algorithms a) MF b) OSP c) ACE and d) TCIMF

Table 3.4: Target detection results using different TD algorithms for Grass as background subspace (image size of 140x244).

Target subspace – Blue Felt Total target pixels – 56		Background subspace – Grass			
TD algorithm	Pixels detected in the entire image	TP	FP	FN	TN
MF	64	38	26	18	34078
ACE	16	11	5	45	34099
OSP	93	31	62	25	34042
TCIMF	60	38	22	18	34082

Following is **observed** from Table 3.4:

In case of grass as background subspace, the detection algorithm MF detects 38 target pixels (true positives) out of total 64 detections in the image with false positives of 26. This value is lesser than the false positives obtained when background subspace contains Trees as discussed in Table 3.4.

In this case of subset of subspace, TCIMF also detects 38 target pixels out of total detections of 60 pixels, however the false positives are 22 which is lesser than those obtained after implementing MF.

OSP detects only 31 target pixels out of total detections of 93 thereby increasing the number of false positives to 62. ACE detects poorly in this case as well with detection of only 11 target pixels and a loss of 45 target pixels.

From the observations mentioned above, following may be inferred:

Here, TCIMF, and MF once again appear perform better than OSP and ACE. Both these algorithms detect a total of 60 and 64 pixels respectively, four and eight pixels higher than the actual number of target pixels, and each having true positives of 38 pixels. Here, the false positives for MF and TCIMF respectively are also 26 and 22. Thus in this case, these algorithms appear to give approximately 67% true positives.

Here it appears that the grass subspace gives a similar result as that of mixed subspace.

3.5.3.4 Target detection using Background Subspace – Gravel Roads

The subset of background subspace selected for this part is Gravel roads. Impact of this background subspace on detection of target is studied and results are shown in Figure 3.11. Numeric values obtained for True Positives, True Negatives, False Positives and False Negatives are tabulated in Table 3.5.

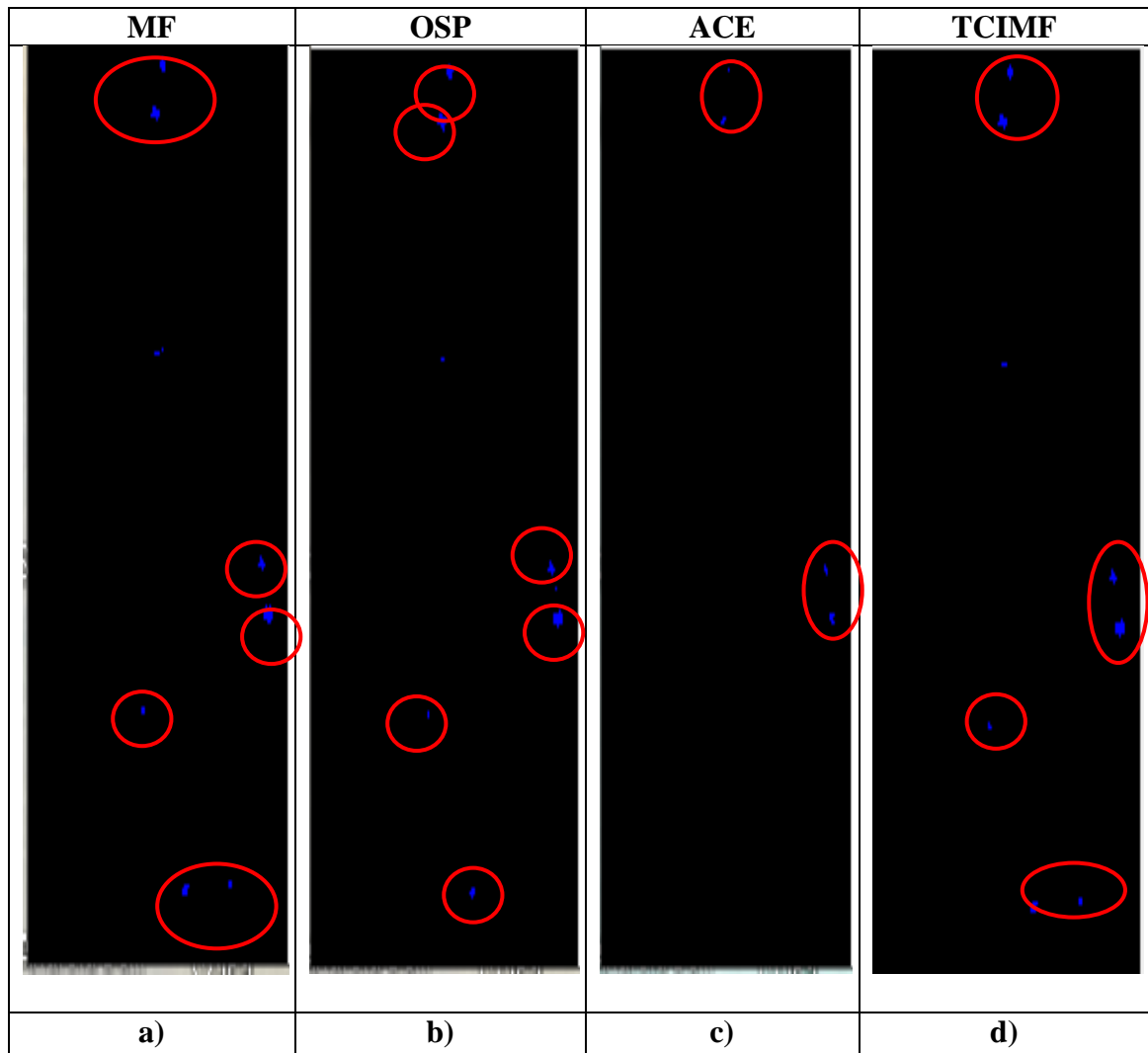


Figure 3.11: Results of detection considering background subspace – (Gravel) Roads for algorithms a) MF b) OSP c) ACE and d) TCIMF

Table 3.5: Target detection results using different TD algorithms for Roads (Gravel) background subspace (image size of 140x244).

Target subspace – Blue Felt Total target pixels – 56		Background subspace – Roads (Gravel)			
TD algorithm	Pixels detected in the entire image	TP	FP	FN	TN
MF	69	38	31	18	34073
ACE	25	20	5	36	34099
OSP	60	33	27	23	34077
TCIMF	64	38	26	18	34078

Following is observed from the results in this case:

In case of gravel roads as background subspace, MF is able to detect 38 target pixels (true positives) out of total detections of 69 pixels which is same as the target pixels detected with MF when background subspace is Mixed but the number of false positives in this case are 31.

In this background subspace, TCIMF also detects 38 target pixels out of total detections of 64 pixels, with false positives of 26. However, OSP detects 33 target pixels successfully but false positives in this case are 27. ACE detects poorly in this case as well with detection of only 11 target pixels.

From the observations mentioned above, following may be inferred:

Here, TCIMF, and MF once again appear perform better than OSP and ACE. Both these algorithms detect a total of 64 and 69 pixels respectively, eight and thirteen pixels higher than the actual number of target pixels, and each having true positives of 38 pixels. Here, the false positives for MF and TCIMF respectively are 31 and 26. Thus in this case, these algorithms appear to give approximately 67% true positives.

Here again it appears that the roads subspace performs same as that of mixed subspace.

In order to further explore these results a detailed analysis is performed which is discussed in the next subsection.

3.5.3.5 Analysis of the impact of different background subspaces on the detection of target

All the results obtained for all the background subspace combinations are compiled and tabulated in Table 3.6.

Table 3.6: Target detection results for target Blue Felt after performing characterization using target and background subspaces

Target Subspace – Blue Felt Total pixels – 56		Background Subspace - Mixed (Roads (Gravel), Trees, Grass, Red Felt), only Grass, Only Trees, Only Roads			
TD Algorithm	Detections	Mixed	Trees	Grass	Roads
MF	Pixels Detected	59 105.3%	74 132.1%	64 114.2%	69 123.2%
	TP	38 67.8%	38 67.8%	38 67.8%	38 67.8%
	FP	21	36	26	31
	FN	18 32.1%	18 32.1%	18 32.1%	18 32.1%
ACE	Pixels Detected	25 44.1%	16 28.5%	16 28.5%	25 44.6%
	TP	21 37.5%	11 19.6%	11 19.6%	20 35.7%
	FP	4	5	5	5
	FN	35 62.5%	45 80.3%	45 80.3%	36 64.2%
OSP	Pixels Detected	59 105.3%	74 132.0%	93 171.4%	60 107.1%
	TP	33 58.9%	32 57.1%	31 55.3%	33 58.9%
	FP	26	42	62	27
	FN	23 41.0%	24 42.8%	25 44.6%	23 41.0%
TCIMF	Pixels Detected	59 105.3%	71 126.7%	60 107.1%	64 114.2%
	TP	37 66.0%	40 71.4%	38 67.8%	38 67.8%
	FP	22	31	22	26
	FN	19 33.9%	16 28.5%	18 32.1%	18 32.1%

The results of detection corresponding to different combinations of background subspaces utilizing the target detection algorithms MF, ACE, OSP and TCIMF, and the retrieved values for TP, TN, FP, FN has also been represented in the form of a graph as shown in Figure 3.12. for further analysis.



Figure 3.12: Graphic representation of the results of detection considering four different combinations of background subspaces.

Both from Table 3.6 and Figure 3.12, following may be **observed**:

The total number of target pixels are 56. Across all the target subspaces, all the algorithms except ACE detects more pixels than the actual number of target pixels. MF and TCIMF appear to be closer to the actual number of target pixels in terms of true positives. However, in the case of MF, this performance remains same across all the subspaces but in

the case of TCIMF there is a marginal improvement in the case of trees vs. all other subspaces.

Similarly, the false negatives in the case of MF remains constant across all the subspaces however, it varies in the case of all other algorithms.

From the above observations, following may be inferred:

For any given algorithm, if the algorithm is performing well for detection of target pixels, in that case the different background subspaces appear to influence the results less. Yet, in the case of trees subspace, a marginal improvement in true positives has been observed. This may be attributed to the similarities between the spectra of blue felt and trees as seen in Figure 3.3.

With MF the number of detected target pixels is higher and constant for all background subspaces, with lesser number of false positives. TCIMF also shows better results for detection of target pixels than OSP and ACE and generates lesser false positives than these. OSP performs better in case of Mixed background subspace as compared to cases where subset of background subspaces is selected.

For any given background subspace, if the algorithm performs well, values for false positives and false negatives is also less. It may also be inferred that target and background subspaces may aid target detection marginally.

3.5.4 Impact of background subspaces and illumination conditions on detection:

In this section, background subspaces have been considered along with illumination conditions to understand its effect on target detection. Results have been analyzed separately for different subspaces in Table 3.7.

Table 3.7 : Results of detection wrt the illumination conditions for target placements with mixed, trees, grass and gravel roads as background subspace.

Target Id's	Illumination conditions	Target pixels	TD algorithm	Pixels Detected (Mixed)	Pixels Detected (Trees)	Pixels Detected (Grass)	Pixels Detected (Roads)
T1	Full Illumination (Over Gravel Road)	4	MF	4	4	4	4
			ACE	3	1	1	3
			OSP	4	4	4	4
			TCIMF	4	4	4	4
T2	Full Illumination (Over Gravel Road)	9	MF	8	8	8	8
			ACE	6	3	3	5
			OSP	8	8	8	8
			TCIMF	8	9	8	8
T3	Full Illumination (Over Grass – Open Field)	4	MF	4	4	4	4
			ACE	4	3	3	4
			OSP	4	4	4	4
			TCIMF	4	4	4	4
T4	Full Illumination (Over Grass – Open Field)	9	MF	9	9	9	9
			ACE	8	4	4	8
			OSP	8	8	8	8
			TCIMF	9	9	9	9
T5	Under Tree Shade (On path)	4	MF	0	0	0	0
			ACE	0	0	0	0
			OSP	0	0	0	0
			TCIMF	0	0	0	0
T6	Under Partial Tree Shade	4	MF	3	3	3	3
			ACE	0	0	0	0
			OSP	2	2	2	3
			TCIMF	3	4	3	3
T7	Under Partial Tree Shade	9	MF	7	7	7	7
			ACE	0	0	0	0
			OSP	7	6	5	6
			TCIMF	6	7	7	7
T8	Under trees (Full shade)	9	MF	0	0	0	0
			ACE	0	0	0	0
			OSP	0	0	0	0
			TCIMF	0	0	0	0
T9	Under trees (Full shade)	4	MF	3	3	3	3
			ACE	0	0	0	0
			OSP	0	0	0	0
			TCIMF	3	3	3	3

From the Table 3.7 following may be observed:

Mixed background subspace:

- i. For targets T1, T2, T3, T4 placed in **full illumination** the algorithms MF and TCIMF perform the best (minimum detection of 88.8%, and maximum detection of 100%) followed by OSP and ACE (minimum detection of 66.6%, and maximum detection of 100%).
- ii. For targets T5 and T8 placed under **complete shade**, none of the algorithm is able to detect any of the target pixels (detection is 0%).
- iii. However, for targets T6, T7 and T9 that are under **partial shade**, the algorithms MF and TCIMF are able to detect a few target pixels (minimum detection of 66.6%, and maximum detection of 77.7%) whereas, OSP and ACE perform poorly resulting in greater loss of target pixels (minimum detection of 0.0%, and maximum detection of 77.7%).

Trees background subspace:

- i. For targets T1, T2, T3, T4 placed in **full illumination**, and a subset of background subspace (Trees), algorithm TCIMF performs the best (minimum and maximum detections = 100%), MF also gives good results of detection (minimum detections of 88.8% and maximum detections of 100%), followed by OSP and ACE (minimum detections of 25% and maximum detections of 100%).
- ii. For targets T5 and T8 placed under **complete shade**, none of the algorithm is able to detect any of the target pixels (detection is 0%).
- iii. However, for targets T6, T7 and T9 that are under **partial shade**, the algorithms MF and TCIMF are able to detect target pixels (minimum detections of 75% and maximum detections of 100%) whereas, OSP and ACE perform poorly resulting in

loss of target pixels (minimum detections of 0% and maximum detections of 66.6%).

Grass background subspace

- i. For targets T1, T2, T3, T4 placed in **full illumination**, with grass as background subspace, algorithms TCIMF and MF perform best (minimum detections of 88.8% and maximum detections of 100%), followed by OSP and ACE performs poorly (minimum detections of 25% and maximum detections of 100%).
- ii. For targets T5 and T8 placed under **complete shade**, none of the algorithm is able to detect target pixels (detection is 0.00%)
- iii. However, for targets T6, T7 and T9 that are under **partial shade**, the algorithms MF and TCIMF are able to detect target pixels (minimum detections of 75% and maximum detections of 77.7%) whereas, OSP and ACE perform poorly resulting in loss of target pixels (minimum detections of 0.00% and maximum detections of 55.5%).

(Gravel) Roads background subspace:

- i. **Full illumination** targets T1,T2, T3, T4 are detected well with TCIMF and MF considering **gravel roads as background subspace** (minimum detection of 88.8% and maximum detection of 100%), OSP also performs good (minimum detection of 88.8% and maximum detection of 100%), but ACE leads to greater loss of target pixels (minimum detection of 55.5% and maximum detection of 100%),.
- ii. Targets under **full shadow** of trees, T5 and T8 are not detected by any algorithm (detection is 0%).
- iii. Targets, T6, T7 and T9 are placed under **partial shadow** of trees and target pixels are well detected for these target ID's by TCIMF and MF (minimum detection of

75% and maximum detection of 77.7%), followed by OSP (minimum detection of 0% and maximum detection of 75%),. ACE is not able to detect these targets (detection is 0%).

Therefore, from the above observations, it may be **deduced** that:

Illuminations affects the detection of targets greatly, where target pixels of targets in full illumination placed over Gravel roads and Grass are detected well in comparison to those under trees.

Also, the targets in partial shade are detected whereas the targets in full shade are not detected by the above discussed algorithms for any combination of background subspace.

3.6 Conclusions

In this chapter, a study of detection of full pixel and subpixel targets has been performed using different background subspaces, varying background types and varying illumination conditions *etc.*

In case of detection using target and background subspaces, it may be concluded that for any given algorithm, if the algorithm is performing well for detection of target pixels, the different background subspaces appear to influence the results less. Yet, in the case of trees subspace, a marginal improvement in true positives has been observed. This may be attributed to the similarities between the target and the background spectra. Therefore, the target and background separation continue to be a challenge and affects the target detection. Further, with MF the number of detected target pixels is higher and constant for all background subspaces, with lesser number of false positives. TCIMF also shows better results for detection of target pixels than OSP and ACE and generates lesser

false positives than these. OSP performs better in case of Mixed background subspace as compared to cases where subset of background subspaces is selected. Also, for any given background subspace, if the algorithm performs well, values for false positives and false negatives are also less. Thus, it may be inferred that target and background subspaces may aid target detection marginally.

It may be further concluded after studying the impact of target detection algorithms that, MF produces comparatively better results of detection of target pixels and lower number of false positives. TCIMF follows next and performs better than OSP. ACE, however, appears to give poor results of detection with a greater number of false positives.

Also, based on target condition (full illumination or shade), it can be concluded that the targets that are placed under open sky are detected well as compared to those placed under trees and their shadow. Illumination affects the detection of targets greatly, where target pixels of targets in full illumination placed over Gravel roads and Grass are detected well in comparison to those under trees. Also, the targets in partial shade are detected whereas the targets in full shade are not detected by the above discussed algorithms for any combination of background subspace.

Lastly to study the impact of different types of backgrounds, implementations were performed and based on the analysis of spectral profiles, it may be concluded that the surrounding vegetation (trees) has a greater impact on the spectral behaviour of pixel containing blue felt target. The gravel roads have minimum impact on spectral variation of this target out of the three background types.

The experimental dataset used in this study has been taken from SHARE-2012 campaign. Advantage has been taken of the targets deployed which could conveniently be used for the study presented. The controlled dataset made available however leaves the

question of scalability open. The results need to be compared with other similar experiments with similar or different datasets.

Chapter 4

End Member Extraction in Mixed Pixels using Spectral Unmixing and Spectral Indices Approaches

4.1 Introduction to the Problem

Uptill this chapter, various aspects of target detection (full pixel and subpixel targets) in hyperspectral data have been studied. A study on the loss of target information (both full pixel and subpixel) while performing dimensionality reduction (Chapter 2), study of impact of background characterization on detection of targets as well as whether the separation of target and background subspaces aid the process of target detection (Chapter 3) have also been discussed.

A target need not necessarily be always an object of defined shape, size and orientation. It can also be any natural land cover class or any artificial impervious / pervious surfaces. These can also be treated as a full pixel / subpixel target as long as hypothesis of binary classification are applied to them for their detection. In this chapter, certain impervious surfaces have been considered as targets.

In hyperspectral data, particularly in cases of wide spread surfaces which may be considered as target, there might arise a situation where adjacent end members may jointly occupy a single pixel thereby leading to generation of mixed pixels (Altmann *et al.* 2012, Boardmann *et al.* 1995, Boardmann 1998, Borel and Gerstl 1994). In case of mixed pixel targets, the resulting spectra of any given pixel contains a target spectra and also the spectra of other end members present within that pixel at the time of data collect. This complicates the detection of targets in hyperspectral data particularly the targets that are small in size as compared to the spatial resolution of the sensor which captured the data.

The target detection algorithms, in most of the cases, do not detect targets that are present in the mixed pixels. In all such cases, spectral unmixing is performed to separate the target spectra from the background spectra (Chang and Du 2004, Clark 2016, Keshava *et al.* 2002). Spectral unmixing algorithms provide the end members present within the pixel and their corresponding abundance fractions (fraction of pixel area covered by each end member present in the image). However, errors may occur during the process of generation of end members, calculations of abundance fractions and creation of the initial abundance maps of each end member within the pixel (Lu *et al.* 2013, Makido *et al.* 2007). These issues have not been adequately studied. The limitations of spectral unmixing approach in extraction of end members are discussed in the subsection 4.2.1.

Another technique that may be explored for extraction of end members from the hyperspectral data is Spectral Indices based approach. A spectral index is defined as the ratio between reflectance values obtained at two or more wavelength ranges (Benediktsson *et al.* 2003, Bhaskaran *et al.* 2000, Bouzekri *et al.* 2015). The computation using spectral indices is relatively easy and fast as compared to other spectral techniques for end member extraction. As reported in the literature, several techniques for development and analysis of spectral indices for multispectral data, specifically related to vegetation and crop monitoring have been reported (Liang *et al.* 2012, Usman *et al.* 2015, Verhoye and De-wolf. 2002). However, the utilization of these spectral indices to extract impervious / pervious surfaces in urban land cover mapping using hyperspectral data is still limited and continues to pose a problem.

Utilization of multispectral data limits the detection of targets which are spectrally similar or have lesser spectral differences, such as dry and bare soil, bushes / shrubs and trees, concrete road or asphalt road *etc.* To perform analysis in these areas, a high spatial and spectral resolution hyperspectral data has been explored.

Accordingly, this objective has been subdivided into following tasks:

1. End member extraction and abundance estimation using spectral unmixing,
2. Evaluating spectral indices for end member identification.

The layout of this chapter is as follows. The objective end member extraction using spectral unmixing and spectral indices has been briefly introduced. Next in section 4.2, spectral unmixing and spectral indices based approaches for end member extraction have been reviewed. For reasons of assessment different sets of data have been used which are explained in section 4.3. Section 4.4 gives the methodology and implementations and results are discussed in section 4.5.

4.2 Spectral Unmixing and Spectral Indices based approach for end member extraction.

In this section, spectral unmixing and spectral indices based approaches have been reviewed to understand their utility in the process of end member extraction.

4.2.1 Review of spectral unmixing based approaches

4.2.1.1 Spectral Unmixing for end member extraction and abundance estimation

The estimation of fraction of an end member within a pixel in case of mixed pixels occurring in the image is known as abundance fraction estimation. Spectral unmixing is necessary to generate the end members and their corresponding abundance maps. Most unmixing algorithms search for the major end members occurring in the image (full pixel end members / pure spectra). All other pixels in the image are considered to be a linear combination of these identified end members. Thus it is relevant to first generate such pure full pixel end members. This process is also referred as end member extraction (Manolakis 2002, Segl *et al.* 2003, Shao *et al.* 2018, Song *et al.* 2020, Villa *et al.* 2011).

Following this, unmixing is performed to determine the existence of these end member spectra in adjacent mixed pixels and lastly the abundance maps are generated using

the computed abundance fractions. A linear mixture model (LMM) is widely used unmixing algorithm that models the spectra of a pixel as a linear combination of individual end member spectra and its abundance fraction. This algorithm assumes that sum of the abundance of each end member equals one but can not be less than zero (Manolakis *et al.* 2005) . Mathematically, in case of L spectral bands, the spectrum of any pixel and the spectra of the end members can be represented by L-dimensional vectors. The general equation for LMM is explained in equation 4.1:

$$x = \sum_{k=1}^M a_k s_k + w \triangleq Sa + w \quad (4.1)$$

$$S \triangleq [s_1 \ s_2 \ \cdots \ s_M]$$

$$a \triangleq [a_1 a_2 \cdots a_M]^T$$

x , spectrum of the mixed pixel,

s_k , spectra of the end members,

a_k , is their abundances;

M, number of the end members;

W, L dimensional error vector accounting for lack of fit and noise effects

$$a_k \geq 0 \text{ (non negativity constraint)}$$

$$\sum_{k=1}^M a_k = 1 \text{ (additivity constraint)}$$

Many algorithms have been proposed in literature for implementing spectral unmixing in case of hyperspectral data (Fan *et al.* 2009, Heylen *et al.* 2014, Heylen *et al.* 2016, Karabhari *et al.* 2019, Lee *et al.* 2006). A brief summary of spectral unmixing algorithms is provided in Table 4.1.

Table 4.1: A summary of spectral unmixing algorithms for hyperspectral images

Algorithms	Characteristics
Pixel purity index (PPI)	<p>Non-statistical, supervised end member extraction method</p> <p>Limitations:</p> <ol style="list-style-type: none"> i. It requires a human supervision. ii. It requires a way out to produce an appropriate initial set of endmembers as the number of iterations will otherwise be very high. iii. It requires a proper learning on how to procure accurate values of threshold for the pixel purity index counts. iv. Only considers the spectral information in endmembers detection with no attention to spatial information.
N – FINDR	<p>Geometric end member extraction method, non-parameterized and simplex-growing algorithm. Iterative, fully automated, non-parametrized. Creates a Simplex with max. volume found, selects random end member for initialization.</p> <p>Limitations:</p> <ol style="list-style-type: none"> i. It works for finding all the present endmembers thereby increasing the computational complexities. ii. Requires prior knowledge of the number of endmembers that are required to be extracted. iii. Does not include spatial information for end member detection
Optical Real-time Adaptive Spectral Identification System (ORASIS)	<p>It is a fully automated, parameterized method for end member extraction.</p> <p>It provides low computational complexity and converges once all the exemplar spectra are found in data. It mostly applies in oceanography and target detection.</p> <p>Limitations:</p> <ol style="list-style-type: none"> i. It is a simplex-shrinking algorithm that finds endmembers from a scene autonomously.
Iterative error analysis (IEA)	<p>It is a fully automated, non – parameterized algorithm that shows minimum error in unmixing. It is mostly applicable to land cover and mineral mapping.</p> <p>Limitations:</p> <ol style="list-style-type: none"> i. Does not include spatial information for end member detection

<p>Convex cone analysis (CCA)</p>	<p>It is a fully automated, geometric, parameterized algorithm. It is mostly applicable to anomaly detection and target detection.</p> <p>Limitations:</p> <ol style="list-style-type: none"> i. Complexity is very high if there are large numbers of corners in the convex cone. ii. Does not include spatial information for end member detection
<p>Vertex Component Analysis (VCA)</p>	<p>Geometric end member extraction method, unsupervised algorithm</p> <p>Limitations:</p> <ol style="list-style-type: none"> i. Computational complexity is high as the algorithm iterates until all endmembers are exhausted ii. Only considers the spectral information in endmembers detection with no attention to spatial information
<p>Automatic Target Generation Procedure (ATGP)</p>	<p>Fully automated, non-parametrized and iterative. Iterative orthogonal projections of the data are obtained, and then largest magnitude vector of this projection is found.</p> <p>Limitations:</p> <ol style="list-style-type: none"> i. Slightly more convergence time than NFindr
<p>Independent Component Analysis end member Extraction (ICA-EEA)</p>	<p>Nonparametric statistical unmixing approach. It considers spatial information and thus has the potential to improve the quality of the endmembers. It does not require a priori information about target.</p> <ol style="list-style-type: none"> i. Compute component scores using covariance to rank the components, compute mean, sort in descending order, retrieve maxpixels. ii. Generate Abundance maps using FCLS algorithm, compute sum of each pixel abundance, compute the error between decomposed and real signature <p>Limitations:</p> <ol style="list-style-type: none"> i. This algorithm performs poorly when simulations are considered with very few materials present.

From the above review and based upon the literature survey, four algorithms have been selected, for the present work:

- i. Independent component analysis – end member extraction algorithm (ICA-EEA),
- ii. Automated target detection procedure (ATGP),
- iii. N-Findr and,
- iv. Pixel purity index (PPI).

ICA-EEA utilises the independent component analysis approach to isolate the end members. ATGP on the other hand, works on principle of orthogonality. The orthogonal iterative projections are utilised to extract the end members. PPI works by random projections of data on vectors and selection of end members which appear at the extrema of the projection.

These algorithms have been used to estimate the total number of end members present in the image with a pure / unique spectra, to utilize a constrained least squares algorithm using the recovered endmember spectra to generate the abundance maps, to assess the generated abundance maps and to compute the errors corresponding to each.

4.2.1.2 Limitations of Spectral unmixing

The selection of end member to be fed to any of the spectral unmixing algorithms may be done in three ways as under,

- i. First, is to determine end members spectra from the image itself
- ii. Second, is to select a reference spectra from a collection in the laboratory / library (standard library or user defined)
- iii. Third, field spectra.

Spectral unmixing suffers from various disadvantages some of which are mentioned below:

- i. It assumes that all the end members falling within a mixed pixel are combined linearly while in reality, it may not be so due to various reasons (Manolakis *et al.* 2001, Manolakis 2016, Drumetz *et al.* 2016).
- ii. Spectral unmixing requires providing reference spectra to the unmixing algorithms to produce end member spectrum and abundance fractions present within a mixed pixel. This reference spectra can be either a ground spectra or a pure pixel spectra drawn from the image itself. This pure pixel is assumed to be one of the end members present in the mixed pixel. Radiance to reflectance conversion often leads to certain erroneous spectra which may affect the results of spectral unmixing. In addition, it has been studied from literature that most of the algorithms for unmixing, work by finding the set of pure pixels. However, the algorithms such as LMM may not be able to find such pure pixels perfectly owing to the instrument noise and external noise. Due to large volumes of data in hyperspectral images, this process is even more difficult as the output may also contain the noisy pixels, outliers, or defects that lie outside the main end members (pure pixels) (Shao and Lan 2019, Halimi *et al.* 2016, Somers *et al.* 2011, Zare and Ho. (2014), Ghaffari *et al.* 2017).
- iii. Another issue that arises is that the end members that are very obvious to locate / identify on the ground may be much more difficult to determine from the remote sensing image itself. As an example, consider a case of a forest where 50 percent of the image pixels contain trees but actually in that image trees occupy less than half of any single pixel. In this case end

members determined from this image would not include a full pixel “tree” end member (Manolakis 2016).

- iv. In cases where there are say ‘ n ’ number of end members occupying a single pixel but one of these end members is very less in terms of the fractional occupancy within the pixel. The spectral unmixing approaches have not been effective in spectrally revolving such an end member (Costanzo 2000).
- v. Also, the spectral unmixing based approaches are completely dependent on the spectra and do not consider any wavelength based absorption variation (Zhang *et al.* 2006).

4.2.2 Concept of Spectral Indices for end member identification

A Spectral index is a combination of spectral reflectance from two or more wavelengths that indicate the relative abundance of features of interest (Im *et al.* 2012, Altmann *et al.* 2012). These wavelengths depend upon energy absorption features in different regions of the EM spectrum and are a better representation of an end member. This approach addresses the extraction based on the physical properties of the surfaces by utilizing the spectral information contained in the hyperspectral image.

The spectral based approach is proposed to be studied by considering an urban area which can be divided into a set of impervious (which do not allow water to percolate) and pervious (which allow water to percolate) surfaces (Hu and Wang 2011, Weng 2012, Im *et al.* 2012, Bhaskaran *et al.* 2000, Foody 2002, Liang *et al.* 2012, Schueler 1994). The approach commences with the exploration of the spectral information for impervious (primarily man-made) and pervious (primarily natural) surfaces. Although, there are a large number of impervious and pervious surfaces, however, for the purpose of this study, only a few of them have been considered. These impervious and pervious surfaces can be categorized in three levels and Table 4.2 (a) and (b).

Table 4.2 (a) - Level-wise categorization of major pervious surfaces

Level 1 (Major class of urban surfaces)	Level 2 (Sub-class)	Level 3
Pervious	Water	Open Water Perennial Ice/Snow Canopy Level
	Soil	Bare Rock Clay Sand Quarries
	Vegetation	Grasslands Forest Upland Shrub land

Table 4.2 (b) - Level-wise categorization of major impervious surfaces

Level 1 (Major class of urban surfaces)	Level 2 (Sub-class)	Level 3
Impervious Surface	Roofs	Plastic Glass Asbestos sheet
	Roads	Concrete Bitumen Gravel Stone Tiles Asphalt
	Pavements	
	Paths	

Many spectral indices have been developed and reported in the literature particularly for the multispectral data there appears to a few which works for hyperspectral data.

4.2.2.1 Brief review of existing spectral indices

The pervious surfaces such as water bodies mentioned above can be studied using Modified Normalized Difference Water Index (MNDWI) (to enhance open water features in urban land cover by suppressing the other land cover features such as soil, vegetation

etc.) (Xu 2010), Normalized Difference Water Index (NDWI) (Gao 1996, McFeeters 1996, Xu 2010), Normalized Difference Moisture Index (NDMI), Normalized Difference Snow Index (NDSI) (Salomonson *et al.* 2004) etc.

Pervious surfaces such as Barren land (soil and rocks) can be identified using Simple Ratio Clay Index (SRCI) (Khasanah *et al.* 2013), Normalized Difference Soil Index (NDSI) (Waqar *et al.* 2012, Hall *et al.* 1995) and Normalized Difference Clay Index (NDCI) (Shabao *et al.* 2015) as explained. The longer the wavelength the larger is the difference between the finer grain features and coarser grain features of the soil.

For identification of vegetation, various indices have been developed and studied such as Normalized difference vegetation index (NDVI) (Usman *et al.* 2015), Infrared Percentage Vegetation Index (IPVI) (Crippen 1990), Renormalized difference Vegetation Index (RDVI) (Roujean *et al.* 1995), Green Ratio Vegetation Index (GRVI) (Wolf 2010), Soil Adjusted Vegetation Index (SAVI) (Huete 1988, Rondeaux *et al.* 1996) etc. Various indices reported in the literature for pervious surfaces have been summarized in Table 4.3.

Table 4.3 - Spectral indices for identification of pervious surfaces

Spectral Index	Formulation	Wavelength (µm)
Spectral Indices for Water		
MNDWI (Xu 2010)	$\frac{Green - SWIR}{Green + SWIR}$	Short Wave Infrared (SWIR): - Min:1.55; Mid:1.65; Max:1.75
NDWI (Gao 1996, McFeeters 1996, Xu 2010)	$\frac{Green - NIR}{Green + NIR}$	Near Infrared (NIR): - 0.72-0.80; 0.83-0.99
NDMI (Hall <i>et al.</i> 1995)	$\frac{\rho_{795} - \rho_{990}}{\rho_{795} + \rho_{990}}$	0.72-0.80; 0.83-0.99
NDSI (Salomonson <i>et al.</i> 2004)	$\frac{Green - SWIR1}{Green + SWIR1}$	Green: - 0.5-0.6; SWIR1: - 1.55- 1.75

Spectral Indices for Soil		
NDSI (Waqar <i>et al.</i> 2012)	$\frac{MIR - Green}{MIR + Green}$	MIR: -1.66; Green: - 0.56
Clay Ratio (Khasanah <i>et al.</i> 2013)	$\frac{SWIR}{NIR}$	SWIR: - Min:1.55; Mid:1.65; Max:1.75 NIR: - 0.72-0.80; 0.83-0.99
SRCI (Khasanah <i>et al.</i> 2013)	$\frac{SWIR1}{SWIR2}$	SWIR1:- 1.55-1.75 μ m SWIR2:- 2.08-2.35 μ m
NDCI (Shabao <i>et al.</i> 2015)	$\frac{\rho_{795} - \rho_{990}}{\rho_{795} + \rho_{990}}$	0.72-0.80; 0.83-0.99
Spectral Indices for vegetation		
NDVI (Gutman 1991, NOAA. 1990, Myneni <i>et al.</i> 1995, Usman <i>et al.</i> 2015)	$\frac{NIR - Red}{NIR + Red}$	NIR: - 0.72-0.80; 0.83-0.99 Red: - 0.43-0.48
IPVI (Crippen 1990)	$\frac{NIR}{NIR + Red}$	NIR: - 0.72-0.80; 0.83-0.99 Red: - 0.43-0.48
RDVI (Roujean <i>et al.</i> 1995)	$\frac{NIR - Red}{\sqrt{NIR + Red}}$	NIR: - 0.72-0.80; 0.83-0.99 Red: - 0.43-0.48
GRVI (Wolf 2010)	$\frac{NIR}{Green}$	NIR: - 0.72-0.80; 0.83-0.99 Green:- 0.56
SAVI (Huete 1988, Rondeaux <i>et al.</i> 1996)	$\frac{1.5 * (NIR - Red)}{NIR + Red + 0.5}$	NIR: - 0.72-0.80; 0.83-0.99 Red: - 0.43-0.48

Similarly, in the case of impervious surfaces such as roads, roofs *etc.*, spectral indices such as Normalized Difference Built-up Index (NDBI) (Zha *et al.* 2003, Hongmai *et al.* 2005), Built-up Area Extraction Index (BAEI) (Wolf 2010), Normalized Built-up

Area Index (NBAI), and Normalized Difference Impervious Surface Index (NDISI) (Xu 2010), New built up index (NBI) (Zhang 2009), Morphological building index (MBI) (Samsudin *et al.* 2016) have been reported in the literature. Some of these have been summarized in Table 4.4

Table 4.4 - Spectral indices for impervious surfaces

Spectral Index	Formulation	Wavelength (µm)
NDBI (Zha <i>et al.</i> 2003, Hongmai <i>et al.</i> 2005)	$\frac{SWIR - NIR}{SWIR + NIR}$	SWIR: - Min:1.55; Mid:1.65; Max:1.75 NIR: - 0.72-0.80; 0.83-0.99
BAEI (Wolf 2010)	$\frac{Red + L}{Green + SWIR1}$	L =0.3
NBAI (Zhang 2009, Hongmai <i>et al.</i> 2005)	$\frac{SWIR - TIRS}{SWIR + TIRS}$	TIRS: -10.6- 11.19
NDISI (Xu 2010)	$\frac{T_b - (MNDWI + \rho_{NIR} + \rho_{SWIR1})/3}{T_b + (MNDWI + \rho_{NIR} + \rho_{SWIR1})/3}$ where, $MNDWI = \frac{\rho_{GREEN} - \rho_{SWIR1}}{\rho_{GREEN} + \rho_{SWIR1}}$	T_b is brightness temperature of thermal band
MBI (Samsudin <i>et al.</i> 2016)	$MBI = \frac{B_{SWIR2} \times B_{RED} - B_{NIR}^2}{B_{RED} + B_{NIR} + B_{SWIR2}}$	SWIR: - Min:1.55; Mid:1.65; Max:1.75 NIR: - 0.72-0.80; 0.83-0.99 RED:- 0.47-0.48
NBI (Zhang 2009)	$\frac{(B_{RED} \times B_{SWIR})}{(B_{NIR})}$	SWIR: - Min:1.55; Mid:1.65; Max:1.75 NIR: - 0.72-0.80; 0.83-0.99 RED:- 0.47-0.48

4.2.2.2 Development of spectral indices for hyperspectral data

Development of this approach commences with the creation of a spectral library of end members (targets and backgrounds) present in the image. For development of this approach, aerial hyperspectral data collected under AVIRIS – NG campaign of Ahmedabad – INDIA has been considered. The data consists of a total of 425 bands at a spectral bandwidth of 5 nm and spatial resolution of 4-8 m. Field data also has been collected for the same area. The description of the data is given in detail in the next section on Data.

Spectral library creation

The process requires a few pre implementation steps: band selection (removal of bad bands) and finding out the most suitable ranges for detection and identification of impervious / pervious surfaces. LDA / DA (Discriminant analysis) is performed to select appropriate / significant bands using hyperspectral data and ground truth to develop spectral indices. This involves following steps:

- i. Perform geometric correction, set the data to World Geodetic System 84-datum.
- ii. QUAC (Quick atmospheric correction) – obtain reflectance data
- iii. Removal of bad bands (38) – Water absorption bands (1400-1900 nm), noisy bands with low SNR.

Spectral subset selected therefore contains 387 bands (details in data description under section 4.3). Ground truth spectra has been obtained and end members have been categorized into classes impervious (targets) / pervious surfaces (backgrounds). Identification and extraction of impervious surfaces is then done from data set.

The obtained ground truth spectra are then resampled according to the number of good bands retained in the hyperspectral image. Spectral library has been created for all the impervious and pervious surfaces. The procedure for creation of spectral library for the purpose of this study is summarised in Figure 4.1.

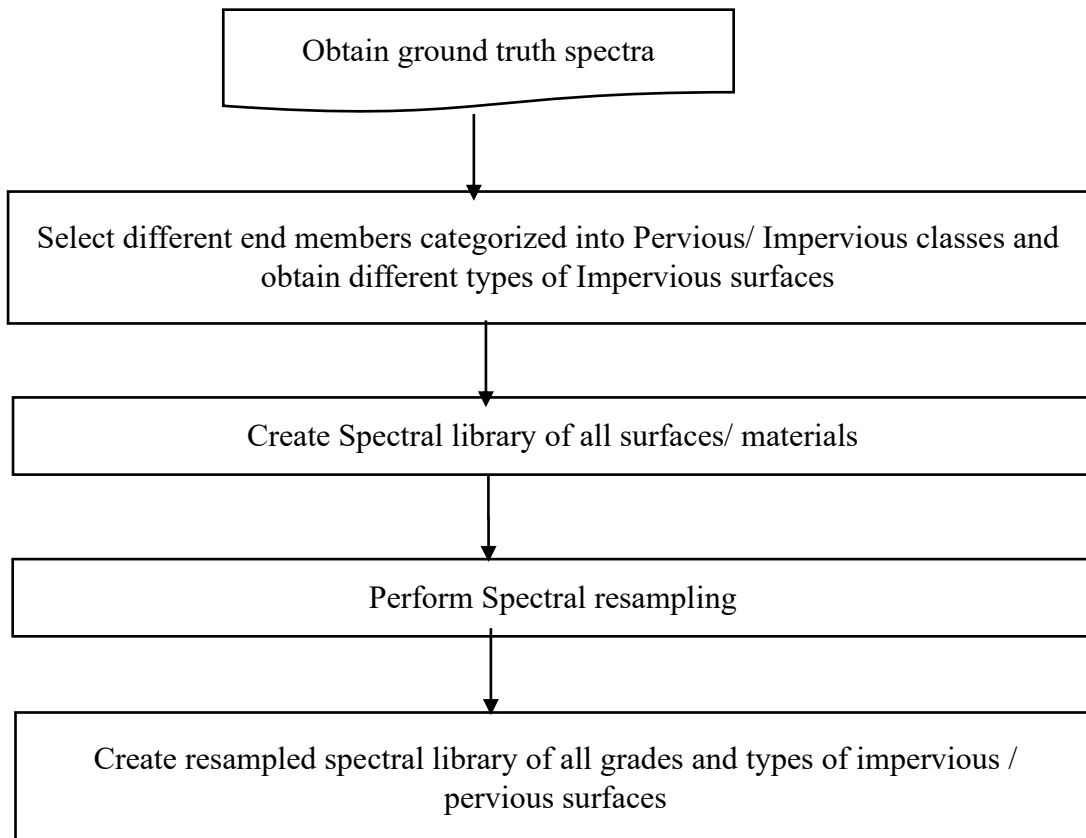


Figure 4.1: Flowchart representing the order of implementation to create spectral library

It is already discussed that while performing end member extraction, the most suitable spectral bands have been selected. The spectral subsetting into eight EM regions, Full spectral region, Ultraviolet, Visible, UV+visible, VNIR, Far NIR, Early SWIR, Far SWIR has been done to further extract significant spectral bands for developing spectral indices / performing end member extraction.

Endmember Extraction using Indices

Following the successful creation of spectral library, spectral indices have been explored for end member identification / extraction from the data.

Surfaces that are to be detected (target) are identified and their corresponding reflectance is obtained in all the bands. To implement spectral indices, two most significant bands are selected in particular wavelength range. Here the pervious surfaces are selected as backgrounds and their reflectance values in all the bands is also obtained.

Band ratio (ratio of two significant spectral wavelengths) is computed. To evaluate a spectral index, the least effective wavelength is first removed using OIF (Optimum Index Factor). OIF aids in evaluating the most informative band ratio in terms of standard deviation and correlation between the two spectral bands. Therefore, using these values of standard deviation and correlation, the best OIF using equation 4.2 can be evaluated if the significant information on variance of two spectral bands is present.

$$OIF = \frac{Std_{\lambda_1} + Std_{\lambda_2}}{|Corr_{\lambda_1, \lambda_2}|} \quad (4.2)$$

where, *Std* is standard deviation of significant spectral wavelengths, *Corr* is the correlation coefficient between the spectral wavelengths.

Thereafter, the wavelengths corresponding to highest OIF are analyzed further using band ratio. For the detection of the target, the band ratio is then converted into normalised difference for building up of spectral indices. The normalised difference value (Equation 4.2) contains the reflectance measurements that enhance the object detection. Normalized spectral index computation is done using the following equation,

$$Normalised\ Spectral\ Index = \frac{R(\lambda_2) - R(\lambda_1)}{R(\lambda_2) + R(\lambda_1)} \quad (4.3)$$

where, $R(\lambda_1)$ represents the reflectance measurements of the significant spectral band from the numerator of the band ratio and $R(\lambda_2)$ indicates the reflectance measurements of another significant spectral band from the denominator of the band ratio.

Five existing spectral indices have been selected after literature review (Zha *et al.* 2003, Hongmai *et al.* 2005, Wolf 2010, Xu 2010, Zhang 2009, Samsudin *et al.* 2016) and explored further in this study. These are NBI (New built up index), NDBI (Normalized difference building index, NBAI (Normalized built up area index), BRBA and MBI (Morphological building index). A flowchart explaining the implementations of spectral indices is given in Figure 4.2.

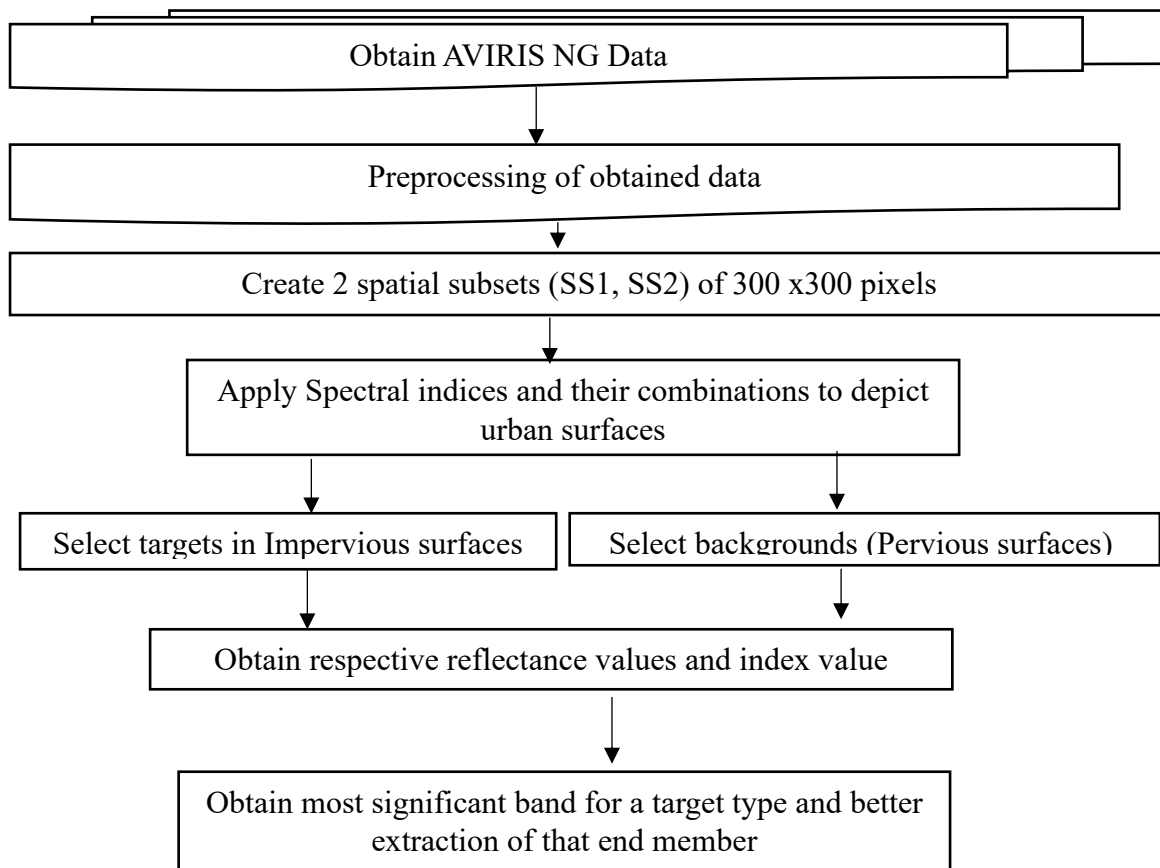


Figure 4.2: A Flowchart for step by step explanation of implementing spectral indices for end member extraction

4.3 Experimental Data Set

The tasks under this study are, end member extraction and abundance estimation using spectral unmixing, evaluating spectral indices for end member identification, and a comparison of both techniques in terms of end member generation. Different data sets have been considered for the first two tasks.

4.3.1 End member extraction and abundance estimation using spectral unmixing

The data set used for this study is being referred as **Data set-2**. Spectral unmixing based approach has been studied using this data set because it contains specific mixed pixel targets obtained as part of SHARE-2012 campaign. The truth data is also available in this case. This data set is explained in previous chapter 2, section 2.2.2.

Here for the purpose of these tasks, we have discussed the implementations on a spatial subset of 150x150 pixels from the entire data set, also referred to as Subset – 4. This subset contains various components *e.g.* fabric materials (yellow felt, yellow cotton, blue felt, blue cotton, pink felt, golden felt *etc.*) placed on asphalt court, grass and shrubs, a basketball court *etc.* The large (24' x 24') 50/50 blue felt / blue cotton target is visible in the upper right area of the asphalt court in Figure 4.3 while the smaller (16' x 16') 75/25 yellow felt/yellow cotton target is in the upper left. The six 10' x 10' whole panels of the fabrics are seen clearly just below the unmixing targets placed on asphalt court. The two of these small panels just below and to the left of the blue target are pink felt (on the left) and yellow cotton (on the right). The four small panels across the lower part of the asphalt area are (from left to right): yellow felt, blue cotton, gold felt, and blue felt. A RGB image representing the targets is shown in Figure 4.4.



Figure 4.3: A true colour representation of spatial subset 4 (100x112) selected from Data set – 2, target YF is marked with red circle.

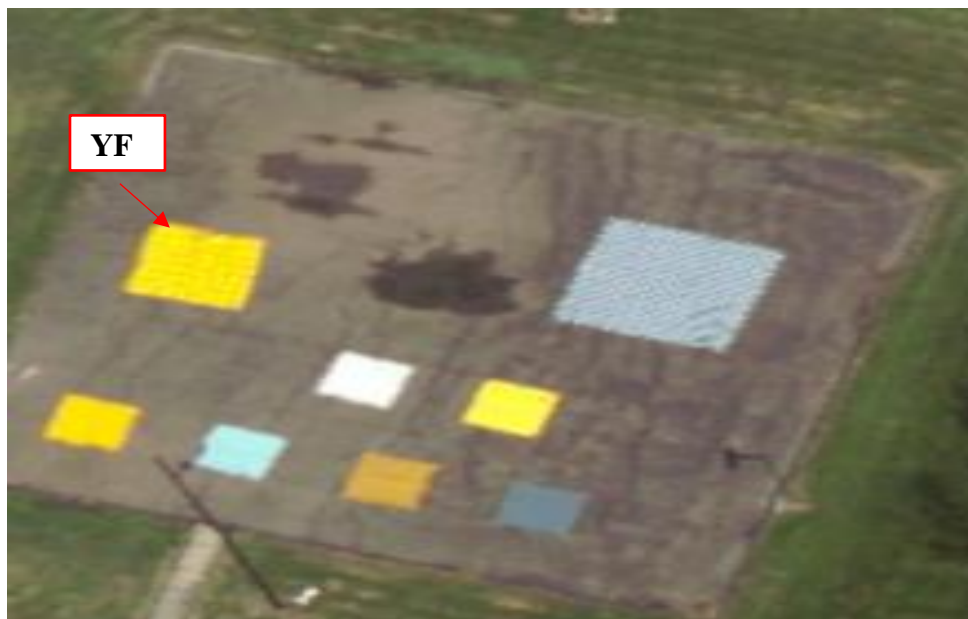


Figure 4.4: A zoomed in RGB image depicting the target YF placed on the asphalt court.

Target in Data Set-4: For the present work, the target under consideration is YF - Yellow Felt. This is a (8x8) mixed pixel target containing yellow felt and yellow cotton arranged in a 2x2 repeating pattern in the ratio of 75% and 25% of area fraction per pixel (comprising

of 3 yellow felt squares and 1 yellow cotton square) respectively as shown in Figure 4.3. Total number of target pixels under consideration are 64.

4.3.2 Evaluating spectral indices for end member extraction

For this study a Data set – 4, which is a hyperspectral data (AVIRIS-NG) of an urban area having relevant impervious and pervious surfaces, has been explored. This data set has been collected as a part of the AVIRIS- NG (Airborne Visible/Infrared Imaging Spectrometer-Next Generation) data campaign which was conducted collectively by Indian Space Research Organization (ISRO) and National Aeronautics and Space Administration (NASA) under the Hyperspectral Imaging program. This 84 days data collection campaign was conducted in India using AVIRIS-NG sensor which covered a total of 57 different sites. The flight campaign was organized in nine airport bases Ahmedabad, Udaipur, Bhubaneswar, Hyderabad, Mangalore, Coimbatore, Chandigarh, Patna, Kolkata. The flight path taken for the collection is shown in Figure 4.5. This collection campaign commenced on December 16th, 2014.

Various field collections were also performed to collect the ground truth making it suitable for exploration by varied application areas (Urban mapping, vegetation, soil quality, water quality monitoring, forest, weather monitoring *etc.*). The part of data set selected for this work is the one collected over Ahmedabad city in the year 2016 referred to as Data set – 4.

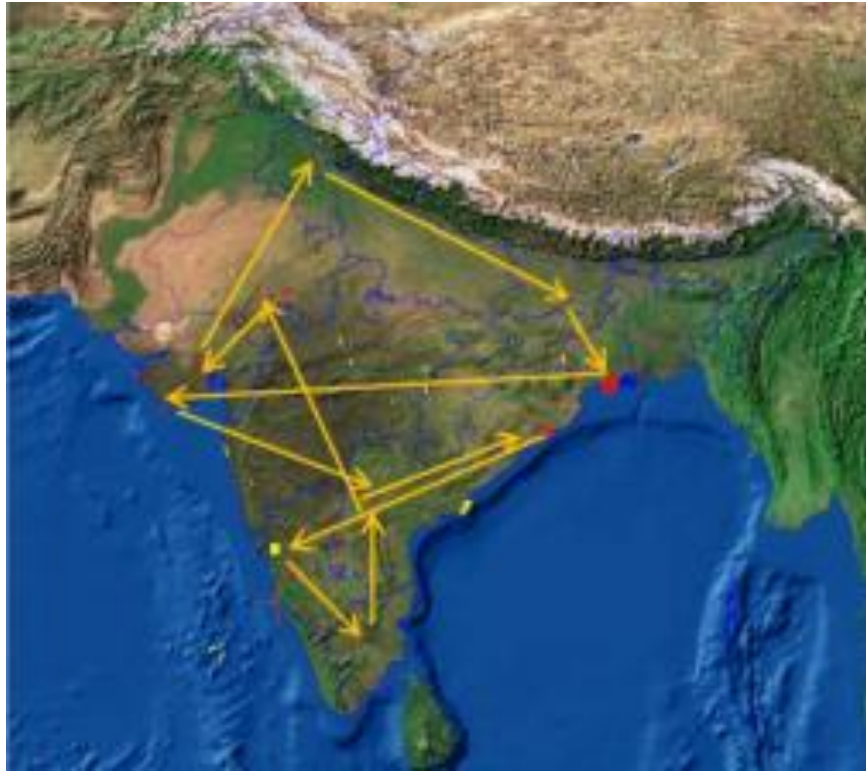


Figure 4.5: Flight paths during AVIRIS-NG data collection campaign

4.3.2.1 Data Acquisition and characteristics

General acquisition parameters and the corresponding values are given in Table 4.5.

Table 4.5: General acquisition parameters for Data set – 4

Sensor	Data Type	Data size	Spectral Resolution	Spectral region	Spatial Resolution
AVIRIS - NG	Hyperspectral	724x9946 pixels	425 bands, 5 nm interval	~380 nm to ~2510 nm	4 m - 8 m

The spectral signatures obtained along with site information have been used for detection, accuracy assessment and validation of detection results. This data set has been explored for end member identification using spectral indices.

The image in Figure 4.6 represents RGB band display of the Ahmedabad dataset containing the various major landmarks. Labelled numbers from 1 to 15 represent the various site ID's allotted to these landmarks as shown in Table 4.6. The dataset consists of a variety of natural and man-made components.

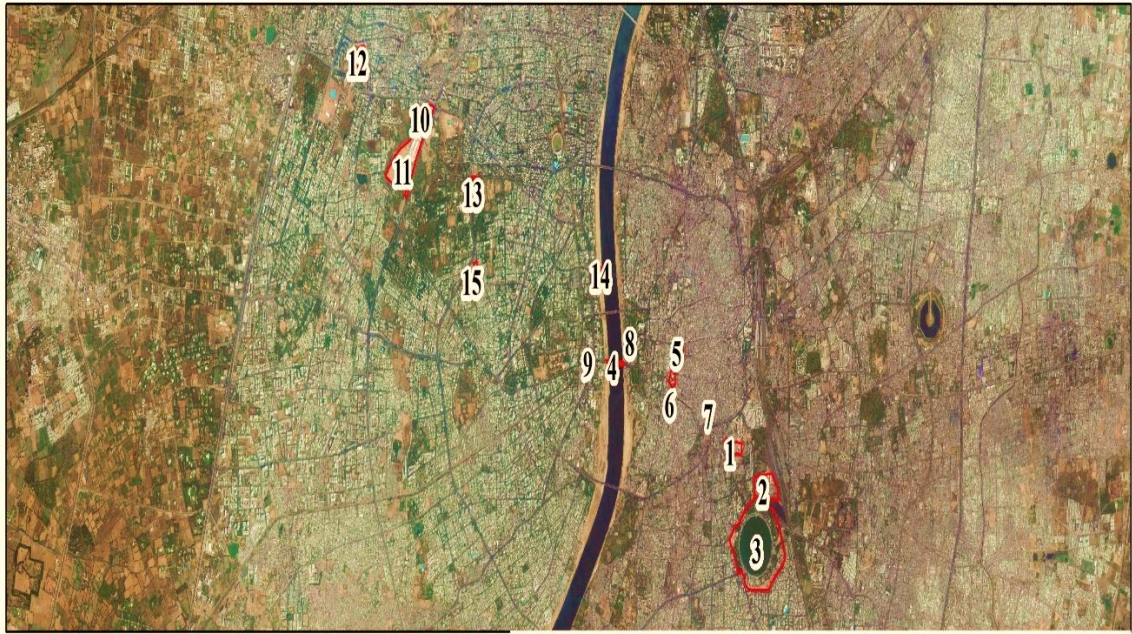


Figure 4.6: RGB image showing Ahmedabad city and the site ID's allotted to 15 landmarks.

Table 4.6: Site ID's allocated to a few areas in Hyperspectral data collected by AVIRIS -NG sensor over Ahmedabad city

Site Id	Site Name
1	Ten Acre Mall
2	Kankaria Railway Yard
3	Kankaria Lakefront
4	Elish Bridge
5	Jamia Masjid
6	AMC Main office
7	Raipur poll House
8	Lal Darwaza Bus Terminal
9	Town Hall
10	Gujarat University Conventional Hall
11	GMDC Ground
12	Drive – in Cinema
13	CEPT University
14	Sabarmati Riverfront
15	Gulbai Tekra Slums

4.3.2.2 Ground truth data

Extensive ground truth collection was done over Ahmedabad city. Spectra from various materials were obtained. A few for the reference are shown in below Figures 4.7 and 4.8.

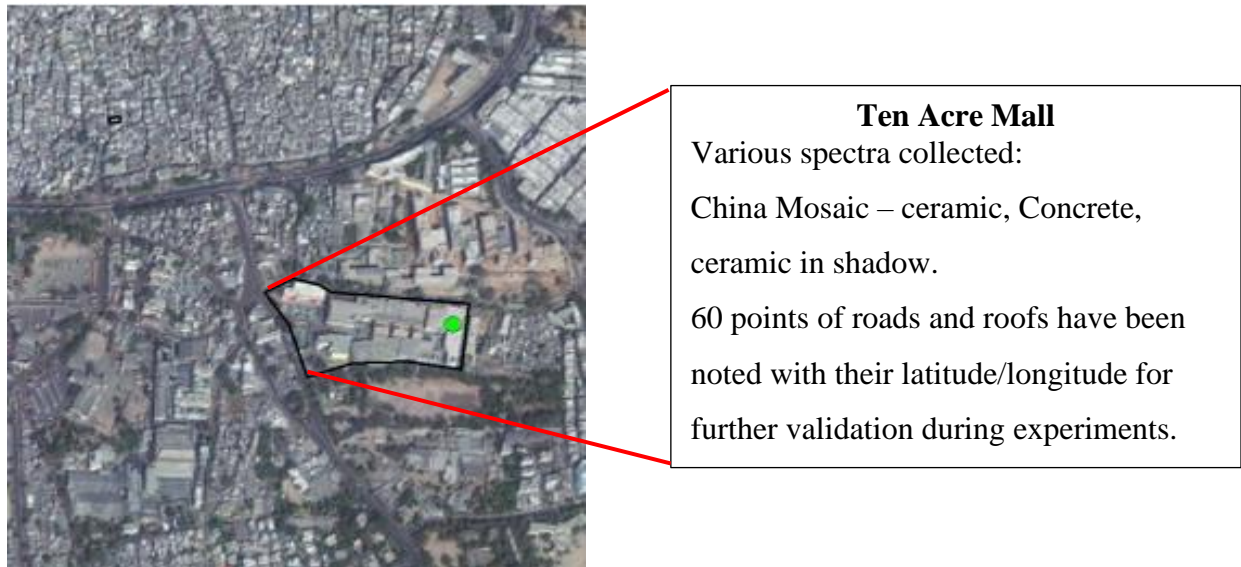


Figure 4.7: Zoomed image showing the Site id 1 – Ten Acre Mall

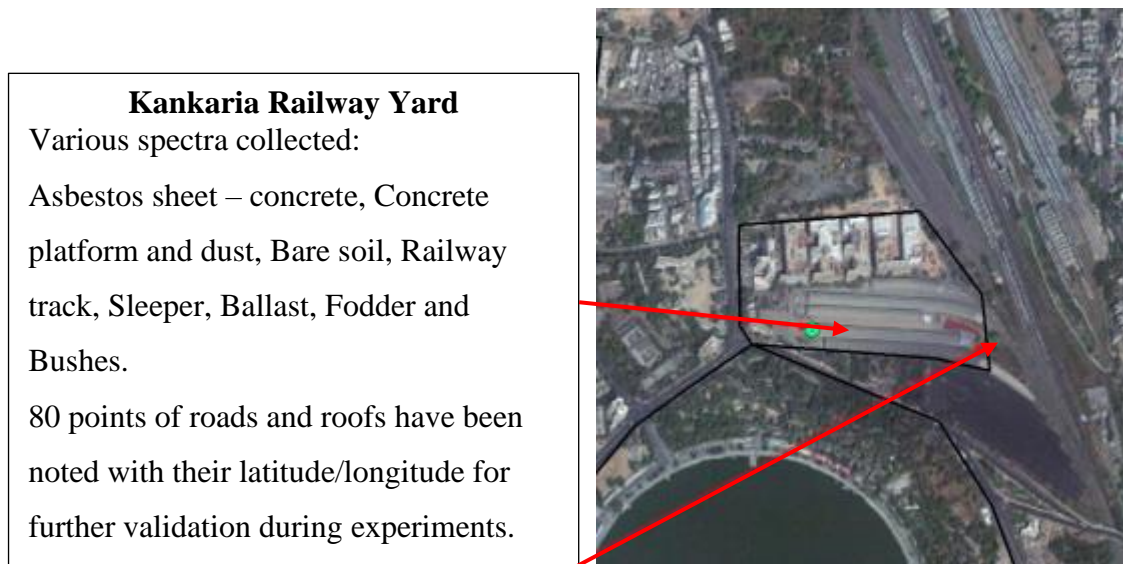


Figure 4.8: Zoomed image showing the Site id 2 – Kankaria Railway Yard

Figure 4.9 shows some of the images of targets taken during the collection campaign.



Figure 4.9: Field pictures taken during the ground data collection.

4.3.2.3 Spatial subsets:

Two spatial subsets SS1 and SS2 as shown in Figure 4.10 have been created each of 300x300 pixels. Subset SS1 covers site ID's: Anant University and Subset SS2 covers site ID's: 1 (Ten Acre mall), 2 (Kankaria Railway yard), 3 (Kankaria Lakefront).

The reason for selection of AVIRIS - NG data set in this objective is that this data provides ample opportunities for researchers to work in detection and identification of impervious / pervious surfaces using super resolution mapping, target detection, land cover mapping *etc.* However, since the data set was made available at a very late stage hence some of the works discussed in other chapters could not be implemented on this data. Hence this data set has only been studied and analysed for identification of target (impervious) and background (pervious) surfaces.

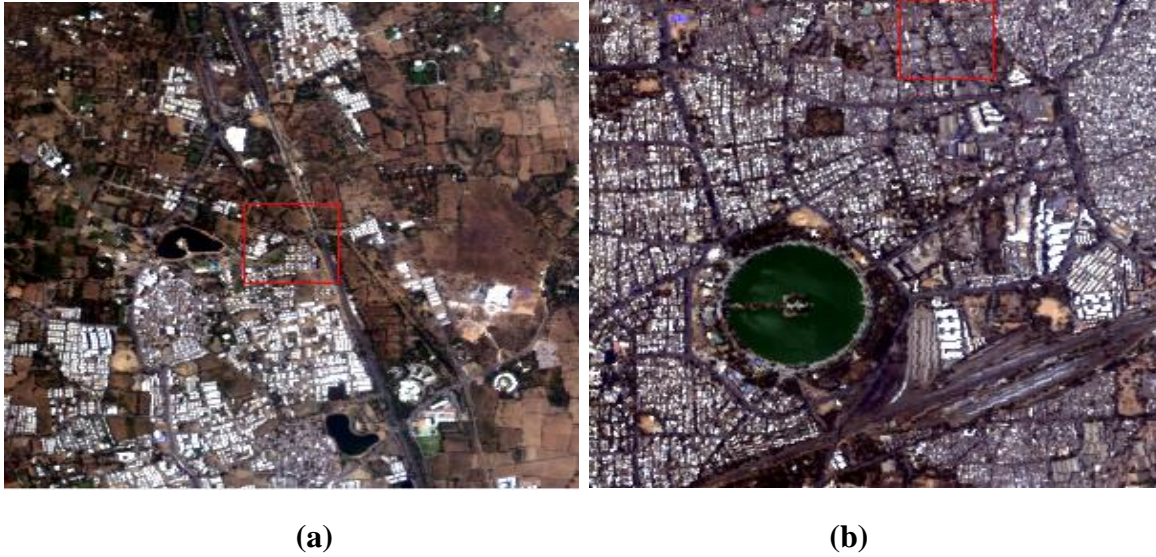


Figure 4.10: (a) Subset SS1 (b) Subset SS2

These subsets contain both pervious and impervious surfaces as under.

Major Impervious surfaces : Roof, Pavement / Pathway / Platform, Road, Floor, Bridge, Basketball courts, Railway Track, Parking lots, Unpaved parking lot.

Major Pervious surfaces : Vegetation, Water and Soil.

Impervious surfaces considered as targets and pervious surfaces considered as backgrounds are shown in Table 4.7.

Table 4.7: Levels of division of surface types

Level 1 (Major class of urban surfaces)	Level 2 (Sub-Class)
Impervious (targets)	Building/Roofs
	Roads
Pervious (backgrounds)	Vegetation
	Soil

4.4 Methodology

This section presents details of implementation under the same three categories of tasks.

4.4.1 End member extraction and abundance estimation using spectral unmixing

The **methodology** followed is to first obtain the in-scene spectrum of the target and to apply Principal component transformation to reduce dataset to useful bands.

Following this the endmember generation is done using Automatic Target generation procedure (ATGP), Independent Component Analysis Endmember Extraction Algorithm (ICA-EEA), N-FINDR and Pixel Purity Index (PPI). After the generation of end members, abundance fractions of the target end member within the mixed pixels have been computed, corresponding to the abundance maps created for each algorithm. The number of target pixels retained with each algorithm has been calculated. Also, the error between the ground spectra and the recovered end member (target) spectra is computed and respective ROC curves have been generated for comparing the performance of above-mentioned algorithms.

All codes have been implemented in MATLAB. Steps of implementation have been explained in flowchart given in Figure 4.11.

4.4.1.1 Identification of pure end members from the image

First the identification of pure end members has been performed. For obtaining this, a principal component transformation on the full band data has been done to remove the bad and noisy bands. Thereafter the algorithms ATGP, ICA-EEA, NFindr and PPI are implemented to obtain the pure end members within the image.

4.4.1.2 Generation of Abundance maps using FCLS

Next, abundance estimation is done using in-scene extracted end members and using ground truth spectra. Abundance maps are generated using fully constrained least squares algorithm.

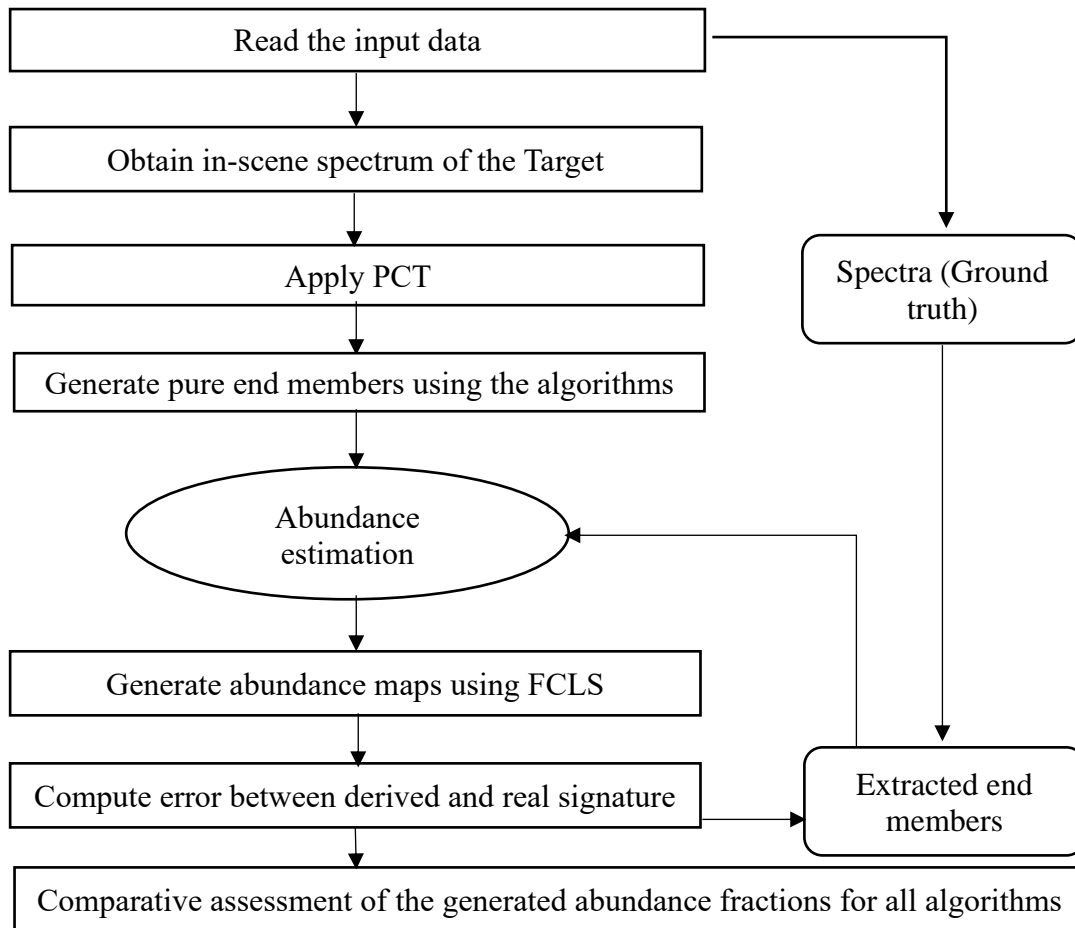


Figure 4.11: Flowchart to show the steps of implementation for spectral unmixing

4.4.1.3 Computation of Fractional abundances.

From the abundance maps, the abundance fraction of target in YF is computed using the four algorithms for further analysis.

4.4.1.4 Accuracy assessment

Error is computed between the derived and the real spectral signature of end members. Abundance maps are generated for each end member computed. From these abundance maps, the abundance fractions for the target within the mixed pixel is computed.

From here, based on the threshold values the total number of target pixels detected are calculated. Lastly, the error is computed, and output abundance images obtained from all the algorithms are analyzed using ROC (Receiver optimization curves) and histograms.

4.4.2 Evaluating Spectral Indices for end member identification

The methodology including various theoretical aspects of spectral indices based approach have already been discussed in section 4.2.2. The steps of implementation are summarised below.

Step 1. Spectral Library creation.

Step 2. Identification of significant wavelengths using OIF.

Step 3. Implementation of selected spectral indices

Step 4. Accuracy assessment of spectral indices

4.5 Results and Discussions

All implementations have been done in MATLAB. The **results** of implementation are discussed step by step.

4.5.1 End member extraction and abundance estimation using spectral unmixing

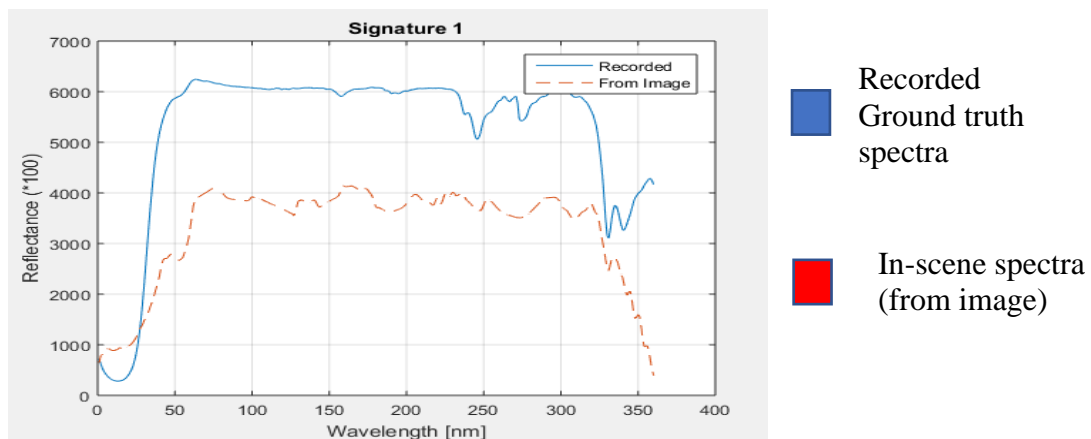
4.5.1.1 Identification of pure end members from the image

The in-scene end member spectra from the image for the target yellow felt is retrieved and plotted with the recorded ground truth spectra as given in Figure 4.3 (a). For the identification of pure end members from the hyperspectral image, first the dimensionality reduction is performed using principal component transformation.

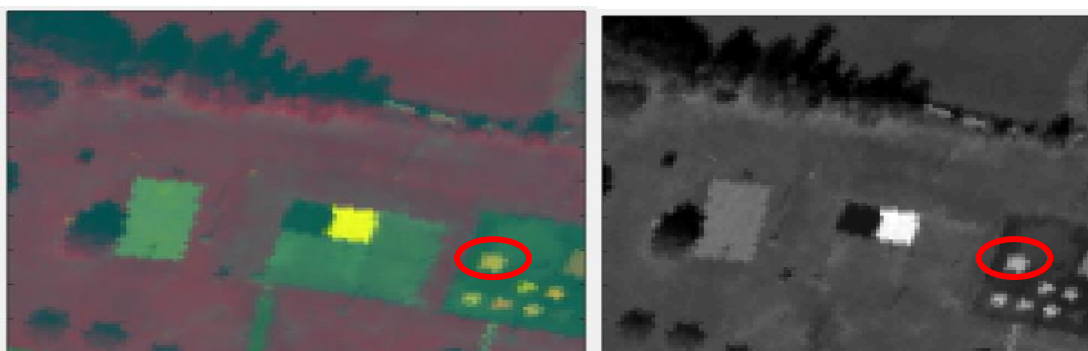
Results of PCT Principal component transformation is applied to the input image to obtain the best bands. All the bands of the image are then screened, and the reduced set of good bands are obtained as shown in Figure 4.12.

Here, the **Input** is a 2D image M , q is the number of components (20 in this case), **Output** is: 2D matrix ($q \times N$), V which is the transformation matrix and Λ which is the eigenvalues. $[p, N] = \text{size}(M)$, remove data mean and compute covariance matrix C , then find eigenvalues of the covariance matrix using `eigs` function. $[V, D] = \text{eigs}(C, q)$. Now we select the first 'k' eigenvectors with highest eigenvalues (here, $k=20$). Now original data is projected into these 20 eigenvectors resulting in 20 dimensions. Then we transform data using $M_{\text{pct}} = V' * M$ and $\lambda = \text{diag}(D)$.

Using this, out of 360 Input bands, recovered **best bands are 20**. Following this, we have defined the number of potential end members 'q' that may be present in the image, in this case q selected is 12, pure pixel end members.



(a)



(b)

(c)

Figure 4.12 (a). The graph representing the spectra of target obtained from the image in red and the spectra recorded using ground truth values in blue. **(b)** True color image representing the components 2,5,9 in the reduced image (20 bands) after performing PCT **(c).** The gray scale image representing the component number 10 in the reduced set.

Afterwards, using image retrieved spectra, twelve pure pixel image end members are recovered using the four algorithms, ATGP, ICA-EEA, N-Findr and PPI and the results are shown in below Figures 4.13 (a) to (d).

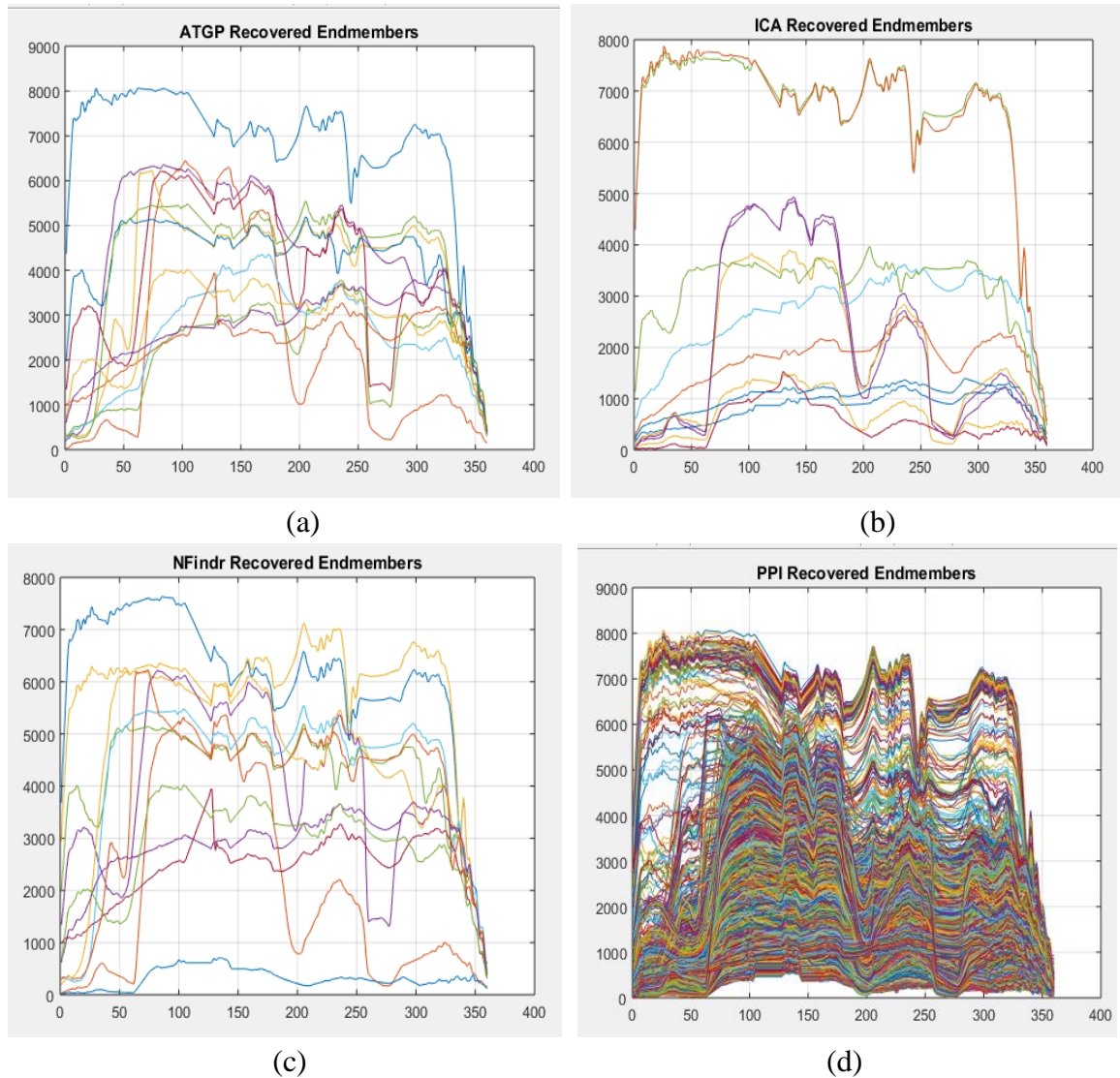


Figure 4.13 End members recovered by (a) ATGP, (b) ICA-EEA (c) NFindr (d) PPI

From Figure 4.13 (d), it is observed that the end member extraction using PPI has not produced satisfactory results and is therefore discontinued for further processing.

4.5.1.2 Generation of Abundance maps using FCLS

From the above obtained end members, their corresponding fractions in all the pixels is computed and abundance maps (representing the abundance of each of these end members in their respective maps) are then generated.

Abundance map for ATGP

The abundance maps generated using ATGP for the 12 end members are shown here. The fractional composition for the yellow felt in YF is obtained from Abundance map 4.

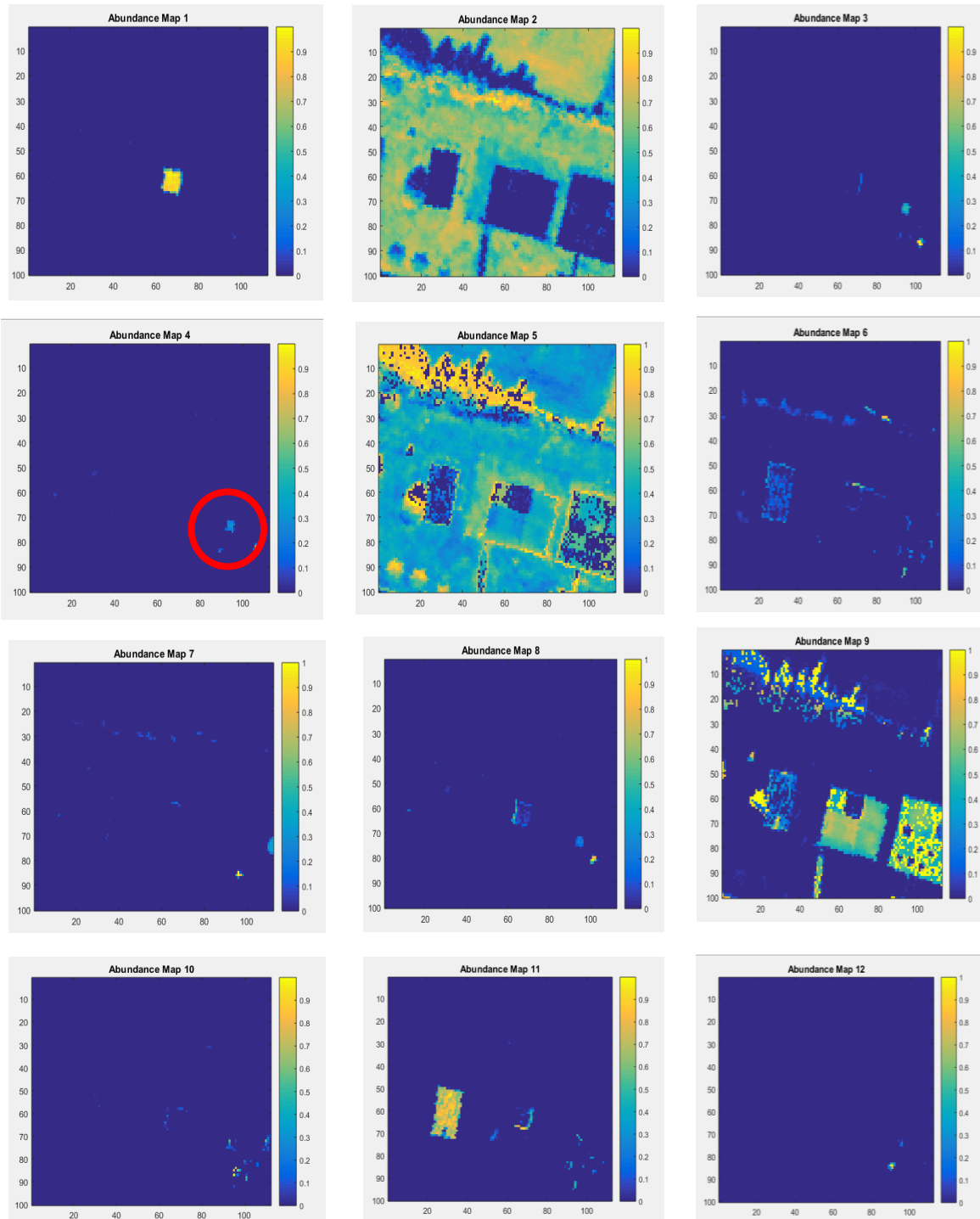


Figure 4.14: Abundance maps generated using ATGP

N-Findr

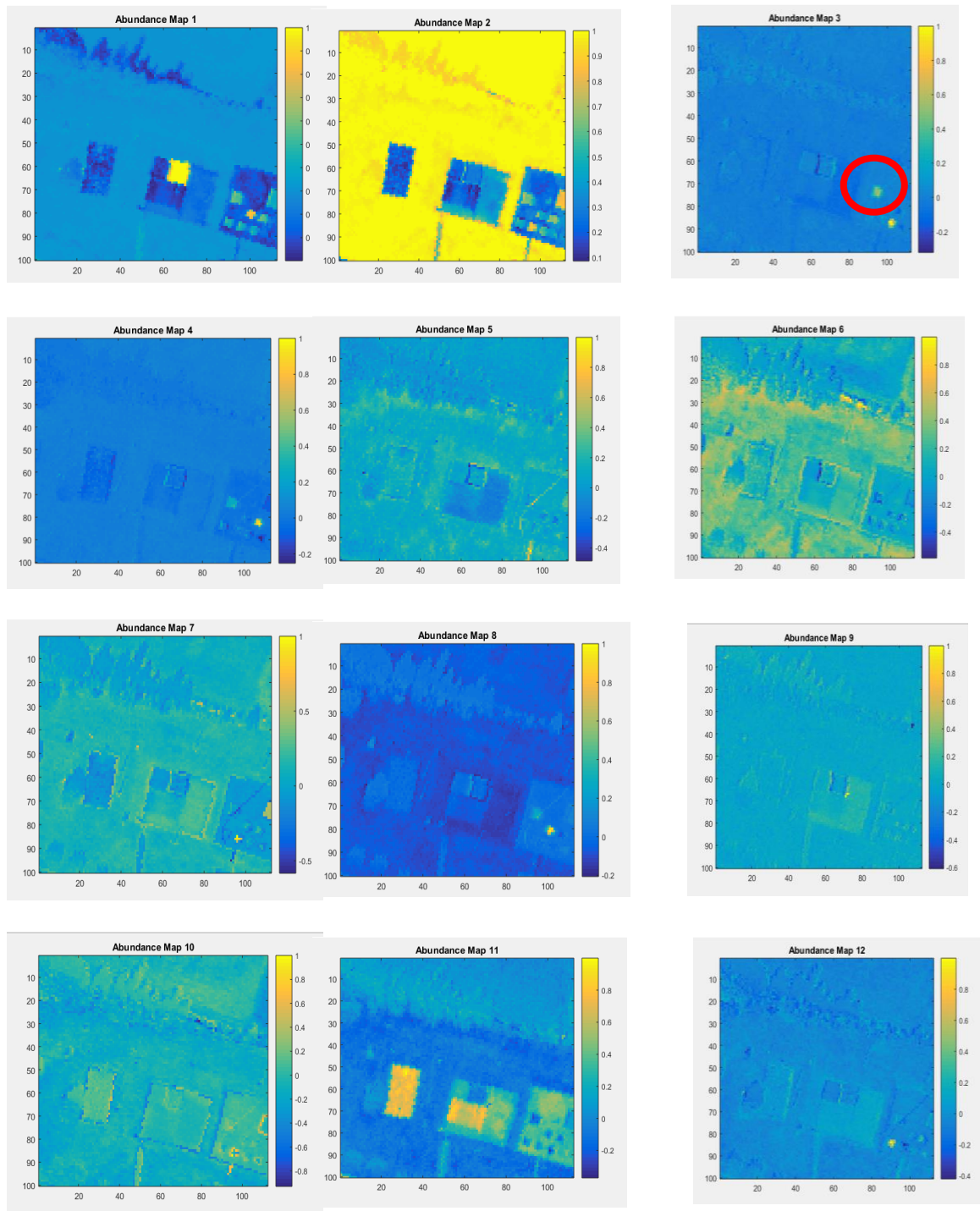


Figure 4.15: Abundance maps generated using N-Findr

The abundance maps generated using N-Findr for the 12 end members are shown here.

The fractional composition for yellow felt in YF is shown in Abundance map 3.

ICA-EEA

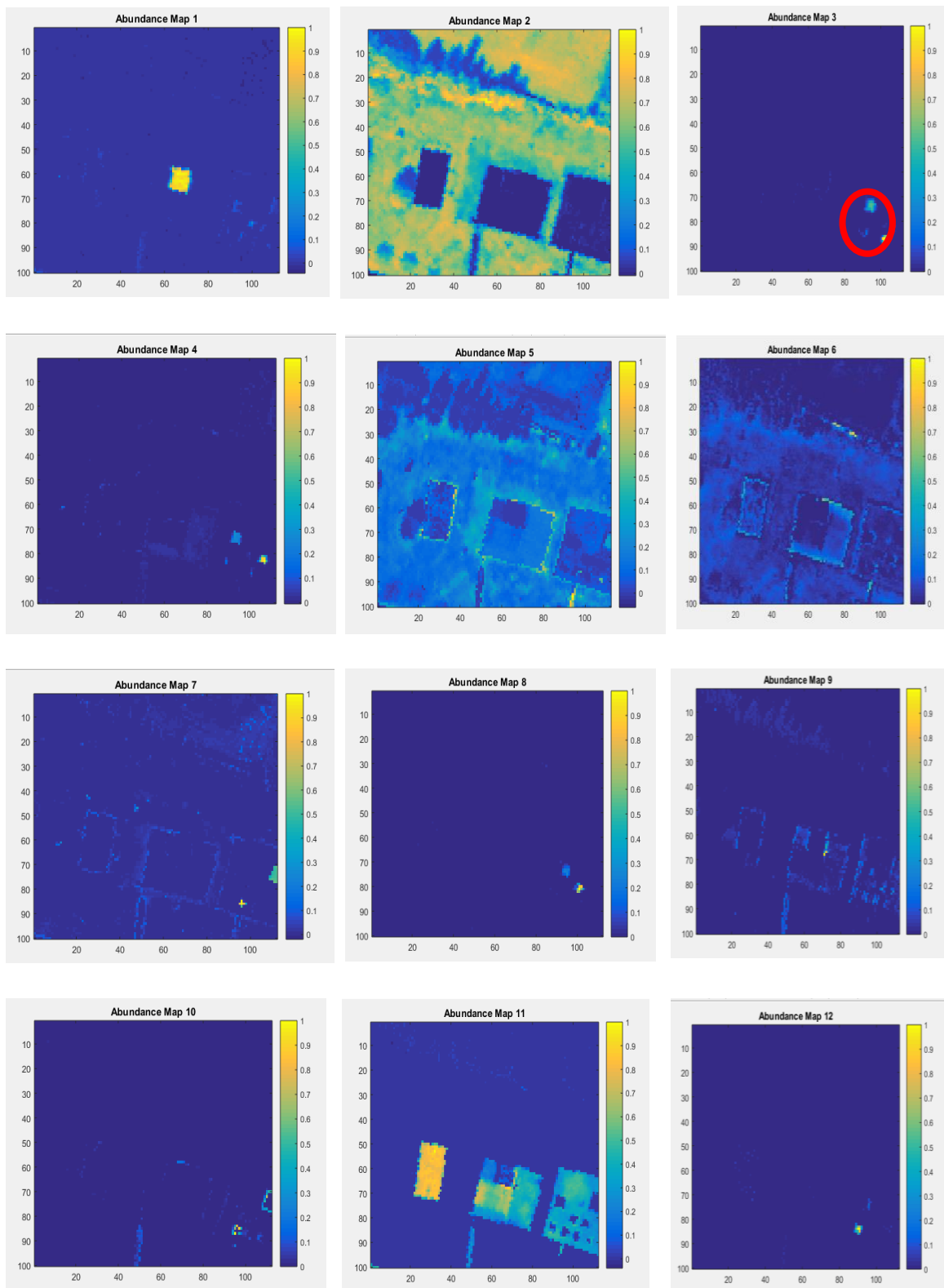


Figure 4.16: Abundance maps generated using ICA-EEA

The fractional composition for yellow felt in YF is shown in Abundance map 3.

After this, the error corresponding to each algorithm is then studied to find the deviation from the real signature.

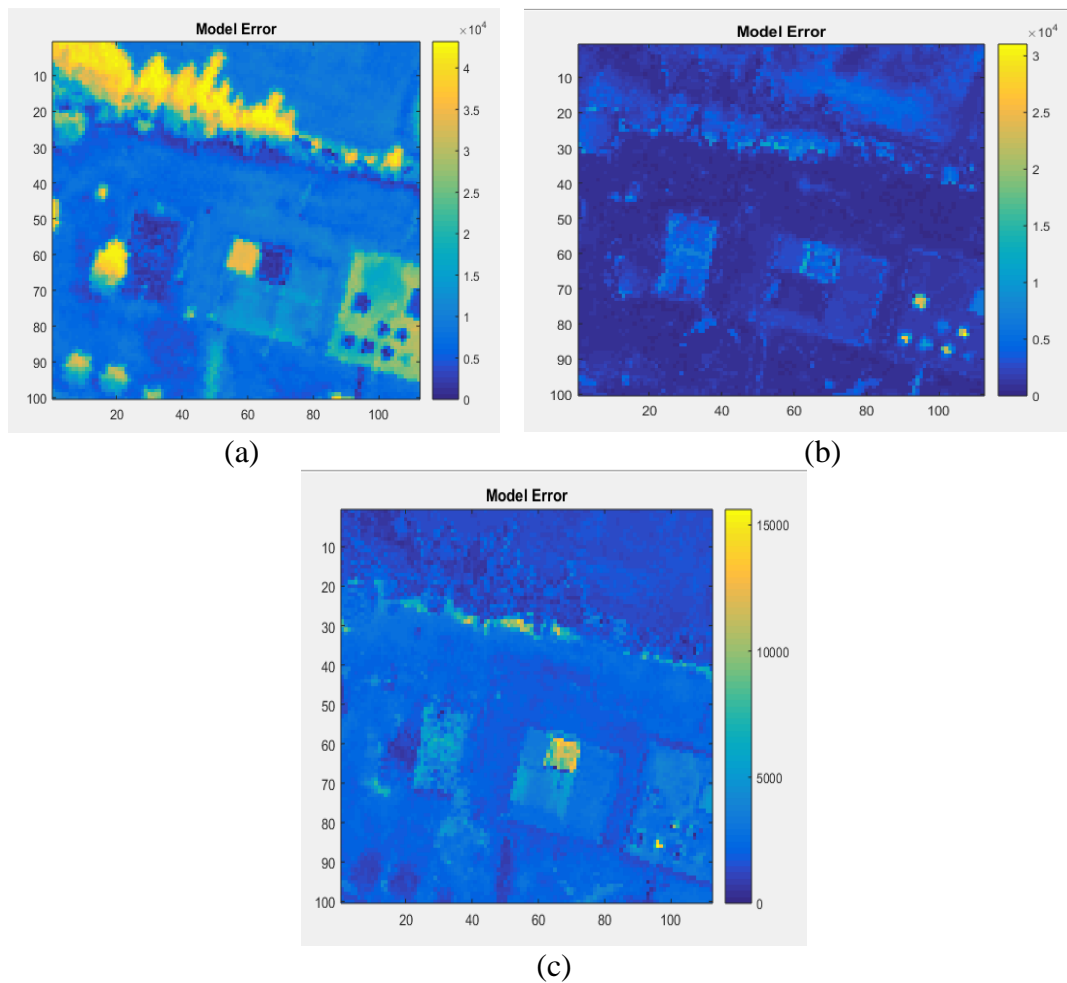


Figure 4.17 Combined abundance image showing error is shown for (a) ATGP, (b) ICA-EEA, (c) NFindr

4.5.1.3 Computation of Fractional abundances.

The abundance fractions obtained for target yellow Felt in YF is shown in tables given below for ATGP, ICA-EEA, and NFindr. After obtaining these fractions, a random value of 1 is assigned to indicate the target detection if fractional abundance value is greater than 40% for Yellow felt in every pixel; otherwise, it is assigned a value of 0. This aids in understanding the presence or absence of the target in the pixel. This is done as Yellow Felt is present in the ratio of 75% in every pixel as given in the ground truth information.

Table 4.8: Abundance fraction of yellow felt in mixed pixel target YF (8x8) - ATGP

0.69	0.4	0.73	0.72	0.5	0.48	0.58	0.68
0.59	0.21	0.4	0.43	0.34	0.45	0.24	0.6
0.65	0.24	0.47	0.5	0.58	0.64	0.46	0.45
0.42	0.36	0.48	0.49	0.45	0.59	0.62	0.45
0.26	0.46	0.42	0.43	0.49	0.54	0.48	0.48
0.35	0.63	0.41	0.25	0.48	0.69	0.3	0.67
0.45	0.74	0.78	0.68	0.58	0.47	0.45	0.74
0.45	0.65	0.68	0.75	0.46	0.45	0.68	0.37

Table 4.9: Abundance fraction of yellow felt in mixed pixel target YF (8x8) - ICA-EEA

0.72	0.69	0.81	0.79	0.9	0.89	0.45	0.71
0.73	0.28	0.46	0.46	0.27	0.9	0.48	0.76
0.55	0.41	0.6	0.58	0.54	0.67	0.49	0.49
0.48	0.44	0.55	0.55	0.49	0.69	0.62	0.35
0.73	0.49	0.48	0.55	0.48	0.35	0.25	0.48
0.7	0.84	0.83	0.38	0.81	0.74	0.38	0.68
0.69	0.82	0.75	0.75	0.75	0.68	0.49	0.71
0.49	0.75	0.74	0.69	0.56	0.45	0.46	0.78

Table 4.10: Abundance fraction of yellow felt in mixed pixel target YF (8x8) -NFindr

0.68	0.73	0.35	0.61	0.63	0.54	0.25	0.35
0.67	0.69	0.46	0.36	0.02	0.45	0.48	0.69
0.55	0.24	0.68	0.45	0.42	0.45	0.49	0.45
0.88	0.4	0.45	0.46	0.46	0.62	0.62	0.4
0.11	0.44	0.46	0.46	0.42	0.08	0.25	0.47
0.24	0.35	0.41	0.47	0.53	0.01	0.39	0.59
0.45	0.75	0.82	0.41	0.6	0.69	0.48	0.74
0.49	0.79	0.71	0.12	0.47	0.71	0.45	0.79

Now, after assigning values of 1 (≥ 0.40) and 0 (< 0.40) corresponding to obtained fractions, for yellow felt in the mixed pixel target, the values generated are shown in below tables.

Table 4.11 Values corresponding to target detected/non detected in YF (8x8) - ATGP

1	1	1	1	1	1	1	1
1	0	1	1	0	1	0	1
1	0	1	1	1	1	1	1
1	0	1	1	1	1	1	1
0	1	1	1	1	1	1	1
0	1	1	0	1	1	0	1
1	1	1	1	1	1	1	1
1	1	1	1	1	1	1	0

Table 4.12: Values corresponding to target detected/non detected in YF (8x8) – ICA-EEA

1	1	1	1	1	1	1	1
1	0	1	1	0	1	1	1
1	1	1	1	1	1	1	1
1	1	1	1	1	1	1	0
1	1	1	1	1	0	0	1
1	1	1	0	1	1	0	1
1	1	1	1	1	1	1	1
1	1	1	1	1	1	1	1

Table 4.13: Values corresponding to target detected/non detected in YF(8x8)-NFindr

1	1	0	1	1	1	0	0
1	1	1	0	0	1	1	1
1	0	1	1	1	1	1	1
1	1	1	1	1	1	1	1
0	1	1	1	1	0	0	1
0	0	1	1	1	0	0	1
1	1	1	1	1	1	1	1
1	1	1	0	1	1	1	1

4.5.1.4 Accuracy Assessment

Thus, the number of target pixels detected for Yellow Felt in the mixed pixel target YF are counted and are shown below:

Table 4.14: Accuracy of unmixing results obtained using three selected algorithms.

Algorithm	Total number of target pixels	Number of target pixels detected	Accuracy of detection
ATGP	64	54	84.3%
ICA-EEA	64	57	89.0%
NFindr	64	50	78.1%

Thus it may be observed from the results in Table 4.14 that:

- i. ICA-EEA detects more number of target pixels with highest accuracy of 89%
- ii. ATGP performs well with an accuracy of 84.3%, followed by NFindr which detects with an accuracy of 78.1%.

ROC curves

Following the creation of abundance maps, the ROC curves have been implemented to show the error between the target spectra obtained from the ground truth for the target and the spectra obtained from the image itself for the target under consideration. The curves quantify the variability measured among the recovered values.

For analysis, the values of True positives, true negatives, false positives and false negatives are computed and further the values of TPR and FPR are computed and these values give the TPR and FPR.

TPR (True positive rate) = $TP / TP+FN$, (/ stands for division)

FPR (False positive rate) = $FP / FP+TN$

Here only resulting ROC curves are shown in figure 4.19 and not entire set of values calculated.

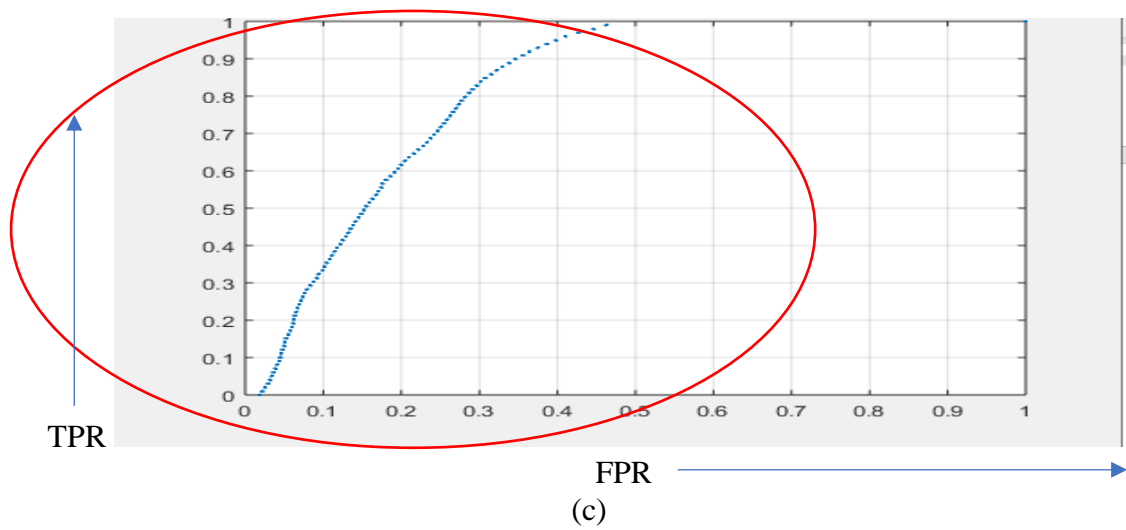
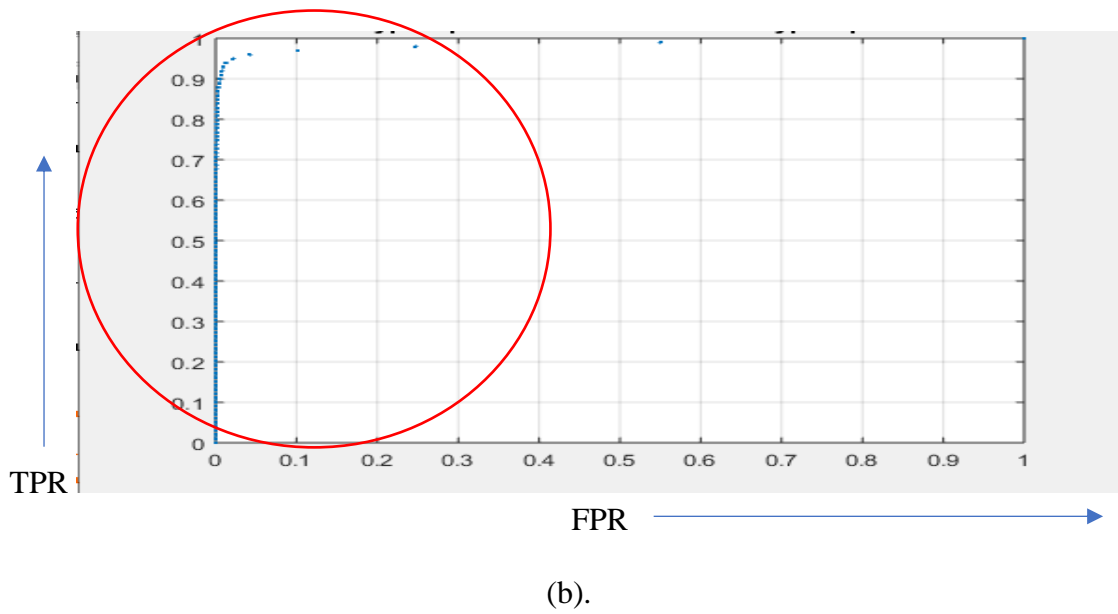
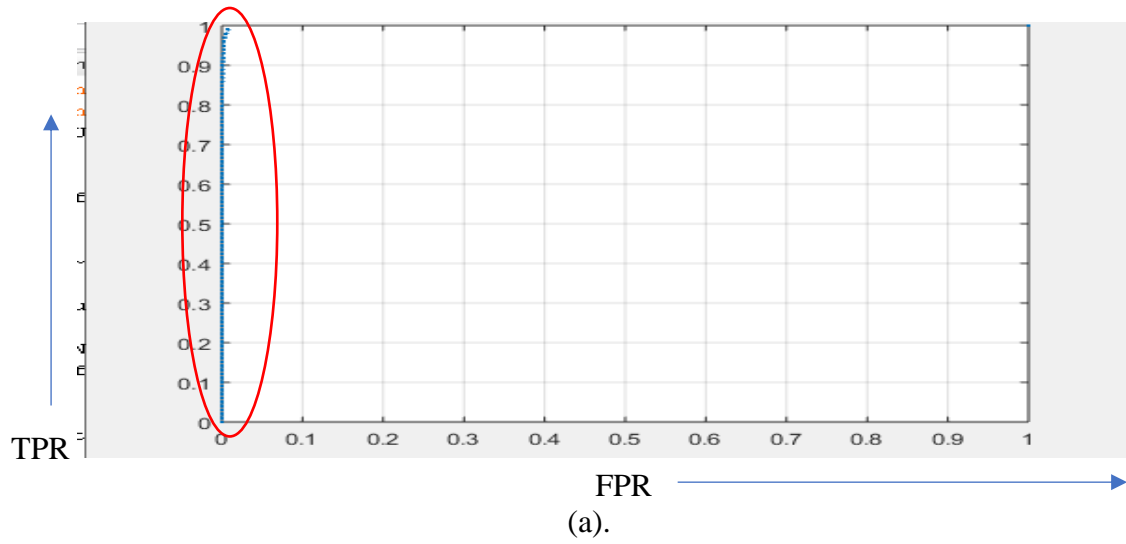


Figure 4.19. ROC curves obtained for (a) ATGP, (b) ICA-EEA, (c) NFindr. (The circle/ellipse highlights the results.)

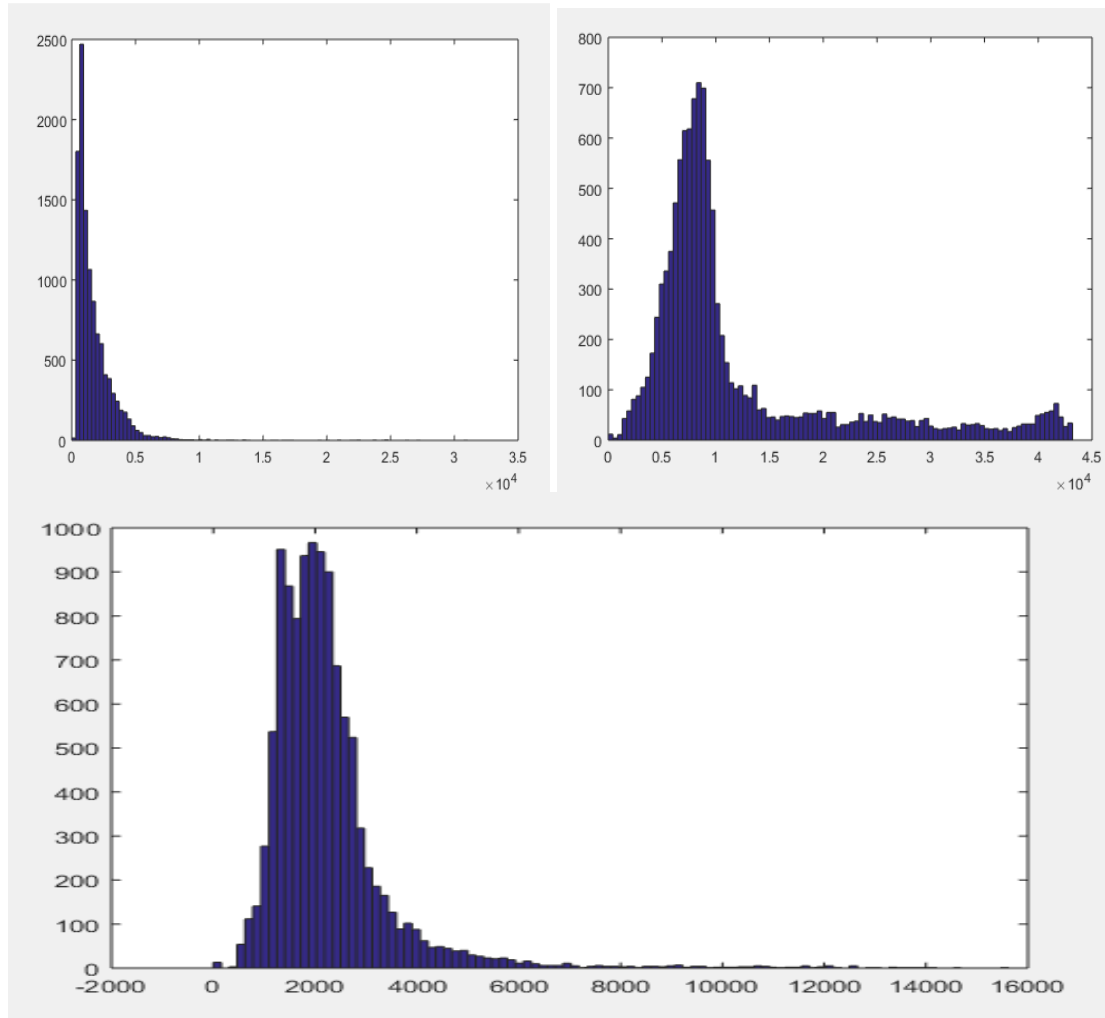


Figure 4.20. Histograms showing the affinity of endmembers obtained for (a) ATGP, (b) ICA-EEA, (c) NFindr.

From the results following may be observed:

- From the Table 4.14, it is observed that ICA-EEA generates end member spectra with more accuracy while the results of generation with PPI are worst amongst the four algorithms.
- ROC curves also depict that the error between the generated spectra from the image and the ground truth spectra is least. ATGP may also be considered as an end member extraction algorithm owing to good results of detection for mixed pixel targets as TPR is more.

4.5.2 Evaluating Spectral Indices for end member identification

The results of implementation of spectral indices on Data set-5, subset SS1 and SS2, are shown step by step in below sub sections.

4.5.2.1 Spectral library creation

The spectral library has been created for selected impervious surfaces / targets (roads and roofs) and impervious surfaces / backgrounds (vegetation and soil).

Impervious surfaces (targets)

Roads – Parking lot bitumen road, bitumen road, concrete road (Figure 4.17).

Roofs – Asbestos sheet, Red mangalore tile roof, bitumen membrane roof, reinforced cement, wood tile roof, bitumen water proofing, Corrugated GI sheet, corrugated GI sheet in shadow, AC duct Iron, convention hall metal sheet and convention hall metal sheet shadow, PVC fibre, Polythene blue, polythene black, green cloth shed, redcarpet cloth, plastic+cloth. (Figure 4.21)

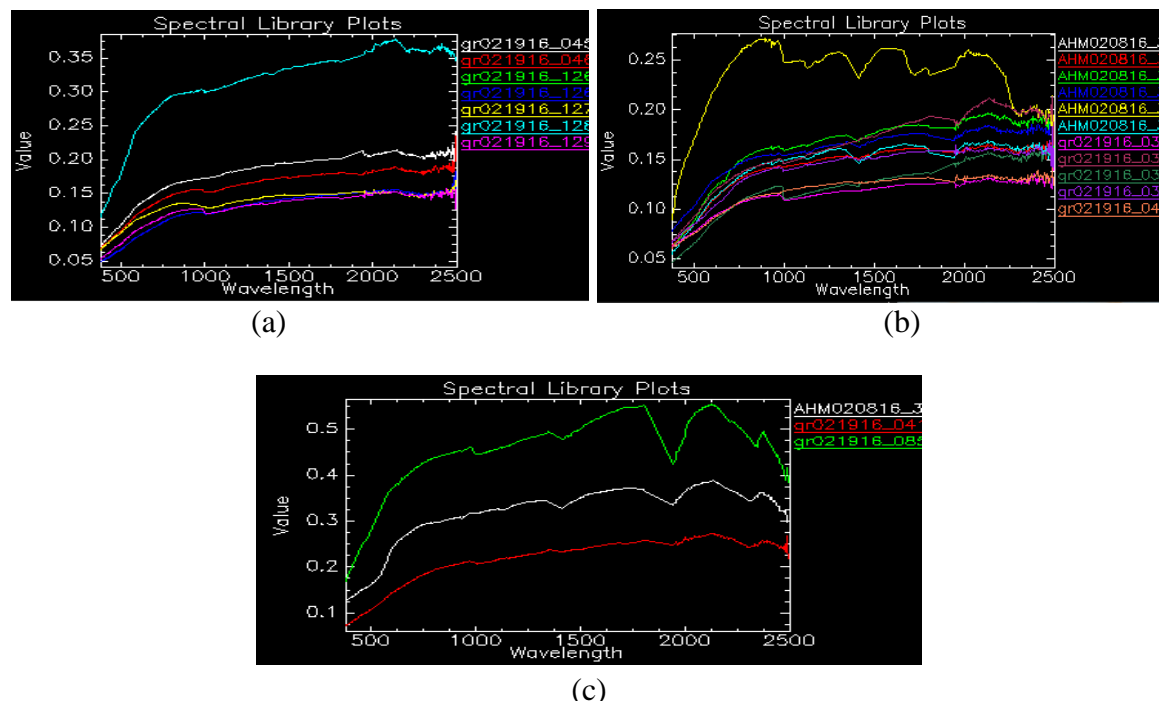
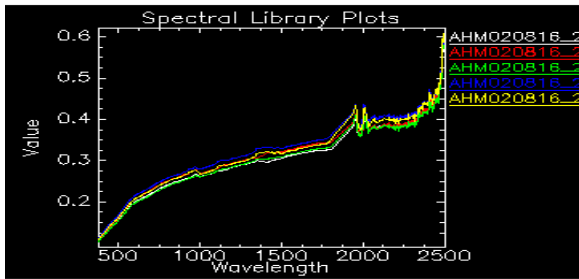
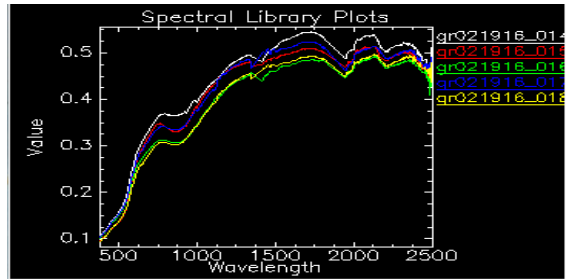


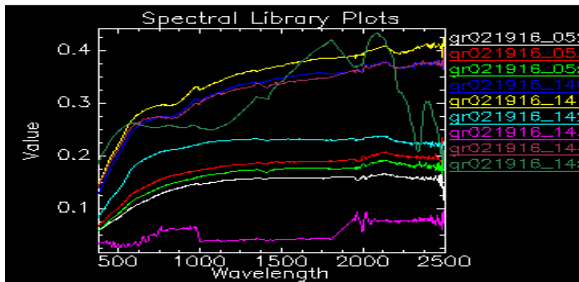
Figure 4.21: Spectral library for Impervious surfaces – Road (a). Parking lot-Road (Bitumen), (b). Bitumen Road (c). Concrete Road



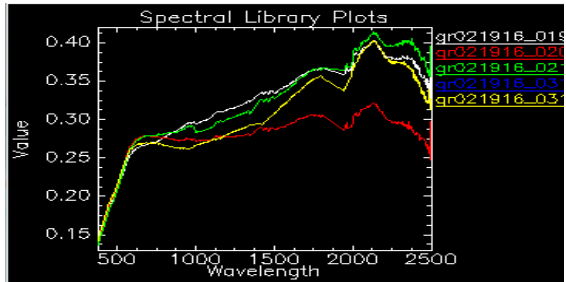
(a)



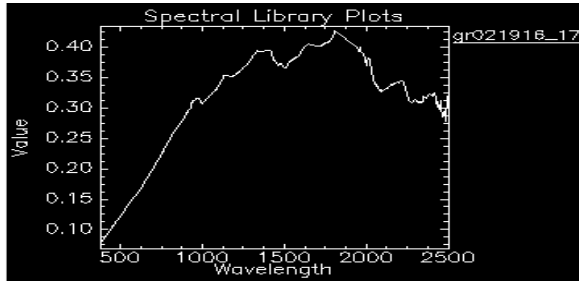
(b)



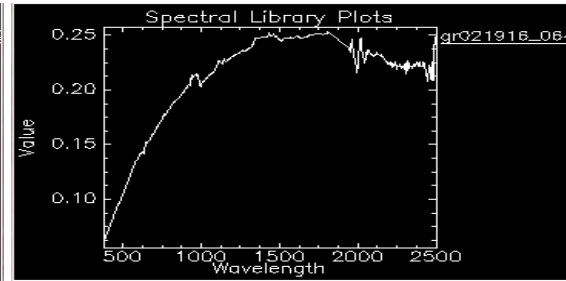
(c)



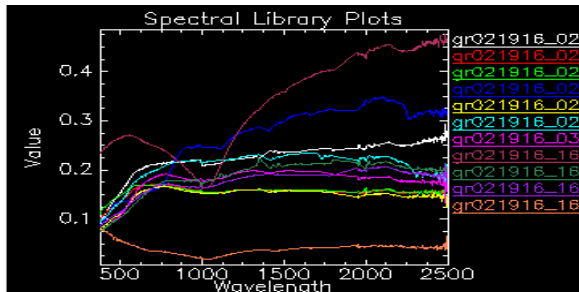
(d)



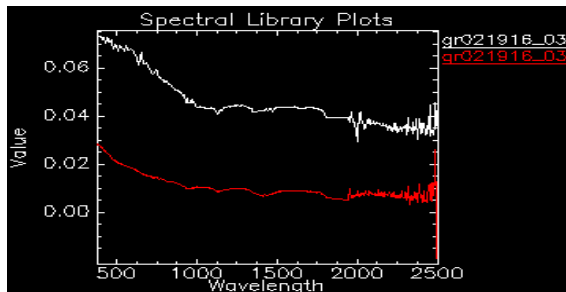
(e)



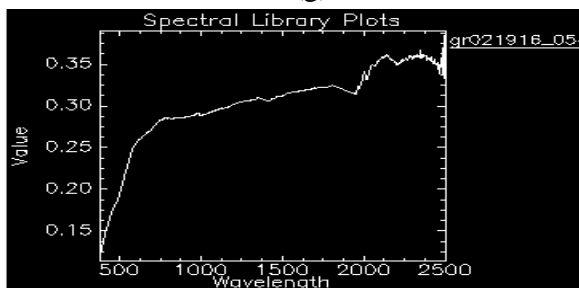
(f)



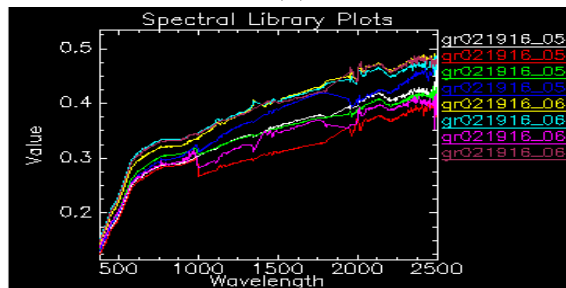
(g)



(h)



(i)



(j)

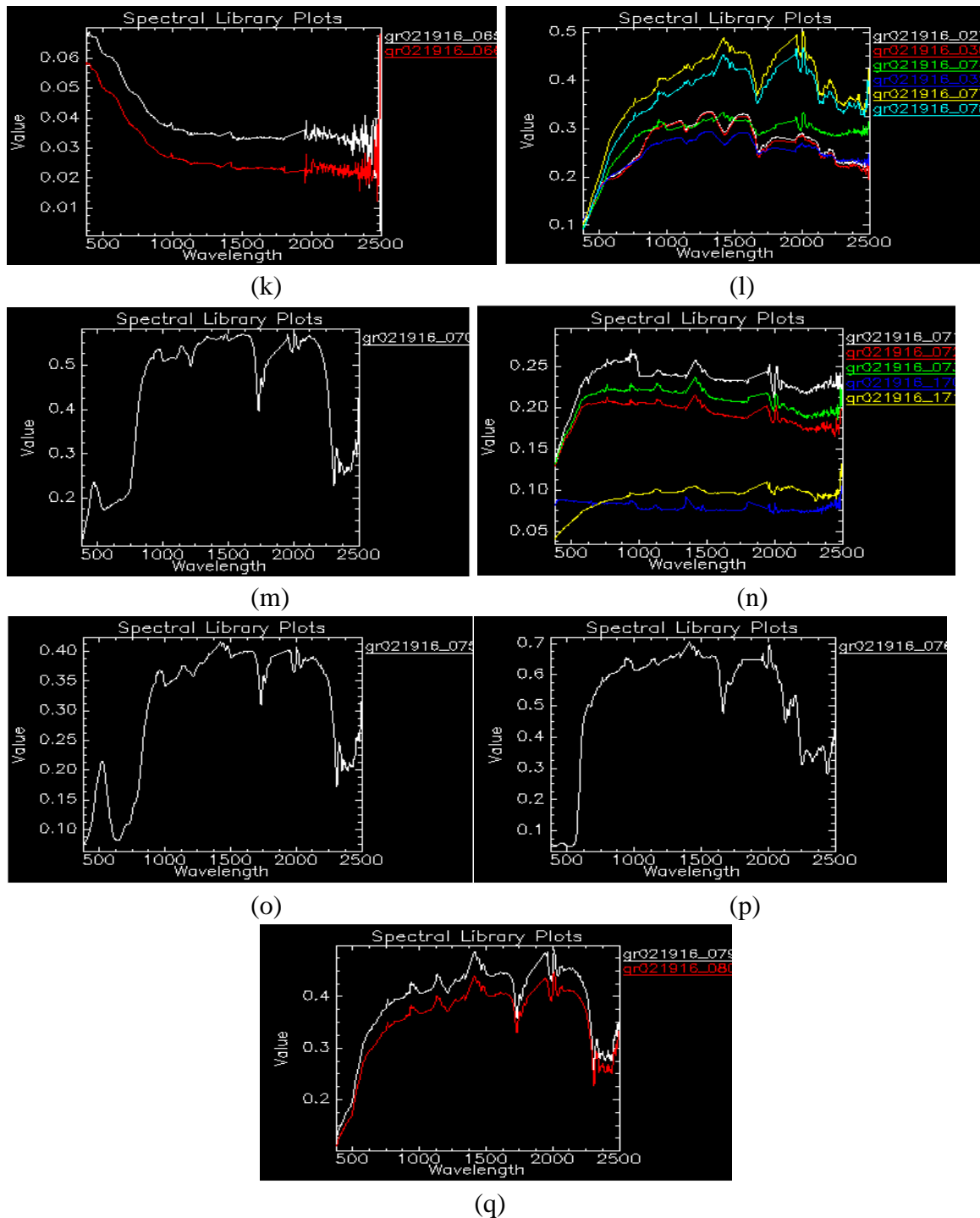


Figure 4.22: Spectral library for Impervious surfaces – Roof (a). Asbestos sheet, (b) Red mangalore tile roof, (c) bitumen membrane roof, (d) reinforced cement, (e) wood tile roof, (f) bitumen water proofing, (g) Corrugated GI sheet, (h) corrugated GI sheet in shadow, (i)AC duct Iron, (j)convention hall metal sheet and (k) convention hall metal sheet shadow, (l) PVC fibre, (m) Polythene blue, (n) polythene black, (o) green cloth shed, (p) redcarpet cloth, (q) plastic+cloth.

Pervious surfaces (backgrounds)

Soil – Bare soil, ground, sand, unpaved soil, excavation soil. (Figure 4.19)

Vegetation – Bushes, Lawn grass (Figure 4.20)

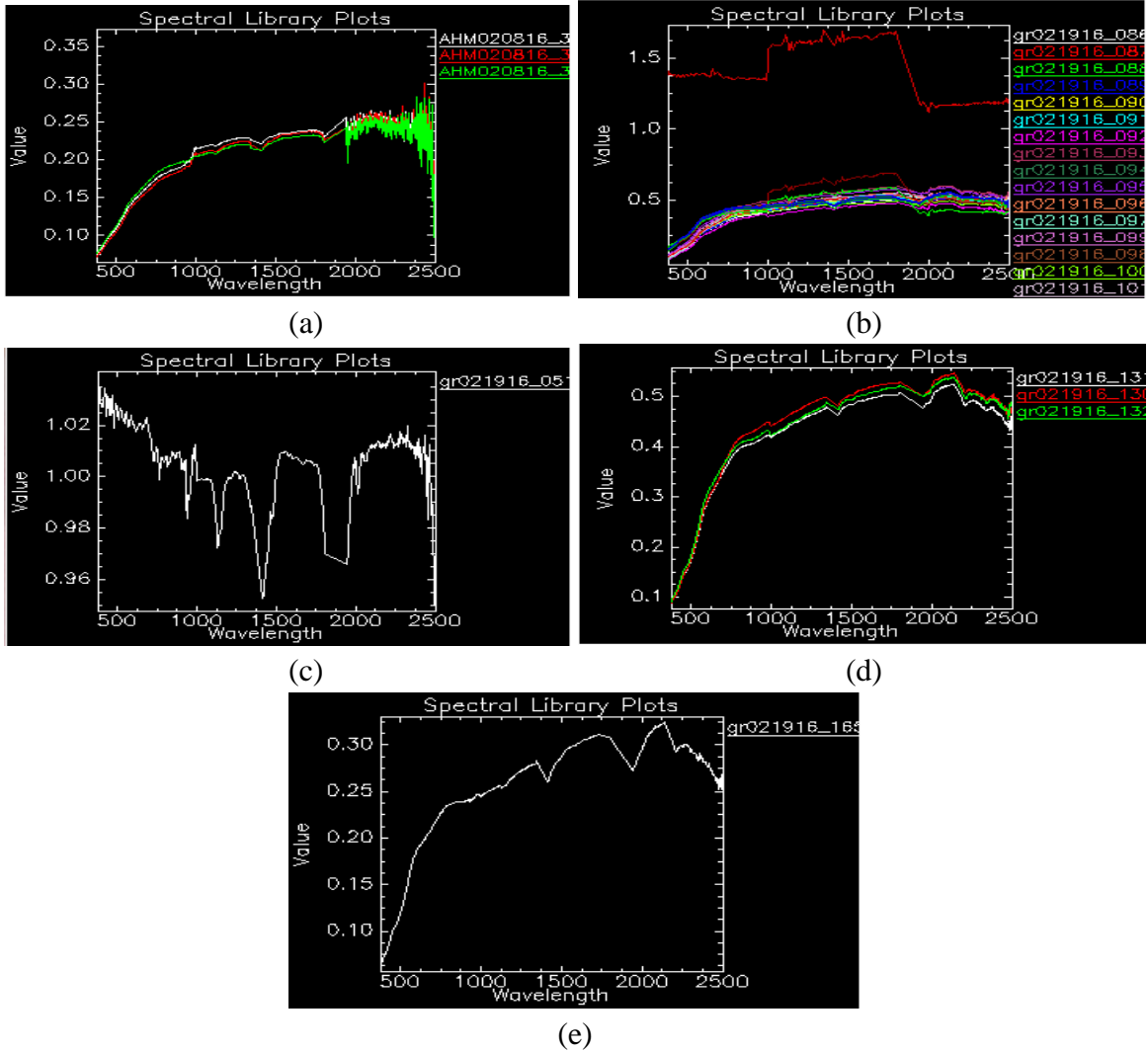


Figure 4.23: Spectral library for Pervious surfaces – Soil (a). Bare soil, (b). Ground, (c) Sand, (d) unpaved soil, (e) excavation soil

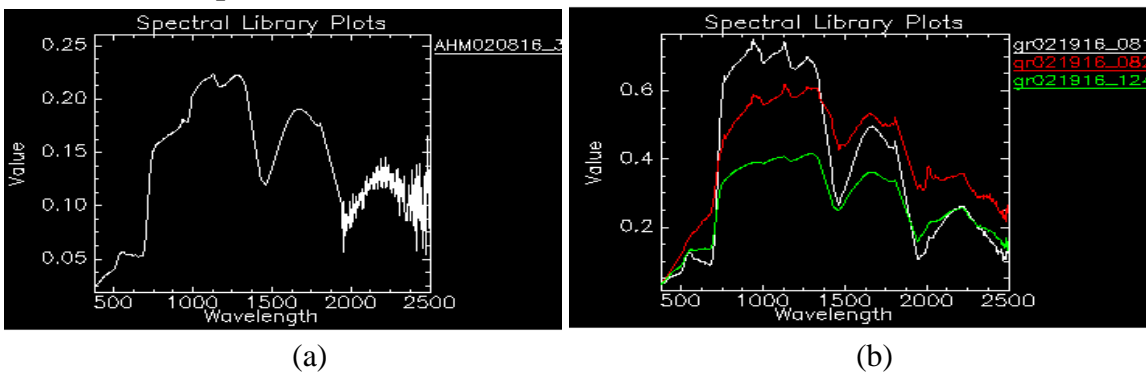


Figure 4.24: Spectral library for Pervious surfaces – Vegetation (a). Bushes, (b). Lawn grass

4.5.2.2 Selection of appropriate wavelength regions

Spectral Subsetting into eight EM regions has been done as shown in Table 4.15 below:

Table 4.15: Selection of appropriate spectral bands

EM region	Spectral range	Number of bands selected
Full Spectral range	376.44 to 2500 nm	387
Ultraviolet	376.44 to 401.49 nm	6
Visible	406.49 to 702 nm	60
UV+Visible	376.44 to 702 nm	66
VNIR	707.01 to 997.52 nm	59
Far NIR	1002.52 to 1349.12 nm & 1413.23 to 1499.39 nm	99
Early SWIR	1503.39 to 1909.92 nm & 1944.15 to 1999.25 nm	74
Far SWIR	2004.26- 2500 nm	100

4.5.2.3 Implementation of Spectral indices

(a) Impervious surface: Roof and roads (targets) detection using New built up index (NBI)

The most suitable wavelengths are first selected using OIF as shown below:

SN	Significant Band	Wavelength (nm)
1	B _{GREEN}	561
2	B _{RED}	666.94
3	B _{NIR}	967
4	B _{SWIR2}	1613
5	B _{SWIR}	2194
6	NIR2	992
7	B _{BLUE}	466

This index is then implemented using Red, SWIR and NIR bands and the equation 4.4:

$$NBI = \frac{(B_{RED} \times B_{SWIR})}{(B_{NIR})} \quad (4.4)$$

Detection results:

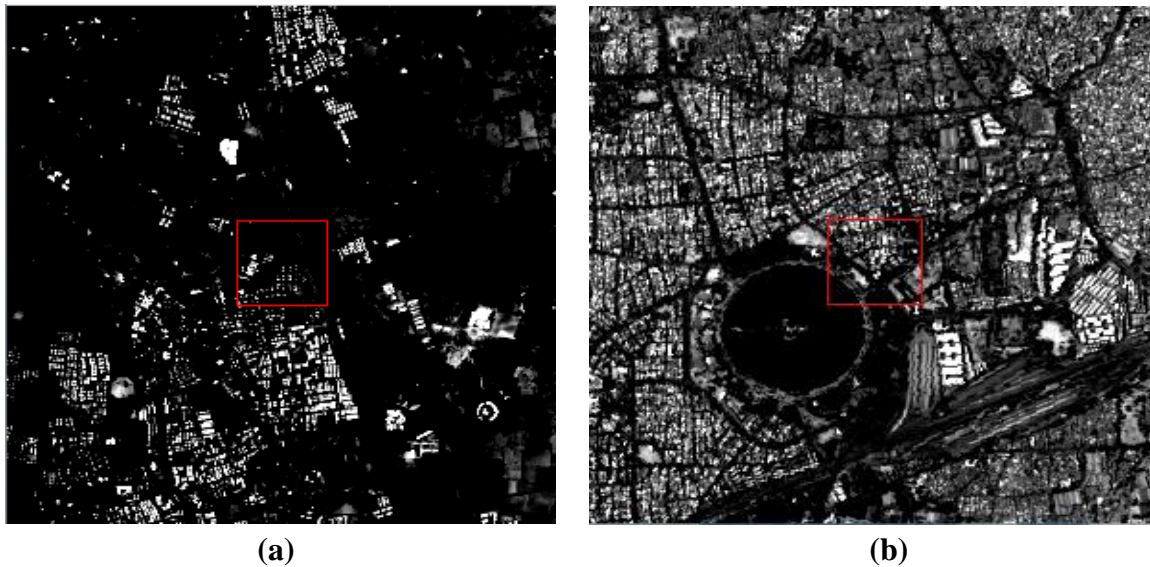


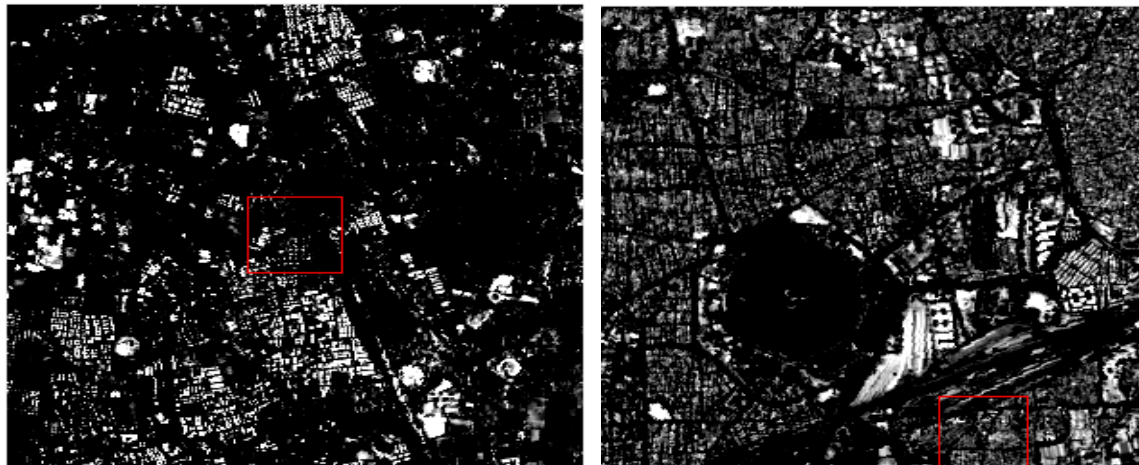
Figure 4.25: Impervious surface detection using NBI in (a) SS1, (b) SS2

(b) Impervious surface - Roof and roads (targets) detection using Normalised difference built up index (NDBI)

This index is implemented using the SWIR and NIR bands from the obtained OIF wavelengths as shown in section 4.5.2.3 (a) and the equation 4.5:

$$NDBI = \frac{(B_{SWIR} - B_{NIR})}{(B_{SWIR} + B_{NIR})} \quad (4.5)$$

Detection results:



(a)

(b)

Figure 4.26: Impervious surface detection using NDBI in (a) SS1, (b) SS2

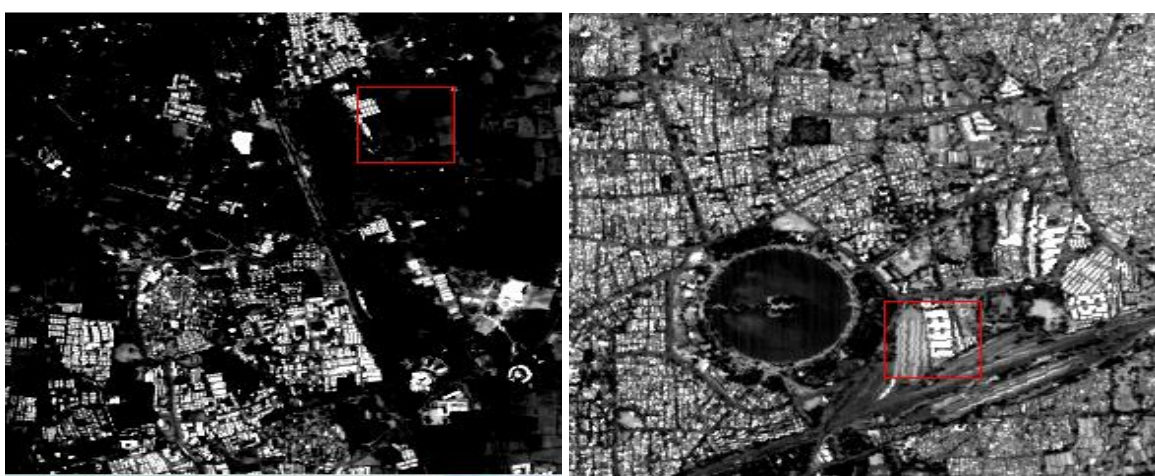
(c) Impervious surface - Roof and roads (targets) detection using Normalised built up area index (NBAI)

This index is implemented using the equation 4.6:

$$NBAI = \frac{(B_{SWIR} - \frac{B_{SWIR2}}{B_{GREEN}})}{(B_{SWIR} + \frac{B_{SWIR2}}{B_{GREEN}})} \quad (4.6)$$

Here 3 wavelength bands, SWIR (2194), SWIR2(1613) and Green(561) are considered from obtained set of best wavelengths as mentioned in section 4.5.2.3 (a).

Detection results:



(a)

(b)

Figure 4.27: Impervious surface detection using NBAI in (a) SS1, (b) SS2

(d) Impervious surface - Roof and roads (targets) detection using - The band ratio for built up area (BRBA)

This index is implemented using the equation 4.7:

$$BRBA = \frac{B_{RED}}{B_{SWIR}} \quad (4.7)$$

The subset of wavelengths selected using OIF Red (666.94) and SWIR(2194) are utilised for calculations.

Detection results:

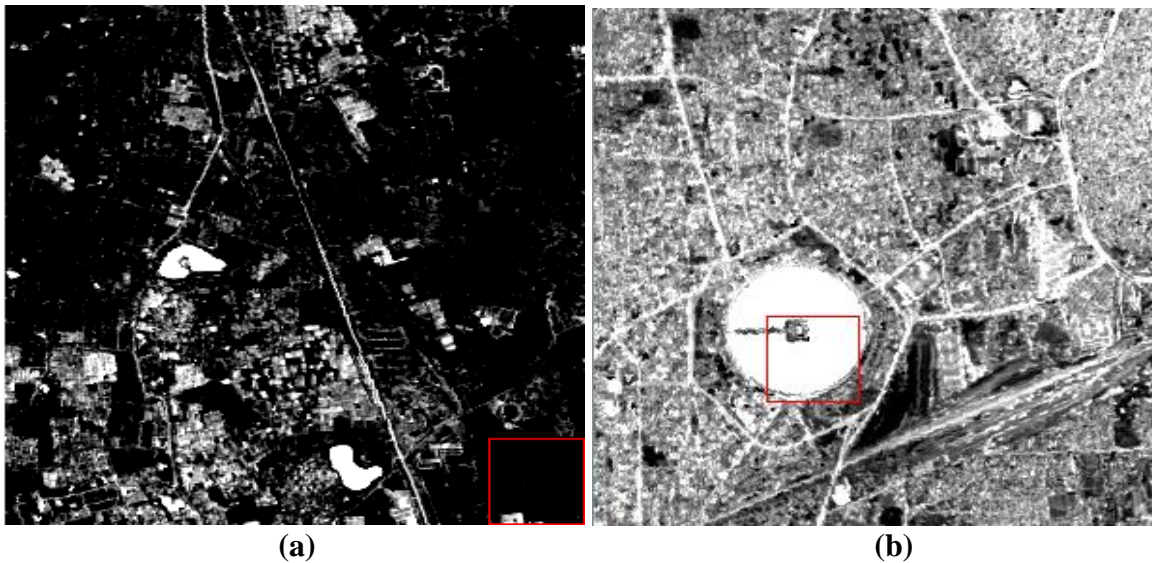


Figure 4.28: Impervious surface detection using BRBA in (a) SS1, (b) SS2

(e) Impervious surface - Roof and roads (targets) detection using Morphological building index (MBI)

This index is implemented using the equation 4.8:

$$MBI = \frac{B_{SWIR2} \times B_{RED} - B_{NIR}^2}{B_{RED} + B_{NIR} + B_{SWIR2}} \quad (4.8)$$

The corresponding wavelengths selected using a subset of wavelengths obtained using OIF are BSWIR2 (1613nm), RED(666.94nm), NIR (967 nm)

Detection results:

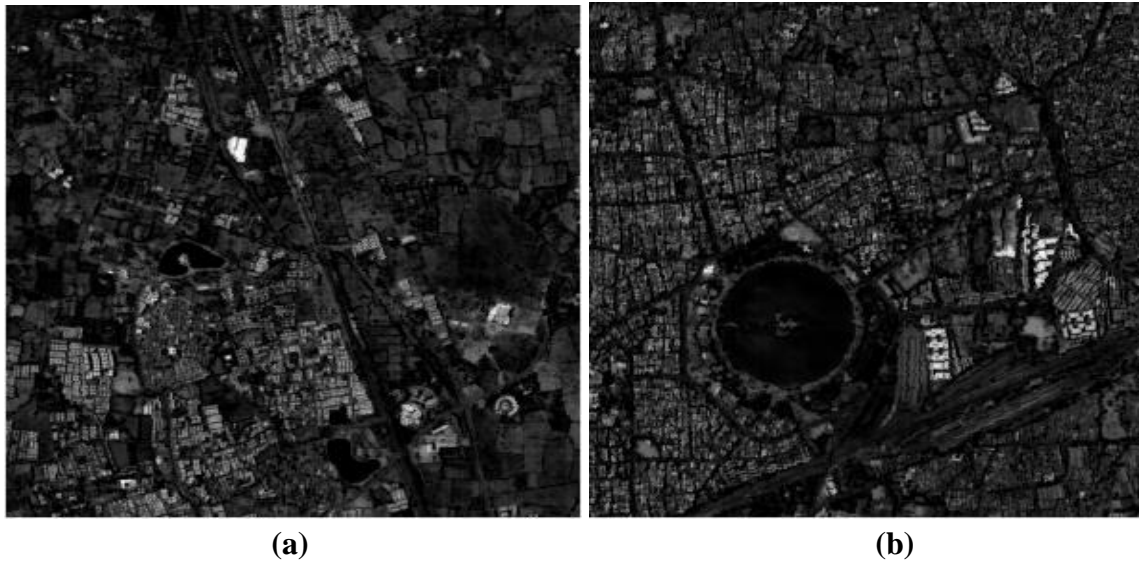


Figure 4.29: Impervious surface detection using MBI in (a) SS1, (b) SS2

In order to validate the above results, archived google earth images of the same period have been referred to confirm broad location and targets. The google earth images of Ten Acre Mall and Kankaria Railway Yard are shown in Figure 4.30 (a) and (b), respectively.



Figure 4.30: Google Earth images of target sites (a) Ten Acre Mall, (b) Kankaria Railway Yard

A ROI of 49x49 pixels from detected results of Spectral indices approach was then further analyzed. This ROI consisted of both impervious and pervious surfaces. Further within this ROI, a window of 30x30 pixels consisting of impervious surface (both roads and roofs) have been further investigated. As mentioned in the data section 4.3.2.2, 80

locations of Kankaria Railway Yard and 60 locations of Ten Acre Mall are correctly known. Therefore, while analyzing this 30x30 window, these locations only have been the focus.

Figure 4.31 (a) shows the 49x49 ROI of Kankaria Railway Yard. Figure 4.31 (b)-(f), are the detection results achieved using NBI, NBAI, BRBA, MBI and NDBI respectively. Figure (a) to (f) all have been converted to binary grey scale image (converted to unsigned int using MATLAB). Next, to determine the number of correctly identified pixels, Figure 4.31 (b) to (f) has been subtracted from (a). The results obtained are shown in Figure 4.31 (g) to (k). These results have been analyzed within the 30x30 window but only for the known locations, having impervious (both roads and roofs) surfaces. After subtraction, all values resulting in 0 for the known locations (80), have been assumed to be correct detection. These results are summarized in Table 4.16.

Similarly, as shown in Figure 4.32 (a), the 49x49 ROI of Ten Acre Mall has been considered for detection of impervious surfaces. Figure 4.32 (b) to (f), are the detection results achieved using NBI, NBAI, BRBA, MBI and NDBI respectively. After conversion of Figure (a) to (f) to binary grey scale image, further the determination of the number of correctly identified pixels is done by subtracting Figure 4.32 (b) to (f) from (a). The results obtained are shown in Figure 4.32 (g) to (k). These results have been analyzed within the 30x30 window but only for the known locations, having impervious (both roads and roofs) surfaces. After subtraction, all values resulting in 0 for the known locations (60), have been assumed to be correct detection. These results are also summarized in Table 4.16.



Kankaria Railway Yard – AVIRIS image

(a)

Detection results using Spectral Indices of impervious surfaces (Roads and Roofs)



(b)



(c)



(d)



(e)



(f)

Subtraction images



(g)



(h)



(i)



(j)



(k)

Figure 4.31: Impervious surface extraction and corresponding subtraction images for site Kankaria Railway Yard using (a) NBI (b) NBAI (c) BRBA (d) MBI (e) NDBI



Ten Acre Mall – AVIRIS image

(a)

Detection results using Spectral Indices of impervious surfaces (Roads and Roofs)



(b)



(c)



(d)

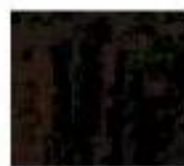


(e)

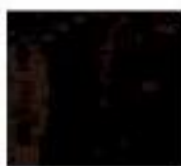


(f)

Subtraction images



(g)



(h)



(i)



(j)



(k)

Figure 4.32: Impervious surface extraction and corresponding subtraction images for site Ten Acre Mall using (b,g) NBI (c,h) NBAI (d,i) BRBA (e,j) MBI (f,k) NDBI

Table 4.16 summarizes the assessment of pixels detected using spectral indices for the known locations. It is observed that for Kankaria Railway Yard, out of 80 known pixels, BRBA detects a minimum of 10 pixels (12.5% accuracy) while NDBI detects a maximum of 76 pixels (95% accuracy). Amongst other algorithms, NBAI and NBI also perform reasonably well. Similarly, for Ten Acre Mall, BRBA detects a minimum of 10 (16.66% accuracy) and NDBI detects a maximum of 58 (96.66% accuracy). Amongst the others, NBAI and NBI appear to perform well.

Analysis of the NDBI with rest of the spectral indices indicates the possibility that SWIR (2194 nm) and NIR (967 nm) bands appear to be performing much better than other bands / wavelength regions. Similarly, a comparison of NDBI, NBAI and MBI suggest that SWIR (2194 nm), NIR (967 nm) and Green (561 nm) band alone may be sufficient for reasonable detections of impervious surfaces using spectral indices-based approach.

Table 4.16: Assessment of pixels detected using Spectral Indices

Subset	Site	Pixels on ground	Index	Pixels detected	Accuracy (%)
Subset 2	Kankaria Railway Yard	80	NBI	61	76.25
			NBAI	50	62.5
			BRBA	10	12.5
			MBI	48	60
			NDBI	76	95
	Ten Acre Mall	60	NBI	48	80
			NBAI	50	83.33
			BRBA	10	16.66
			MBI	11	18.33
			NDBI	58	96.66

Conclusions:

In this study, two tasks namely, end member extraction and abundance estimation using spectral unmixing and evaluation of spectral indices based approach for end member identification have been performed.

The results of endmember extraction and abundance estimation using spectral unmixing indicate that ICA-EEA and ATGP perform best while recovering the image end members including the target spectra, followed by NFindr, while PPI performed poorly in this case . Error was also found to be least in ICA-EEA and ATGP in comparison to NFindr and PPI.

Evaluation of spectral indices-based approach for end member identification, indicate that this approach which is essentially based upon identification of significant wavelengths related to a particular end member may be more suitable in extraction of impervious (roads and roofs) surfaces. The results indicate upto a maximum of 96.66% accuracy using spectral indices based approach. Further, spectral indices based approach appear to suggest that appropriate indices evolved using SWIR (2194 nm) and NIR (962 nm) may be most suitable in detection of impervious surfaces (roads and roofs).

Chapter 5

Random Recursive Vs Non-Random Non-Recursive Super Resolution Mapping Algorithms

5.1 Introduction

This chapter further extends the study of extraction of full pixel and subpixel targets in hyperspectral data. Here, any object or material whose information is to be extracted from any type of remote sensing data is being referred as a “target”. In target detection, detection merely implies differentiation between full pixel signatures of a target and the background. The process of target detection in hyperspectral images, however, involves a series of steps viz classification, identification, discrimination, and quantification (Chang, 2003). A complete target detection may therefore necessitate detection of not only the full pixels of a target but also the recovery of all the subpixel components of the target residing in surrounding pixels (Foody *et al.* 2005, Foody *et al.* 2007).

Most target detection algorithms, however, suffer from the limitation that they can detect only the full pixels of the target and thus leaving out the components of the target that may simultaneously reside partially in several surrounding pixels. In this case, target detection has to deal with not only detection of full pixel targets but also recovery of components of the target from surrounding mixed pixels. In some other cases, the target may even be embedded completely within a pixel. In this case, this is purely a problem of subpixel target detection. In the former case, the problem is addressed by full pixel target detection followed by spectral unmixing to determine the abundance fraction of the target in the surrounding pixels. The problem in this case however is that, though spectral unmixing gives the abundance fractions, it does not give the spatial distribution/

arrangement of subpixels of target with the surrounding pixels (Atkinson. 1997, 2004,2005,2013, Chan *et al.* 2011, Foody and Cox 1994, Foody 2002). Lack of availability of spatial distribution within a mixed pixel is a major limiting factor in successfully completing the entire target detection process mentioned above. The process of optimizing the spatial distribution of subpixels inside any given pixel based on the available abundance fractions is known as super resolution (Gu *et al.* 2008, Guo *et al.* 2009).

A scale factor in super resolution is a number, the square of which determines the number of subpixels into which a mixed pixel is proposed to be sub-divided / super resolved. The product of end member fractions and the total number of subpixels of a pixel (based on the scale factor) determines the number of subpixels of that endmember / component (Kasetkasem *et al.* 2005, Li *et al.* 2011). The super resolution therefore provides a means to suggest the most optimized spatial distribution/ arrangement of these subpixels belonging to different end members/ components inside the mixed pixel (Ling *et al.* 2014).

Most of these super resolution algorithms are currently under evolution with applications primarily in the field of land cover mapping (Ling *et al.* 2013, Ling *et al.* 2011, Kling *et al.* 2010, Mertens *et al.* 2006, 2003). Detection of full pixels of a target, recovery of target fractions/ components inside the surrounding pixels using spectral unmixing and their correct spatial distribution/ arrangement determined using super resolution algorithms, may not only aid target detection but also its identification and recognition. Study and development of super resolution algorithms is therefore extremely important particularly in small military target detection. Many super resolution mapping algorithms, such as, MRF (Markov Random Field) (Kasetkasem *et al.* 2005), HNN (Hopfield Neural Network) (Tatem *et al.* 2001, Tatem *et al.* 2002), Atkinson's pixel swap algorithm (Atkinson, 2005, Thronton *et al.* 2006), PSO (Particle swarm optimization), linear

optimization *etc.* have been reported in the literature. Most of these super resolution algorithms reported in literature, work on random allocation of location to the subpixels of different end members within the pixel. In addition, it has been observed that a recursive procedure is followed for obtaining the results of super resolution thereby increasing the computational complexity and time consumption (Atkinson, 2001 and 2005). The limitations associated with these algorithms are summarized in the section 5.2.

This chapter also extends the study to extraction and mapping of impervious surfaces in multi sensor, multi resolution, temporal urban data. Urbanization linked Land-use is known to increase the total area of impervious surfaces (building rooftops, streets, highways, parking lots, and sidewalks *etc.*) significantly and which in turn has adverse environmental effects at local, regional and global scales (Kuang et al. 2014, Weng 2008). Water cannot percolate through these impervious surfaces directly (Weng 2012, Scheuler, 1994) which not only affects the amount of runoff to streams and lakes but also influences non-point source pollution, water quality and the aesthetics of landscapes. Traditionally, ground surveys and aerial photo interpretation have been the most accurate methods of mapping of impervious surfaces and its area assessment, but they are not time effective. Availability of finer resolution spectral, spatial and temporal data can facilitate cost effective mapping and monitoring of changing impervious surfaces which in turn can assist in various aspects of urban planning, management of surface runoff/flooding and in monitoring the environment. A lot of work has been reported in the literature regarding mapping of impervious surfaces using a variety of remote sensing data, however, there is hardly work reported from within the country. Besides, the present ongoing research indicates immense scope for development of alternative approaches for cost effective and better approaches for mapping and area estimation of impervious surfaces. Also, from the review of literature, it is derived that many pixel and subpixel based algorithms as well as

feature based algorithms have been proposed for mapping and estimation of impervious surfaces using low, medium as well as high resolution datasets. However, there are several issues in mapping and estimation that need to be dealt with, such as since the impervious surfaces are mainly distributed in complicated urban areas, the accuracy of impervious surfaces is limited by the complexity of impervious surfaces. Also, due to the low spatial resolution of the sensors, mixed pixels arise which complicates the process of accurate detection and estimation of impervious surfaces. Further, the impervious surfaces from low spatial resolution images are often too coarse to use in urban environments and most of the impervious surface mapping techniques provide the fraction of impervious surfaces by using classification approaches, however, the accurate spatial distribution of these surfaces within the image remains unknown (Wand *et al.* 2017, Atkinson 2013, Linden *et al.* 2009, Foody *et al.* 2005). In all such cases, an appropriate super resolution mapping method may prove useful. However, due to the nature of subpixel landcover fractions present, a non – random non – recursive algorithm is likely to perform better and faster.

5.2 Limitations of Random-Recursive Super resolution Algorithms

Several Super resolution algorithms such as Pixel Swap (PS) (Atkinson, 2001), Hopfield Neural Network (HNN) (Tatem *et al.* 2002), Particle Swarm Optimization (PSO) (Kennedy and Eberhart, 1995), Markov random field (MRF) (Geman and Geman, 1984, Kasetkasem *et al.*, 2005) *etc.* A brief review of these algorithms has been presented in subsection 1.2.2.3 (under Section 1.2). Most of these super resolution algorithms work on random allocation of location to the subpixels of different end members within the pixel. There are several limitations of this random, recursive Super resolution algorithms, some of which are mentioned here.

Being based on recursive optimisation, the implementation of algorithm commences with random allocation of subpixels and the number of subpixels allocated to

each class depends upon its fractions. Therefore, even for a small size of the dataset, the process becomes computationally intensive (Wang *et al.* 2006, Wang 2013). In addition, the subpixels are randomly distributed, and a series of iterations are required to cluster those subpixels based on a distance weighed attractiveness function. Since all the subpixels of a given target/class based on its abundance fraction are likely to be clustered together, this iterative procedure only leads to additional computational constraint (Atkinson, 2005).

In the case of linear targets, the algorithm works well only when the targets are at least one pixel wide and fails for targets which are about one half of the width of the pixel. Besides, certain subpixels once allocated to the incorrect class, continue to cluster the misclassified pixels (Atkinson, 2001 and 2005).

Further, these techniques generally use a non-linear parameter in the calculation of distance dependent weight, which may not be determined deterministically for different scale factors and may vary for different applications. This adds uncertainty to the procedure. As a result, the convergence of the algorithm usually becomes difficult to achieve (Atkinson, 2001 and 2005).

From the limitations discussed above, it is evident that the major issues lie in the underlying criteria to allocate the subpixels to a particular class / end member. The algorithms are usually based on initialization with random allocation of subpixels and follow a time consuming, computationally complex process that decreases the accuracy of the subpixel mapping results (Wang *et al.* 2006, Wang 2013). Thus, there is a need to overcome the limitations in case of random-recursive algorithms, as reported in the literature (Zhong *et al.* 2015, Xian 2019, Wang *et al.* 2012, Wang *et al.* 2017).

This focus in this chapter is to compare non-random non-recursive based super resolution algorithms with random – recursive algorithms on the basis of efficiency and computation time while being used in the process of identification of targets in image. One

random recursive super resolution mapping algorithm reported in the literature (Pixel Swap) has been compared with the non- random non-recursive based technique (Inverse Euclidean distance) using both synthetic as well as real hyperspectral data. The comparison has been carried out at different scale factors.

5.3 Experimental Data Set

5.3.1 Synthetic Data

A total of four synthetic (consisting of different shapes) and one real hyperspectral data set (consisting of aircrafts as targets) have been used in these experiments. Since for validation of results, the availability of reference data is a pre-requisite (Thornton *et al.*, 2006), the synthetic data set has been generated, where abundance fractions within the subpixels is available and are used as the reference data for analyzing the super resolution algorithm. Experiments after performing on the synthetic data have also been performed on hyperspectral data where targets under consideration are aircrafts. The exact number of subpixels occupied by the aircraft in the mixed pixels, if any, is however not available in this case.

Synthetic data set, each of 30x30 pixels have been generated approximating the shape of a vehicle, a temple, a circle, and an aircraft. In each case, a number of synthetic images have been generated for super resolution experiments at different scale factors namely, 3,5,7,9, and 11. For these scale factors, the pixel gets super resolved into 3^2 , 5^2 , 7^2 , 9^2 , and 11^2 subpixels corresponding to each of the scale factor.

As an example, for super resolution at a scale factor of 7, the procedure for generating 30x30 pixels image is as given below:

- (a) Determine the size of existing image (in this case 30x30 pixels) and scale factor (in this case 7). The size of the subpixel image used therefore be (30x7,30x7) *i.e.* (210,210)
- (b) Create a target of the desired shape as a binary image (consisting of 1 and 0) within the subpixel image of 210x210 pixels. This image acts as a reference image.
- (c) Degrade the 210x210 pixels image to size 30x30 pixels using 7x7 filter that adds the values in all the 49 pixels and then divides it by 49. Fractions arrived at may be modified slightly if required. For example, in the case of 210x210 pixels approximating the shape of a vehicle, the fractions in the edge pixels have been modified to 0.75
- (d) Repeat the above steps at different scale factors for different shapes.

The four images corresponding to different shapes have been referred as Synthetic – I, Synthetic – II, Synthetic – III and Synthetic – IV as shown in Figure 5.1(a), (b), (c) and (d).

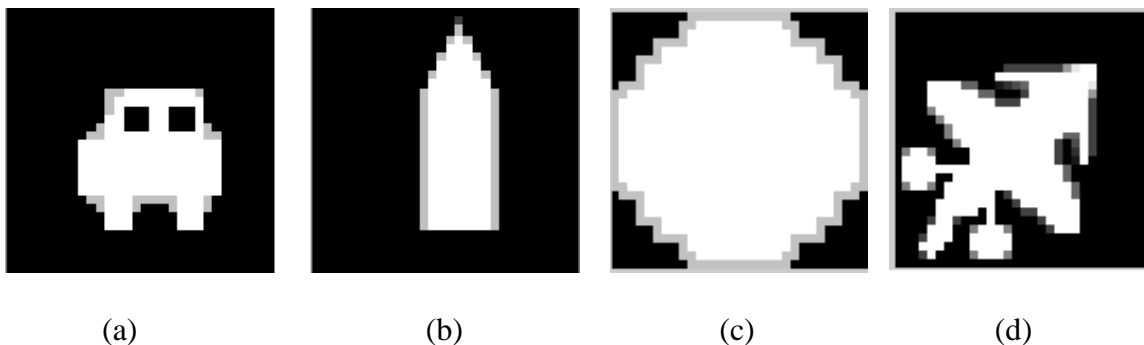
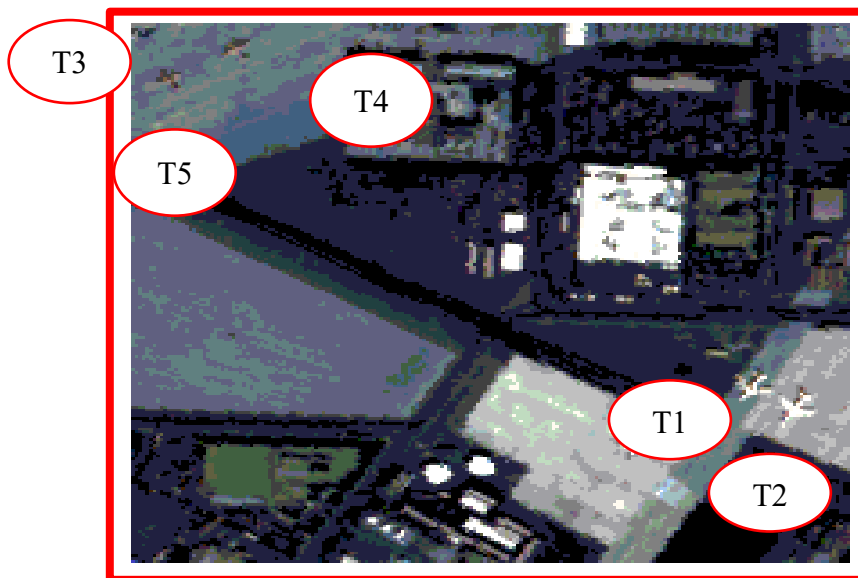


Figure 5.1: 30x30 pixels approximating the shape of (a) a vehicle (Synthetic- I) (b) a temple (Synthetic- II) (c) a circle (Synthetic- III) (d) an Aircraft (Synthetic- IV). Edges of these shapes have fractions from 0.25 to 0.9.

5.3.2 Hyperspectral Data

189 bands of an archived AVIRIS hyperspectral data (reflectance image, size 400x400 pixels in 224 bands, spatial resolution 4 meters) after removing water absorption

and bad bands, captured over a Naval station in San Diego, California, have been used for super resolution experiments (Figure 5.2(a)). This image contains 5 aircrafts located at pixel coordinates (244,145), (232,137), (228,134), (89,11) and (70,22) which have been considered as targets. Each of these aircrafts/targets has been identified using ID's from T1 to T5. Two of these targets T1 and T2 are in illumination. Targets T3, T4 and T5 which are in shadow may be considered as difficult targets for detection.



(a)



(b)



(c)

Figure 5.2: (a). Subset of 200x200 pixels selected from AVIRIS Dataset containing five targets: T1, T2, T3, T4, T5 (b). Spatially segmented image of 40x40 pixel size, with three targets: T3, T4 and T5 (c). Spatially segmented image of 40x40 pixel size, with two targets: T1, and T2

Image of size 40x40 pixels containing three aircrafts each shown in Figure 5.2(b) and two targets shown in Figure 5.2(c) have been segmented from the original image 5.2(a). The

segmented region contains both the pixels *i.e.* pixels fully occupied by target (aircraft) and those partially occupied by target (aircraft).

5.3.3 Multi - sensor, Multi – resolution, Temporal Urban dataset

Multi-sensor, Multi-resolution, Temporal data for urban region – UDAIPUR (24.5854° N, 73.7125° E), INDIA has been selected for extending the non – random non – recursive super resolution on a real urban dataset. Data from space borne sensors – LANDSAT-8 and SENTINEL-2B and airborne sensor- AVIRIS-NG have been selected. This data is shown in Figure 5.3(a). It is however mentioned that there is no ground truth available in this case and hence the study is based on comparative visual analysis of the results. After performing corrections and data pre-processing, spectral unmixing has been implemented using LMM (Linear Mixture Model) and resulting images for impervious surfaces are shown on Figure 5.3(b).

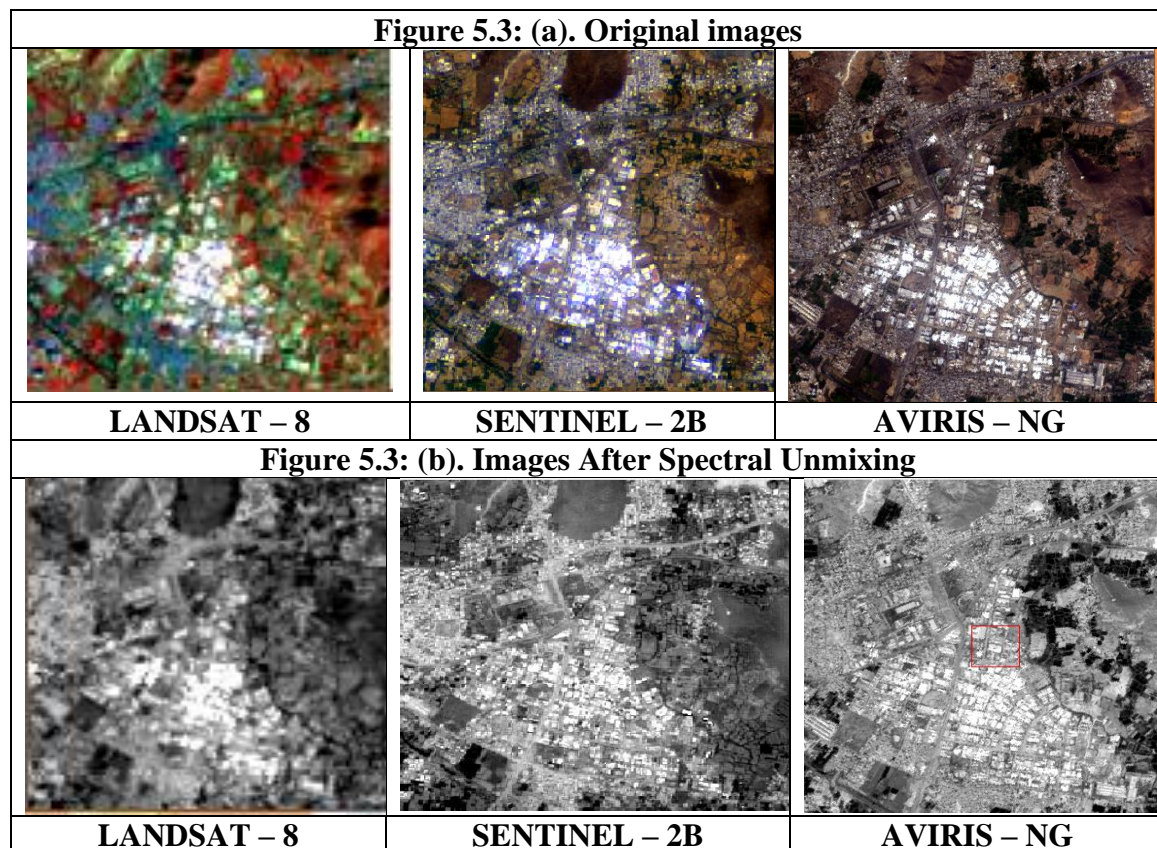


Figure 5.3: (a). Original Images of Udaipur region acquired from different sensors and (b). Images obtained as results of spectral unmixing using LMM

The data specifications of this Multi sensor, Multi – resolution, Temporal urban dataset is summarized in Table 5.1.

Table 5.1: Specifications of Multi sensor, Multi –resolution, Temporal urban dataset

SN	Parameters	Description		
1	Image Location	Udaipur, Rajasthan, India	Udaipur, Rajasthan, India	Udaipur, Rajasthan, India
2	Name of Sensor	Sentinel-2B	Landsat-8	AVIRIS-NG
3	Date of Data acquisition	02/06/2018	30/11/2017	02/02/2016
4	Spatial Resolution	10 meter	30 meter	8.1 meter
5	Wavelength Range	443 nm – 2190 nm	430 nm – 2290 nm	376 nm – 2500 nm
6	Number of Samples, Lines and Bands	352, 352 ,13	117, 117, 7	400, 400, 380
7	Level of data	Level 2	Level 2	Level 1 and Level 2
8	Coordinate system	WGS-84 / UTM Zone 43N	WGS-84 / UTM Zone 43N	WGS-84 / UTM Zone 43N

5.4 Methodology and Implementation

Two algorithms, one random recursive (Pixel Swap) and one Non-random non-recursive (Inverse Euclidean Distance) super resolution algorithms have been identified for comparison and implemented on both the synthetic as well as hyperspectral datasets.

5.4.1 Common Steps of Both Random Recursive (Pixel Swap) and Non-random Non- Recursive (Inverse Euclidean Distance) Super resolution Algorithms

Two steps namely, spectral unmixing for estimation of the abundance fractions and super resolution mapping using abundance fractions are common to both the approaches and have been explained here first.

Spectral Unmixing for Estimation of Subpixel Abundance Fractions

Spectral unmixing is first step in super resolution. Spectral unmixing, using linear mixture model (LMM) may be stated as,

$$r = \sum_{k=1}^m a_k s_k + w \quad (5.1)$$

Where, r is mixed pixel spectrum, s_k is spectra of constituents, a_k is estimated abundance fractions within a pixel, and w is noise / error component. Thus, the abundance fractions may be estimated provided the end member spectra are known from existing spectral libraries or alternatively, they may be drawn from the image itself (Rosin, 2001, Vikhamar *et al.* 2002). In the present study, an unsupervised spectral unmixing method named Simplex Maximum Angle Convex Cone (SMACC) has been used to estimate end member fractions by automatically generating the end member signatures from the image itself. Abundance fractions, thus obtained, form the input for super resolution as discussed in the next subsection.

Super Resolution Mapping Using Abundance Fractions

In super resolution mapping, the derivation / generation of a subpixel map (at a fine spatial resolution) from a coarse resolution input image is done by optimizing abundance fractions within the mixed pixels (Kasetkasem *et al.* 2005, Tatem *et al.* 2001, Tatem *et al.* 2002, Muad *et al.* 2012, Muad and Oody 2019). Depending upon the spatial resolution required, the process may be performed at varied scale factors. The main criteria behind super resolution algorithms is the quantification of the number of target subpixels within a given pixel that are to be super resolved and to model an attractive influence that defines the relationship between various subpixels (within the pixel under consideration) and pixels in the neighbourhood.

The calculation of the number of target subpixels at any pre-determined scale factor is done with the help of abundance fractions obtained after spectral unmixing. To exemplify

this, let us consider a scale factor of 7. This implies that the pixel to be super resolved is to be mapped onto a grid of seven rows and seven columns of subpixels. Thus, within each pixel, a total of 49 subpixels are generated. Now, if the abundance fraction value of end member is estimated to be 0.7 and the scale factor is 7, it implies that 70% (*i.e.*, $49 \times 0.7 = 34$ subpixels, rounded off to integer value) of the total number of subpixels belong to that end member. Modelling attractive influence between each subpixel and the neighbourhood pixels, however, requires defining an appropriate distance function.

5.4.2 Random Recursive (Pixel Swap) Super resolution Algorithm

Proposed by Atkinson (2001 and 2005) to achieve subpixel mapping, the objective of this algorithm is to change the spatial arrangement of subpixels in such a way that the spatial correlation between neighboring subpixels is maximized. The results obtained from soft classification (to identify the land cover class within each pixel) are utilized for transformation into subpixel classes. The method of initialization is a measure to compute the accuracy and efficiency of mapping at subpixel level. A random initialization is considered and further the algorithm intends to find the spatial arrangement of subpixels and works in a recursive manner to find their correct allocation by finding the maximum correlation among the neighboring subpixels. This algorithm works for a binary land cover class problem and not for multi class problem.

Land cover class proportions for each pixel obtained from a soft classification (or unmixing) are input to the Pixel Swap algorithm. Based on the scale factor, the number of subpixels is calculated corresponding to the pixel in the coarse spatial resolution image. The number of subpixels for any given target/class in each pixel remains fixed throughout the Pixel Swap procedure. During this Pixel swapping process, each subpixel is allocated

to a single land cover class such that the original class fractions in the coarse resolution image are maintained (Atkinson, 2005).

The steps for implementing the algorithm can be summarized as

(i) Randomly allocate subpixels to binary targets/classes based on pixel proportions.

(ii) For each iteration for each pixel.

(aa) For each subpixel within the pixel:

(ab) Calculate attractiveness for each neighbouring subpixel within a window. The pixel neighbourhood considered here is 2x2 pixels. The attractiveness A_i of a pixel i is predicted as a distance weighted function of its neighbours, $q = 1, 2, \dots, q$ and is given by:

$$A_i = \sum_{q=1}^q \lambda_{iq} z(y_q) \quad (5.1)$$

Where, $z(y_q)$ is the (binary target/class of the q th pixel at location y_q and

$$\lambda_{iq} = \exp\left(\frac{-h_{iq}}{a}\right) \quad (5.2)$$

Where, h_{iq} is the distance between the location y_i of a pixel i for which attractiveness is desired, location y_q of a neighbouring pixel q , and a is the nonlinear parameter.

(ac) Find minimum attractiveness A_i for all subpixels currently allocated to 1 (*i.e.* $A_i = \min (A_i) | z(y_q) = 1$)

(ad) Find maximum attractiveness A_q for all the subpixels currently allocated to 0 (*i.e.* $A_q = \min (A_q) | z(y_q) = 0$)

(iii) If, $A_i < A_q$ then swap the single pair of subpixel allocations

(iv) Continue till threshold is achieved and no more swaps can be made.

5.4.3 Non - Random and Non - Recursive (Inverse Euclidean Distance) Super resolution Algorithm

Euclidean distance Algorithm is based on a non-random non-recursive assignment of subpixels to binary end members. For ease of explanation, an $m \times n$ image is considered as shown below:

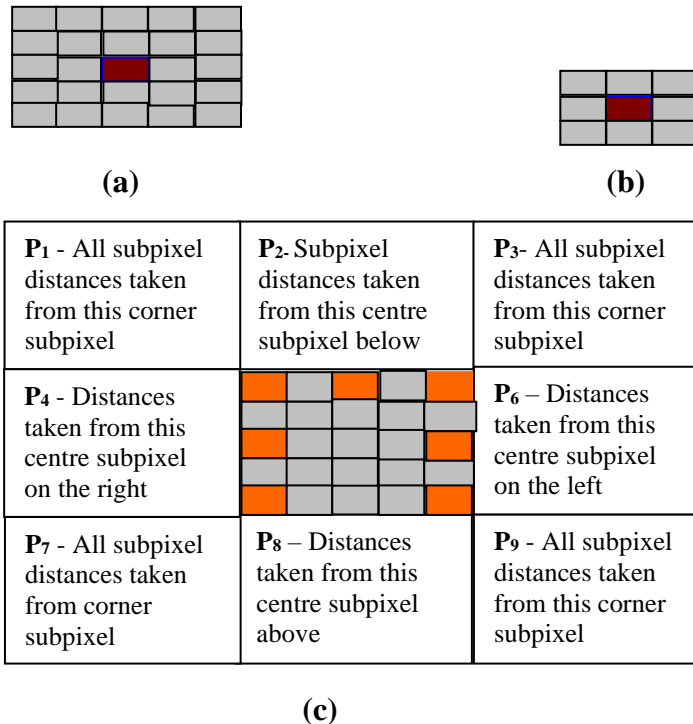


Figure 5.4: (a) An M x N Image array for super resolution, (b) 8- pixel neighbourhood (c) Central pixel for super resolution mapping

From this image, any 3x3 pixel clique may be selected considering that its central pixel is the pixel that is to be super resolved. For scale factor of 7 for super resolution, a 7 x 7 subpixel grid may be obtained at this central pixel. Thus, 49 subpixels within the central pixel should be spatially distributed across the pixel. So, this means a value of 0 or 1 is to be assigned to 49-pixel locations. However, the exact subpixels locations which are to be assigned these binary classes (*i.e.* the value of 0 or 1) are yet to be ascertained.

It is logical to assume that a pixel in the neighbourhood with higher abundance fraction of the end member is likely to attract a greater number of subpixels from the pixel

under consideration. Note that at any point of time, there will be a pixel with certain number of subpixels under super resolution and a neighbourhood pixel would exert certain attraction on these subpixels in inverse proportion of the Euclidean distance between the two. The pixel under super resolution is referred as super resolution pixel and neighbourhood pixel exerting certain attraction is referred as end member center.

Next step is defining an appropriate distance function to model the attractive influence:

Pixel Neighbourhood:

A group of pixels that exert or experience an attraction from the surrounding pixels is termed as pixel neighbourhood. The pixel neighbourhood may be represented using various schemes (such as 2x2, 4x4 and 8x8 pixels schemes *etc.*) as shown in Figures 5.5 (a) to 5.5 (c).

All the subpixels of an end member (under consideration) within a pixel, experience an attraction from neighbourhood pixels provided it has some fraction/proportion of the similar end member. Let the pixel under super resolution be referred as super resolution pixel and neighbourhood pixel exerting certain attraction be referred as end member center. In Figure 5.5, the black colored pixel is super resolution pixel and grey pixels are considered end member center one by one.

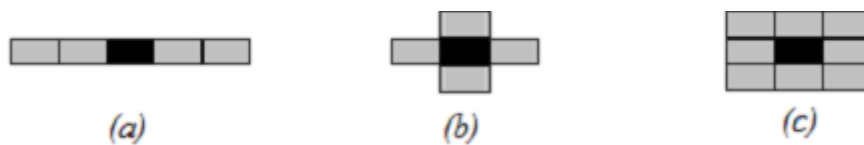


Figure 5.5. (a) 2x2 pixel neighbourhood. (b) 4x4 pixel neighbourhood. (c) 8x8 pixel neighbourhood (Kasetkasem, 2005)

Pixel Clique:

To understand super resolution mapping, let us consider that an image of size say $m \times n$ pixels is used. In such an image, the centrally located pixels are surrounded by eight pixels from all sides whereas, the corner pixels will be surrounded by pixels only from three sides. A subset of an image thus obtained, is called Clique, where two separate elements appear are mutual neighbours in an image (Baralde *et al.* 2001). Several cliques are thus possible in an image and they appear to be an important factor in determining the number of pixels directly influencing the pixel under consideration.

Further, implementation of the Inverse Euclidean Distance Algorithm is discussed in the following steps.

Step 1. Computation of the subpixels that are attracted to each of the neighbourhood pixel:

For ease of understanding, consider the 3x3 clique (Figure 5.6) with nine pixels also shown in Figure 5.5(c) and numbered as PX1 to PX9. Let the abundance fractions of an end member in it be af1 to af9. Further, let af1 to af9 be 0.3, 0.3, 0.3, 0.3, 0.7, 0.2, 0.2, 0.2, 0.2.

PX1/af1	PX2/af2	PX3/af3
PX4/af4	PX5/af5	PX6/af6
PX7/af7	PX8/af8	PX9/af9

Figure 5.6. Abundance fractions of endmember in PX1 to PX9 in a 3x3 pixel array is af1 to af9 (Arora *et al.* 2013)

The super resolution pixel under consideration is PX5 and the scale factor is 7. Thus, the number of subpixels of target that get attracted towards the end member are $49 \times 0.7 = 34$. This is determined in two steps. First, the total number of subpixels in the pixel under super resolution at a given scale factor is determined. Next, the number of subpixels from the pixel under super resolution getting attracted to each of the neighbouring pixels is determined which is in direct proportion to the abundance fractions of the end member in these respective neighbourhood pixels.

The allocation of the number of subpixels is always an integer, thus, the obtained values are rounded off to next higher value. The total number of subpixels of an end member is however maintained and the number of subpixels in excess/shortfall are adjusted with the pixel having the lowest value of abundance fraction. This calculation has been further explained in Table 5.2.

Step 2. Modelling the Attractive Influence:

The number of subpixels in the super resolution pixel that experience attractive influence from the neighbouring pixels have been calculated in Step 1, however, the exact spatial locations of these subpixels is still unknown. The attraction experienced by a subpixel in the super resolution pixel is computed as a function of inverse Euclidean distance between a subpixel in the super resolution pixel and the end member center as:

$$A_{ij} = \frac{1}{d_{ij}} \quad (5.2)$$

$$d_{ij} = \sqrt{(i - x_c)^2 + (j - y_c)^2} \quad (5.3)$$

Where, i is row coordinate of end member center, and j is column coordinate of end member center (neighboring pixel), x_c and y_c are the centers of the rows and column coordinates of subpixels (within the super resolution pixel) and d_{ij} is the Euclidean distance. It may be noted that for any *super resolution pixel* and an end member *center*, the attractive influence experienced by the subpixels in the *super resolution pixel* can be determined *ab initio* itself at each of the different scale factors, these values arranged in decreasing order of attractiveness and saved for subsequent recall. These values are recalled during super resolution. The advantage of this procedure is that re-computation of attractiveness values is not required at run time thus reducing the time of computation.

Step 3. Achieving super resolution:

In Step 1, the number of subpixels in PX5 that experiences attractive influence from the end member *center* is determined, and in Step 2, the attractive influence experienced

by subpixels in any super resolution pixel for any given clique is determined, ranked, and then saved. Super resolution process is now started with the first pixel (which is converted into subpixels according to scale factor). This pixel is called as *super resolution pixel*. Its corresponding clique is then determined and the pixel having highest abundance fraction of target in the neighbourhood is obtained. The pixel that has the highest value of abundance fraction of target is considered as end member *center*. Number of subpixels in any *super resolution pixel* experiencing attraction from any given end member is known from Step 1. The ranked attractiveness is already available from Step 2. The number of subpixels determined in Step 1 is therefore assigned a binary value of 1 according to descending order of ranking available from Step 2. Next the end member is moved to the pixel that has the second higher abundance fraction value for the end member and process is continued till all the pixels of the clique have been used. Thereafter, the *super resolution pixel* is moved to the next pixel and the next concerned clique is used to progress the super resolution. The process continues till all the pixels have been super resolved.

Table 5.2. Computation of number of subpixels attracted to neighbourhood pixels

<i>Computation of the subpixels that are attracted to each of the neighbourhood pixel:</i>			
<p>Consider a 3x3 pixel neighbourhood extracted from an $m \times n$ image such that its central pixel is the pixel that is to be super resolved. Assuming a scale factor of 7 for super resolution, a 7x7 subpixel grid may be obtained at this central pixel. Thus, 49 subpixels within the central pixel should be spatially distributed across the pixel. So, this means a value of 0 or 1 is to be assigned to 49-pixel locations.</p> <p>However, the exact subpixels locations which are to be assigned these binary classes (value of 0 or 1) are yet to be ascertained.</p> <p>The 3x3 pixel neighbourhood with 9 pixels as shown in above matrix are from PX1 to PX9.</p> <p>Let the abundance fractions of an end member in it be af1 to af9. Further, let af1 to af9 be 0.3, 0.3, 0.3, 0.7, 0.2, 0.2, 0.2, 0.2.</p>	PX1/af1	PX2/af2	PX3/af3
	PX4/af4	PX5/af5	PX6/af6
	PX7/af7	PX8/af8	PX9/af9
	Abundance fractions of end member in PX1 to PX9 in a 3x3 pixel array is af1 to af9		

The *super resolution pixel* under consideration is PX5. Thus, the number of subpixels of end member that get attracted towards neighboring pixels are $49*0.7=34$.

Subpixels that are attracted to each of the neighbourhood pixel is then calculated as follows,

- (a) Sum of abundance fractions for the end member in all the surrounding neighbourhood pixels PX1 to PX9 (except PX5) is obtained (e.g. $\text{Sum } (T_a) = (af1+af2+af3+af4+af6+af7+af8+af9) = (0.3+0.3+0.3+0.3+0.2+0.2+0.2+0.2) = 2.0$).
- (b) Total number of subpixels of end member in central pixel = $N_s = 49*0.7=34.3=$ say 34 pixels (because only integer values have been considered).
- (c) Number of subpixels of end member in central pixel attracted towards the pixel PX1 = $(N_s*a1)/ T_a = (34*0.3)/2.0=5.1=$ say 5 pixels.
- (d) The abundance fraction values for af1 to af4 is 0.3. Therefore, 5 subpixels each in the pixels PX1 to PX4 can be assumed to be assigned to target.
- (e) Ignore PX5 as it is under super resolution.
- (f) Number of subpixels attracted towards pixel PX6 = $(N_s*af6)/ T_a = (34*0.2)/2.0=3.4=$ say 3 pixels (because only integer values have been considered).
- (g) The abundance fraction values for af6 to af9 is 0.2. Thus, 3 subpixels each in pixel PX6 to PX9 can be assumed to be assigned to target.

5.4.4 Implementation

5.4.4.1 Implementations on Synthetic Data

The super resolution experiments in the case of synthetic data have been implemented as under:

- (a) The synthetic images have been created as explained above corresponding to each of the scale factors. By virtue of the process of creation of these synthetic images, the original images before degradation are available as reference images.
- (b) Super resolution is carried out using Pixel Swap as well as Inverse Euclidean distance algorithm at scale factors of 3,5,7,9, and 11.
- (c) Comparative assessment

5.4.4.2 Implementations on Hyperspectral Data

The process of super resolution in case of hyperspectral data has been implemented as under:

- (a) Implementation using Pixel Swap algorithm.
- (b) Implementation using Inverse Euclidean distance algorithm:
 - Step 1: Compute subpixels attracted to each of the neighbourhood pixel.
 - Step 2: Modelling the Attractive Influence.
 - Step 3: Perform Super resolution.

5.4.4.2 Implementations on Multi - sensor, Multi – resolution, Temporal Urban Data

The process of super resolution in case of LANDSAT-8, SENTINEL 2B AND AVIRIS-NG data has been implemented as under:

- (a) Implementation of Spectral Unmixing – using Linear Mixture Model (LMM) using ENVI-5.2.
- (b) Obtaining Abundance fractions for both Impervious (Road and Roof) and Pervious Surfaces (Vegetation and Soil).
- (c) Utilizing these fractions for implementation of super resolution using Inverse Euclidean distance algorithm (Implementations done in MATLAB):
 - Step 1: Compute subpixels attracted to each of the neighbourhood pixel.
 - Step 2: Modelling the Attractive Influence.
- (d) Perform Super resolution (on a 30x30 pixel subset obtained at same Latitude and Longitude values in the three datasets).

5.5 Results and Discussions

In this chapter, a comparative assessment of random recursive and non - random non recursive super resolution algorithms have been declared. A set of experiments have

been conducted on two different sets of Synthetic and Hyperspectral data using the two approaches of super resolution.

5.5.1 Super Resolution Using Synthetic Data

Four synthetic data have been considered, Synthetic – I (approximating shape of a vehicle), Synthetic – II (approximating shape of a temple), Synthetic - III ((approximating shape of a circle) and Synthetic – IV (approximating shape of an aircraft). In case of Synthetic data, the target information at each pixel is known *a priori*. Therefore, the classification accuracy assessment has been performed using percent correct measure. In addition, the CPU processing time has also been recorded for both the super resolution methods.

The classification accuracy and CPU time for Synthetic data I, II, III, and IV are given in Table 5.3, 5.4, 5.5 and 5.6, respectively. It can be seen from the Table 5.3, that for Synthetic – I data, the classification accuracy in the case of pixel swapping method across various scale factors is as high as 79.76% but remains constant across all the scale factors. Further, although the pixel swapping method takes only 2.81 seconds of CPU time to converge at a scale factor of 3 but thereafter the CPU time increases alarmingly to 28.78 seconds with the increase in scale factor with no increase in classification accuracy. On the other hand, the classification accuracy of 83.17% obtained using the inverse Euclidean distance method is higher than the corresponding value for pixel swapping method at the same scale factor of 3. The CPU time in this case is marginally higher than that of the pixel swapping method. In case of inverse Euclidean distance method, the CPU time in this case does not increase appreciably, with the increase in scale factor. Thus, for this complex target, although pixel swapping algorithm attains a lower accuracy than the inverse Euclidean distance algorithm, the efficiency of pixel swapping algorithm is significantly more in comparison to that of the inverse Euclidean distance algorithm.

It can be seen from the Table 5.4 that for Synthetic – II data, the classification accuracy in the case of pixel swapping method across various scale factors is as high as 81.45%. Further, although the pixel swapping method takes only 2.12 seconds of CPU time to converge at a scale factor of 3 but thereafter the CPU time increases alarmingly to 27.82 seconds with the increase in scale factor with no increase in classification accuracy. On the other hand, the classification accuracy of 86.53% obtained using the inverse Euclidean distance method is higher than the corresponding value for pixel swapping method at the same scale factor of 3. The CPU time in this case is marginally higher than that of the pixel swapping method. However, here also a gradual drop in the classification accuracy with increase in the scale factor has been observed in case of inverse Euclidean distance method. However, the CPU time in this case does not increase appreciably, with the increase in scale factor.

In case of synthetic data III, the values of classification accuracy and CPU time taken at each scale factor are shown in Table 5.5. It can be seen from the table that the classification accuracy in the case of pixel swapping method across various scale factors is as high as 83.88% but remains constant across all the scale factors. This may apparently be due to a fixed value of non-linear parameter a across different scale factors. Further, although the pixel swapping method takes only 1.92 seconds of CPU time to converge at a scale factor of 3 but thereafter the CPU time increases alarmingly to 30.92 seconds with the increase in scale factor with no increase in classification accuracy. On the other hand, the classification accuracy of 86.16%, obtained using the inverse Euclidean distance method is higher than the corresponding value for pixel swapping method at the same scale factor of 3. The CPU time in this case is marginally higher than that of the pixel swapping method. However, a gradual drop in the classification accuracy with increase in the scale factor has been observed in case of inverse Euclidean distance method. However, the CPU

time in this case does not increase appreciably, with the increase in scale factor. In fact, the IED method takes one tenth of the CPU time taken at a scale factor of 11 by the pixel swapping method. Thus, for a target with simple geometry such as a circle, although pixel swapping algorithm attains a higher accuracy than the inverse Euclidean distance algorithm, the efficiency of pixel swapping algorithm is significantly low in comparison to that of the inverse Euclidean distance algorithm.

The classification accuracy and CPU time for synthetic data IV, for both the methods are given in Table 5.6. It can be seen from this table that the accuracy of super resolved target detection using pixel swapping method is significantly lower than that produced from the inverse Euclidean distance method. This demonstrates the superlative performance of the IED algorithm for detecting subpixel targets of complex shapes such as an aircraft, where the pixel swapping method fails miserably. Further, the classification accuracy of the IED method increases with increase in the scale factor. Thus, for detecting shapes of complex targets, a higher scale factor may be suitable.

Moreover, examining the efficiency of the two algorithms in terms of CPU times, it can again be seen that there is a distinct difference between the performance of the two algorithms. The IED algorithm takes significantly lesser CPU time than the other algorithm. Further, the CPU time for the Euclidean distance method remains largely constant across all the scale factors. This demonstrates the effectiveness of the IED algorithm in creation of super resolution maps at any given spatial resolution. The main reason of greater computational efficiency in case of Euclidean distance method is the fact that the pixel swapping method requires a series of iterations before achieving the convergence of randomly allocated subpixels to a target class. In contrast Euclidean distance method does not involve any iteration as the attractive influence experienced by subpixels for each scale factor are stored *ab initio* itself and are simply recalled at the run time for super resolution.

Table 5.3: Classification accuracy for shape approximating vehicle (Synthetic-I)

Scale Factor	Pixel Swapping Method		Inverse Euclidean Distance	
	Classification Accuracy (%)	CPU Time (secs)	Classification Accuracy (%)	CPU Time (secs)
3	79.76	02.81	83.17	4.29
5	79.76	03.01	85.45	4.90
7	79.76	08.13	85.66	5.10
9	79.76	19.20	85.66	7.50
11	79.76	28.78	85.66	7.83

Table 5.4: Classification accuracy for shape approximating temple (Synthetic-II)

Scale Factor	Pixel Swapping Method		Inverse Euclidean Distance	
	Classification Accuracy (%)	CPU Time (secs)	Classification Accuracy (%)	CPU Time (secs)
3	81.45	02.12	86.53	6.20
5	81.45	05.19	87.71	6.45
7	81.45	12.89	87.41	7.20
9	81.45	20.50	86.58	7.38
11	81.45	27.82	86.58	8.04

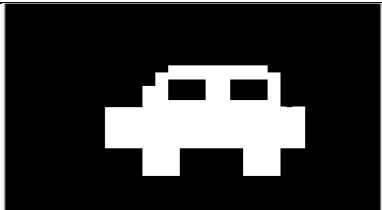

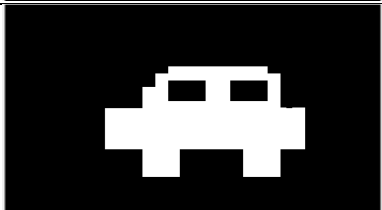
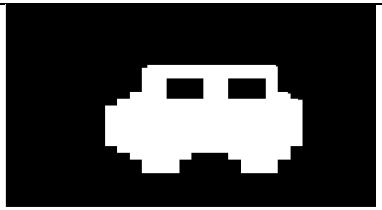
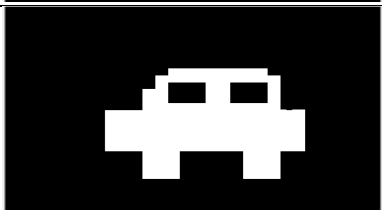

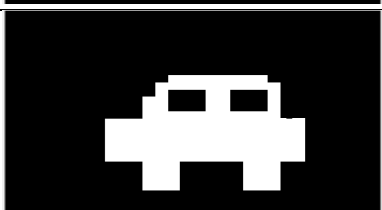

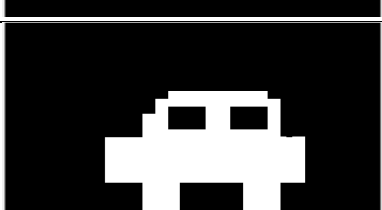

Table 5.5: Classification accuracy for shape approximating circle (Synthetic-III)

Scale Factor	Pixel Swapping Method		Inverse Euclidean Distance	
	Classification Accuracy (%)	CPU Time (secs)	Classification Accuracy (%)	CPU Time (secs)
3	83.88	01.92	86.16	02.28
5	83.88	07.15	77.03	02.67
7	83.88	13.15	75.01	02.78
9	83.88	21.00	73.67	03.10
11	83.88	30.92	73.11	03.37

Table 5.6: Classification accuracy for shape approximating aircraft (Synthetic-IV)

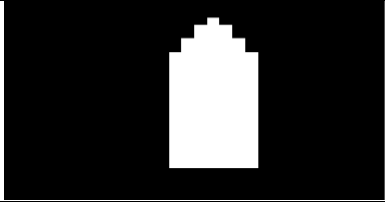
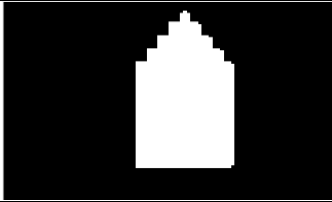
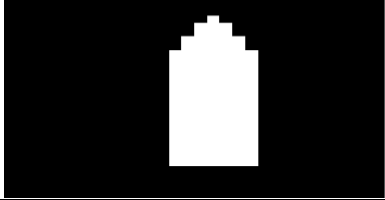
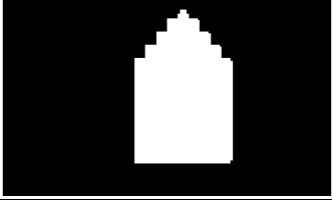
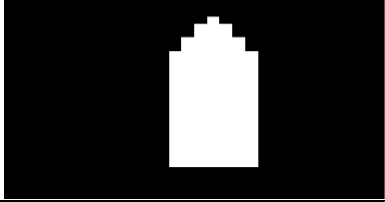
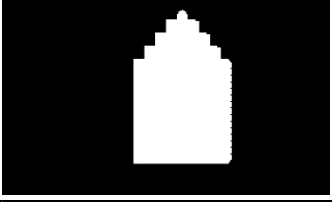
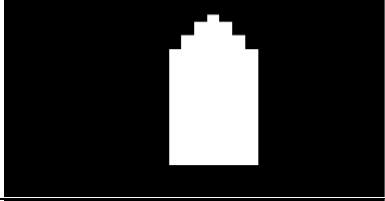
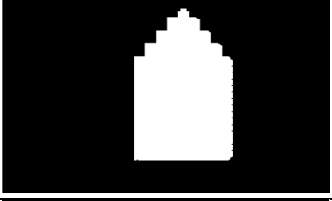
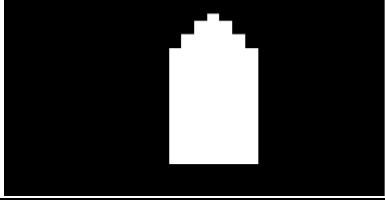
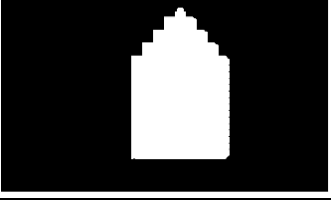
Scale Factor	Pixel Swapping Method		Inverse Euclidean Distance	
	Classification Accuracy (%)	CPU Time (secs)	Classification Accuracy (%)	CPU Time (secs)
3	38.05	01.95	75.94	09.25
5	38.05	07.07	81.85	09.25
7	38.05	13.00	81.65	09.28
9	38.05	20.98	81.98	09.54
11	38.05	30.81	82.22	09.59

The Super resolved images generated from Synthetic data – I, II, III and IV are shown in Figure 5.7, 5.8, 5.9 and 5.10, respectively. It can be seen from the super resolved images for Synthetic –I that the shape of the recovered vehicle is apparently constant for pixel swapping method across all the scale factors whereas a continuous improvement in the shape of the circle by varying scale factor 3 to 7 can be seen for the Euclidean distance method. For higher scale factors, the performance of the IED algorithm, however, deteriorates. A possible reason for this may be the use of a linear parameter for calculation.

Scale factors	Pixel Swap	IED
3x3		
5x5		
7x7		
9x9		
11x11		

(a)
(b)

Figure 5.7: Super resolution in case of Synthetic-I data containing targets approximating the shape a vehicle

Scale factors	Pixel Swap	IED
3x3		
5x5		
7x7		
9x9		
11x11		

(a)

(b)

Figure 5.8: Super resolution in case of synthetic-II data containing targets approximating the shape a temple

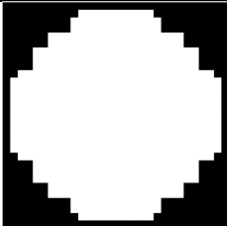
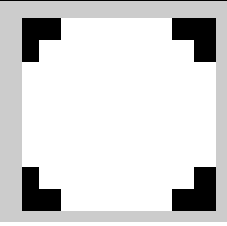
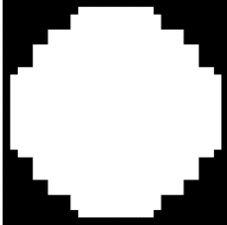
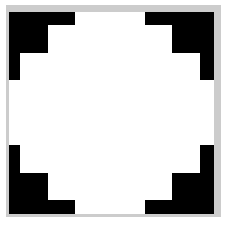
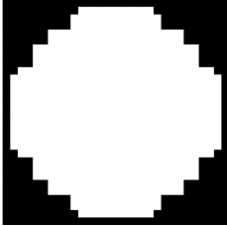
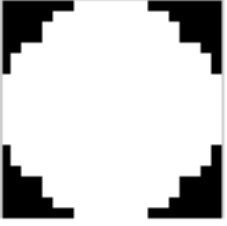
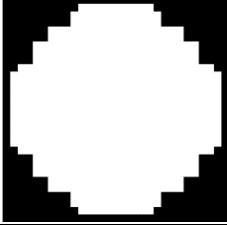
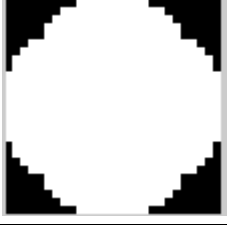
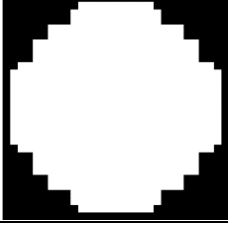
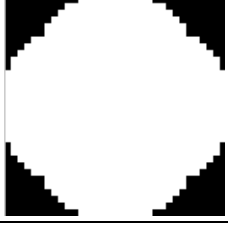
Scale factors	Pixel Swapping Method	IED
3x3		
5x5		
7x7		
9x9		
11x11		

Figure 5.9: Super resolution in case of synthetic-III data containing targets approximating the shape a circle


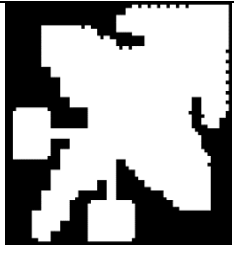
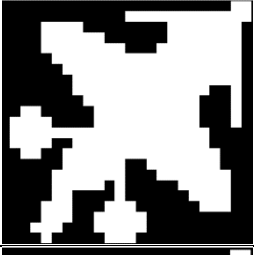

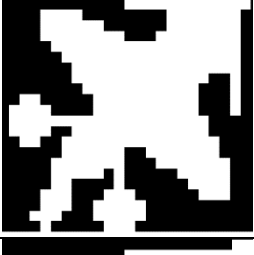

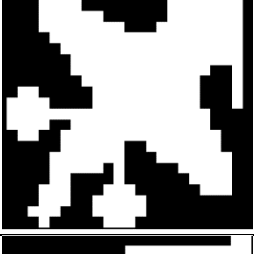

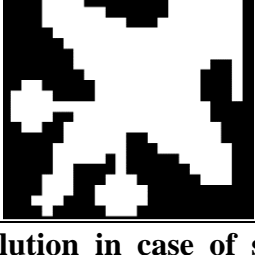

Scale factors	Pixel Swapping Method	Inverse Euclidean Distance Method
3x3		
5x5		
7x7		
9x9		
11x11		

Figure 5.10: Super resolution in case of synthetic-IV data containing targets approximating the shape of an aircraft

The super resolution images for synthetic data II- IV, as obtained from the two algorithms, are shown in Figure 5.8- Figure 5.10. Focusing on shape of the target (let us take case of the aircraft), these figures depict almost constant performance of pixel swapping method across all the scale factors thereby signifying that scale factor does not have any impact on refining the shape of the target in this method. In contrast, in case of

the IED method, the shape of the target improves marginally over all the scale factors, which signifies the role of scale factor in this method. Further, the CPU time remains constant over all the scale factors. This clearly demonstrates the effectiveness of the IED algorithm over the pixel swapping method.

It may be observed from these results that the pixel swapping method involves random initial allocation of subpixels and correct target class clusters are obtained through a series of iterations. Since these iterations may also result in translation or rotation of several pixels away from the target class, it also has the chances of lowering the classification accuracy.

5.5.2 Super Resolution Using Hyperspectral (*AVIRIS*) Data

The earlier experiments on synthetic data highlighted the major limitations of the random – recursive (pixel swapping) method as,

- (i) It required longer processing time,
- (ii) The classification accuracy did not improve beyond a certain point
- (iii) Its performance depended on selection of an appropriate value of the non-linear parameter for estimation of attractiveness function and could super resolve only the simple shapes.

Despite these limitations, the pixel swapping method has been implemented on both the *AVIRIS* –I and *AVIRIS*- II datasets. The abundance fractions of each pixel in these images have been obtained using the unsupervised spectral unmixing method as discussed earlier. The results of the pixel swapping method across different scale factors are as shown in Figure 5.11. As is evident from the pictorial views, pixel swapping method fails completely for both the *AVIRIS* –I and *AVIRIS*- II data. The reason for this failure can be many. The main reason can be attributed to the fact that due the iterative nature of super resolution procedure, the method did not converge as the abundance fractions found were non-integer

values. Besides, it was also difficult to predict an appropriate value for the non-linear parameter for calculation of the attractiveness function.

The inverse Euclidean distance method produces good results as shown in Figure 5.12. The figure shows super resolution at all the super resolution scale factors *i.e.* 3, 5, 7, 9, 11. These super resolved images can be compared with the input images. Visual examination of these images suggests that the performance of the super resolution is better at lower super resolution scale factors as compared to those at higher scale factors. The reason for success of this method lies in the fact that it does not involve any iterative convergence and is based on the stored rankings of attractiveness values of the super resolved subpixels. Due to non-availability of reference data, the results have not been evaluated quantitatively. The CPU time taken by the IED method was however found to increase with the increase in scale of the super resolution. On the other hand, the CPU time taken by the Atkinson's Pixel swapping method was not only higher for both the data sets *i.e.* synthetic as well as *AVIRIS* data set, but it also failed completely for the *AVIRIS* data set.

The IED method has also been extended to include more than one abundance fraction. This has been accomplished using three fractions corresponding to three end members including the target. Three binary images corresponding to different abundance fractions have been generated and then mapped together using three separate colours *i.e.* Red, Green and Blue, as shown in Figure 5.12. The RGB image highlights the subpixel targets more accurately than shown in grey shade images. It has also been noticed that if the abundance fractions are selected carefully, then the RGB combination can highlight different parts of the target under different illumination conditions. Thus, super resolved binary images not only makes detection of subpixel target possible but also enhances the full pixel targets detected. Further it also facilitates the discrimination, classification,

identification, and quantification of the targets which otherwise may not be possible using only the spectral properties.


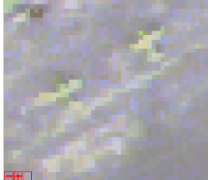

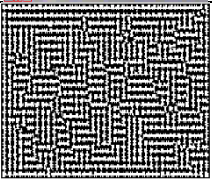
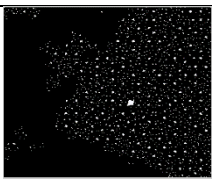
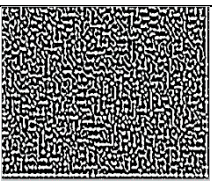
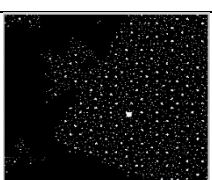
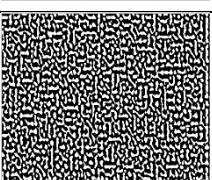
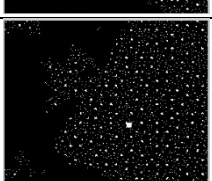

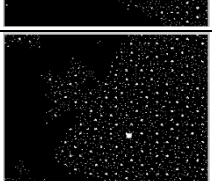
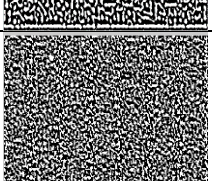
Image	Two Planes	Three Planes
Input Image		
Image at scale factor 3		
Image at scale factor 5		
Image at scale factor 7		
Image at scale factor 9		
Image at scale factor 11		

Figure 5.11: Super resolution of AVIRIS data using Atkinson’s pixel swapping method



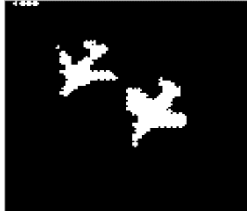

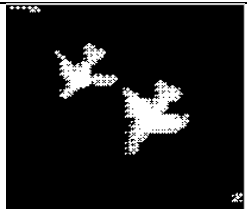
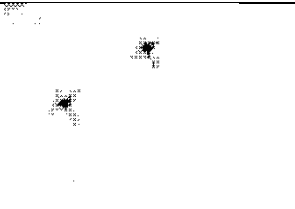
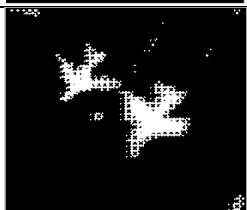
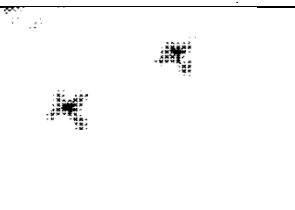
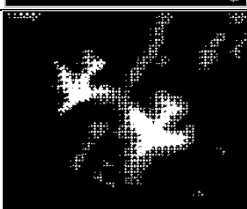
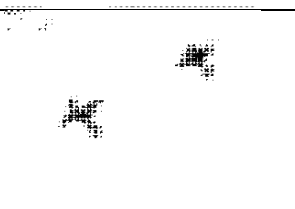
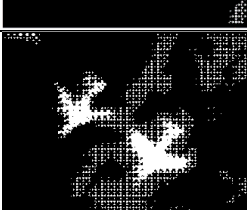
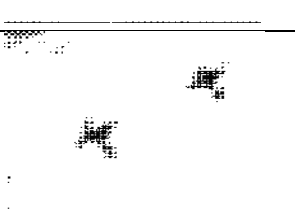
Image	40x40 Binary Image with Two Aircrafts	40x40 Binary image with Three Aircrafts
Input Image		
Image at scale factor 3		
Image at scale factor 5		
Image at scale factor 7		
Image at scale factor 9		
Image at scale factor 11		

Figure 5.12: Super resolution of *AVIRIS* data using inverse Euclidean distance-based method

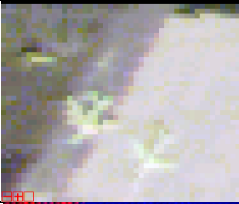

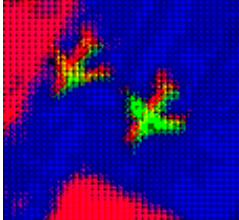
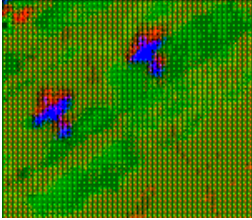
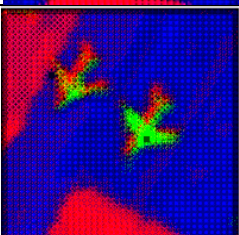
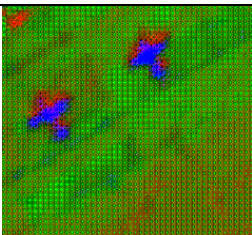
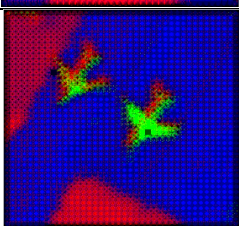
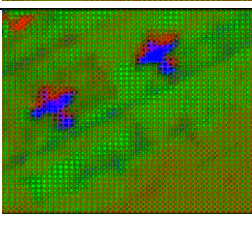
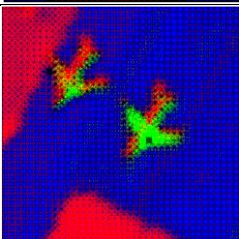
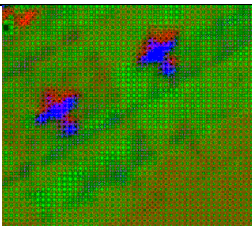
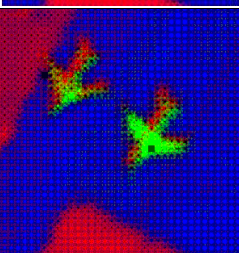
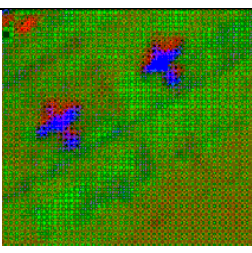
Image	40x40 RGB Image with Two Aircrafts	40x40 RGB Image with Three Aircrafts
Input Image		
Image at scale factor 3		
Image at scale factor 5		
Image at scale factor 7		
Image at scale factor 9		
Image at scale factor 11		

Figure 5.13: RGB implementation of inverse Euclidean distance based super-resolved *AVIRIS* data

5.5.3 Preliminary results on Multi-Sensor, Multi-Resolution, Temporal Urban dataset

The results of implementation of non – random non – recursive algorithm (IED) on Multi-Sensor, Multi-Resolution, Temporal Urban dataset (LANDSAT – 8, SENTINEL – 2B and AVIRIS – NG are shown in Figures 5.14-5.17.

Figure 5.14 shows super resolution at different scale factors of LANDSAT -8 data. The left column of the figure shows the unmixed image (Impervious and Pervious) of UDAIPUR region. The middle column shows 30x30 zoomed pixels of the selected subset which has been used for super resolution. The right column shows the super resolved image of the Impervious surface (in black).

Figure 5.15 shows super resolution at different scale factors of SENTINEL – 2B data. The left column of the figure shows the unmixed image (Impervious and Pervious) of UDAIPUR region. The middle column shows 30x30 zoomed pixels of the selected subset which has been used for super resolution. The right column shows the super resolved image of the Impervious surface (in black).

Similarly, Figure 5.16 shows the results for AVIRIS – NG data. The left column of the figure shows the unmixed image (Impervious and Pervious) of UDAIPUR region. The middle column shows 30x30 zoomed pixels of the selected subset which has been used for super resolution. The right column shows the super resolved image of the Impervious surface (in black).

Figure 5.17 shows a comparison of Super Resolution in Different Data Sets at different resolutions. Further, Table 5.7 gives the computation time in seconds using IED on Multi-sensor, Multi- resolution Temporal Urban data.


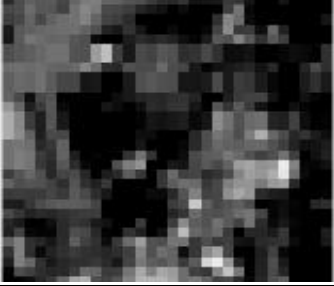
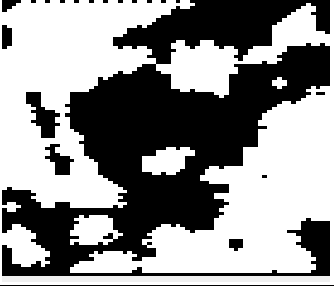

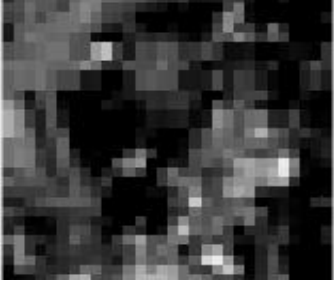
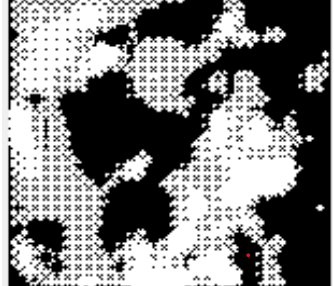

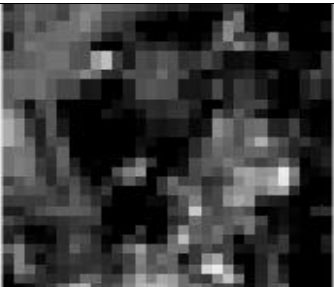
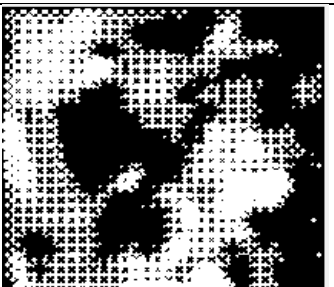
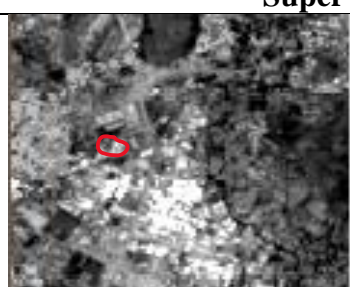
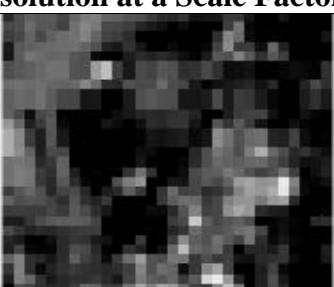
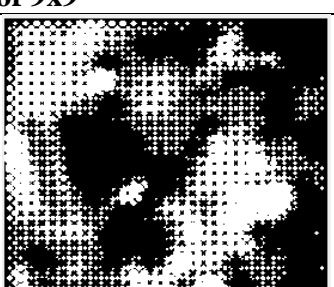
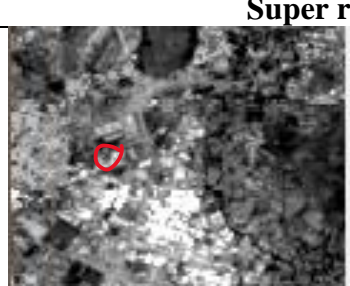
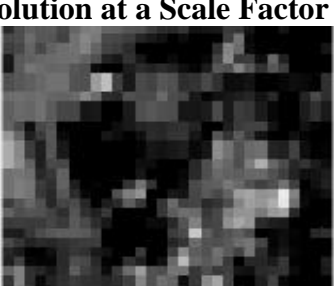
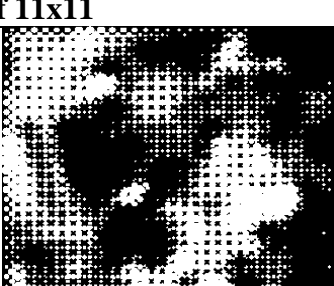
Super resolution at a Scale Factor of 3x3		
Unmixing Image	Zoomed image of circled area (in red)	Super resolved Image
		
Super resolution at a Scale Factor of 5x5		
		
Super resolution at a Scale Factor of 7x7		
		
Super resolution at a Scale Factor of 9x9		
		
Super resolution at a Scale Factor of 11x11		
		

Figure 5.14: Super Resolution in Landsat – 8


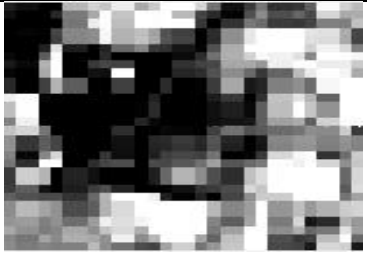


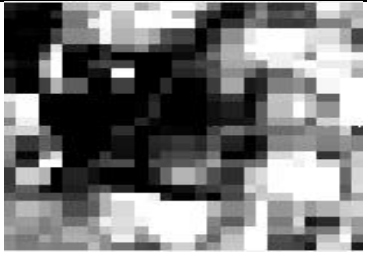


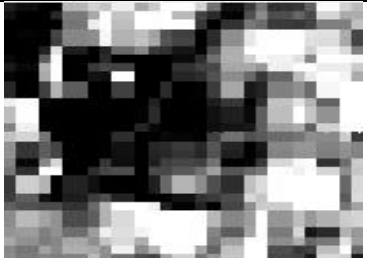


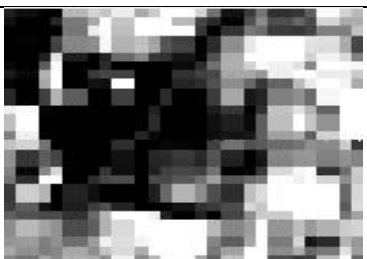
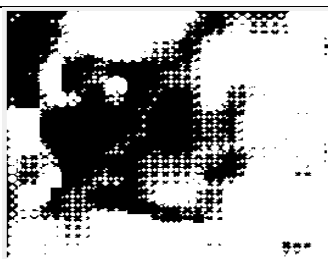



Super resolution at a Scale Factor of 3x3		
Unmixing Image	Zoomed image of circled area (in red)	Super resolved Image
		
Super resolution at a Scale Factor of 5x5		
		
Super resolution at a Scale Factor of 7x7		
		
Super resolution at a Scale Factor of 9x9		
		
Super resolution at a Scale Factor of 11x11		
		

Figure 5.15: Super Resolution in SENTINEL -2B


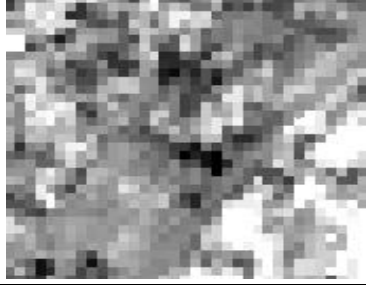


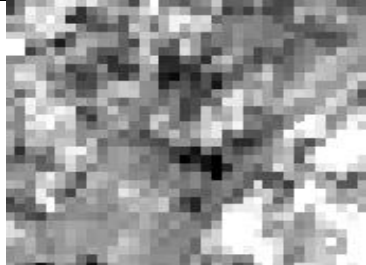


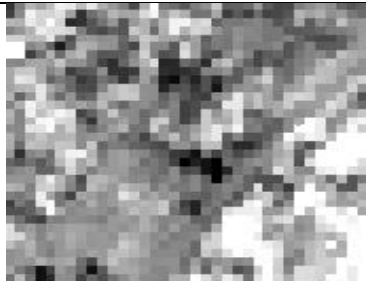
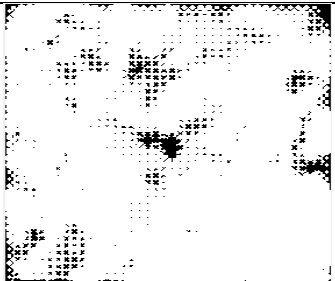

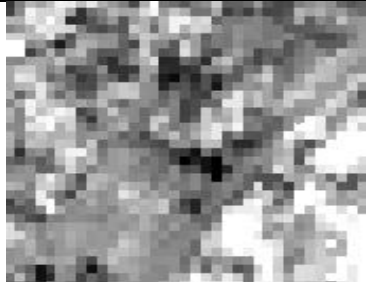
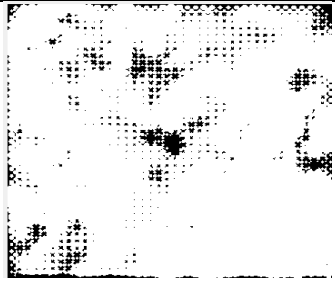

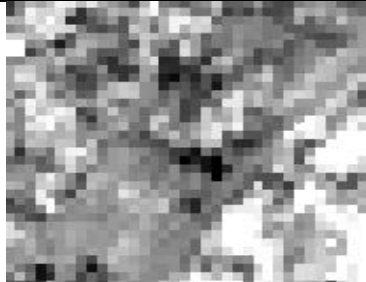
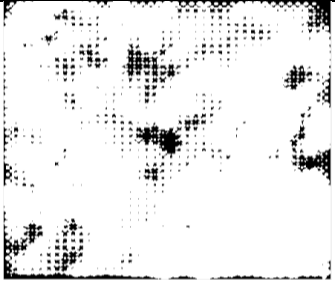
Super resolution at a Scale Factor of 3x3		
Unmixing Image	Zoomed image of circled area (in red)	Super resolved Image
		
Super resolution at a Scale Factor of 5x5		
		
Super resolution at a Scale Factor of 7x7		
		
Super resolution at a Scale Factor of 9x9		
		
Super resolution at a Scale Factor of 11x11		
		

Figure 5.16: Super Resolution in AVIRIS – NG




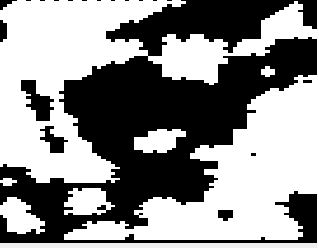

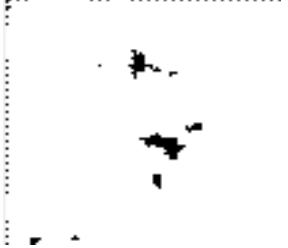
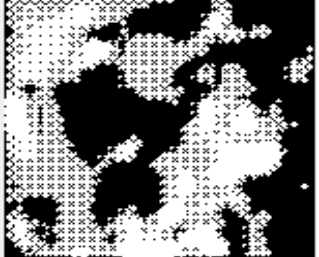




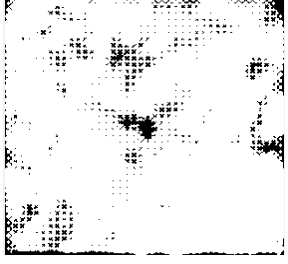
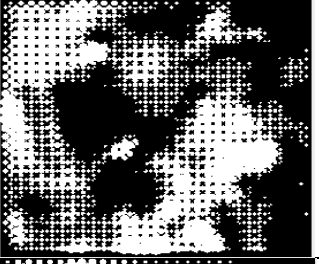

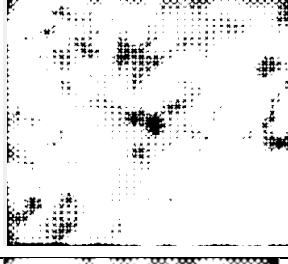
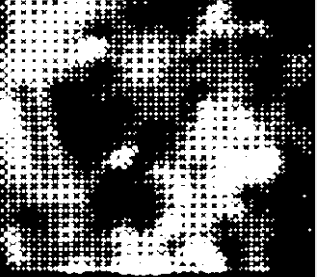


DATA	LANDSAT - 8 @ 30 METERS	SENTINEL - 2B @ 10 METERS	AVIRIS - NG @ 8.1 METERS
Unmixing Image			
Scale Factor of 3x3			
Scale Factor of 5x5			
Scale Factor of 7x7			
Scale Factor of 9x9			
Scale Factor of 11x11			

Figure 5.17: Comparison of Super Resolution in Different Data Sets of Different Resolutions

Table 5.7: Computation time using IED on Multi-sensor, Multi- resolution Temporal Urban data

COMPUTATION TIME (in seconds)			
CPU Time	LANDSAT - 8	SENTINEL – 2B	AVIRIS - NG
Scale factor @ 3x3	5.54	3.09	4.47
Scale factor @ 5x5	6.98	4.68	6.78
Scale factor @ 7x7	6.06	4.46	6.98
Scale factor @ 9x9	7.12	5.06	6.89
Scale factor @ 11x11	9.26	7.61	12.28

The following may be observed from the results obtained:

In case of Sentinel data, the super resolution using IED appears to perform better in comparison to AVIRIS data, with clear separation of impervious and pervious surfaces and therefore may be considered suitable for identification and area estimation in case of urban land cover mapping. The algorithm also gives useful results in case of 30-meter LANDSAT data after super resolution. However, since the AVIRIS data is already at 8.1-meter resolution, the enhancement of this fine resolution data is not giving results as obtained in case of LANDSAT and SENTINEL.

But in case of AVIRIS data, it may be observed that as the scale factor increases from 3 to 11, the clarity about separation of impervious and pervious surfaces is more and therefore a higher scale factor may prove to be useful of extraction of impervious surfaces in case of AVIRIS data.

The computation time shows a marginal increase as the scale factor increases from 3 to 11 across all the three data sets, however, the computation time is insignificant.

In this work, however due to lack of ground truth data, assessment of accuracy of super resolution could not be carried out.

5.6 Conclusions

Many a times, a small target occupies a few pixels fully and simultaneously occupies surrounding pixels only partially. Thus, the surrounding pixels present a case of

mixed pixel and many target detection algorithms which are capable of detecting only full pixels fail to recover the subpixel components. Recovery of these subpixel components along with full pixels, however, may significantly aid super resolution and thereby enhance the identification and recognition of target. Though spectral unmixing algorithms such as Linear Mixture Model (LMM) provide abundance fractions of end members within the pixel, but these do not provide their spatial distribution. Super resolution aids in optimizing the spatial distribution based on the available abundance fractions.

However, most of the super resolution algorithms follow random recursive approaches which have severe limitations of computational complexity and convergence. Due to difference in the background in which a full pixel and a subpixel target may be embedded, the algorithms developed for detection of these targets treat the two cases separately. However, in practice, most of the targets occupy some pixels fully and several others only partially. Therefore, there is a requirement of integrating both the full pixel and subpixel target detection. A two-stage procedure has been discussed here. The first stage involves detection of full pixel targets using any of the full pixel target detection method. In the second stage, spectral unmixing which results in both the endmember spectra as well as the abundance fractions has been considered. While the endmember spectrum has usually been exploited for detection and classification, abundance fractions have not been fully exploited as the spatial distribution of the endmembers at subpixel level is not known.

In this work, a random – recursive (pixel swap) method has been compared with a non-random and non-recursive (Inverse Euclidean Distance) approach to achieve super resolution for target identification. The results in Synthetic and hyperspectral data have been compared. A major advantage of non-random non-recursive (Inverse Euclidean distance) method is its comparatively lower CPU time and higher accuracy. The efficiency of the algorithm is as high as 87.71% in the case of synthetic images across all scale factors

and it also aids the recognition of targets in real hyperspectral data. The performance is also found to be significantly better than random-recursive method for detecting targets of complex shapes in the synthetic dataset.

Further, the CPU time for super resolution using random-recursive (pixel swapping) method of a 30x30 pixels synthetic image at a scale factor of 11 was found to be 10 times higher than that for the non-random non recursive (inverse Euclidean distance) method. The non-random non recursive (inverse Euclidean distance) method was also found to perform equally well in detecting targets in hyperspectral data. In addition, the results of implementation of IED on Multi – sensor, Multi – resolution Temporal Urban datasets suggests that non-random non-recursive based super resolution mapping may be useful in more accurate mapping of impervious surfaces in urban datasets. Thus, it may be concluded that non-random non-recursive based super resolution mapping of subpixel targets performs better than the random recursive methods and not only aid in subpixel target detection but also facilitate its correct discrimination, classification, identification, and quantification.

Chapter 6

Summary, Conclusions, Contributions and Future Work

6.1 General

The research presented in this thesis addresses the issues and problems associated with super resolution which in turn is expected to aid detection, identification and enhancement of full pixels, sub pixel and mixed pixel targets in hyperspectral data. Various combinations of data sets such as synthetic and real hyperspectral have been explored to understand problems associated with Super resolution and target detection. The study emphasizes subpixel target enhancement using super resolution for aiding detection of full pixel targets. The work has been done in line with the research gaps identified after a detailed literature survey in respect of super resolution technique and associated problems and limitations.

6.2 Objectives and Methodology

Chapter 1 presents an introduction that outlines the problem of target detection, problems and issues associated with super resolution, research gaps and objectives. An insight into various issues that need to be dealt while performing target detection as well as its utilization in various remote sensing applications have been covered. The problem of mixed pixels, its impact on target detection and possibilities to address the issues using spectral unmixing is also addressed.

Chapter 2 through Chapter 5 presents the work done under each of the objectives. All the objectives have been broken into two - three tasks based on the problems sought to be addressed. The problem statements, experimental datasets, methodology and step by step explanation of tasks, discussion of results and brief conclusions corresponding to each objective has been covered under respective chapter.

Chapter 2 presents an investigation of the various existing dimensionality reduction (DR) algorithms with a view to achieve maximum possible dimensionality reduction while ensuring minimal or no loss of the target data. Various combinations of dimensionality reduction algorithms (ICA, PCA and MNF) and target detection algorithms (SAM, ACE, MF, CEM, MTMF, NED, TCIMF, SID and OSP) have been studied step by step, with a view to achieve maximum possible dimensionality reduction while ensuring minimal or no loss of the target data.

In Chapter 3, the efficient characterization of target and background subspaces for full pixel and sub pixel target detection have been carried out. The tasks presented under this objective include detection of low probability full pixel / subpixel targets with known spectral signatures, detection of mixed pixel targets using background and target subspaces, analysis of the impact of various combinations of background subspaces on full pixel and subpixel target detection and a study of the impact of illumination conditions on the detection of targets. To establish the role of background types and subspaces in accurate detection of full pixel and subpixel targets, a study of detection of full pixel and subpixel targets has been performed using different background subspaces, varying background types and varying illumination conditions *etc.* The target detection algorithms Matched Filter (MF), Orthogonal subspace projection (OSP), Adaptive coherence estimator (ACE) and Target constrained interference minimized filter (TCIMF) have been evaluated to analyze the results of detection by altering the parameters such as background types, subspaces and illumination conditions.

To handle the problems of mixed pixels and extraction of end members, spectral unmixing techniques have been studied and implemented in Chapter 4. Also, the extraction of end members has been studied using another approach *i.e.* Spectral index. The tasks performed under this study include end member extraction and abundance estimation using

spectral unmixing, evaluating spectral indices for end member identification. In case of spectral unmixing for end member extraction, to estimate the total number of end members present in the image with a pure / unique spectrum, a few selected end member extraction algorithms (ICA-EEA, ATGP, N-Findr and VCA) have been evaluated and a constrained least squares algorithm using the recovered endmember spectra has been utilized to generate the abundance maps. For the identification and extraction of different types of surfaces present in the image using spectral indices, the spectral information for impervious (primarily man-made) and pervious (primarily natural) surfaces has been analyzed. This study on end member extraction using spectral indices has been carried using AVIRIS-NG hyperspectral data to find the optimum bands for forming the band ratios and to identify the impervious and pervious surfaces using spectral band ratios.

Though it has been observed that spectral unmixing, provides the abundance fractions of each end members within the pixels, the spatial distribution of these end members within the subpixels remains unknown. To overcome this limitation, a random recursive and non- random non-recursive approach for super resolution has been compared in Chapter 5. To identify the spatial distribution, super resolution has been carried out using two different sets of approaches, a non-random non-recursive based approach, and a random recursive based approach. The task here is to assess the comparative performance of non-random non-recursive super resolution algorithms in addressing the problem of allocating the subpixels of a particular class by performing a comparison with random recursive super resolution algorithm using both synthetic as well as real hyperspectral data. One random recursive (Pixel swap) super resolution method and one non-random non-recursive (Inverse Euclidean distance) super resolution method reported in the literature have been considered for analysis of performance between the two types and their results have been discussed.

6.3 Conclusions

From chapter 2, it may be concluded that in the case of full pixel targets, both dimensionality reduction and target detection result in the loss of target information, however, there is a greater loss of target information in the case when dimensionality reduction precedes target detection in comparison to a case where target detection is applied without dimensionality reduction. Also, from this chapter, it may be concluded that background characterization appears to aid in improvement of full pixel target detection. In the case of subpixel target detection, however, there appears to be loss of subpixel target information in the case where detection alone is performed in comparison to a case where dimensionality reduction precedes target detection.

From Chapter 3, in case of detection using target and background subspaces, it may be concluded that for any given algorithm, if the algorithm is performing well for detection of target pixels, the different background subspaces appear to influence the results less. Yet, in some cases, a marginal improvement in true positives may be observed. Therefore, the target and background separation continue to be a challenge and affects the target detection. Further, with MF, the number of detected target pixels are higher and constant for all background subspaces, with lesser number of false positives. TCIMF also shows better results for detection of target pixels than OSP and ACE and generates lesser false positives than these. OSP performs better in case of Mixed background subspace as compared to cases where subset of background subspaces is selected. Also, for any given background subspace, if the algorithm performs well, values for false positives and false negatives are also less. Thus, it appears that target and background subspaces aid target detection only marginally. But MF and TCIMF appear to aid the detection better in comparison to OSP and ACE. Also, based on target condition (full illumination or shade), it is reinforced that the targets that are placed under open sky are detected well as compared

to those placed under trees and their shadow. Lastly, after assessing the impact of different types of backgrounds, it may be concluded that when target spectra match(es) the background spectra, it adversely affects the detection.

In Chapter 4, the results of endmember extraction and abundance estimation using spectral unmixing indicate that ICA-EEA and Nfindr perform best while recovering the image end members including the target spectra, followed by ATGP, while PPI performed poorly in this case. Error was found to be least in ICA-EEA and ATGP in comparison to NFindr and PPI. Evaluation of spectral indices based approach for end member identification, indicate that this approach which is essentially based upon identification of significant wavelengths related to a particular end member may be more suitable in extraction of impervious (roads and roofs) surfaces. The results indicate upto a maximum of 96.66% accuracy using spectral indices based approach. Further, spectral indices based approach appear to suggest that appropriate indices evolved using SWIR (2194 nm) and NIR (962 nm) may be most suitable in detection of impervious surfaces (roads and roofs).

From Chapter 5, it may be concluded that the computation time is lesser, and accuracy of detection is higher with non-random non-recursive super resolution approach and thus may be a better approach in development of super resolution algorithms. Further, the CPU time for super resolution using random-recursive (pixel swapping) method of a 30x30 pixels synthetic image at a scale factor of 11 was found to be 10 times higher than that for the non-random non recursive (inverse Euclidean distance) method. The non-random non recursive (inverse Euclidean distance) method was also found to perform equally well in detecting targets in hyperspectral data.

6.4 Major contributions

The outcome of this research by way of various experiments discussed in this thesis lead to major research contributions which are summarised as under -

(a) In the case of for full pixel target detection, both DR and TD contribute to the loss of target information, however, there is a definite greater loss of target information in case DR precedes TD. This contribution is helpful in cases where it is already known that target pixels in an image may be rare.

In the case of subpixel target detection however, there appears to be a greater loss of subpixel target information in case where TD alone is performed as compared to case where DR precedes TD.

(b) The number of target pixels in any target detection task are very limited, Background characterization appears to significantly improve detection of targets. Further, the illumination, background type, the target detection algorithm, and the background subspace, all have an impact on both subpixel and full pixel target detection. It is reinforced that illumination has a favorable impact on detection of targets as the targets kept under open sky / sunlight are always much easier to detect. The study of background type indicates that the spectral contrast between background and the target aids target detection. It was evident that spectral contrast between the background subspaces and the target determines the ease in target detection.

(c) Chapter 4 compares the endmember extraction algorithms chosen from literature. The results from algorithms that are non-parameterized and do not require any initialization using target spectra are seen to be performing better than algorithms which are parameterized and require an initialization vector and are the former ones are therefore recommended for the purpose of end member extraction.

(d) Comparative assessment of non-random non-recursive super resolution algorithm with a random-recursive suggest that non-random non-recursive based super resolution performs better and has much lesser computation time.

6.5 Limitations

In Chapter 2, a study on loss of target information both in full pixel and subpixel targets during the DR process has been studied. To carry out this study there was a requirement of ground truth data with subpixel abundance fractions. This was available only in the SHARE 2012 data provided by RIT, USA. This data was limited in terms of targets available with subpixel abundance fractions (only one such data was available), therefore the conclusions drawn need to be supported by carrying out similar research experiments with more data.

It has been reported in literature that target detection requires both spatial and spectral properties of the data to be exploited and utilized. Since the retrieved spectra, in case of mixed pixel targets, is a combination of both the target as well as rest of the end members present in the pixel, it is of significance to consider the spectra of non-target end members as background. Also, in the case of mixed pixel targets, the interference is more from the non – target end members present within the pixel also known as background components, which may further affect accurate detection of subpixel targets. Accordingly target and background subspaces have been studied in Chapter 2 to enable better results of detection, however, the results could not substantiate any major advantage in detection results. This may be due to the limitations of underlying algorithms used. This needs to be further explored as it is logical to expect that background characterization must result in significant improvement in subpixel target detection.

In Chapter 4, end member extraction has been performed using two different approaches, spectral unmixing and spectral indices. Individually both the approaches and different techniques for implementations have been studied and experimented, however a comparative analysis may be further performed to analyze which approach suits better for

end member extraction. Also, a fusion of both approaches may be studied to further enhance the results of end member extraction.

In Chapter 5, one random recursive and one non-random non-recursive techniques for super resolution have been studied. From the results, IED was observed to be performing well in both synthetic and hyperspectral datasets. However, a few things need to be explored further. First at what scale factor most optimal results can be obtained because the algorithm is based on a linear parameter in the distance based attractive function and it is likely that the performance will deteriorate at certain higher scale factors. Further, a non-random non-recursive based super resolution mapping was also implemented on a Multi – sensor, Multi – resolution, Temporal Urban dataset, however, a detailed accuracy assessment could not be done for the want of ground truth data with abundance fractions. Third, IED is basically a binary classifier and although three different binary images have been generated and mapped using RGB in one of the experiments, however, the algorithm needs to be improved to handle multi class problems.

6.6 Future Work

Based on the limitations discussed above, it is considered that following works be undertaken in future to understand the problem of target detection and enhancement.

Lack of availability of data has been one of the major limitations of this work. It would be extremely useful if the non-random non recursive algorithm and random recursive algorithm presented in this thesis is compared using with complex land use land cover data of any Indian city.

From the study of DR linked TD algorithms with a view to ensure minimal loss of target information, it has been observed that when DR precedes TD for detection of full pixel targets, there is a loss of target information in comparison to the case when TD is

performed without DR. From this, it may appear that DR should not be performed in such cases, however, it is known that the huge volume of data associated with hyperspectral data adds to the complexity in processing of such images. Therefore, the work may be done to find an optimal solution to perform DR linked TD while ensuring that the target pixels are not lost.

In the case of detection of subpixel targets, an approach that may aid in detection using target and background subspaces has been investigated. From the results it has been observed that the separation of target and background subspaces only aid the detection process marginally. A better way needs to be evolved to provide target and background subspace separation and may be studied in future for efficient detection of subpixel and full pixel targets.

Non-random non-recursive based approaches have been studied and from the results it is concluded that these approaches aid the efficient detection and enhancement of target in hyperspectral data. New algorithms to perform super resolution mapping based on non-random non-recursive approach need to be investigated and implemented on hyperspectral data. Besides, it also needs to be investigated that at what scale factors non-recursive approaches may fail to map inherent non-linearity present in the mixed pixels.

References:

- Aasen H., Honkavaara E., Lucieer A., Zarco-Tejada P.J. (2018), “Quantitative remote sensing at ultra-high resolution with UAV spectroscopy: A review of sensor technology, measurement procedures, and data correction workflows”. *Remote Sens*; 10:1091. doi: 10.3390/rs10071091.
- Adão T., Hruška J., Pádua L., Bessa J., Peres E., Morais R., Sousa J.J (2017). “Hyperspectral imaging: A review on UAV-based sensors, data processing and applications for agriculture and forestry”. *Remote Sens.*; 9:1110. doi: 10.3390/rs9111110.
- Agarwal, A., El-Ghazawi, T., El-Askary, H., & Le-Moigne, J. (2007). “Efficient hierarchical-PCA dimension reduction for hyperspectral imagery.” *IEEE International Symposium on Signal Processing and Information Technology* :353-356
- Altmann, Y., Halimi, A., Dobigeon, N. and Tourneret, J.Y. (2012) “Supervised nonlinear spectral unmixing using a post-nonlinear mixing model for hyperspectral imagery” *IEEE Transactions on Image Processing*, 21(6):3017–3025
- Arora Manoj K. and Tiwari K.C. (2013), “Subpixel Target Enhancement in Hyperspectral Images,” *Defence Science Journal*, Vol. 63, No. 1, pp. 63-68
- Atkinson, P.M. (1997), “Mapping sub-pixel boundaries from remotely sensed images”. In *Innovations in GIS 4*; Kemp, Z., Ed.; Taylor and Francis: London, UK; pp. 166–180.
- Atkinson P. M. (2004), “Super resolution land cover classification using the two-point histogram,” *Geoenv. IV—Geostatistics for Environ. Appl. Proc.*, vol. 13, pp. 15–28.
- Atkinson P. M. (2005), “Sub-pixel target mapping from soft-classified, remotely sensed imagery,” *Photogramm. Eng. RemoteSens.*, vol.71, no. 7, pp. 839–846.
- Atkinson P.M. (2013), “Downscaling in remote sensing”. *Int. J. Appl. Earth Obs. Geoinf.*, 22, 106–114.
- Bajorski, P., Ientilucci, E. J., & Schott, J. R. (2004). Comparison of basis-vector selection methods for target and background subspaces as applied to subpixel target detection. In *Algorithms and technologies for multispectral, hyperspectral, and ultraspectral imagery X* (Vol. 5425, pp. 97-108). International Society for Optics and Photonics
- Bakken, S., Orlandic, M., & Johansen, T. A. (2019). The effect of dimensionality reduction on signature-based target detection for hyperspectral remote sensing. In *CubeSats and SmallSats for Remote Sensing III* (Vol. 11131, p. 111310L). International Society for Optics and Photonics.
- Bhaskaran S. and Datt B. (2000), “Applications of hyperspectral remote sensing in urban regions,” *ACRS*.
- Benediktsson J.A., Pesaresi M., and Arnason K. (2003), “Classification and feature extraction for remote sensing images from urban areas based on morphological

- transformations,” *IEEE Transaction on Geoscience and Remote Sensing*, vol. 41(9), pp. 1940-1949, 2003.
- Bezdek J. C., Ehrlich R., and Full W. (1984), “FCM: The fuzzy c-means clustering algorithm,” *Comput. Geosci.*, vol.10, no.2–3, pp.191–203.
- Binol, H., Ochilov, S., Alam, M.A., and Bal, A. (2016) “Target oriented dimensionality reduction of hyperspectral data by Kernel-Fukunaga–Koontz Transform.” Elsevier Ltd, <http://dx.doi.org/10.1016/j.optlaseng.2016.03.009> 1016-03 0090143-8166
- Bioucas-Dias JM, Plaza A, Camps-Valls G, Scheunders P, Nasrabadi N, Chanussot J (2013), “Hyperspectral remote sensing data analysis and future challenges”. *IEEE Geosci Remote Sens Mag* 1(2):6–36
- Baozhi Cheng and Chunhui Zhao, (2020) “A new anomaly target detection algorithm for hyperspectral imagery based on optimal band subspaces”, *Journal of Applied Science and Engineering*, Vol. 23, Issue 2. [https://doi.org/10.6180/jase.202006_23\(2\).0005](https://doi.org/10.6180/jase.202006_23(2).0005)
- Bitar AW, Cheong L, Ovarlez J (2018) Target and background separation in hyperspectral imagery for automatic target detection. In: 2018 IEEE international conference on acoustics, speech and signal processing (ICASSP), pp 1598–1602
- Bitar A.W., Ovarlez JP., Cheong LF., Chehab A. (2020) Automatic Target Detection for Sparse Hyperspectral Images. In: Prasad S., Chanussot J. (eds) *Hyperspectral Image Analysis. Advances in Computer Vision and Pattern Recognition*. Springer, Cham
- Boardman, J. W., Kruse, F. A., and Green, R. O. (1995) “Mapping target signatures via partial unmixing of AVIRIS data.” in *Summaries of the VI JPL Airborne Earth Science Workshop*. Pasadena, CA
- Boardman, J.W. (1998) “Leveraging the high dimensionality of AVIRIS data for improved sub-pixel target unmixing and rejection of false positives: Mixture Tuned Matched Filtering.” In: *Proceedings of the 7th Annual JPL Airborne Geoscience Workshop*, JPL Publication 97(1): 55
- Borel, C. and Gerstl, S. (1994) “Nonlinear spectral mixing models for vegetative and soil surfaces.” *Remote Sensing of Environment*, 47(3):403–416
- Bouzekri S., Lasbet A.A., Lachehab A (2015), “A New Spectral Index for Extraction of Built-Up Area Using Landsat-8 Data,” *Journal of Indian Society Remote Sensing*, vol. 43(4), pp. 867–873.
- Camps-Valls, G.; Tuia, D.; Gómez-Chova, L.; Jiménez, S.; Malo, J. (2011) *Remote sensing image processing. Synth. Lect. Image Video Multimed. Process.*, 5, 1–192.
- Chan J. C. W., Ma J. L., Van de Voorde T., and Canters F. (2011), “Pre-liminary results of superresolution-enhanced angular hyperspectral (CHRIS/Proba) images for land-cover classification,” *IEEE Geosci. Remote Sens. Lett.*, vol. 8, no. 6, pp. 1011–1015.
- Chang, C.I., Liu, J.M., Chieu, B.C., Wang, C.M., Lo, C.S., Chung, P.C., Ren, H., Yang, C.W. and Ma, D.J. (2000), “A generalized constrained energy minimization

- approach to subpixel target detection for multispectral imagery,” *Optical Engineering* 39(5), 1275-1281
- Chang, C.-I. (2003) “Hyperspectral Imaging: Techniques for Spectral Detection and Classification.” Norwell, MA: Kluwer
- Chang, C.-I., and Du, Q. (2004) “Estimation of number of spectrally distinct signal sources in hyperspectral imagery,” *IEEE Trans. Geosci. Remote Sens.*, 42(3):608–619
- Chang, C.-I., (2005) “Orthogonal subspace projection (OSP) revisited: A comprehensive study and analysis.” *IEEE Transactions on Geoscience and Remote Sensing*, 43(3): 502-518
- Chang C.I. (2007), “Hyperspectral Data Exploitation: Theory and Applications”. John Wiley & Sons Inc.; Hoboken, NJ, USA:
- Chang C.I. (2013), “Hyperspectral Data Processing: Algorithm Design and Analysis”. Hoboken, NJ: John Wiley & Sons
- Chang S., Du B. and Zhang L. (2020), "A Subspace Selection-Based Discriminative Forest Method for Hyperspectral Anomaly Detection," in *IEEE Transactions on Geoscience and Remote Sensing*, vol. 58, no. 6, pp. 4033-4046, doi: 10.1109/TGRS.2019.2960391.
- Chang S., Du B., Zhang L., and Zhao R. (2017), “IBRS: An iterative background reconstruction and suppression framework for hyperspectral target detection,” *IEEE J. Sel. Topics Appl. Earth Observ. Remote Sens.*, vol. 10, no. 7, pp. 3406–3417.
- Chen, P., Nelson, J. D., & Tournieret, J. Y. (2016). Toward a sparse Bayesian Markov random field approach to hyperspectral unmixing and classification. *IEEE Transactions on Image Processing*, 26(1), 426-438.
- Chen, Jie, Yingying Song, and Hengchao Li. (2020), “Processing and Analysis of Hyperspectral Data” <https://www.intechopen.com/books/processing-and-analysis-of-hyperspectral-data>
- Chen Y., Nasrabadi N.M. (2011), T.D. Tran, Sparse representation for target detection in hyperspectral imagery, *IEEE J. Sel. Top. Signal Process.* 5 (3) 629–640.
- Chen, J. Y. and Reed, S. I., (1987), “A detection algorithm for optical targets in clutter,” *IEEE Trans. Aerosp. Electron. Syst.*, AES-23(1): 46–59
- Chisense C., (2012) “Classification of Roof Materials Using Hyperspectral Data,” *International Archives of the Photogrammetry, Remote Sensing and Spatial Information Sciences*, vol. XXXIX-B7, ISPRS
- Cisz A.P., Schott J.R. (2005), “Performance comparison of hyperspectral target detection algorithms in altitude varying scenes”, in: *Algorithms and Technologies for Multispectral, Hyperspectral, and Ultra spectral Imagery XI*, vol. 5806, International Society for Optics and Photonics, pp. 839–849.

- Clark M.L. (2016) “Mapping land cover with hyperspectral and multispectral satellites using machine learning and Spectral Mixture Analysis”; Proceedings of the 2016 IEEE International Geoscience and Remote Sensing Symposium (IGARSS); Beijing, China.
- Cocks, T., Janssen R., Stewart A., Wilson I., and Shields T. (1998) “The HyMap airborne hyperspectral sensor: the system, calibration and performance.” Proc. 1st EARSeL Workshop on Imaging Spectroscopy, 37-43
- Cohen Y., Blumberg D.G., Rotman S.R. (2012), Subpixel hyperspectral target detection using local spectral and spatial information, *J. Appl. Remote Sens.* 6 (1) 1–16.
- Costanzo, D.J. (2000), “Hyperspectral imaging spectral variability experiment results”. In Proceedings of the IEEE, International Geoscience and Remote Sensing Symposium, Honolulu, HI, USA.
- Cracknell A. P. (1998), “Synergy in remote sensing-what’s in a pixel?”, *Int. J. Remote Sens.*, vol. 19, no. 11, pp. 2025–2047.
- Crippen R. (1990), “Calculating the Vegetation Index Faster,” *Remote Sensing of Environment*, vol. 34, pp. 71-73, 1990.
- Dadon, M. M., Rotman, S. R., Blumberg, D. G., Adler-Golden, S., & Conforti, P. (2016). Target detection in the presence of multiple subpixel targets in complex backgrounds. In 2016 8th Workshop on Hyperspectral Image and Signal Processing: Evolution in Remote Sensing (WHISPERS) (pp. 1-3). IEEE.
- Dalla Mura M, Benediktsson JA, Chanussot J, Bruzzone L (2011) “The evolution of the morphological profile: from panchromatic to hyperspectral images”, Springer, Berlin, Heidelberg, pp 123–146
- Davood, A., Safari, A. (2012), “Support Vector Machine for Target Detection in Hyperspectral Images.” *TS06I - Remote Sensing II*, 6135
- Drumetz, L.; Veganzones, M.A.; Henrot, S.; Phlypo, R.; Chanussot, J.; Jutten, C. (2016), “Blind hyperspectral unmixing using an extended linear mixing model to address spectral variability”. *IEEE Trans. Image Process.* 2016, 25, 3890–3905.
- Du B., Zhang (2014), “Target detection based on a dynamic subspace”, *Pattern Recognition*. 47 (1) 344–358.
- Du, Q., and Chang, C. I. (2004) “A signal-decomposed and interference-annihilated approach to hyperspectral target detection.” *IEEE Transactions on Geoscience and Remote Sensing* 42(4): 892-906, doi:10.1109/TGRS.2003.821887
- Eckardt A., Reulke R. (2018), “Low-cost hyperspectral systems for atmospheric and surface studies”, *Imaging Spectroscopy XXII: Applications, Scenarios, and Processing*, Proceedings of SPIE Optical Engineering and Applications, San Diego, USA, 2018. International Society for Optics and Photonics; Washington, DC.

- Eismann, M. T. (2012). *Hyperspectral Remote Sensing*, SPIE Press, Bellingham, Washington. doi:10.1117/3.899758
- Fan W., Hu, Miller J., M. Li, (2009) Comparative study between a new nonlinear model and common linear model for analyzing laboratory simulated-forest hyperspectral data, *Int. J. Remote Sens.* 30 (11), 2951–2962.
- Farrell, M. D., & Mersereau, R. M. (2005). On the impact of PCA dimension reduction for hyperspectral detection of difficult targets. *IEEE Geoscience and Remote Sensing Letters*, 2(2), 192-195.
- Foody G. M. and Cox D. P. (1994), “Sub-pixel land-cover composition estimation using a linear mixture model and fuzzy membership functions,” *Int. J. Remote Sens.*, vol. 15, no. 3, pp. 619–631.
- Foody G. M. (1996), “Approaches for the production and evaluation of fuzzy land cover classification from remotely-sensed data,” *Int. J. Remote Sens.*, vol. 17, no. 7, pp. 1317–1340.
- Foody G. M., (2002) “The role of soft classification techniques in the refinement of estimates of ground control point location”, *Photogramm. Eng. Remote Sens.*, vol. 68, no. 9, pp. 897–903.
- Foody G. M., Muslim A. M., and Atkinson P. M. (2005), “Super resolution mapping of the waterline from remotely sensed data,” *Int. J. Remote Sens.*, vol. 26, no. 24, pp. 5381–5392.
- Foody G. M. and Doan H. T. X. (2007), “Variability in soft classification prediction and its implications for sub-pixel scale change detection and super resolution mapping,” *Photogramm. Eng. Remote Sens.*, vol. 73, no. 8, pp. 923–933.
- Freitas S., Silva H., Almeida J., Silva E (2018). “Hyperspectral imaging for real-time unmanned aerial vehicle maritime target detection”. *J. Intell. Robot. Syst*; 90:551–570. doi: 10.1007/s10846-017-0689-0.
- Gao B.C. (1996), “NDWI—a normalized difference water index for remote sensing of vegetation liquid water from space,” *Remote Sensing of Environment*, vol. 58, pp. 257–266.
- Gao L., Yang B., Du Q., Zhang B. (2015), “Adjusted spectral matched filter for target detection in hyperspectral imagery”, *Remote Sens.* 7 (6) 6611–6634.
- Garzonio R., Di Mauro B., Colombo R., Cogliati S (2017). “Surface reflectance and sun-induced fluorescence spectroscopy measurements using a small hyperspectral UAS”. *Remote Sens.*; 9:472. doi: 10.3390/rs9050472.
- Gautam A.K., Preet P., Rawat T.S., Roy Chowdhury P., Sinha L.K. (2020), “Detection of Camouflaged Targets in Hyperspectral Images”. In: Sastry P., CV J., Raghavamurthy D., Rao S. (eds) *Advances in Small Satellite Technologies. Lecture Notes in Mechanical Engineering*. Springer, Singapore

- Geng, X., Yang, W., Ji, L., Wang, F., & Zhao, Y. (2017). The match filter (MF) is always superior to constrained energy minimization (CEM). *Remote Sensing Letters*, 8(7), 696-702.
- Ghaffari, O.; Zoj, M.J.V.; Mokhtarzade, M. (2017), "Reducing the effect of the endmembers' spectral variability by selecting the optimal spectral bands". *Remote Sens.*, 9, 884.
- Ghamisi P., Yokoya N., Li J., Liao W., Liu S., Plaza J., Rasti B., Plaza A (2017). "Advances in hyperspectral image and signal processing: A comprehensive overview of the state of the art". *IEEE Geosci. Remote Sens. Mag*; 5:37–78. doi: 10.1109/MGRS.2017.2762087.
- Gholizadeh, H., Zoj, M. J. V., & Mojaradi, B. (2011). Impact of informative band selection on target detection performance. In *Image and Signal Processing for Remote Sensing XVII* (Vol. 8180, p. 81801C). International Society for Optics and Photonics.
- Goetz A.F (2009), "Three decades of hyperspectral remote sensing of the Earth: A personal view". *Remote Sens. Environ.*;113: S5–S16. doi: 10.1016/j.rse.2007.12.014.
- Govender, K. Chetty M., and Bulcock H. (2011), "A review of hyperspectral remote sensing and its application in vegetation and water resource studies," *Water Sa*, vol. 33, no. 2, pp. 145–152.
- Green, A. A., Berman, M., Switzer, P., and Craig, M. D. (1988), "A transformation for ordering multispectral data in terms of image quality with implications for noise removal." *IEEE Trans. Geoscience and Remote Sens.*26:65-74
- Gross, W., Boehler, J., Schilling, H., Middelmann, W., Weyermann, J., Wellig, P., ... & Kneubühler, M. (2015). "Assessment of target detection limits in hyperspectral data. In *Target and Background Signatures*" (Vol. 9653, p. 96530J). International Society for Optics and Photonics.
- Gu Y., Zhang Y., and Zhang J. (2008), "Integration of spatial-spectral information for resolution enhancement in hyperspectral Images," *IEEE Trans. Geosci. Remote Sens.*, vol. 46, no. 5, pp. 1347–1358.
- Guilfoyle, K. J., Althouse, M. L. and Chang, C.I. 2001 "A quantitative and comparative analysis of linear and nonlinear spectral mixture models using radial basis function neural networks." *IEEE Transactions on Geoscience and Remote Sensing*, 39: 2314–2318
- Guo Z, Wittman T, Osher S (2009), "L1 and its application to hyperspectral image enhancement"
- Gutman G. G (1991), "Vegetation Indices from AVHRR An Update and Future Prospects", *Remote Sensing of Environment*, 35, 121 – 136.
- Haldar S.K. (2013), "Mineral Exploration Principles and Applications", Elsevier, Pages 95-115, <https://doi.org/10.1016/B978-0-12-416005-7.00006-4>

- Halimi, A.; Honeine, P.; Bioucas-Dias, J.M. (2016), “Hyperspectral unmixing in presence of endmember variability, nonlinearity, or mismodeling effects”. *IEEE Trans. Image Process*, 25, 4565–4579.
- Hall D.K., Foster J.L., Chien J.L., & Riggs G.A. (1995), “Determination of actual snow-covered area using Landsat TM and digital elevation model data in Glacier National Park, Montana,” *Polar Record*, vol. 31(177), pp.191-198.
- Hao, X., Wu, Y., & Wang, P. (2020). Angle Distance-Based Hierarchical Background Separation Method for Hyperspectral Imagery Target Detection. *Remote Sensing*, 12(4), 697.
- Heylen R., Scheunders P. (2016), “A multilinear mixing model for nonlinear spectral unmixing”, *IEEE Trans. Geosci. Remote Sens.* 54 (1) 240–251.
- Heylen R., Parente M., Gader P. (2014), “A review of nonlinear hyperspectral unmixing methods”, *IEEE J. Sel. Top. Appl. Earth Obs. Remote Sens.* 7 (6) 1844–1868.
- Hruska R., Mitchell J., Anderson M., Glenn N.F. (2012), “Radiometric and geometric analysis of hyperspectral imagery acquired from an unmanned aerial vehicle”. *Remote Sens.*; 4:2736–2752. doi: 10.3390/rs4092736.
- Honkavaara E., Heikki S., Kaivosoja J., Pölonen I., Hakala T., Litkey P., Mäkynen J., Pesonen L. (2013), “Processing, and assessment of spectrometric stereoscopic imagery collected using a lightweight UAV spectral camera for precision agriculture”. *Remote Sens.*; 5:5006–5039. doi: 10.3390/rs5105006.
- Hongmei Zhao, Xiaoling Chen (2005), “Use of normalized difference bareness index in quickly mapping bare areas from TM/ETM+,” *Proceedings of IEEE International Geoscience and Remote Sensing Symposium*, pp. 1666–1668.
- Hu X. and Wang Q. (2011), “Estimating impervious surfaces from medium spatial resolution imagery: A comparison between fuzzy classification and LSMA,” *Int. J. Remote Sens.*, vol. 30, no. 20, pp. 5645–5663
- Huete A. (1988), “A Soil-Adjusted Vegetation Index (SAVI),” *Remote Sensing of Environment*, vol. 25, pp. 295-309.
- Hyvarinen, A., & Oja, E. 2000. “Independent component analysis: algorithms and applications”. *Neural Networks*, 15(4): 411-430
- Im J., Lu Z., Rhee J., Quackenbush L.J. (2012), “Impervious surface quantification using a synthesis of artificial immune networks and decision/regression trees from multi-sensor data,” *Remote Sensing of Environment*, vol. 117, pp. 102–113.
- Imani, M. (2019). Difference-based target detection using Mahalanobis distance and spectral angle. *International Journal of Remote Sensing*, 40(3), 811-831.
- Jakob S., Zimmermann R., Gloaguen R (2017). “The need for accurate geometric and radiometric corrections of drone-borne hyperspectral data for mineral exploration: Mephysto—A toolbox for pre-processing drone-borne hyperspectral data”. *Remote Sens.*; 9:88. doi: 10.3390/rs9010088.

- Jensen, J.R. (2007), “Remote sensing of the environment: An Earth resource perspective”. Prentice Hall, Upper Saddle River, N.J.
- Jiao C., Chen C., McGarvey R.G., Bohlman S., Jiao L., Zare A., (2018), “Multiple instance hybrid estimator for hyperspectral target characterization and sub-pixel target detection”, *ISPRS J. Photogramm. Remote Sens.* 146 235–250.
- Jong S.M., Meer F.D., Clevers J.G. (2004),” Basics of Remote Sensing”. In: Jong S.M.D., Meer F.D.V. (eds) *Remote Sensing Image Analysis: Including the Spatial Domain. Remote Sensing and Digital Image Processing*, vol 5, Springer, Dordrecht.
- Karbhari V. Kale, Mahesh M. Solankar and Dhananjay B. Nalawade (2019). “Hyperspectral Endmember Extraction Techniques, Processing and Analysis of Hyperspectral Data”, Jie Chen, Yingying Song and Hengchao Li, IntechOpen, DOI: 10.5772/intechopen.88910. Available from: <https://www.intechopen.com/books/processing-and-analysis-of-hyperspectral-data/hyperspectral-endmember-extraction-techniques>.
- Kasetkasem, T.; Arora, M.K. Varshney, P.K (2005). “Super resolution land cover mapping using a Markov random field-based approach”. *Remote Sens. Environ.*, 96, 302–314.
- Kelly E.J. (1986), “An adaptive detection algorithm”, *IEEE Trans. Aerosp. Electron. Syst.* AES-22 (12) 115–127.
- Kerekes J.P., Schott J.R. (2007), “Hyperspectral imaging systems”. In: Chang C.I., editor. *Hyperspectral Data Exploitation: Theory and Applications*. 1st ed. John Wiley & Sons; Hoboken, NJ, USA. pp. 19–46.
- Kerekes John P., Ludgate Kyle Giannandrea, Anne Marie, Raqueno Nina G, and Goldberg Daniel S, (2013) “SHARE 2012: Subpixel detection and unmixing experiments”, *Algorithms and Technologies for Multispectral, Hyperspectral, and Ultraspectral Imagery XIX*, Proc. of SPIE Vol. 8743, 87430H.
- Keshava, N.; Mustard, J.F. (2002), “Spectral unmixing”. *IEEE Signal Process. Mag.*, 19, 44–57.
- Keshava, N. (2003) “A Survey of Spectral Unmixing Algorithms.” *Lincoln Laboratory Journal*. 14(1)
- Khan M.J., Khan H.S., Yousaf A., Khurshid K., Abbas A. (2018), “Modern trends in hyperspectral image analysis: A review”. *IEEE Access.*; 6:14118–14129. doi: 10.1109/ACCESS.2018.2812999.
- Khasanah A.N. and Danoedoro P. (2013), “Mapping Clay Fraction Using Hyperion Imagery in Relation to Different Kind of Parents Material in D.I.Yogyakarta,” *Asian Conference on Remote Sensing*.
- Koonsanit, K., Jaruskulchai, C., and Eiumnoh, A. (2012) “Band Selection for Dimension Reduction in HyperSpectral Image Using Integrated Information Gain and Principal Components Analysis Technique.” *International Journal of Machine Learning and Computing*, 2(3)

- Landgrebe D (1999). Information extraction principles and methods for multispectral and hyperspectral image data. In: Chen C., editor. *Information Processing for Remote Sensing*. Volume 1. World Scientific Publishing Co., Inc.; River Edge, NJ, USA. pp. 3–37.
- Landgrebe, D (2002). Hyperspectral image data analysis. *IEEE Signal Process.*, 19, 17–28.
- Launius, Roger D. (1994); *NASA: A History of the U.S. Civil Space Program*. Malabar, Florida: Krieger Publishing Company.
- Launius, Roger D. (2005); *Sputnik and the Origins of the Space Age* , <https://history.nasa.gov/sputnik/sputorig.html>
- Lee S. and Lathrop R. G. (2006), “Subpixel analysis of Landsat ETM+ using self-organizing map (SOM) neural networks for urban land cover characterization,” *IEEE Trans. Geosci. Remote Sens.*, vol. 44, no. 6, pp. 1642–1654.
- Li, X.; Ling, F.; Du, Y.; Feng, Q.; Zhang, Y. (2014), “A spatial–temporal hopfield neural network approach for super-resolution land cover mapping with multi-temporal different resolution remotely sensed image”’s. *ISPRS J. Photogramm. Remote Sens*, 93, 76–87
- Li X., Zhao T.X., and Chen X. (2011), “A super-resolution approach for spectral unmixing of remote sensing images,” *Int. J. Remote Sens.*, vol. 32, pp. 6091–6107.
- Liang, Shunlin, Xiaowen Li, and Jindi Wang (2012), eds. *Advanced remote sensing: terrestrial information extraction and applications*, Academic Press.
- Lillesand, T., Kiefer, R., and J. Chipman, *Remote Sensing and Image Interpretation*, 6th ed., New York, NY: John Wiley & Sons, 2008, pp. 756.
- Ling, F.; Du, Y.; Li, X.; Zhang, Y.; Xiao, F.; Fang, S.; Li, W. (2014), “Super resolution land cover mapping with multiscale information by fusing local smoothness prior and downscaled coarse fractions”. *IEEE Trans. Geosci.Remote Sens.*, 52, 5677–5692.
- Ling, F.; Li, X.; Du, Y.; Xiao, F. (2013), “Sub-pixel mapping of remotely sensed imagery with hybrid intra- and inter-pixel dependence”. *Int. J. Remote Sens.*, 34, 341–357.
- Ling F., Li W. B., Du Y., and Li X. D. (2011), “Land cover change mapping at the subpixel scale with different spatial-resolution remotely sensed imagery,” *IEEE Geosci. Remote Sens. Lett.*, vol. 8, no. 1, pp. 182–186.
- Ling F., Du Y., Xiao F., Xue H. P., and Wu S. J. (2010), “Super-resolution land-cover mapping using multiple sub-pixel shifted remotely sensed images,” *Int. J. Remote Sens.*, vol. 31, no. 19, pp. 5023–5040.
- Liu Y., Gao G., and Gu Y. (2017), “Tensor matched subspace detector for hyperspectral target detection,” *IEEE Trans. Geosci. Remote Sens.*, vol. 55, no. 4, pp. 1967–1974.

- Liu, S., Bruzzone, L., Bovolo, F., & Du, P. (2016). Unsupervised multitemporal spectral unmixing for detecting multiple changes in hyperspectral images. *IEEE Transactions on Geoscience and Remote Sensing*, 54(5), 2733-2748.
- Lu X., Wu H., Yuan Y., Yan P., and Li X. (2013), "Manifold regularized sparse NMF for hyperspectral unmixing," *IEEE Trans. Geosci. Remote Sens.*, vol. 51, no. 5, pp. 2815–2826.
- Makido Y. and Shortridge A. (2007), "Weighting function alternatives for a subpixel allocation model," *Photogramm. Eng. Remote Sens.*, vol. 73, no. 11, pp. 1233–1240.
- Makido Y., Shortridge A., and Messina J. P. (2007), "Assessing alternatives for modeling the spatial distribution of multiple land-cover classes at sub-pixel scales," *Photogramm. Eng. Remote Sens.*, vol. 73, no. 8, pp. 935–943.
- Malgorzata, Veróné Wojtaszek, and Barsi Árpád (2010), "Data acquisition and integration" *Remote Sensing*, Nyugat-magyarországi Egyetem.
- Manolakis D. G, Lockwood RB, Cooley TW (2016), "Hyperspectral imaging remote sensing: physics, sensors, and algorithms". Cambridge University Press
- Manolakis, D., Shaw, G. and Keshava, N. (2000) "Comparative analysis of hyperspectral adaptive matched filter detector," in *Proc. SPIE*, pp. 2–17
- Manolakis, D., Siracusa, C., and Shaw G. (2001), "Hyperspectral Subpixel Target Detection Using the Linear Mixing Model." *IEEE Transactions on Geoscience and Remote Sensing*, 39(7)
- Manolakis, D.; Shaw, G. (2002), "Detection algorithms for hyperspectral imaging applications". *IEEE Signal Process. Mag.*, 19, 29–43.
- Manolakis D, Marden D and Shaw G. (2003), "A Hyperspectral Image Processing for Automatic Target Detection Applications", *Lincoln Laboratory Journal*, vol. 14(1).
- Maria Axelsson; Ola Friman; Trym Vegard Haavardsholm; Ingmar Renhorn (2016), "Target detection in hyperspectral imagery using forward modeling and in-scene information", *ISPRS Journal of Photogrammetry and Remote Sensing*, ISSN: 0924-2716, Vol: 119, Page: 124-134, 2016, DOI: 10.1016/j.isprsjprs.2016.05.008.
- Marinoni, A., Plaza, A., & Gamba, P. (2017). A novel pre unmixing framework for efficient detection of linear mixtures in hyperspectral images. *IEEE Transactions on Geoscience and Remote Sensing*, 55(8), 4325-4333.

- Mark Garcia (2017), “60 years ago, the Space Age began”, <https://www.nasa.gov/feature/60-years-ago-the-space-age-began/>, Source:NASA
- McFeeters S. (1996), “The use of Normalized Difference Water Index (NDWI) in the Delineation of Open Water Features,” *International Journal of Remote Sensing*, vol. 17, pp. 1425-1432.
- Mertens, K.C.; De Baets, B.; Verbeke, L.P.C.; de Wulf, R.R (2006). “A sub-pixel mapping algorithm based on sub-pixel/pixel spatial attraction models”. *Int. J. Remote Sens*, 27, 3293–3310.
- Mertens K. C., Verbeke L. P. C., Ducheyne E. I., and De Wulf R. R. (2003), “Using genetic algorithms in sub-pixel mapping,” *Int.J.RemoteSens.*, vol. 24, no. 21, pp. 4241–4247.
- Mianji F. A. and Zhang Y. (2011), “SVM-based unmixing-to-classification conversion for hyperspectral abundance quantification,” *IEEE Trans. Geosci. Remote Sens.*, vol. 49, no. 11, pp. 4318–4327.
- Muad, Anuar M. and Giles M. Foody. (2012) “Super-resolution mapping of lakes from imagery with a coarse spatial and fine temporal resolution.” *Int. J. Appl. Earth Obs. Geoinformation* 15: 79-91.
- Muad A. M. and Foody G. M. (2019), “Impact of land cover patch size on the accuracy of patch area representation in HNN-based super resolution mapping,” *IEEE J. Sel. Topics Appl. Earth Observ. Remote Sens.*, vol. 5, no. 5, Oct. 2012. Abdalla R, Introduction Chapter: From Land Surveying to Geomatics - Multidisciplinary Technological Trends, Trends in Geomatics - An Earth Science Perspective, Rifaat Abdalla, IntechOpen, January 26.
- Muhammad A. and Haq I. (2011). “Linear Unmixing and Target Detection of Hyperspectral Imagery Using OSP.” *International Conference on Modeling, Simulation and Control IPCSIT* 10
- Myint S.W., Lam N.S.N., and Taylor J.M. (2004), “Wavelets for urban spatial feature discrimination: Comparisons with fractal, spatial autocorrelation, and spatial co-occurrence approaches,” *Photogrammetry Engineering of Remote Sensing*, vol. 70(7), pp. 803-812.
- Myneni, R. B., Hall, F. G., Sellers, P. J. and Marshak, A. L. (1995). “The interpretation of spectral vegetation indexes”, *IEEE Transactions on Geoscience and Remote Sensing*, 33: 481–486.
- Nasrabadi N.M. (2014), “Hyperspectral target detection: an overview of current and future challenges, *IEEE Signal Process*”. *Mag.* 31 (1) 34–44.
- Navalgund, Ranganath & V, Jayaraman & Roy, Parth. (2007), “Remote sensing applications: An overview,” *Current science*, vol. 93(2), pp.1747-1766.
- NOAA. (1990), *The Global Vegetation Index Users’ Guide*, revised October 1990, NOAA NESDIS, National Climate Data Center, Washington, D.C

- Prasad T., John L., Alfredo H. (2001), "Hyperspectral Remote Sensing of Vegetation". CRC Press; Boca Raton, FL, USA.
- Priyadarshini, K.N., Sivashankari, V., Shekhar, S. and Balasubramani, K., (2019). Comparison and Evaluation of Dimensionality Reduction Techniques for Hyperspectral Data Analysis. In Multidisciplinary Digital Publishing Institute Proceedings (Vol. 24, No. 1, p. 6).
- Qingxiang Liu and John C. Trinder (2018). "Sub-Pixel Technique for Time Series Analysis of Shoreline Changes Based on Multispectral Satellite Imagery", *Advanced Remote Sensing Technology for Synthetic Aperture Radar Applications, Tsunami Disasters, and Infrastructure*, Maged Marghany, IntechOpen.
- Rai Arun Kumar and Jain Kamal, (2014), "Enhancing object boundaries by subpixel mapping of satellite image," *Journal of Geomatics*, Vol. 8, no. 2, pp. 216-221
- Ren, H., & Chang, C. I. (2000). Target-constrained interference-minimized approach to subpixel target detection for hyperspectral images. *Optical Engineering*, 39(12), 3138-3145.
- Rhonda D. P., Layne T. W., Christine e. B. and Randolph H. W. (2008). "An Adaptive Noise Reduction Technique for Improving the Utility of Hyperspectral Data," *Pecora17 – The future of land imaging*.
- Richards, J.A.; Richards, J (1999). "Remote Sensing Digital Image Analysis; Springer: Berlin/Heidelberg, Germany"; Volume 3.
- Rodarmel, C. and Jieshan (2002). "Principal Component Analysis for Hyperspectral Image Classification," *Surveying and Land Information Systems*, 62(2)
- Rondeaux G., M. Steven, and F. Baret (1996), "Optimization of Soil-Adjusted Vegetation Indices," *Remote Sensing of Environment*, vol. 55, pp. 95-107, 1996.
- Rosin, P. (2001). Robust pixel unmixing. *IEEE Transactions on Geoscience and Remote Sensing*, 39: 1978–1983.
- Rotman, S. R., Vortman, M., & Biton, C. (2010). The impact of band selection on hyperspectral point target detection algorithms. In *2010 IEEE International Geoscience and Remote Sensing Symposium* (pp. 4761-4763). IEEE.
- Rustamov, Rustam B., Sabina Hasanova, and Mahfuza H. Zeynalova, (2018) eds. *Multi-purposeful Application of Geospatial Data*, BoD–Books on Demand.
- Salomonson, V., and I. Appel (2004), "Estimating Fractional Snow Cover from MODIS Using the Normalized Difference Snow Index," *Remote Sensing of Environment*, vol. 89, pp. 351-360.
- Samsudin, Sarah Hanim & Shafri, Helmi & Hamedianfar, Alireza. (2016), "Development of spectral indices for roofing material condition status detection using field spectroscopy and WorldView-3 data. *Journal of Applied Remote Sensing*," vol.10(2).

- Schneider, W. (1993). Land use mapping with subpixel accuracy from landsat TM image data, *Proceedings of the 25th International Symposium on Remote Sensing and Global Environmental Change*, pp. 155–161.
- Schneider, W. (1999). Land cover mapping from optical satellite images employing subpixel segmentation and radiometric calibration, *Machine Vision and Advanced Image Processing in Remote Sensing* (I. Kanellopoulos, G. Wilkinson, and T. Moons, editors), Springer, London.
- Schueler, T.R (1994). The importance of imperviousness. *Watershed Prot. Tech*, 1, 100–111.
- Segl K., Heiden U., Mueller M. and Kaufmann H. (2003), “Endmember detection in urban environments using hyperspectral HyMap data,” *Third EARSeL Workshop on Imaging Spectroscopy*, Herrschin.
- Sellar R.G., Boreman G.D (2005). “Classification of imaging spectrometers for remote sensing applications”. *Opt. Eng.* 2005; 44:013602. doi: 10.1117/1.1813441.
- Sergio Bernabé, Sebastián López, Antonio Plaza, and Roberto Sarmiento, (2013) “GPU Implementation of an Automatic Target Detection and Classification Algorithm for Hyperspectral Image Analysis,” *IEEE geoscience and remote sensing letters*, Vol. 10, No. 2.
- Shabou, Marouen, Bernard Mougnot, Zohra Chabaane, Christian Walter, Gilles Boulet, Nadhira Aissa, and Mehrez Zribi, (2015) “Soil clay content mapping using a time series of Landsat TM data in semi-arid lands,” *Remote sensing*, vol. 7(5), pp. 6059-6078
- Shang, X., Song, M., Wang, Y., Yu, C., Yu, H., Li, F., & Chang, C. I. (2020). Target-Constrained Interference-Minimized Band Selection for Hyperspectral Target Detection. *IEEE Transactions on Geoscience and Remote Sensing*.
- Shao, Y., & Lan, J. (2019). A spectral unmixing method by maximum margin criterion and derivative weights to address spectral variability in hyperspectral imagery. *Remote Sensing*, 11(9), 1045.
- Shao Y, Lan J, Zhang Y, Zou J (2018). “Spectral Unmixing of Hyperspectral Remote Sensing Imagery via Preserving the Intrinsic Structure Invariant. *Sensors (Basel)*.”;18(10):3528. Published 2018 Oct 18. doi:10.3390/s18103528.
- Sharma, L.K. and Verma, R.K., (2020). AVIRIS-NG hyperspectral data analysis for pre- and post-MNF transformation using per-pixel classification algorithms. *Geocarto International*, pp.1-12.
- Shaw, G., and Burke, H. (2003). “Spectral imaging for remote sensing.” *Lincoln Lab. Journal*, 14:3–28
- Shen Z., Qi J., and Wang K. (2009), “Modification of pixel swapping algorithm with initialization from a sub-pixel/pixel spatial attraction model,” *Photogramm. Eng. Remote Sens.*, vol. 75, no. 5, pp. 557–567

- Schueler, T.R. (1994), "The importance of imperviousness". *Watershed Prot. Tech.* 1, 100–111.
- Shih, H. C., Stow, D. A., Tsai, Y. M., & Roberts, D. A. (2020). Estimating the starting time and identifying the type of urbanization based on dense time series of landsat-derived Vegetation-Impervious-Soil (VIS) maps—A case study of North Taiwan from 1990 to 2015. *International Journal of Applied Earth Observation and Geoinformation*, 85, 101987.
- Shippert P. (2004) Why use hyperspectral imagery? *Photogrammetric Engineering and Remote Sensing*;70(4):377-396
- Şimşek, M, Ilgın, H. (2020). Band Reduction for Target Detection in Hyperspectral Images." *Communications Faculty of Sciences University of Ankara Series A2-A3 Physical Sciences and Engineering*, 62 (1), 53-62. Retrieved from <https://dergipark.org.tr/en/pub/aupse/issue/51879/676083>
- Snyder D., Kerekes J., Fairweather I., Crabtree R., Shive J., Hager S. (2008), "Development of a web-based application to evaluate target finding algorithms", in: *IEEE International Geoscience and Remote Sensing Symposium*, vol. 2, IEEE, pp. II-915.
- Somers, B.; Asner, G.P.; Tits, L.; Coppin, P. (2011), "Endmember variability in spectral mixture analysis: A review". *Remote Sens. Environ.*, 115, 1603–1616.
- Song, F., Yan He, Ming-yi, and Jiang-hong Wei Jiang. (2007). "ICA-Based Dimensionality Reduction and Compression of Hyperspectral Images". *Journal of Electronics & Information Technology*, 29(12):2871-75
- Song X., Zou L., and Wu L. (2020), "Detection of Subpixel Targets on Hyperspectral Remote Sensing Imagery Based on Background Endmember Extraction," in *IEEE Transactions on Geoscience and Remote Sensing*, doi: 10.1109/TGRS.2020.3002461
- Steinwendner, J., W. Schneider, and F. Suppan, (1998). Vector segmentation using spatial subpixel analysis for object extraction, *International Archives of Photogrammetry and Remote Sensing*, 32:265–271
- Stojče Dimov Ilčev (2019), "Global Satellite Meteorological Observation (GSMO) Applications", vol. 2, Springer International Publishing.
- Stuart MB, McGonigle AJS, Willmott JR, (2019). "Hyperspectral Imaging in Environmental Monitoring: A Review of Recent Developments and Technological Advances in Compact Field Deployable Systems. *Sensors (Basel)*;19(14):3071. Published 2019 Jul 11. doi:10.3390/s19143071
- Su Y., Foody G.M., Muad A. and Cheng K. (2012): Combining Pixel Swapping and Contouring Methods to Enhance Super-Resolution Mapping, *IEEE journal of selected topics in applied earth observations and remote sensing*, 5(5), 1428-1437, doi: 10.1109/JSTARS.2012.2216514.

- Su Y. F., Foody G. M, Muad A. M, and Cheng K. S. (2012), "Combining Hopfield neural network and contouring methods to enhance super- resolution mapping," *IEEE J. Sel. Topics Appl. Earth Observ. Remote Sens.*, vol. 5, no. 5.
- Tan Q., and Wang J., (2007), "Hyperspectral Versus Multispectral Satellite Data for Urban Land Cover and Land Use Mapping— Beijing, An Evolving City,".
- Tatem, A.J.; Lewis, H.G.; Atkinson, P.M (2002).; "Nixon, M.S. Super-resolution land cover pattern prediction using a hopfield neural network". *Remote Sens. Environ.* 2002, 79, 1–14.
- Tatem A. J., Lewis H. G., Atkinson P. M., and Nixon M. S. (2001), "Super- resolution target identification from remotely sensed images using a Hopfield neural network," *IEEE Trans. Geosci. Remote Sens.*, vol. 39, no. 4, pp. 781–796.
- Thornton M. W., Atkinson P. M., and Holland D. A. (2006), "Sub-pixel mapping of rural land cover objects from fine spatial resolution satellite sensor imagery using super-resolution swapping," *Int.J.RemoteSens.*, vol. 27, no. 3, pp. 473–491.
- Tiwari, K.C., Arora, M.K. and Singh, D. (2011), An assessment of independent component analysis for detection of military targets from hyperspectral images. *International Journal of Applied Earth Observation and Geoinformation*, 13(5), pp.730-740.
- Townshend J. R. G. (1981), "The spatial resolving power of earth resources satellites," *Prog. Phys. Geog.*, vol. 5, pp. 32–55.
- Townshend J. and Justice C. (1981), "Information extraction from remotely sensed data: A user view," *Int. J. Remote Sens.*, vol. 2, no. 4, pp. 313–329.
- Usman M., Liedl R., Shahid M.A., Abbas A. (2015), "Land use/land cover classification and its change detection using multi-temporal MODIS NDVI data," *Journal of Geographical Science*, vol. 25(12), pp. 1479-1506.
- Verhoeve, J.; De Wulf, R. (2002), "Land cover mapping at sub-pixel scales using linear optimization techniques". *Remote Sens. Environ.*, 79, 96–104.
- Villa A., Chanussot J., Benediktsson J. A., and Jutten C., "Spectral unmixing for the classification of hyperspectral images at a finer spa- tial resolution," *IEEE J. Sel. Topics Signal Process.*, vol. 5, no. 3, pp. 521–533, June 2011, DOI: 10.1109/JSTSP.2010.2096798.
- Vikhamar, D. and Solberg, R. (2002). Subpixel mapping of snow cover in forests by optical remote sensing. *Remote Sensing of Environment*, 84: 69–82.
- Viskovic L., Kosovic I. N. and Mastelic T., (2019) "Crop Classification using Multi-spectral and Multitemporal Satellite Imagery with Machine Learning," 2019 International Conference on Software, Telecommunications and Computer Networks (SoftCOM), Split, Croatia, pp. 1-5, doi: 10.23919/SOFTCOM.2019.8903738.

- Wang, J., and Chang, C-I. (2006), “Independent Component Analysis-Based Dimensionality Reduction with Applications in Hyperspectral Image Analysis”, *IEEE Transactions on Geosci. and Remote Sensing*, 44(6)
- Wang, Y., Huang, S., Liu, D., & Wang, B. (2013). A new band removed selection method for target detection in hyperspectral image. *Journal of Optics*, 42(3), 208-213.
- Wang, L.G.; Wang, Q.M., (2013), “Subpixel mapping using Markov random field with multiple spectral constraints from subpixel shifted remote sensing images”. *IEEE Geosci. Remote Sens. Lett.*, 10, 598–602.
- Wang, L.; Zhang, Y.; Li, J. (2006) “Bp Neural Network Based Subpixel Mapping Method. In *Intelligent Computing in Signal Processing and Pattern Recognition*”; Huang, D.-S., Li, K., Irwin, G.W., Eds.; Springer: Berlin, Germany; pp. 755–760.
- Wang, Q.; Atkinson, P.M (2017). “The effect of the point spread function on sub-pixel mapping”. *Remote Sens. Environ.*, 193, 127–137.
- Wang, Q.; Wang, L.; Liu, D (2012). “Particle swarm optimization-based sub-pixel mapping for remote-sensing imagery”. *Int. J. Remote Sens.* 2012, 33, 6480–6496.
- Wang Z., Xue J.-H, (2017), “The matched subspace detector with interaction effects, *Pattern Recognit.* 68 24–37
- Wang Z., Zhu R., Fukui K., Xue J.-H (2017), Matched shrunken cone detector (MSCD): bayesian derivations and case studies for hyperspectral target detection, *IEEE Trans. Image Process.* 26 (11) 5447–5461.
- Wang Z., Xue J.-H. (2018), Matched shrunken subspace detectors for hyperspectral target detection, *Neurocomputing* 272 226–236.
- Waqar M.M., Mirza J.F., Mumtazard R., Hussain E., (2012), “Development of new indices for Extraction of Built-Up Area and Bare Soil on Landsat Data,” *Open Access Scientific Reports*.
- Webb, A. R., & Copsey, K. D. (2011). *Statistical Pattern Recognition*, Wiley.
- Wendel A., Underwood J. (2017), “Illumination compensation in ground based hyperspectral imaging.” *ISPRS J. Photogramm. Remote Sens.*; 129:162–178. doi: 10.1016/j.isprsjprs.2017.04.010
- Weng Qihao, (2013), “Introduction to remote sensing Systems, Data and Applications”, Taylor and Francis/CRC Press.
- Weng Q., (2012), “Remote sensing of impervious surfaces in the urban areas: requirements, methods, and trends,” *Remote Sensing of Environment*, vol. 117, pp. 34–49.
- Wenzhong Shi, Zelang Miao, Qunming Wang, & Hua Zhang, (2014) “Spectral–Spatial Classification and Shape Features for Urban Road Centerline Extraction,” *IEEE Geoscience and Remote Sensing Letters*, vol. 11(4), pp. 788–792.

- Wilcox C.C., Montes M., Yetzbacher M., Edelberg J., Schlupf J. (2018), “Micro- and Nanotechnology Sensors, Systems, and Applications X”, Proceedings of SPIE Defence and Security, Orlando Florida, United States, May 2018. International Society for Optics and Photonics; Washington, DC, USA. “An ultra-compact hyperspectral imaging system for use with an unmanned aerial vehicle with smartphone-sensor technology”
- Willett R.M., Duarte M.F., Davenport M.A., Baraniuk R.G. (2014). “Sparsity and structure in hyperspectral imaging: Sensing, reconstruction and target detection”. *IEEE Signal Proc. Mag*; 31:116–126. doi: 10.1109/MSP.2013.2279507.
- Wolf A. (2010), “Using World View-2 Vis-NIR MSI Imagery to Support Land Mapping and Feature Extraction Using Normalized Difference Index Ratios,” Unpublished report, Longmont, CO: Digital Globe.
- Xian-Hua Han (2019). “Hyperspectral Image Super-Resolution Using Optimization and DCNN-Based Methods, Processing and Analysis of Hyperspectral Data”, Jie Chen, Yingying Song and Hengchao Li, IntechOpen, DOI: 10.5772/intechopen.89243. Available from: <https://www.intechopen.com/books/processing-and-analysis-of-hyperspectral-data/hyperspectral-image-super-resolution-using-optimization-and-dcnn-based-methods>
- Xiaochen Yang, MingzhiDong, ZiyuWang ,LianruGao, LefeiZhang, Jing-HaoXue, (2020), “Data-augmented matched subspace detector for hyperspectral subpixel target detection”, *Pattern Recognition*, 106, 107464, 0031-3203, <https://doi.org/10.1016/j.patcog.2020.107464>
- Xu Xiong, Zhong Yanfei, and Zhang Liangpei (2014), “Adaptive Subpixel Mapping Based on a Multiagent System for Remote-Sensing Imagery,” *IEEE transactions on geoscience and remote sensing*, vol. 52, no. 2, pp. 787 – 804
- Xu H. (2006), “Modification of Normalised Difference Water Index (NDWI) to Enhance Open Water Features in Remotely Sensed Imagery,” *International Journal of Remote Sensing*, vol. 27(14), pp. 3025-3033.
- Xu H. (2010), “Analysis of impervious surface and its impact on urban heat environment using the normalized difference impervious surface index (NDISI),” *Photogrammetry Engineering and Remote Sensing*, vol.76, pp. 557–565.
- Yang D, Li Z, Xia Y, Chen Z. (2015), “Remote sensing image super-resolution: Challenges and approaches”, Published in IEEE Conference.
- Yang X., Zhang L., Gao L., Xue J.-H (2019), MSDH: Matched subspace detector with heterogeneous noise, *Pattern Recognition. Lett.* 125, 701–707.
- Zabalza, J., Ren, J., Yang, M., Zhang, Y., Wang, J., Marshall, S., and Han, J. (2014) “Novel Folded-PCA for improved feature extraction and data reduction with hyperspectral imaging and SAR in remote sensing.” *ISPRS Journal of Photogrammetry and Remote Sensing*, 93

- Zare, A.; Ho, K.C. (2014), "Endmember variability in hyperspectral analysis: Addressing spectral variability during spectral unmixing". *IEEE Signal Process. Mag.*, 31, 95–104.
- Zha Y., J. Gao, and S. Ni. (2003), "Use of Normalized Difference Built-Up Index in Automatically Mapping Urban Areas from TM Imagery," *International Journal of Remote Sensing*, vol. 24(3), pp. 583-594
- Zhang, J., Cao, Y., Zhuo, L., Wang, C., & Zhou, Q. (2015). Improved band similarity-based hyperspectral imagery band selection for target detection. *Journal of Applied Remote Sensing*, 9(1), 095091.
- Zhang, J.; Rivard, B.; Sánchez-Azofeifa, A. (2006); Castro-Esau, K. Intra- and inter-class spectral variability of tropical tree species at La Selva, Costa Rica: Implications for species identification using HYDICE imagery. *Remote Sens. Environ*, 105, 129–141.
- Zhang Y., Du B., Zhang L. (2015), "A sparse representation-based binary hypothesis model for target detection in hyperspectral images", *IEEE Trans. Geosci. Remote Sens.* 53 (3) 1346–1354.
- Zhang Y Zhang., L., Du B., and Wang S. (2015), "A nonlinear sparse representation-based binary hypothesis model for hyperspectral target detection," *IEEE J. Sel. Top. Appl. Earth Observat. Remote Sens.*, vol. 8, no. 6, pp. 2513–2522,
- Zhang Y. (2009), "Optimisation of building detection in satellite images by combining multispectral classification and texture filtering," *ISPRS Journal of Photogrammetric and Remote Sensing*, vol. 54, pp. 50–60.
- Zhang, Gai gai, "HTD-Net: A Deep Convolutional Neural Network for Target Detection in Hyperspectral Imagery." *Remote Sensing* 12.9 (2020): 1489.
- Zhang L, Zhang Q, Du B, Huang X, Tang YY, Tao D (2018) Simultaneous spectral-spatial feature selection and extraction for hyperspectral images. *IEEE Trans Cybern* 48(1):16–28
- Zhang, L., Zhang, L., Tao, D., Huang, X., and Du, B. (2013) "Hyperspectral Remote Sensing Image Subpixel Target Detection Based on Supervised Metric Learning", *IEEE* 0196-2892
- Zhang L., Zhang L., Tao D., Huang X., Du B. (2014), "Hyperspectral remote sensing image subpixel target detection based on supervised metric learning", *IEEE Trans. Geosci. Remote Sens.* 52 (8) 4955–4965.
- Zhang, X., Pan, Z., Hu, B., Zheng, X., & Liu, W. (2018). Target detection of hyperspectral image based on spectral saliency. *IET Image Processing*, 13(2), 316-322.
- Zhao R., Du B., Zhang L., and Zhang L. (2016), "A robust background regression-based score estimation algorithm for hyperspectral anomaly detection," *ISPRS J. Photogram. Remote Sens.*, vol. 122, pp. 126–144.

- Zhao, R., Shi, Z., Zou, Z., & Zhang, Z. (2019). Ensemble-based cascaded constrained energy minimization for hyperspectral target detection. *Remote Sensing*, 11(11), 1310.
- Zhao R., Du B., Zhang L., and Zhang L. (2016), “Beyond background feature extraction: An anomaly detection algorithm inspired by slowly varying signal analysis,” *IEEE Trans. Geosci. Remote Sens.*, vol. 54, no. 3, pp. 1757–1774.
- Zhong P., Gong Z., Shan J. (2019), “Multiple instance learning for multiple diverse hyperspectral target characterizations”, *IEEE Trans. Neural Netw. Learn. Syst.*
- Zhong, Y.; Wu, Y.; Xu, X.; Zhang, L (2015). “An adaptive subpixel mapping method based on map model and class determination strategy for hyperspectral remote sensing imagery”. *IEEE Trans. Geosci. Remote Sens.*, 53,1411–1426.
- Zhou W., Huang G., and Cadenasso M.L (2011), “Does spatial configuration matter? Understanding the effects of land cover pattern on land surface temperature in urban landscapes,” *Landscape Urban Plan.*, vol. 102, pp. 54–63.
- Zhou Z, Li X, Wright J, Candés E, Ma Y (2010) Stable principal component pursuit. In: 2010 IEEE International symposium on information theory, pp 1518–1522
- Ziemann, A., & Theiler, J. (2017). Simplex ACE: a constrained subspace detector. *Optical Engineering*, 56(8), 081808

Biodata

Amrita Bhandari, born on March 7th, 1987 in Fazilka (Punjab), completed her senior secondary education in Non-medical stream from Campus School, Hisar (Haryana), affiliated to CBSE Board. Thereafter, she joined B.Tech in Computer science and Engineering and received her degree with Honors from The Technological Institute of Textiles and Sciences, affiliated to Maharishi Dayanand University, Rohtak. Her M.Tech

degree with Gold medal (for being a university topper) was conferred upon her by The Thapar Institute of Engineering and Technology, Patiala (previously, Thapar University). She worked as a Functional Level Engineer (SAP and Salesforce Consultant) with The Trident Limited, Ludhiana immediately after the completion of her masters. Afterwards, she joined Bharati Vidyapeeth College of Engineering, New Delhi as Assistant Professor in the Department of Information Technology. In order to pursue her research interest, she joined as a research scholar in the Department of Civil Engineering under the supervision of Dr. K. C. Tiwari. During this research period, she also worked as a Research Associate under a project sponsored by ISRO, SAC Ahmedabad with Dr. K.C. Tiwari as PI. Her research area is “Target Detection and Enhancement in Hyperspectral data using Super resolution mapping”. She wants to pursue AI and ML based target detection applications and use target detection algorithms for various urban applications.